BULLETIN OF THE MINERAL RESEARCH AND EXPLORATION

2023 | 172 | ISSN : 0026-4563
E-ISSN : 2651-3048

CONTENTS

Research Articles

Erratum

LOCATION OF MANAGEMENT
Bilimsel Dokümantasyon ve Tanıtma Dairesi Başkanlığı
Maden Tetkik ve Arama Genel Müdürlüğü
Çukurambar Mahallesi
Dumlupınar Bulvarı No: 11 06530
Çankaya/ANKARA
e-mail: bilimsel_dairesi@mta.gov.tr

Bull. Min. Res. Exp. is indexed and abstracted in TR Dizin, Emerging Source Citation Index (ESCI), Scopus, The ICI Journals Master List (Copernicus), Directory of Open Access Journals (DOAJ), Open Academic Journals Index (OAJI), Georef, MIAR, EBSCO and Zoological Record.

The Bulletin of the Mineral Research and Exploration is published in three issues in a year. Each volume is published in Turkish and English in pdf format on the website of Bulletin of the Mineral Research and Exploration and English issue published in print. The English volüme of the "Bulletin of the Mineral Research and Exploration" can be obtained from "BDT Department" free of charge, either directly or ordered by adding postage fee from the correspondence address. Typesetting and printing operations are carried out and followed by the Publication Service of the Scientific Documentation and Publicity Department. e-mail: bilimsel_dairesi@mta.gov.tr

The section of "notes to the authors", format, copyright and other information can be obtained from www.mta.gov.tr as PDF files.

Printed Date: 08/12/2023
Printing House: Neyir Matbaacılık-Matbaacılar Sitesi 1341 cd. No: 62 İvedik OSB-Yenimahalle/Ankara
Phone: 0312 395 53 00 • Fax: 0312 395 84 20 • www.neyir.com
Periodical
ISSN: 0026-4563
E-ISSN: 2651-3048

Bulletin of the Mineral Research and Exploration

http://bulletin.mta.gov.tr

Determination of alteration zones applying fractal modeling and Spectral Feature Fitting (SFF) method in Saryazd porphyry copper system, central Iran

Behzad BEHBAHANI[a], Hamid HARATI[b*], Peyman AFZAL[c] and Mohammad LOTFI[a]

[a] *Islamic Azad University, Department of Geology, North Tehran Branch, Tehran, Iran*
[b] *Payame Noor University, Department of Geology, PO Box 19395-4697, Tehran, Iran*
[c] *Islamic Azad University, Department of Petroleum and Mining Engineering, South Tehran Branch, Tehran, Iran*

Research Article

Keywords:
Alteration, Spectral Feature Fitting (SFF) Method, Concentration-Area Fractal Model, Saryazd Porphyry System.

Received Date: 10.07.2021
Accepted Date: 13.03.2023

ABSTRACT

The target of this research is recognition of the alteration zones utilizing concentration-area fractal methodology according to the reflection of the main minerals of each alteration zone that enhanced by Spectral Feature Fitting (SFF) Method due to Advanced Space-borne Thermal Emission and Reflection Radiometer (ASTER) satellite images in Saryazd porphyry system, central Iran. The alterations and mineralization are developed in Eocene volcanics. Remote sensing results achieved by the SFF method and Concentration-Area (C-A) fractal modeling represent different parts of propylitic, argillic and phyllic alteration zones due to their intensity and pixel values. In addition, the results reveal that there is a ring-shaped structure in the alteration zones, which are correlated with results, derived from X-Ray Diffraction (XRD) analyses and field observations.

1. Introduction

Hydrothermal alteration and mineralized zones associated with porphyry mineralization systems were extended into wall rocks above and around intrusive bodies and their zoning could be an important exploration key to find mineralization in hydrothermal deposits (Pirajno, 2009). Remote sensing data have been utilized to recognize and mapping of different alteration zones. The potential of the recognition by remote sensing data was based on the wavelength variety and spectral power identification of their sensors (Abrams et al., 1983; Rutz-Armenta and Prol-Ledesma, 1998; Çorumluoğlu et al., 2015; Vural et al., 2015; Yazdi et al., 2018; Vural and Aydal, 2020). The short wave infrared (SWIR) spectral domain as an electromagnetic wavelength's portion is one of the essential implements for in recognizing different alteration zones (Sabins, 1999; Hewson et al., 2001; Tangestani and Moore, 2001; Sadeghi et al., 2013; Aramesh et al., 2015; Fakhari et al., 2019). In this study, the SFF method has been utilized to recognize these main minerals for alteration zones such as kaolinite, muscovite, chlorite and hematite. The different parts of the alteration zones were separated utilizing C-A fractal approach to find boundary of each alteration zone and classification them to boundary between each alteration zone and their classification to identify prospect area in Saryazd.

2. Regional Geology

The Urumieh-Dokhtar Magmatic Belt (UDMB) as an Andean-type magmatic arc extends for 2000 km

Citation Info: Behzad, B., Harati, H., Afzal, P., Lotfi, M. 2023. Determination of alteration zones applying fractal modeling and Spectral Feature Fitting (SFF) method in Saryazd porphyry copper system, central Iran. Bulletin of the Mineral Research and Exploration 172, 1-14. https://doi.org/10.19111/bulletinofmre.1264604

**Corresponding author: Hamid HARATI, hamid.harati437@yahoo.com*

from NW to SE and is considered as subduction-related calc-alkaline and alkaline rock masses (Berberian and King, 1981; Hassanzadeh, 1993; Ricou 1994; Moradian, 1997; Mohajjel et al., 2003; Alavi, 2004; Omrani et al., 2008; Agard et al., 2011). The major porphyry copper, molybdenum and gold ores in Iran occurred along the UDMB. Middle segment of the UDMB includes numerous porphyry-related copper deposits and prospects (Ahmadfaraj et al., 2019; Sabahi et al., 2019; Jebeli et al., 2020).

Three major periods of magmatism and associated Cu mineralization are identified along the UDMB during Eocene–Oligocene, Middle to Late Oligocene and Middle to Late Miocene episodes (Shahabpour and Kramers, 1987; Kirkham and Dunne, 2000; McInnes et al., 2005; Jahangiri 2007; Razique et al., 2007; Ahmadian et al., 2008; Ghorbani and Bezanjani, 2011; Asadi et al., 2014). Several Cu mineralization/ deposits in the UDMB were simultaneously formed during the emplacement of Miocene granodiorite to quartz-monzonite intrusions (Zarasvandi et al., 2015). Several porphyry deposits/occurrences were discovered in the central section of the UDMB such as Darreh Zereshk (Aghazadeh et al., 2015; Zarasvandi et al., 20015), Kahang (Afzal et al., 2012), Dali (Asadi Haroni and Sansoleimani, 2012; Ayati et al., 2013) and Zafarghand (Behbahani et al., 2013*a, b*).

2.1. Geology of Saryazd

The Saryazd porphyry system is situated in western border of the crustal central Iranian block, central Iran. There is an intersection between the UDMB and the Central Iranian block (Figure 1). The lithology of the Saryazd area consists Eocene volcanic rocks such as tuff breccia, tuff and devitrified pyroclastics, Olivine-pyroxene basalts, quartz porphyry to monzogranite and quartz monzodiorite porphyry intrusions with outcrops in SW part of the study area. These units infiltrated in volcanics and micritic limestones and thereby caused alteration and mineralization in volcanics. All these rocks are covered by Quaternary alluvial sediments. The main faults predominate in the center of the study area with a NNE - SSW trend in the studied area (Figure 2, Behbahani, 2017).

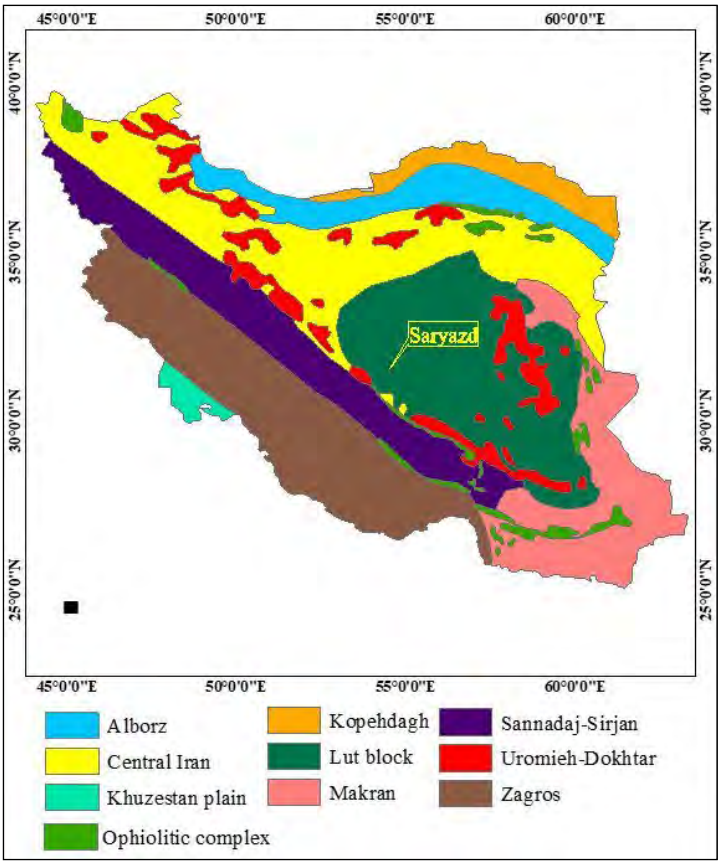

Figure 1- Main geological subdivisions of Iran (modified after Stöcklin, 1968, 1977; Nabavi, 1976).

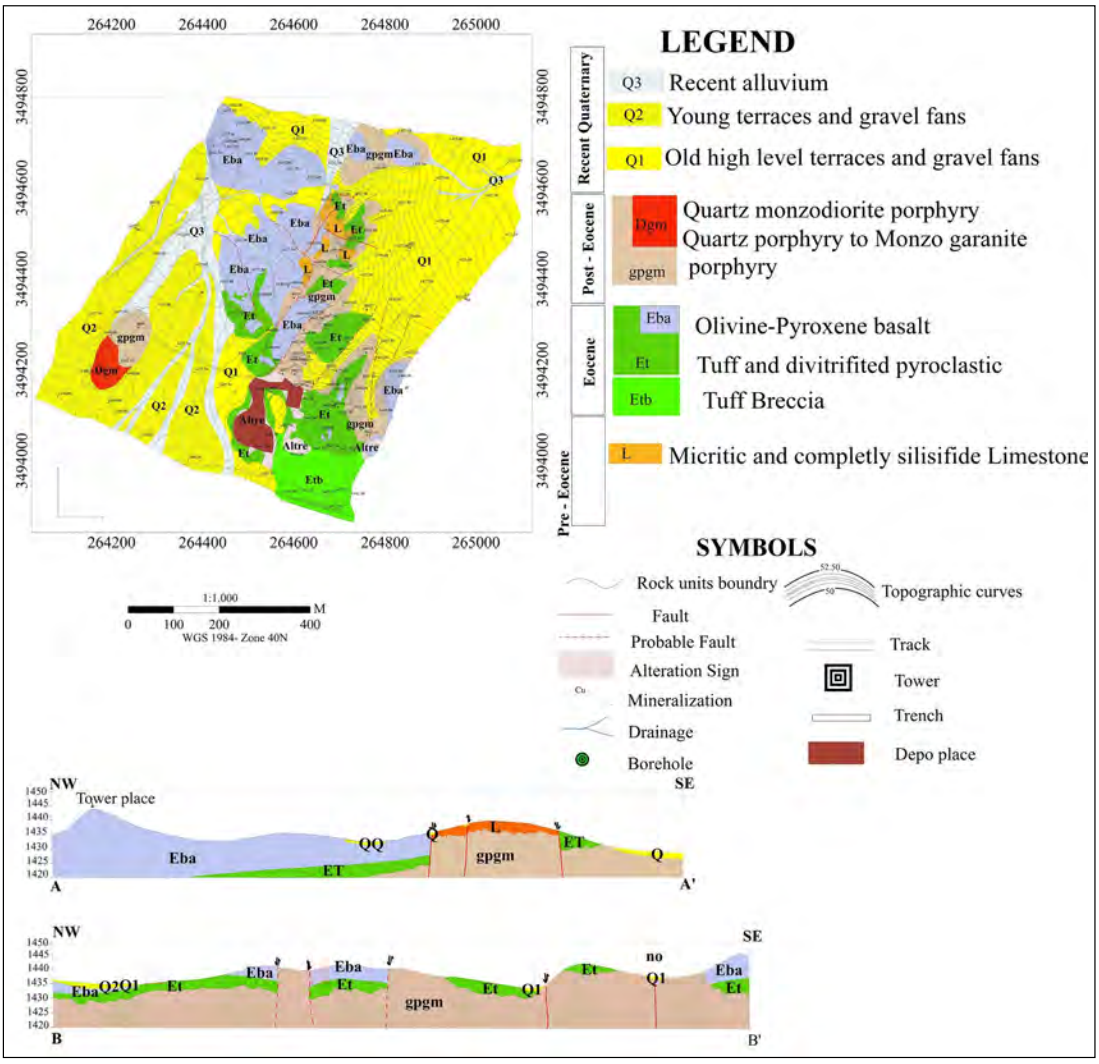

Figure 2- Geological map of the Saryazd system.

3. Methodology

3.1. Spectral Feature Fitting

The SFF method is an absorption feature based technique for corresponding image spectral to situation end members which improved by the U.S. Geological Survey (USGS; Clark et al., 1992; Kruse et al.,1993*a*, *b*; Kruse and Lefkoff, 1993, Swayze and Roger, 1995; Zamyad et al., 2019). Methodology for interpretation of hyper spectral data has still not directly recognized minerals. They represent similarity of a mineral to another known material. In addition, direct methods for identification of different minerals are based on specific spectral features extraction (Yamaguchi and Lyon, 1986; Clark et al., 1987; Kruse, 1988; 1990; Clark and Swayze, 1995). Moreover, the SFF method needs to reduce data to reflectance and remove a continuum from the reflectance data prior to analyses. A continuum is a mathematical function applied to isolate a particular absorption feature for analyses (Clark and Roush, 1984; Kruse et al., 1985; Clark et al., 1992).

3.2. Concentration-Area (C-A) Fractal Model

Cheng et al. (1994) established the C–A fractal model that is applied to detect background and anomalies for various data (pixel value in this scenario) as follows:

$$A(\rho \leq \upsilon) \propto \rho^{-\alpha_1} \boldsymbol{\rho}^{-\alpha_1};\ A(\rho \geq \upsilon) \propto \rho^{-\alpha_2} \boldsymbol{\rho}^{-\alpha_1}\, \boldsymbol{\rho}^{-\alpha_2}$$

The A (ρ) denotes the area with pixel values greater than the value ρ; υ indicates a threshold; and α_1 and α_2 are fractal dimensions. The breaking points between line segments on a C-A logarithmic plot and the corresponding values of ρ have been applied as thresholds to distinguish pixel values into various components, at the similar time showing different items, such as geological and geochemical differences (Goncalves et al., 2001; Lima et al., 2003; Aliyari et al., 2020). Cheng and Li (2002) utilized the C-A model for interpretation of Thematic mapper (TM) images in Mitchell - Sulphurets Cu - Au porphyry system, NW of Canada. Moreover, Afzal et al. (2012) used the fractal modeling for separation of different alteration zones in Khoshnameh area, central Iran. Zamyad et al. (2019) used fractal modeling for classification of alteration zones in Tirka copper mineralization (NE Iran).

4. Application of C-A Fractal Modeling

In this paper, the ASTER data in SWIR used to recognize the alteration zones in various Saryazd porphyry systems. First, the image was corrected and the ENVI 4.7 software and the SFF method was used to extract and map the spectrum of the kaolinite, muscovite, hematite and chlorite, which are the main alteration mineral of porphyry systems (Figure 3 and 4). The related pixels of alteration zones for main mineralization were enhanced and their values were

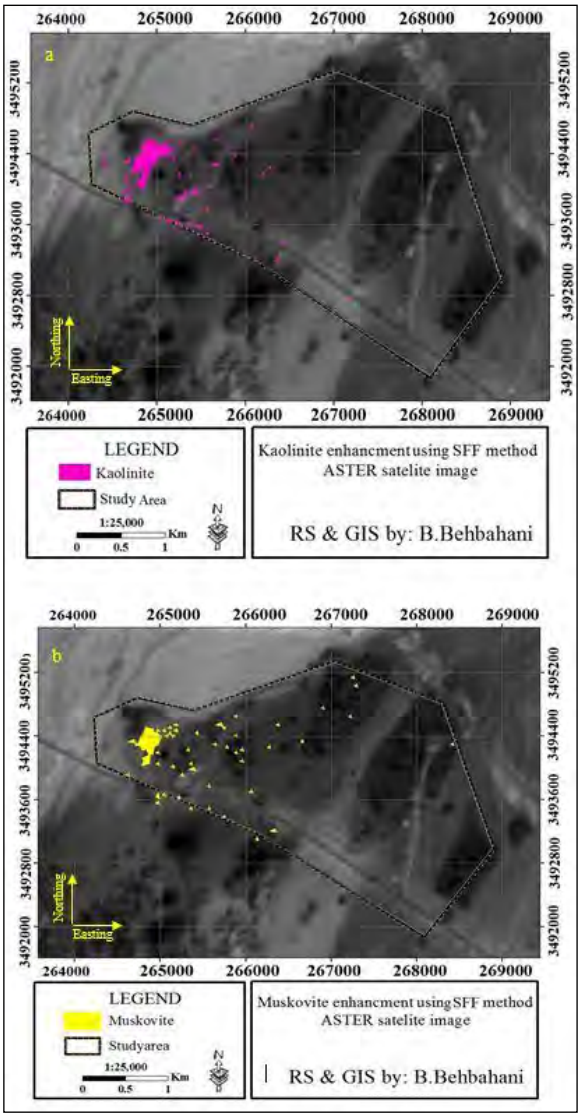

Figure 3- Main minerals of porphyry alteration enhanced by SFF method; a) kaolinite and b) muscovite.

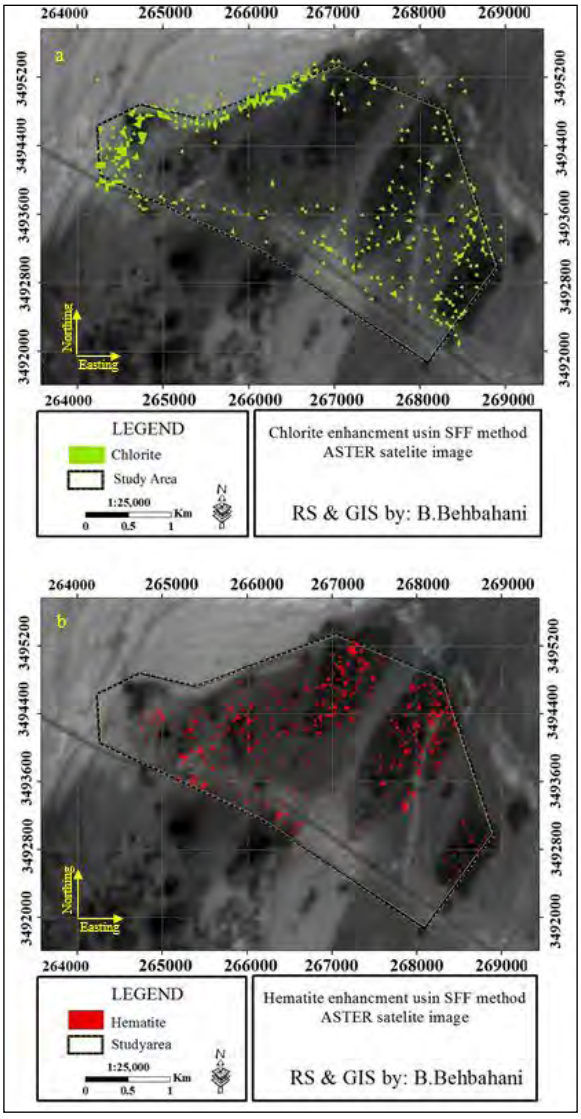

Figure 4- Main minerals of porphyry alteration enhanced by SFF method; a) hematite and b) chlorite.

reclassified using the C-A fractal model and log-log plots were produced for alteration zones (Figure 5 and 6). C-A log-log plot for kaolinite, the main mineral of the argillic alteration reveals five populations (Table 1). The first population is covering pixels by values lower than 31, which is distributed at the NW of the study area. Main populations occurring in the NW part of this area include values higher than 100. Moreover, the last population of kaolinite consists of the pixels by values, which are more than 158. This population includes pixels of the kaolinite at the NW and central sections of the Saryazd region (Figure 7a). Based on the fractal modelling, most parts of the argillic alteration zone are high intensity, which contain pixel values higher than 100. The C-A method for muscovite, being the main mineral of the phyllic alteration, reveals four fractal populations with the first population involving pixel values lower than 141. The main populations have pixel values higher than 186, which is situated at the NW portion of the study area. Furthermore, the last population for muscovite comprises pixel values more than 234 which is located at the NW of the Saryazd system (Figure 7b). The C-A method for chlorite reveals five populations that are distributed in the marginal parts of the studied area, as depicted in Figure 8a. Major populations of chlorite consist of pixel scores > 173 that are distributed in the NW, SE and central sections of the studied area. However, the final population of chlorite pixel values is situated at the NE and central parts of the study system and included the values more than 229. The C-A fractal modeling for hematite shows five major populations that contain pixel values higher than 173 in the SE and NW of the studied area. The last population of hematite pixel values are located in all the parts of the area, which are higher than 218 (Figure 8b).

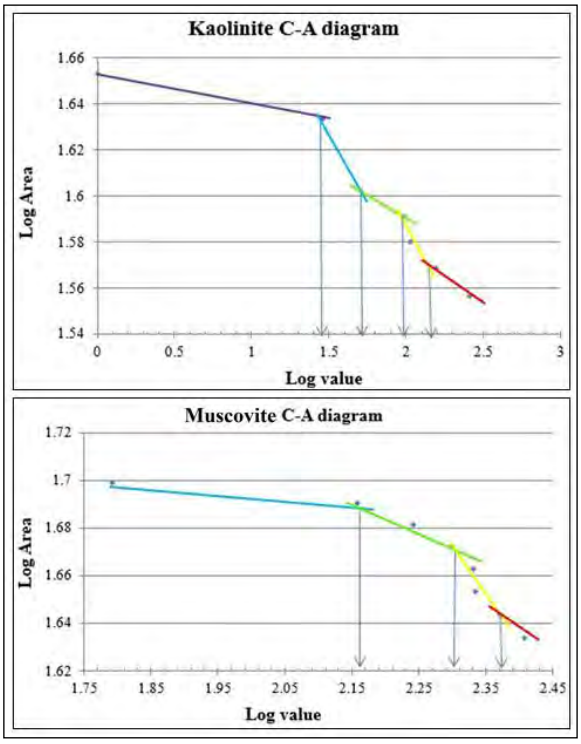

Figure 5- Log - Log plots for pixel values of kaolinite and muscovite.

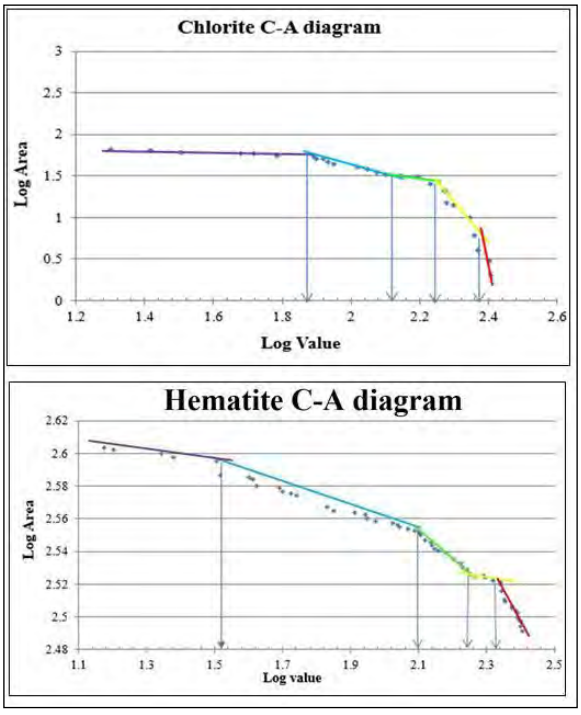

Figure 6- Log - Log plots for pixel values of chlorite and hematite.

Table 1- Specified population pixel values for alterations main minerals using C-A fractal model.

Mineral	1st population	2nd population	3rd population	4th population	5th population
Kaolinite	0-31	31-50	50-100	100-158	158<
Muscovite	0-141	141-186	186-234	234<	-
Chlorite	0-83	83-120	120-173	173-22	229<
Hematite	0-34	34-138	138-173	173-218	218<

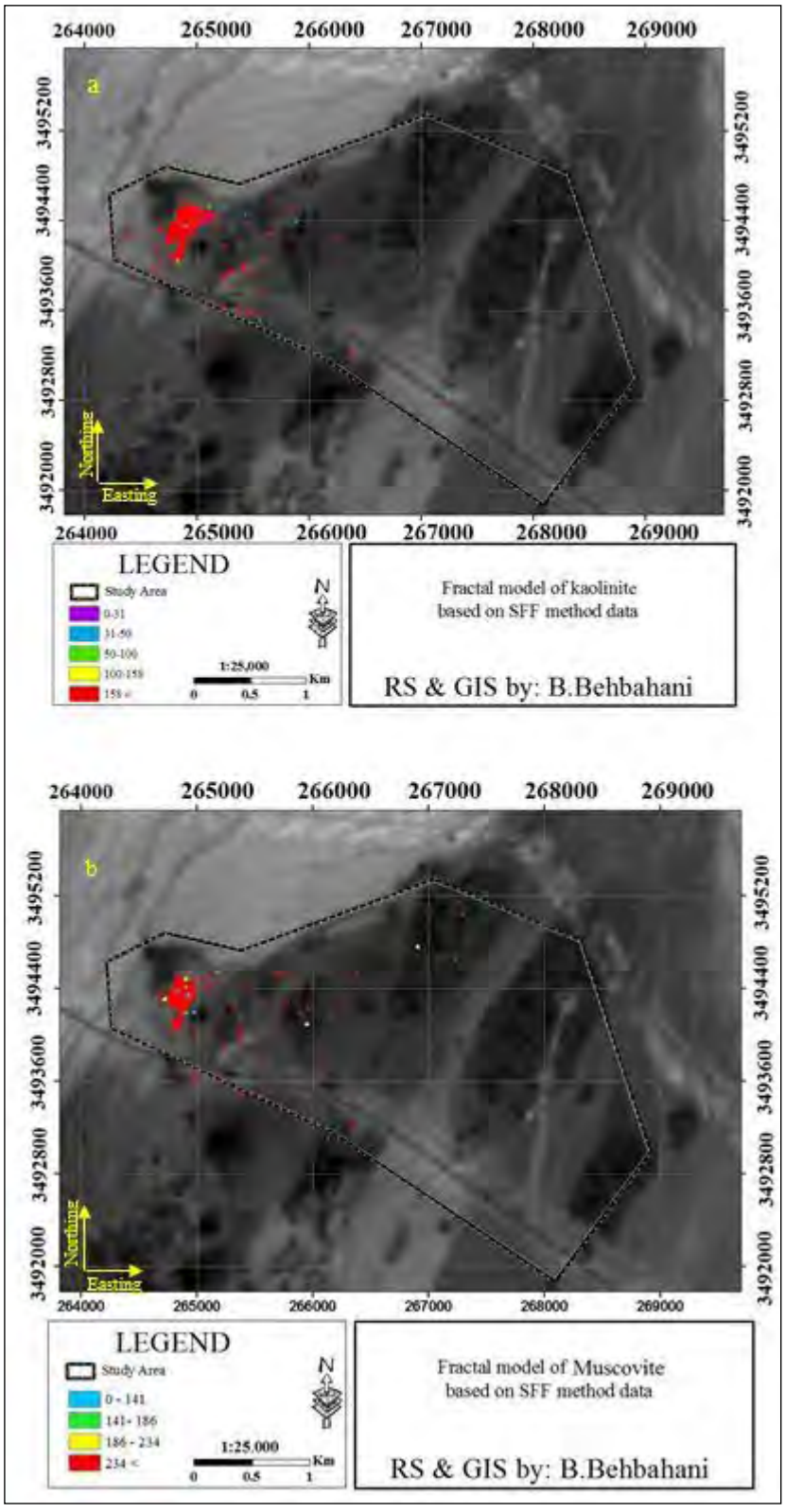

Figure 7- C-A fractal model for; a) kaolinite and b) muscovite pixel values based on SFF method data in 314 the Saryazd porphyry system.

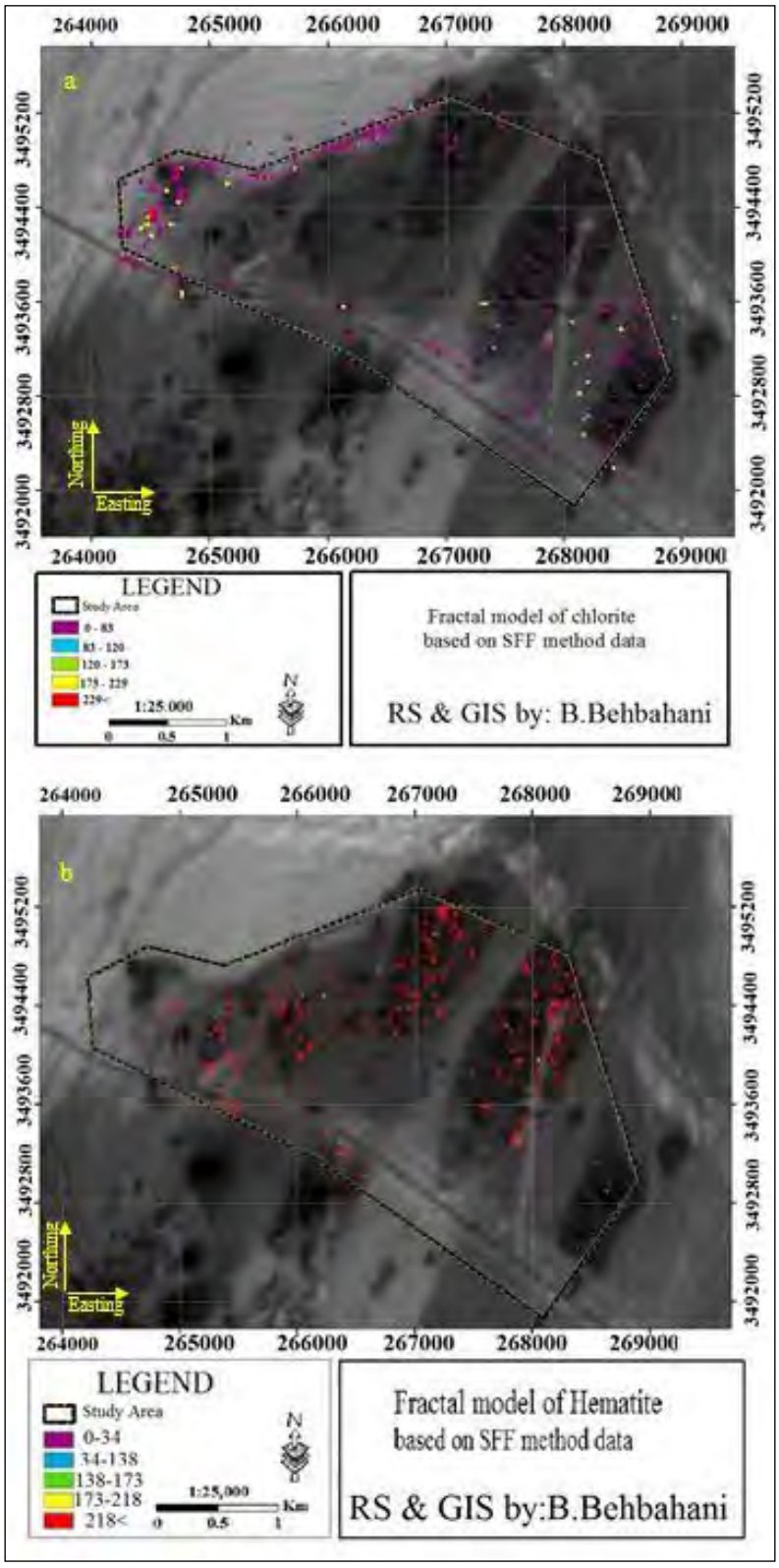

Figure 8- C-A fractal model for; a) chlorite and b) hematite pixel values based on SFF method data in the 345 Saryazd porphyry system.

5. Validation Result with Geological Characteristics

XRD is an appropriate method for mineral analyses (Faheem et al., 2015; Gold et al., 1983). In this research, 21 samples of XRD data were used to determine the minerals of the alteration zones, (Table 1 and Figure 9), thereby determining the accuracy of remote sensing results and the C-A in the Saryazd area (Figure 10). The comparison between the XRD results and C-A fractal modeling shows that pixels marked as high intensity alteration zones are correlated with the altered samples, as depicted in Table 1. Some samples like STZ12 have a series of the main alteration minerals consisting of argillic, phyllic and iron oxide (Table 2).

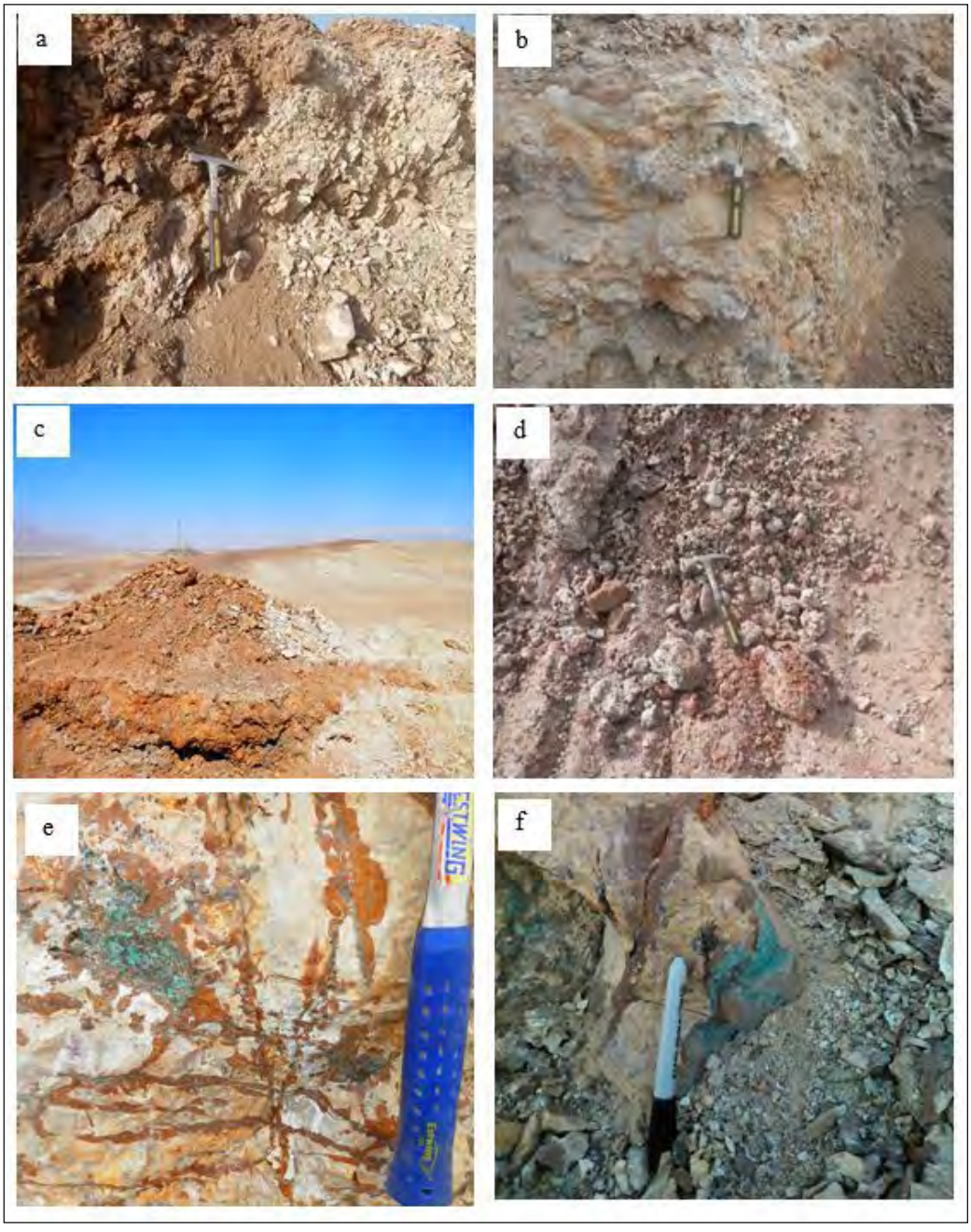

Figure 9- Altered and mineralized parts of the studied area; a) argillic alteration, b) advanced argillic and 348 phylic alterations, c) iron oxide mineralization as siderite, goethite and limonite, d) hematite and argillic 349 alteration, e) stock work structure and mineralization as goethite and malachite which is accorded in 350 Crossed streaks, f) Cu and Fe oxide mineralization in border of Saryazd porphyry system.

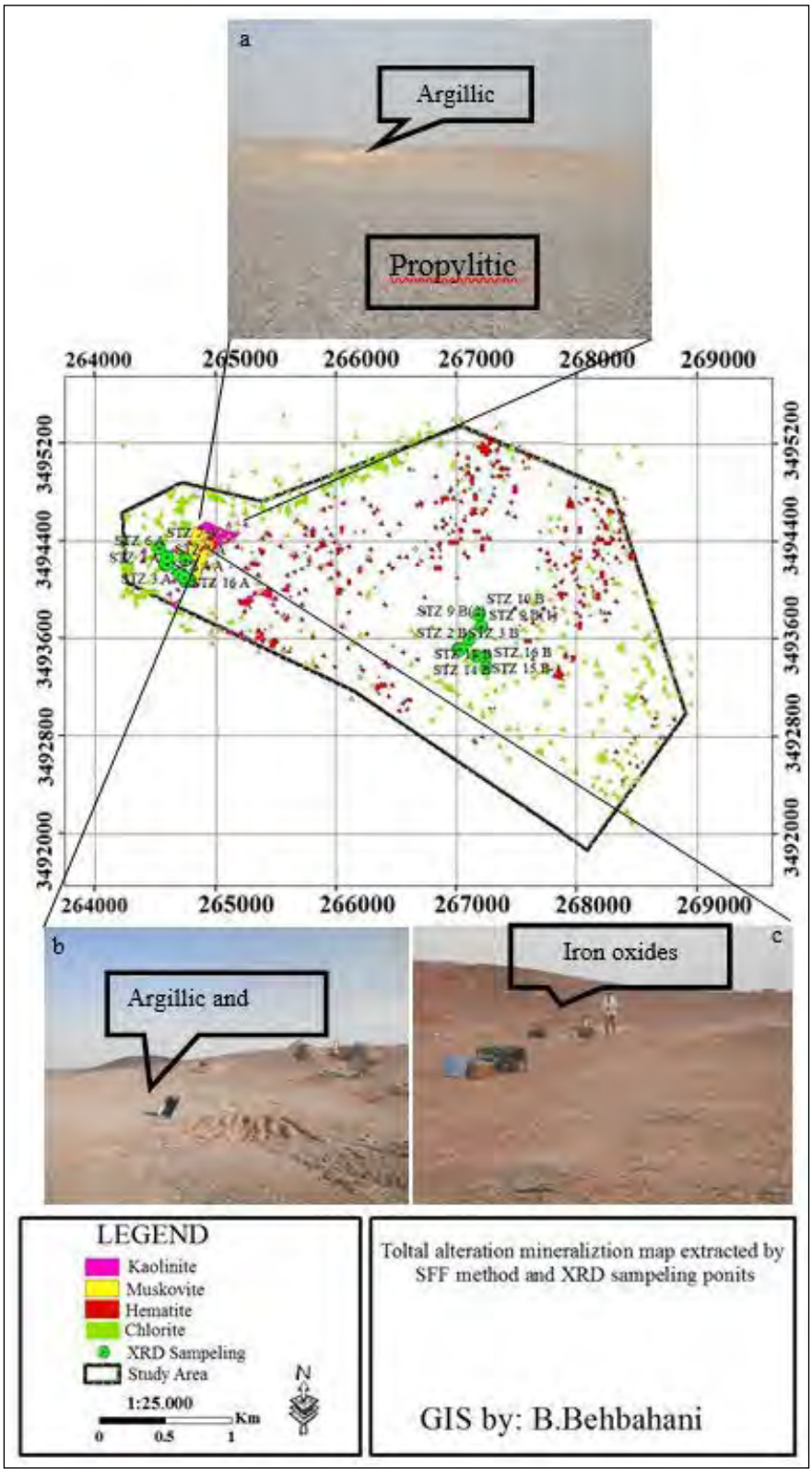

Figure 10- The correlation map of the XRD sampling by ground geology and remote sensing The images 385 show the alteration zones in the data in the Saryazd district; a) argillic and propylitic, b) argillic and 386 phylic, c) Iron oxide alterations out crops.

Table 2- XRD analysis results for alterations of the Saryazd porphyry system.

Samples	Major Phase(s)	Minor Phase(s)
STZ 1 A	Quartz Albite Orthoclase ($KAlSi_3O_8$)	Muscovite-Illite
STZ 2 A	Quartz Albite Orthoclase	Muscovite-Illite Montmorillonite
STZ 3 A	Quartz Albite Orthoclase	Illite
STZ 4 A	Quartz Orthoclase Barite	Kaolinite
STZ 5 A	Quartz Orthoclase	Kaolinite Barite
STZ 6 A	Quartz Albite Orthoclase	Muscovite-Illite
STZ 7 A	Quartz Albite Orthoclase	Muscovite-Illite Calcite Kaolinite Montmorillonite
STZ 10 A	Quartz Orthoclase Montmorillonite Albite	Kaolinite Muscovite-Illite
STZ 12 A	Quartz	Orthoclase Muscovite-Illite Kaolinite Hematite
STZ 14 A	Orthoclase Quartz	Kaolinite Hematite
STZ 15 A	Quartz Orthoclase	Albite Muscovite-Illite Chlorite
STZ 16 A	Albite Quartz Orthoclase	Calcite Kaolinite Muscovite - Illite
STZ 2 B	Quartz Albite Calcite Orthoclase	Kaolinite Muscovite-Illite Dolomite
STZ 3 B	Albite Quartz Calcite	Chlorite Muscovite-Illite
STZ 9 B(1)	Albite Quartz Calcite	Chlorite Muscovite-Illite
STZ 9 B(2)	Quartz Albite Calcite Microcline	Muscovite-Illite
STZ 10 B	Quartz Gypsum Anhydrite	Bassanite Kaolinite Muscovite-Illite
STZ 11 B	Albite Orthoclase Quartz	Kaolinite Hematite
STZ 14 B	Quartz Albite Orthoclase	Calcite Muscovite-Illite Kaolinite Hematite
STZ 15 B	Quartz Orthoclase	Muscovite- Illite Kaolinite
STZ 16 B	Halite	Gypsum Quartz Anhydrite Muscovite-Illite

6. Conclusions

According to the results derived from the C-A fractal modeling and SFF method on the remote sensing data, the high intensity alteration zones were located in the NW of the Saryazd area. The argillic and phyllic alteration zones (kaolinite-muscovite) predominate in this part of the study area where the major Cu mineralization occurs. As mentioned before, the high pixels, which are enhanced by the SFF method, are related to the chlorite. The pixel value of the chlorite is higher than the others, which is the margin of the porphyry system. Moreover, the XRD analyses of the alteration samples validated the results obtained from the SFF and fractal analysis. Consequently, the C-A approach for pixels extracted by the SFF method identified a ring structure in alteration zones, which may also indicate a porphyry mineralization.

References

Abrams, M. J., Brown, D., Lepley, L., Sadowski, R. 1983. Remote sensing for porphyry copper deposits in southern Arizona. Economic Geology 78(4), 591-604.

Afzal, P., Fadakar Alghalandis, Y., Moarefvand, P., Rashidnejad Omran, N., Asadi, H. 2012. Application of power -spectrum – volume fractal method for detecting hypogene, supergene enrichment, leached and barren zones in Kahang porphyry Cu deposit, Central Iran. Journal of Geochemical Exploration 112, 131-138.

Agard, P., Omrani, J., Jolivet, L., Whitechurch, H., Vrielynck, B., Spak-man, W., Monié, P., Meyer, B., Wortel, R., 2011. Zagros orogeny: a subduction-dominated process. Geological Magazine 148, 692–725.

Aghazadeh, M., Houb, Z.G., Badrzadeh, Z., Zhou, L. 2015. Temporal – spatial distribution and tectonic setting of porphyry copper deposits in Iran: constraints from zircon U–Pb and molybdenite Re–Os geochronology. Ore Geology Reviews.

Ahmadian, J., Haschke, M., McDonald, I., Regelous, M., Ghorbani, M. R., Emami, M., Murata, M., 2008. High magmatic flux during Alpine–Himalayan collision: constraints from the Kal-e-Kafi complex, central Iran. Geological Society of America Bulletin.

Ahmadfaraj, M., Mirmohammadi, M., Afzal, P., Yasrebi, A. B., Carranza, E. J., 2019. Fractal modeling and fry analysis of the relationship between structures and Cu mineralization in Saveh region, Central Iran. Ore Geology Reviews 107, 172-185.

Alavi M. 2004. Regional stratigraphy of the Zagros fold - thrust belt of Iran and its proforeland evolution. American Journal of Science 304, 1–20.

Aliyari, F., Afzal, P., Lotfi, M., Shokri, S., Feizi, H. 2020. Delineation of geochemical haloes using the developed zonality index model by multivariate and fractal analysis in the Cu – Mo porphyry deposits. Applied Geochemistry 121, 104694.

Aramesh Asl, R., Afzal, P., Adib, A., Yasrebi, A. 2015. Application of multifractal modeling for the identification of alteration zones and major faults based on ETM+ multispectral data. Journal of the Indian Society of Remote Sensing 43(1), 121-132.

Asadi, S., Moore, F., Zarasvandi, A. 2014. Discriminating productive and barren porphyry copper deposits in the southeastern part of the central Iranian volcano-plutonic belt, Kerman region, Iran: a review. Earth Science Reviews 138, 25-46.

Asadi Haroni, H., Sansoleimani, A. 2012. Prospecting activities at Dalli Cu - Au porphyry deposit, central province of Iran, Iran. Lahijan Research Journal, University of Lahijan 15(6), 34-46 (in Persian with English abstract).

Ayati, F., Yavuz, F., Asadi, H. H., Richards, J. P., & Jourdan, F. 2013. Petrology and geochemistry of calc-alkaline volcanic and subvolcanic rocks, Dalli porphyry copper–gold deposit, Markazi Province, Iran. International Geology Review, 55(2), 158-184.

Behbahani, B. 2017. Presentation a genetic and exploratory model in Saryazd copper deposit (central Iran) based on geology, geochemical, geophysical and fluid inclusion data. PhD Thesis, Islamic Azad University North Tehran branch, 185.

Behbahani, B., Afzal, P., Jafari, M. R., Asadi harooni, H., Ajayebi, K. S., Noori, R. 2013*a*. Remote sensing studies in Zafarghand porphyry system for reconnaissance of prospects. Lahijan Research Journal, University of Lahijan 2(6), 1-10 (in Persian).

Behbahani B., Afzal P., Jafari M. R., Asadi harooni H., Ajayebi K. S. 2013*b*. Geophysical and Geochemical anomaly separation by concentration-area fractal model in Zafarghand Cu-Mo porphyry deposit, Isfahan province. Journal of the Earth, Islamic Azad University North Tehran 8(30), 25-37 (in Persian with English abstract).

Berberian, M., King, G. C. 1981. Towards a paleogeography and tectonic evolution of Iran.Canadian Journal of Earth Sciences 18, 210–265.

Cheng, Q., Agterberg, F. P., Ballantyne, S. B. 1994. The separation of geochemical anomalies from background by fractal methods, Journal of Geochemical Exploration, 51, 109-130

Cheng, Q., Li, Q. 2002. Fractal concentration - area method for assigning a color palette for image representation. Computers and Geosciences 28, 567-575.

Clark, R. N., and Roush,T. L. 1984. Reflectance spectroscopy: quantitative analyses techniques for remote sensing applications, Journal of Geophysical Research 89(7), 6329-6340.

Clark, R. N., King, T.V., Gorelick, N. S. 1987. Automatic continuum analyses of reflectance spectra: in Proceedings, Third AIS workshop, 2- 4 June 1987, JPL Publication, Jet Propulsion Laboratory, Pasadena, California, 138-142.

Clark, R. N., Swayze, G. A., Gallagher, A. 1992. Mapping the mineralogy and lithology of Canyonlands, Utah with imaging spectrometer data and the multiple spectral feature-mapping algorithm. In: Summaries of the Third Annual JPL Airborne Geoscience Workshop, JPL Publication 92-14, 1, 11–13.

Clark, R. N., Swayze, G. A. 1995. Mapping minerals, amorphous materials, environmental materials, vegetation, water, ice, and snow, and other materials: the USGS tricorder Algorithm. In: Summaries of the Fifth Annual JPL Airborne Earth Science Workshop, JPL Publication 95(1), 39–40.

Çorumluoğlu, O., Vural, A., Asri, I. 2015 Determination of Kula basalts (geosite) in Turkey using remote sensing techniques Journal of Arabian Geosciences 8, 10105–10117.

Faheem, M., Giridharan, R., Liang, Y., Van Der, P. 2015. Micro - XRD characterization of a Single Copper filled through Silicon. Journal of Materials Letters.

Fakhari, S., Jafarirad, A., Afzal, P., Lotfi, M. 2019. Delineation of hydrothermal alteration zones for porphyry systems utilizing ASTER data in Jebal - Barez area, SE Iran. Iranian Journal of Earth Sciences 11 (1), 80-92.

Ghorbani, M. R., Bezanjani, R. N. 2011. Slab partial melts from the metasomatizing agent to adakite, Tafresh Eocene volcanic rocks, Iran. Island Arc 20, 188–202.

Gold C. M., Cavell P. A., Smith D. G. W. 1983. Clay minerals in mixtures: samples preparation, analyses, and statistical interpretation. Clays and Clay Minerals 31(3), 191-199.

Goncalves, M. A., Mateus, A., Oliveira, V. 2001. Geochemical anomaly separation by multifractal modeling. Journal of Geochemical Exploration 72, 91–114.

Hassanzadeh J. 1993. Metallogenic and tectonomagmatic events in the SE sector of the Cenozoic active continental margin of central Iran (Shahr e Babak area, Kerman Province). PhD Thesis, University of California, Los Angeles (unpublished).

Hewson, R. D., Cudahy, T. J., Hunting, J. F. 2001. Geologic and alteration mapping at Mt Fitton, South Australia, using ASTER satellite - borne data. Institute of Electrical and Electronics Engineers 2, 724-726.

Jahangiri, A. 2007. Post-collisional Miocene adakitic volcanism in NW Iran: Geochemical and geodynamic implications. Journal of Asian Earth Sciences (30), 433–447.

Jebeli, M., Afzal, P., Pourkermani, M., Jafarirad, A. 2020. Characteristics of fluid inclusions in the Cenozoic volcanic - hosted Kushk-e-Bahram Manto - type Cu deposit of central Iran. Geologos 26 (2), 127-137.

Kirkham, R. V., Dunne, K. P. 2000. World distribution of porphyry, porphyry-associated skarn, and bulk - tonnage epithermal deposits and occurrences. Geological Survey of Canada 3792, 26.

Kruse, F. A. 1988. Use of Airborne Imaging Spectrometer data to map minerals associated with hydrothermally altered rocks in the northern Grapevine Mountains, Nevada and California. Remote Sensing of Environment 24(1), 31-51.

Kruse, F. A. 1990. Artificial intelligence for nalyses of imaging spectrometer Data: Proceedings, ISPRS Commission VII, Working Group 2 analyses of high spectral resolution imaging data. 17 - 21 September 1990, Canada, 59 -68.

Kruse, F. A., Lefkoff, A. B. 1993. Knowledge - based geologic mapping with imaging spectrometers. Remote Sensing Reviews, Special Issue on NASA Innovative Research Program (IRP) results, 8, 3-28.

Kruse, F. A., Raines, G. L., Watson, K. 1985. Analytical techniques for extracting geologic information from multichannel airborne spectroradiometer and airborne imaging spectrometer data: in Proceedings, International Symposium on Remote

Sensing of Environment, Thematic Conference on Remote Sensing for Exploration Geology, 4th Thematic Conference, Environmental Research Institute of Michigan, Ann Arbor, 309-324.

Kruse, F. A., Lefkoff, A. B., Boardman, J. W., Heidebrecht, K. B., Shapiro, A. T., Barloon, J. P., Goetz, A. F. H. 1993*a*. The spectral image processing system (SIPS) - interactive visualization and analyses of imaging spectrometer data. Remote Sensing of Environment 44, 145-163.

Kruse, F. A., Lefkoff, A. B., Dietz, J. B. 1993*b*. Expert System-Based Mineral Mapping in northern Death Valley, California/Nevada using the Airborne Visible/Infrared Imaging Spectrometer (AVIRIS). Remote Sensing of Environment, Special issue on AVIRIS 44, 309-336.

Lima, A., De Vivo, B., Cicchella, D., Cortini, M., Albanese, S. 2003. Multifractal inverse distance weighting interpolation and fractal filtering method in environmental studies: an application on regional stream sediments of (Italy), Campania region. Applied Geochemistry 18, 1853-1865.

McInnes, B. I. A., Evans, N. J., Fu, F. Q., Garwin, S. 2005. Application of thermochronology to hydrothermal ore deposits. Reviews in Mineral Geochemistry 58, 467-498.

Mohajjel, M., Fergusson, C.L., Sahandi, M.R. 2003. Cretaceous – Tertiary convergence and continental collision, Sanandaj - Sirjan Zone, Western Iran. Journal of Asian Earth Sciences 21, 397–412.

Moradian, A. 1997. Geochemistry, geochronology and petrography of feldspathoid bearing rocks in Urumieh-Dokhtar Volcanic Belt, Iran. PhD Thesis, University of Wollongong, 412, Australia.

Nabavi, M. H. 1976. An introduction to geology of Iran (in Persian). Geological Survey of Iran, Tehran.

Omrani, J., Agard, P., Whitechurch, H., Benoit, M., Prouteau, G., Jolivet, L. 2008. Arcmagmatism and subduction history beneath the Zagros Mountains, Iran: a new report of adakites and geodynamic consequences. Lithos 106, 380–398.

Pirajno, F. 2009. Hydrothermal Processes and Mineral Systems. Geological Survey of Western Australia, Springer, 111-114

Razique, A., Lo Grasso, G., Livesey, T. 2007. Porphyry copper – gold deposits at Reko Diq complex, Chagai Hills Pakistan. Proceedings of Ninth Biennial Society for Geology Applied to Mineral Deposits Meeting, Dublin.

Ricou, L. E. 1994. Tethys reconstruction: plates, continental fragments and their boundaries since 260 Ma from Central America to SoutheASTERn Asia. Geodinamica Acta (Paris) 7, 169–218.

Rutz-Armenta, J. R., Prol-Ledesma, R. M. 1998. Techniques for enhancing the spectral response of hydrothermal alteration minerals in thematic mapper images of central Mexico. International Journal of Remote Sensing 19, 1981–2000.

Sabahi, F., Afzal, P., Lotfi, M., Nezafati, N. 2019. Geological, fluid inclusion and isotopic characteristics of the Gardaneshir Zn – Pb deposit, central Iran. Geopersia 9 (2), 221-232.

Sabins, F. F. 1999. Remote sensing for mineral exploration. Ore geology reviews, 14(3-4), 157-183.

Sadeghi, B., Khalajmasoumi, M., Afzal, P., Moarefvand, P., Yasrebi, A. B., Wetherelt, A., Foster, P., Ziazarifi, A. 2013. Using ETM+ and ASTER sensors to identify iron occurrences in the Esfordi 1:100.000 mapping sheet of central Iran. Journal of African Earth Sciences 103–114.

Shahabpour, J., Kramers, J. D. 1987. Lead isotope data from the Sar Cheshmeh porphyry copper deposit, Kerman, Iranian Mineral Deposit 22, 278-281.

Stöcklin, J. 1968. Structural history and tectonics of Iran: a review. American Association of Petroleum Geologists Bulletin 52(7), 1229-1258.

Stöcklin, J. 1977. Structural correlation of the Alpine ranges between Iran and central Asia.

Swayze, G. A., and Roger N. C. 1995. Spectral identification of minerals using imaging spectrometry data: evaluating the effects of signal to noise and spectral resolution using the Tricorder Algorithm." Summaries of the 5th Annual JPL Airborne Earth Science Workshop.

Tangestani, M. H., Moore, F. 2001. Comparison of three principal component analyses techniques to porphyry copper alteration mapping: a case study in Meiduk area, Kerman, Iran. Canadian Journal of Remote Sensing 27,176–182.

Vural, A., Corumluoglu, O., Asri, I. 2015. Exploring Gördes zeolite sites by feature oriented principle component analysis of LANDSAT images. Caspian Journal of Environmental Sciences, 14(14), 285-298.

Vural, A., Aydal, D. 2020. Determination of Lithological Differences and Hydrothermal Alteration Areas by Remote Sensing Studies: Kısacık (Ayvacık-Çanakkale, Biga Peninsula, Turkey). Journal of Engineering Research and Applied Science

Journal of Engineering Research and Applied Science

Yamaguchi, Y., Lyon, R. J. P. 1986. Identification of clay minerals by feature coding of near - infrared spectra, Reno, Nevada, America.

Yazdi, Z., Jafarirad, A., Aghazadeh, M., Afzal, P., 2018. Alteration mapping for Porphyry copper exploration using ASTER and QuickBird multispectral images, Sonajeel Prospect, NW Iran. Journal of the Indian Society of Remote Sensing 46(10), 1581-1593.

Zamyad, M., Afzal, P., Pourkermani, M., Nouri, R., Jafari, M. R. 2019. Determination of hydrothermal alteration zones using remote sensing methods in Tirka area, Toroud, NE Iran. Journal of the Indian Society of Remote Sensing 47(11), 1817-1830.

Zarasvandi, A., Rezaci, M., Sadeghi, M., Lentz, D., Adelpour, M., Pourkaseb, H. 2015. Rare earth element signatures of economic and sub-economic porphyry copper systems in Urumieh-Dokhtar Magmatic Arc (UDMA), Iran. Ore Geology Reviews, 1428.

Bulletin of the Mineral Research and Exploration

http://bulletin.mta.gov.tr

Estimating the recurrence of earthquakes with statistical methods in the city of Bingöl, Eastern Türkiye: a district-based approach

Sadık ALASHAN[a,b,*], Kenan AKBAYRAM[a,b] and Ömer Faruk NEMUTLU[a,b]

[a]*Bingöl University, Centre for Energy, Environment and Natural Disasters, 12000 Bingöl, Türkiye.*
[b]*Bingöl University, Department of Civil Engineering, Bingöl University, 12000 Bingöl, Türkiye.*

Research Article

Keywords:
Bingöl, Earthquake Magnitude, Risk, Probability Functions, Karlıova Triple Junction.

ABSTRACT

This study discusses the temporal distribution of earthquake magnitudes in the city of Bingöl, near Karlıova Triple Junction. We determine the probability distributions and return periods of earthquakes for all districts of Bingöl. Bingöl has eight districts; namely Adaklı, Central, Genç, Karlıova, Kığı, Solhan, Yayladere, and Yedisu. In six of them, active faults were mapped previously (Adaklı, Central, Genç, Karlıova, Solhan, and Yedisu). We consider 5 time-dependent probability distributions for analysis. Using the annual maximum earthquake magnitudes, the best fit arises from the Gumbel distribution for Central, Karlıova, and Adaklı Districts. For the Genç District, where the least maximum earthquake magnitude is reported, the Weibull distribution gives the best fit. The return period and maximum annual earthquake magnitude relations suggest the following results. For the Central and Karlıova Districts along which maximum earthquake magnitudes are reported, every 250 years a 6.7 M, and 7.2 M occurs respectively. These results are compatible with the results of paleo-seismological data reported along the NAFZ and the EAFZ. For a 10-year return period, earthquake magnitudes reach 3.9 and 5.1 in all districts. It is important to note that in the Yedisu District, the maximum earthquake magnitudes seem as 5.1 M for the 1000-year return period, incompatible with previously published findings probably because of low quality seismic data in this region.

Received Date: 25.02.2022
Accepted Date: 19.01.2023

1. Introduction

Three major strike-slip fault zones of Eastern Mediterranean, the North Anatolian Fault Zone (NAFZ), the East Anatolian Fault Zone (EAFZ), and the Varto Fault Zone (VFZ), intersect at the Karlıova Triple Junction (KTJ) in the city of Bingöl, eastern Türkiye (Figure 1). The Bitlis-Zagros Active Thrust Zone (BZATZ), the tectonic boundary between the Eastern Turkish High Plateau and the Arabian Plate (Şengör, 1980), is also very close to Bingöl. Some of the active faults at the eastern end of the V-shaped area between the NAFZ and the EAFZ (e.g., Sudüğünü Fault, Sancak-Uzunpınar Fault Zone) are located in Bingöl (Figure 1b). Many devastating earthquakes, whose historical records date back to the 10th century, were reported in this region (Ambraseys, 1989, 1970; Ambraseys and Jackson, 1998; Köküm and Özçelik, 2020). This is supported by several intense earthquakes in Bingöl and its vicinity during the instrumental period (Table 1).

Although it is impossible to determine an exact date for an expected earthquake, the probable occurrence of earthquakes can be determined with a certain margin of error. Probability distribution functions play a strong role in determining earthquake risks. The statistical modelling of earthquakes is a method

Citation Info: Alashan, S., Akbayram, K., Nemutlu, Ö. F. 2023. Estimating the recurrence of earthquakes with statistical methods in the city of Bingöl, Eastern Turkey: a district-based approach. Bulletin of the Mineral Research and Exploration 172, 15-29. https://doi.org/10.19111/bulletinofmre.1239185

**Corresponding author: Sadık ALASHAN, sadikalashan@bingol.edu.tr*

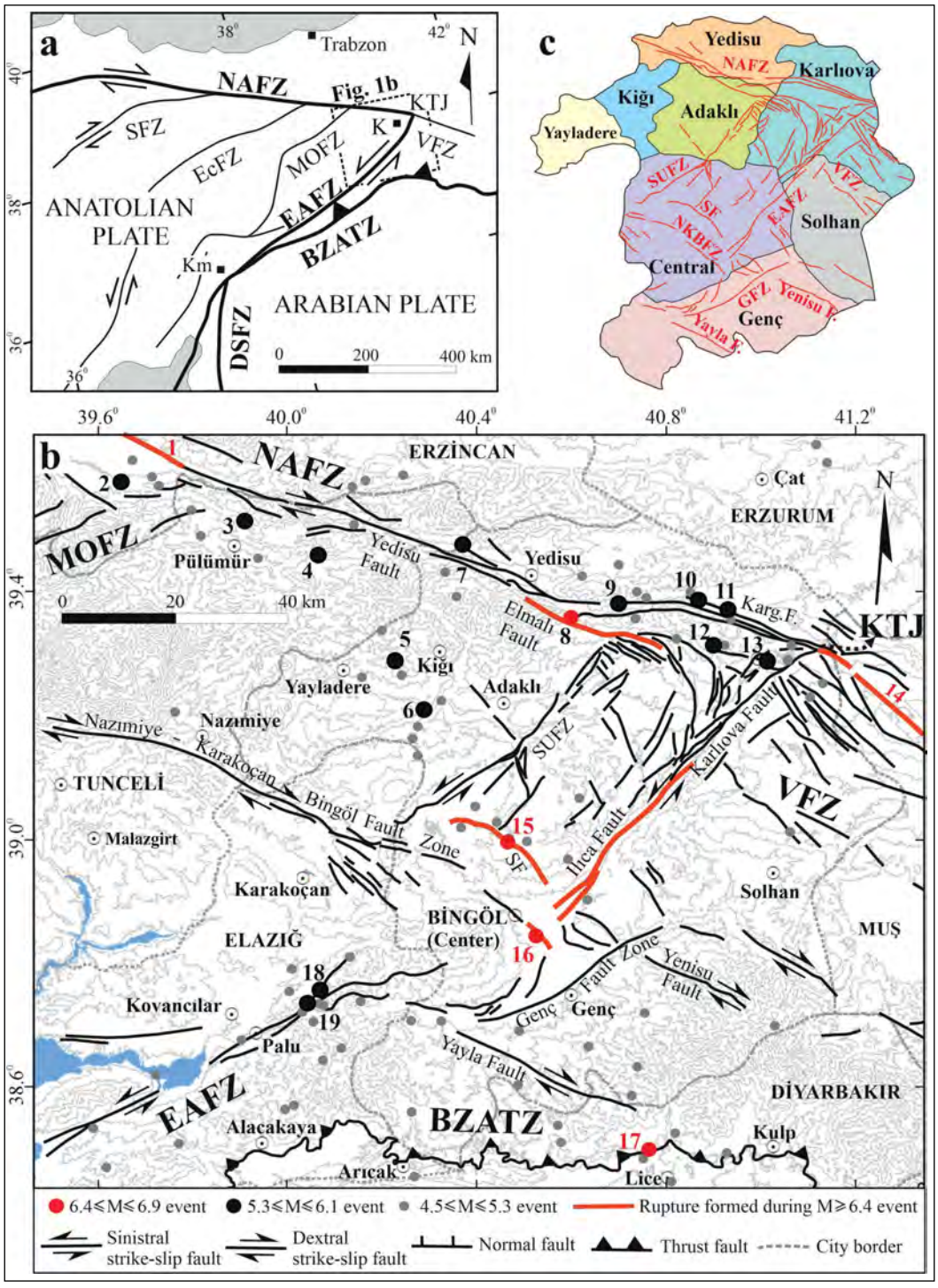

Figure 1- a) Simplified active tectonic map of Eastern and Southeastern Türkiye. Thick lines indicate plate boundary fault zones. Thin black lines are faults formed in the Anatolian Plate. b) The active fault map of the Bingöl and its surrounding. Gray lines are the elevation contours. For the location, see Figure 1a. The faults and their names are adapted from Emre et al. (2013) except Genç Fault Zone which is from Akbayram et al. (2022*a*). The earthquake data of numbered events are given in Table 1. Please note that the epicentre of events 1 and 15 are outside the map (cf., Table 1). The epicentre locations of events are borrowed from the online catalogue of the Kandilli Observatory and Earthquake Research Institute of Boğaziçi University (KOERI, 2022). c) The districts of Bingöl with the active fault zones. BZATZ: Bitlis Zagros Active Thrust Zone; DSFZ: Dead Sea Fault Zone; EAFZ: East Anatolian Fault Zone; EcFZ: Ecemiş Fault Zone; GFZ: Genç Fault Zone; K: Karlıova; Karg. F.: Kargapazarı Fault; Km: Kahramanmaraş; KTJ: Karlıova Triple Junction; MOFZ: Malatya Ovacık Fault Zone; NAFZ: North Anatolian Fault Zone; NKBFZ: Nazimiye Karakoçan Bingöl Fault Zone; SF: Sudüğünü Fault; SFZ: Sungurlu Fault Zone; SUFZ: Sancak Uzunpınar Fault Zone; VFZ: Varto Fault Zone.

Table 1- The seismic data of M≥5.3 earthquakes occurred along the area shown in Figure 1b, recorded in the instrumental period. 1: The epicentres of these events are outside Figure 1b, however, part of their rupture is shown in Figure 1b.

Event no	Magnitude	Date (dd/mm/yy)	Epicenter (N°) - (E°)	References
1[1]	7.9	26/12/1939	39.80 - 39.51	Kalafat et al. (2009), KOERI (2022)
2	6.1	27/01/2003	39.58 - 39.66	Kalafat et al. (2009), KOERI (2022)
3	5.8	15/03/1992	39.53 - 39.93	Tan et al. (2008), KOERI (2022)
4	5.7	05/12/1995	39.43 - 40.11	Tan et al. (2008), KOERI (2022)
5	5.3	02/12/2015	39.29 - 40.23	Altuncu et al. (2019)
6	5.3	06/25/2021	39.17 - 40.22	KOERI (2022)
7	5.9	26/07/1967	39.50 - 40.40	Eyidogan et al. (1991), McKenzie (1972), AFAD (2021)
8	6.9	17/08/1949	39.39 - 40.61	Ambraseys and Jackson (1998), Nalbant et al. (2002)
9	5.9	14/06/2020	39.37 - 40.74	Akbayram et al. (2022b)
10	5.4	23/03/2005	39.41 - 40.80	Demirtaş (2019), KOERI (2022)
11	5.6	12/03/2005	39.41 - 40.86	Demirtaş (2019), KOERI (2022)
12	5.9	14/03/2005	39.41 - 40.81	Demirtaş (2019), KOERI (2022)
13	5.7	06/06/2005	39.38 - 40.84	KOERI (2022)
14	6.9	19/08/1966	39.17 - 41.56	Tan et al. (2008), KOERI (2022)
15	6.4	01/05/2003	39.04 - 40.53	Kalafat et al. (2009), KOERI (2022)
16	6.8	22/05/1971	38.83 - 40.52	Taymaz et al. (1991), KOERI (2022)
17	6.0	06/09/1975	38.51 - 40.77	Tan et al. (2008), KOERI (2022)
18	6.1	08/03/2010	38.76 - 40.08	Tan et al. (2011), KOERI (2022)
19	6.8	08/03/2010	38.70 - 40.05	USGS (2022)

that applies a simple point process approach to various properties of documented seismicity (Hagiwara, 1974; Rikitake, 1974; Utsu, 1984; Anagnos and Kiremidjian, 1988; Campbell et al., 2002; Çobanoğlu et al., 2006;). The best-fit statistical models can be used to predict long-term earthquake generation process in a given area (Hainzl et al., 2006; Shelly et al., 2007; Wu et al., 2013). Gumbel (Gumbel, 1941), Gaussian (Rikitake, 1974), Lognormal (Nishenko and Buland, 1987), Gamma (Bak et al., 2002; Utsu, 1984), and Weibull (Hagiwara, 1974; Rikitake, 1974) statistical distributions of earthquakes used for computation of conditional probabilistic time-dependent seismic renewal models for future earthquakes (Parvez and Ram, 1999; Çobanoğlu et al., 2006; Tripathi, 2006; Yadav et al., 2010; Pasari and Dikshit, 2015, 2018). Determination of a suitable distribution model, which gives the best model for a given area, is important (Pasari and Dikshit, 2018) not only for forecasting future earthquakes but also for probabilistic seismic hazard analyses. The history and global applications of probabilistic modelling was summarized recently in Çoban and Sayıl (2020*a*, 2020*b*). Probabilistic seismic hazard analysis studies mainly focus on large sections (usually for hundreds of kilometers) of major faults (or deformation areas) such as North Anatolian Fault Zone (NAFZ), East Anatolian Fault Zone (EAFZ), Aegean Extensional Province and East Anatolian High Plateau (e.g., Öztürk et al., 2008; Polat et al., 2008; Öztürk and Bayrak, 2012; Şahin and Öksüm, 2021; Alkan and Bayrak, 2022; Çoban and Sayıl, 2020*a*, 2020*b*; Öztürk, 2011).

In this study, our aim is to make the best-fit statistical models to predict long-term earthquake potential in and around the Bingöl city (Figure 1b). Even though the seismicity in Bingöl is well-documented until now, there is no study concentrated solely on the probabilistic earthquake forecasting in this area. One study that conducted probabilistic seismic hazard analysis within the City of Bingöl (Balun et al., 2020) obtained parameters using various attenuation relationships and discussed the earthquake codes. In this study, we use the earthquake data of the Kandilli Observatory and Earthquake Research Institute of Boğaziçi University (KOERI, 2022) and compared the Gumbel, Gaussian (Normal), Lognormal, Gamma, and Weibull distributions to define the best probability distribution for each district of Bingöl. As a result, we identified the best-fitting probability model for the studied catalogue and discussed earthquake forecasting in the study area. Finally, we have calculated return periods and discussed their correlation with the available paleo-seismological data.

2. Short Note on the Seismicity of Bingöl in the Instrumental Period

Figure 1b shows the active fault map of the city of the Bingöl city and surrounding. The red faults are the ruptured fault segments during 6.4≤M≤6.9 events according to the MTA active fault database (Emre et al., 2013). All of the other faults (black lines in Figure 1b) are active faults that did not rupture in the instrumental period. Hence, they can be the sources of the next major earthquakes (Akbayram et al., 2022*a*). Bingöl city has eight districts; namely Adaklı, Central, Genç, Karlıova, Kiğı, Solhan, Yayladere and Yedisu (Figure 1c). In this study, we have calculated the earthquake statistics for each district. Thus, in this section, we introduce the faults and their seismicity based on the districts they are located.

2.1. The Seismicity of the NAFZ in Karlıova, Yedisu and Adaklı Districts of Bingöl

According to Emre et al. (2013), the destructive 6.9 Ms, 1949 earthquake occurred on the Elmalı Fault of the NAFZ lying along the Adaklı and Karlıova District of Bingöl (Figure 1b-1c and Table 1). Others suggested that this earthquake occurred on the Kargapazarı or Yedisu Faults of Karlıova and Yedisu Districts (Ambraseys, 1989; Ambraseys and Jackson, 1998; Barka et al., 1987; Nalbant et al., 2002). The epicentre of 5.9 Ms, 1967 Pülümür earthquake (Ambraseys, 1975) that occurred outside of Bingöl is also very close to Yedisu District. The most recent moderate earthquake (5.9 Mw) occurred on the faults of the NAFZ cropping out along the Karlıova District on 14 June 2020 (AFAD, 2021; KOERI, 2022). These moderate earthquakes are not capable of releasing the strain accumulated in the NAFZ in Bingöl (Akbayram et al., 2022*b*). Previously, the faults of the NAFZ in Bingöl are reported as seismic gaps (Sançar et al., 2009; Zabcı et al., 2017). Zabcı et al. (2017) mapped a 75-km-long throughgoing fault in the seismic gap of the NAFZ and suggested that it is capable of creating a 7.2 Mw earthquake.

2.2. The Seismicity of the EAFZ in Central, Karlıova and Genç Districts of Bingöl

The devastating May 22, 1971, Bingöl (Mw 6.8) earthquake occurred on the Ilıca Fault of the EAFZ in the Central District of Bingöl (Figure 1b-1c and Table 1) (Arpat and Şaroğlu, 1972; Taymaz et al., 1991). The maximum intensity of the earthquake reached VIII (Mercalli scale) in the Central District where 878 people died and 9111 buildings became unusable (AFAD, 2021; KOERI, 2022). Towards NE, along the Karlıova Fault (Figure 1b) of the EAFZ, the last major earthquake (7.2 Ms) was documented in 1866 (Ambraseys and Jackson, 1998). The faults of the EAFZ between the southwestern end of the Ilıca Fault and Palu have not been ruptured in the last 160 years (Akbayram et al. 2021). These faults are interpreted as a part of the Bingöl Seismic Gap (BSG) (Nalbant et al., 2002; Akbayram et al., 2021; Duman and Emre, 2013). Although it is not included in the active fault database of Türkiye, both the morphotectonic analyses (Kıranşan et al., 2021) and seismic data suggest that the Genç Fault Zone (GFZ) (Figure 1b-1c) is also active (Herece 2008; Akbayram et al., 2022*a*). Recently, GFZ is interpreted as an important component of the BSG (Akbayram et al., 2022*a*). Two moderate earthquakes (6.1 and 5.6 Ms) occurred in 2010 along the BSG, very near to Central District of Bingöl City (Events 18, and 19 in Figure 1b and Table 1) (Tan et al., 2011). The events caused the death of 42 people and severely damaged more than 4000 buildings around the epicenter (AFAD, 2021; KOERI, 2022). Nevertheless, these events are hardly capable of releasing the strain accumulated (Nalbant et al., 2002) in the BSG following 1971 earthquake (Akbayram et al., 2021).

2.3. The Seismicity of the Faults Located in the Anatolian Plate in Adaklı, Central, and Karlıova Districts of Bingöl

Bingöl also comprises some intra-plate, NW-SE trending dextral and NE-SW trending sinistral active faults that formed at the easternmost part of the Anatolian Plate (Figure 1) (Dewey and Şengör, 1979; Şengör, 1979; Şengör et al., 1985; Emre et al., 2013; Sançar et al., 2020). The Nazımiye Karakoçan Bingöl Fault Zone (NKBFZ) belongs to the NW-SE trending dextral fault family, and its southernmost part reaches the Central District of Bingöl (Figure 1b-1c) (Emre et al., 2013). The instrumental seismicity of the NKBFZ has been documented very recently. On January 31, 2022, a moderate (4.7 Mw) earthquake has occurred near Karakoçan on the NKBFZ (KOERI, 2022). Along the Sudüğünü Fault (SF), another NW-SE trending dextral fault mapped in the Central District (Figure 1b-1c), a disastrous earthquake (6.4 Ms) occurred on May 1, 2003 (Table 1) (Akkar et al., 2008; Kalafat et al.,

2009; Ulusay and Aydan, 2005; Utkucu et al., 2018). The maximum intensity of the earthquake reached VIII (Mercalli scale) in the Central District where 176 people died, and 6000 buildings became unusable (AFAD, 2021; KOERI, 2022). The Sancak Uzunpınar Fault Zone (SUFZ), a NE-SW trending 50-km-long sinistral fault zone (Emre et al., 2013; Selçuk et al., 2021), lies along the Central and Adaklı Districts (Figure 1b-1c). The Holocene activity of the SUFZ was recently documented by a paleo-seismological trench study (Selçuk et al., 2021). In addition to the aforementioned above, there are some other oblique active faults mapped in the Karlıova district near KTJ (Figure 1b-1c) (Emre et al., 2013). Even though there is no discussion on their active nature (Emre et al., 2013), their instrumental seismicity needs further geophysical analyses such as relocation because they are located in a region of complex faulting, very close to KTJ.

2.4. The Seismicity of VFZ, Yayla, Yenisu Faults in Genç, Karlıova and Solhan Districts

The NW-SE trending dextral faults are not limited to the Anatolian Plate in Bingöl (Figure 1b-1c). Many parallel faults of the Varto Fault Zone (VFZ) are in contact with the NAFZ and the EAFZ at the KTJ, both in Karlıova and Solhan Districts (Figure 1b-1c). The fault structure and seismicity of the VFZ discussed in detail in several studies (Emre et al., 2013; Gürboğa, 2016; Sançar et al., 2015; Seyitoğlu et al., 2019). The epicentre of the devastating Varto earthquake (6.9 Ms) in 1966, located outside Bingöl (Figure 1b), overlaps one of the faults of the VFZ (Table 1). However, its rupture reached Karlıova District of Bingöl (Figure 1b). The tectonic activity of the Yayla and Yenisu Faults located in the Genç District (Figure 1b-1c) is poorly known and needs further study (Emre et al., 2013).

3. Data and Method

In this study, we use the open earthquake database of KOERI. We divided the dataset into there as $1 \leq M < 3$ earthquakes, $3 \leq M$ earthquakes, and $1 \leq M$ earthquakes. In this study, earthquake magnitude classification is based on whether earthquakes can be felt without any instrumentation. According to the Mercalli classification, 3 ≤ M earthquakes are usually felt without any instrument, while others can only be detected with instruments. As mentioned earlier, we have determined the earthquake statistics for each district of Bingöl (Table 2). It is important to note that, in the KOERI database, the $3 \leq M$ earthquakes have been recorded since 1935, whereas the $1 \leq M < 3$ earthquakes have been recorded since 2001. The earthquake time periods recorded for each data set based on magnitude are given in Table 2 for each district. The maximum earthquake number (1393) and the highest earthquake magnitude (6.8) are observed in the Central District (Table 2). Karlıova District where KTJ is located, has maximum number of $1 \leq M < 3$ earthquakes. Although maximum earthquake magnitude for Genç District is only 4.9 M, the mean magnitude of $3 \leq M$ earthquakes are the maximum (3.7 M). Additionally, Genç District has maximum standard deviation for $1 \leq M$ earthquakes. A significant earthquake activity is observed, although there is no reported active fault in Kiğı District in the widely used active tectonic map of Türkiye released by Emre et al. (2013) (Table 2). The maximum earthquake magnitude reaches 5.7 M, and a significant number (654) of events have been documented in Kiğı District since 2000 (Table 2). Although the largest magnitude is 5.5 M, since 1935, the second lowest number of earthquakes has been documented in Solhan District compared to Genç, Yayladere and Yedisu Districts (Table 2). The lowest earthquake number (108) and maximum magnitude value (4.5) have been recorded in Yayladere District (Table 2). It is important to note that the recordings in Yayladere date back only to 1998.

Normal (Gauss), Lognormal, Gamma, Gumbel, and Weibull distributions are used here to analyze earthquake risk for all districts of Bingöl province. Since the study area is quite small, there is not sufficient recorded earthquake data to use conditional probability. In this study, maximum earthquake magnitudes are used instead of earthquake recurrence times for the earthquakes above certain magnitudes measured through years.

3.1. Normal (Gauss) Distribution

Natural events usually fit with the Gauss distribution. The normal distribution is a continuous function dependent X random variable. $f(X)$ gives probability values of a random variable using mean (μ) and standard deviation (σ) (Eq.1). The method has been widely used since the eighteenth century and developed by German mathematician Gauss and his colleagues (Kottegoda and Rosso, 2008).

Table 2- Earthquake statistics for each district of Bingöl.

Location	Earthquakes	Measured Years	Earthquake number	Mean (±0.1)	Maximum Magnitude	Standard Deviation (±0.01)
Adaklı	*1 ≤ M < 3*	2001-2021	182	2.2	2.9	0.48
	3 ≤ M	1935-2020	58	3.5	5.7	0.66
	1 ≤ M	1935-2021	240	2.5	5.7	0.78
Genç	*1 ≤ M < 3*	2000-2021	146	2.2	2.9	0.45
	3 ≤ M	1964-2020	52	3.7	4.9	0.69
	1 ≤ M	1964-2021	198	2.6	4.9	0.82
Karlıova	*1 ≤ M < 3*	2000-2021	868	2.2	2.9	0.52
	3 ≤ M	1949-2020	323	3.4	6.0	0.58
	1 ≤ M	1949-2021	1189	2.6	6.0	0.76
Kiğı	*1 ≤ M < 3*	2000-2021	654	2.1	2.9	0.37
	3 ≤ M	1907-2020	90	3.5	5.7	0.61
	1 ≤ M	1907-2021	744	2.3	5.7	0.62
Central	*1≤M<3*	2000-2021	708	2.4	2.9	0.48
	3≤M	1971-2021	685	3.3	6.8	0.37
	1≤M	1971-2021	1393	2.8	6.8	0.64
Solhan	*1 ≤ M < 3*	2002-2021	126	2.3	2.9	0.48
	3 ≤ M	1954-2014	30	3.6	5.5	0.62
	1 ≤ M	1954-2021	156	2.5	5.5	0.72
Yayladere	*1 ≤ M < 3*	2002-2021	84	2.2	2.9	0.38
	3 ≤ M	1998-2019	24	3.4	4.5	0.39
	1 ≤ M	1998-2021	108	2.5	4.5	0.62
Yedisu	*1 ≤ M < 3*	2002-2021	643	2.0	2.9	0.49
	3 ≤ M	1935-2021	95	3.5	5.3	0.56
	1 ≤ M	1935-2021	728	2.2	5.3	0.70

$$f(X) = \frac{1}{\sigma\sqrt{2\pi}} exp\left[-\frac{1}{2}\left(\frac{X-\mu}{\sigma}\right)^2\right] f(X) = \frac{1}{\sqrt{\quad f2\pi}} exp\left[-\frac{1}{2}\left(\frac{X-\mu}{\sigma}\right)^2\right] \rho_p = \frac{F_G}{F_p} \qquad -\infty < x < \infty \qquad (1)$$

3.2. Lognormal Distribution

Some non-normal variables can be fitted to the Normal distribution using logarithmic transformations (Eq.2). The probability distribution function of Lognormal is given with Eq.3. μ_y and σ_y represent mean and standard deviation of Y random variables.

$$Y = ln\,(x)\rho_p = \frac{F_G}{F_p} \qquad (2)$$

$$f(x) = \frac{1}{x\sigma_y\sqrt{2\pi}} exp\left[-\left(Inx - \mu_y\right)^2/2\sigma_y^2\right] \quad x \gg 0$$

$$(3)\rho_p = \frac{F_G}{F_p}$$

3.3. Gamma Distribution

Gamma distribution is frequently used to examine skewed distributions. Shape and scale parameter is shown as α and β for random variables distributions (Eq.4). Gamma function, $\Gamma(\alpha)$, is calculated with Eq.5. The mean and standard deviation value of the Gamma distribution is obtained using Eqs.6 and 7.

$$f(x) = \frac{1}{\beta^\alpha \Gamma(\alpha)} x^{\alpha-1} e^{-x/\beta} \quad x \geq 0 \qquad (4)$$

$$\Gamma(\alpha) = \int_0^\infty \quad x^{\alpha-1} e^{-x} dx \qquad (5)$$

$$Mean(x) = \alpha\beta \quad (6)$$

$$Var(x) = \alpha\beta^2$$

$$(7) Var(x) = \alpha\beta^2 E(x) = \alpha\beta$$

3.4. Gumbel Distribution

Gumbel distribution is a special case of a Generalized Extreme Value distribution. It is used for extreme value problems. The cumulative probability function is seen on Eq.8 (Gumbel, 1941). In here, x represents random variable, and α shape parameter, and β location parameter. ($\alpha = \frac{\sigma}{1.283}$ and $\beta = \mu - \frac{0.577}{\alpha}$)

$$F(x) = exp\left\{-exp\left[-\left(\frac{y}{\alpha} - \xi\right)\right]\right\}$$

$$\kappa = 0 \; F(x) = exp\left(-\, exp\; exp\; \left(-\frac{x-\beta}{\alpha}\right)\right) \quad (8)$$

3.5. Weibull Distribution

Weibull distribution is used frequently to determine material service life and wind potentials in the literature. Probability distribution function is given by Eqs. 9. If x ≥ 0, α represents scale parameter and, β, shape parameter. Scale and shape parameters can be obtained from Eqs. 10 and 11. $\Gamma(\alpha)$ represents Gamma Function (Eq. 5).

$$f(x) = \alpha\beta x^{\beta-1} e^{-\alpha x^{\beta}} \quad (9)$$

$$E(x) = \beta\Gamma\left(1 + \frac{1}{\alpha}\right) \quad (10)$$

$$Var(x) = \beta^2 \left\{\Gamma\left(1 + \frac{2}{\alpha}\right) - \left[\Gamma\left(1 + \frac{1}{\alpha}\right)\right]^2\right\} \quad (11)$$

Model parameters of Normal (Gaussian), Lognormal, Gamma, Gumbel and Weibull distributions are calculated according to the method of moments. The fitting of the mentioned probability distributions is tested by mean absolute errors (MAE), mean percentage errors (MPE) and Kolmogorov-Smirnov minimum distances (KS). In Eqs. 12, 13, and 14, $\hat{F}(x)$ gives cumulative empirical probability function, $F(x)$, cumulative theoretical distribution function and n, data number, and D, Kolmogorov-Smirnov test statistics. If KS test statistics, D, is smaller than its tabulated values, the empirical probability values agree with the cumulative probability values. MPE values smaller than 5% can be accepted confidently for statistical studies.

$$MAE = \frac{1}{n}\sum_{i=1}^{n} \quad \left|\hat{F}(xi) - F(xi)\right| \quad (12)$$

$$MPE = \frac{1}{n}\sum_{i=1}^{n} \quad \left(\frac{\hat{F}(xi) - F(xi)}{\hat{F}(xi)}\right) \times 100 \quad (13)$$

$$D = \left(\left|\hat{F}(xi) - F(xi)\right|\right) \qquad 1 \le i \le n \quad (14)$$

4. Results and Discussion

4.1. Cumulative Probability Distributions

Figure 2 shows the empirical and theoretical cumulative probability distribution values of the Central District of Bingöl calculated for all of the distribution functions mentioned in previous sections. For sake of brevity, mean absolute errors for other districts are only given in Table 3, and the cumulative probability distribution values for these districts are not shown in separate figures. In Table 3, the lowest mean absolute errors, KS test statistics, and MPE values lower than 5% for each district are shown in bold indicating the best-fit model for all districts. In Figure 2, blue scatter points give empirical cumulative probability values according to the earthquake magnitudes, and black lines represent continuous theoretical cumulative probability values. A data length as "n" and an ordered data order as "i", empirical cumulative probability values are obtained as $(\frac{i}{n+1})$. Theoretical cumulative probability values are calculated using Normal, Lognormal, Gamma, Weibull, and Gumbel probability distribution functions. Comparing the calculated probability distribution functions, a probability distribution function with the least mean absolute error and KS test statistics, D, is selected as the most suitable probability distribution provided that its MPE values are smaller than absolute %5. The Gumbel probability distribution best fits measured earthquake magnitudes of the Central District of Bingöl, and as a result, the black line best fits to blue scatter points in the Gumbel distribution (Figure 2). The mean absolute error and KS test statistics of the measured earthquake magnitudes of the Central District of Bingöl is minimum (0.036 and 0.118<0.274) for Gumbel and maximum (0.072 and 0.189) for Weibull distributions (Table 3). The Gumbel distribution also gives best fits for earthquake magnitudes of Karlıova (0.031 and 0.075<0.270) and Adaklı (0.032 and 0.078<0.286) Districts. The Weibull distribution has maximum

mean absolute errors and KS statistics for Karlıova (0.071 and 0.143) and Adaklı (0.083 and 0.172) Districts measured earthquake magnitudes similar to the Central District. However, the earthquake magnitudes of the Genç (0.034 and 0.103<0.274) and Yayladere (0.028 and 0.072<0.278) districts best fit the Weibull distributions. The lognormal distribution has the minimum mean absolute errors of earthquake magnitudes for Kiğı (0.026) and Solhan (0.036) districts, which have the smallest KS statistics (0.075 and 0.092) for Gumbel distribution. Since the MPE values for Lognormal distribution are lower than Gumbel distribution, the most appropriate distribution for these districts is selected as Lognormal distribution. The earthquake magnitudes of the Yedisu District best fit Normal distribution with mean absolute errors (0.045) and KS statistics (0.093<0.270).

Table 3- Mean absolute, percentage errors, and Kolmogorov-Smirnov test statistics of probability distributions of earthquake magnitudes of all the districts of Bingöl.

		Mean Absolute Errors				
Districts	**Measured Years**	**Normal**	**Lognormal**	**Gamma**	**Weibull**	**Gumbel**
Central	1996-2020	0.062	0.041	0.052	0.072	**0.036**
Adaklı	1999-2020	0.063	0.049	0.054	0.083	**0.032**
Genç	1999-2020	0.042	0.053	0.049	**0.034**	0.075
Karlıova	1995-2020	0.059	0.041	0.045	0.071	**0.031**
Kiğı	1998-2020	0.034	**0.026**	0.027	0.047	0.033
Solhan	2001-2020	0.042	**0.036**	0.037	0.057	0.042
Yayladere	1998-2020	**0.028**	0.034	0.033	**0.028**	0.051
Yedisu	2000-2020	**0.045**	0.048	0.047	0.053	0.067
		Kolmogorov-Smirnov minimum distances				
Districts	**Measured Years**	**Normal**	**Lognormal**	**Gamma**	**Weibull**	**Gumbel**
Central	1996-2020	0.166	0.142	0.141	0.189	**0.118**
Adaklı	1999-2020	0.139	0.111	0.124	0.172	**0.078**
Genç	1999-2020	0.131	0.159	0.143	**0.103**	0.166
Karlıova	1995-2020	0.125	0.101	0.102	0.143	**0.075**
Kiğı	1998-2020	0.111	0.089	0.101	0.122	**0.075**
Solhan	2001-2020	0.155	0.122	0.133	0.184	**0.092**
Yayladere	1998-2020	0.074	0.112	0.103	**0.072**	0.143
Yedisu	2000-2020	**0.093**	0.113	0.104	0.122	0.151
		Mean Percentage Errors				
Districts	**Measured Years**	**Normal**	**Lognormal**	**Gamma**	**Weibull**	**Gumbel**
Central	1996-2020	**-4.90%**	**0.31%**	-6.43%	**-3.39%**	**-4.17%**
Adaklı	1999-2020	**-1.53%**	**1.03%**	**-2.46%**	**1.13%**	**0.16%**
Genç	1999-2020	**-0.07%**	**-2.73%**	**-0.99%**	**2.58%**	**-4.44%**
Karlıova	1995-2020	**-1.90%**	**1.70%**	**-2.52%**	**-1.44%**	**1.75%**
Kiğı	1998-2020	**1.18%**	**3.43%**	**0.72%**	**2.16%**	**3.71%**
Solhan	2001-2020	**3.35%**	**4.00%**	**2.87%**	**4.10%**	5.06%
Yayladere	1998-2020	**4.36%**	**3.47%**	**4.81%**	**4.26%**	6.92%
Yedisu	2000-2020	**3.67%**	**3.87%**	**3.95%**	**4.38%**	7.81%

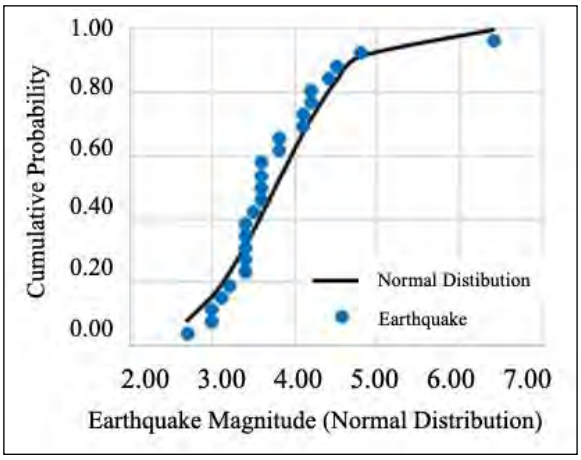

Figure 2- Cumulative probability distribution functions for maximum earthquake magnitudes of the Central District of Bingöl.

In order to determine the earthquake activity for each district of Bingöl, the recorded 1≤M<3 earthquakes are analysed without their probability distributions. Figure 3 shows the number of *1≤M<3* earthquakes recorded in each district of Bingöl since 2001 in order to compare the seismic activity of districts in the study area during the same recording period. In this figure, the horizontal axis shows the years and the vertical axis shows the earthquake numbers. 1≤M<3 earthquake numbers are high for the Central District in 2003 and in 2018 compared to other years. Most of the *1≤M<3* earthquakes recorded in 2003 are the aftershocks of May 1, 2003 (6.4 Ms) earthquake (Table 1) along Sudüğünü Fault (SF) in the Central District (Ulusay and Aydan, 2005; Akkar et al., 2008; Kalafat et al., 2009; Utkucu et al., 2018).

1≤*M*<3 earthquake numbers of Adaklı and Solhan Districts change regularly, no significant increase is observed on the graph. In the Genç and Yayladere Districts, 1≤*M*<3 earthquake numbers are usually low with a significant increase in 2015. Also, the maximum 1≤M<3 earthquake numbers occurred in the Kiğı district in 2015, and the maximum 1≤M earthquake magnitude is 5.5 for the same year. In 2005 and 2020, the maximum 1≤M<3 earthquake number and the maximum 1≤M earthquake magnitude (5.9) was measured in the Karlıova District. The increase in earthquake numbers in these years can be explained by the occurrence of aftershocks of 12-14 March 2005 (5.7 Ml and 5.9 Ml respectively) (Demirtaş, 2019; KOERI, 2022), and 14 June 2020, 5.9 Mw (Akbayram et al., 2022*b*; AFAD 2021; KOERI 2022) events. In the Yedisu District, 1≤M<3 earthquake number is maximum as in Karlıova District. The maximum earthquake magnitude of 1≤M (4.4) occurs in 2020 with the maximum number of earthquakes of 1≤M<3 because some of the aftershocks of 5.9 Mw, 2020 earthquake are superimposed in the Yedisu District (Akbayram et al., 2022*b*).

4.2. The Return Periods Correlated with Maximum Earthquake Magnitudes and Their Discussion on Available Paleo-Seismological Data

In this section, we have given the return periods, and maximum annual earthquake magnitudes according to return periods for each district of Bingöl (Figure 4). However, these values are only meaningful when correlated with available paleo-seismological data that we also discuss in this section. In Figure 4, the horizontal axis represents return periods and the vertical axis maximum earthquake magnitudes according to a selected return period. We have selected the return periods as 10, 50, 100, 250, and 1000 years. For example, according to the figure, the expected maximum earthquake magnitude for the Central District of Bingöl is 7.5 for 1000 years return period.

The earthquake magnitude maxima obtained from the Central District, as 4.7, 5.7, 6.1, 6.7, and 7.5 for 10, 50, 100, 250, and 1000 years return periods. There are four active fault zones mapped in the Central District; the EAFZ, the NKBZF, the SF, and the SUFZ (Figure 1b-1c). Unfortunately, there are no published paleo-seismology results along the segments of the EAFZ, the NKBZF, and the SF in the Central District. However, paleo-seismology studies held along the Palu-Hazar Lake Segment of the EAFZ suggest that every 100 to 365 years a large (M>7) earthquake occurs on this fault zone (Çetin et al. 2003). A study dating seismo-turbidites of Hazar Lake suggests ~190 years of earthquake recurrence in the last 3800 years (Hubert-Ferrari et al. 2020). If we combine these findings and accept that every ~230-250 years (the average of these values) a large earthquake occurs in the faults of the EAFZ in Bingöl (Taymaz et al. 1991).

In Karlıova district, the maximum earthquake magnitude maxima obtained as 5.1, 6.2, 6.6, 7.2, and 8.2 for 10, 50, 100, 250, and 1000 years return

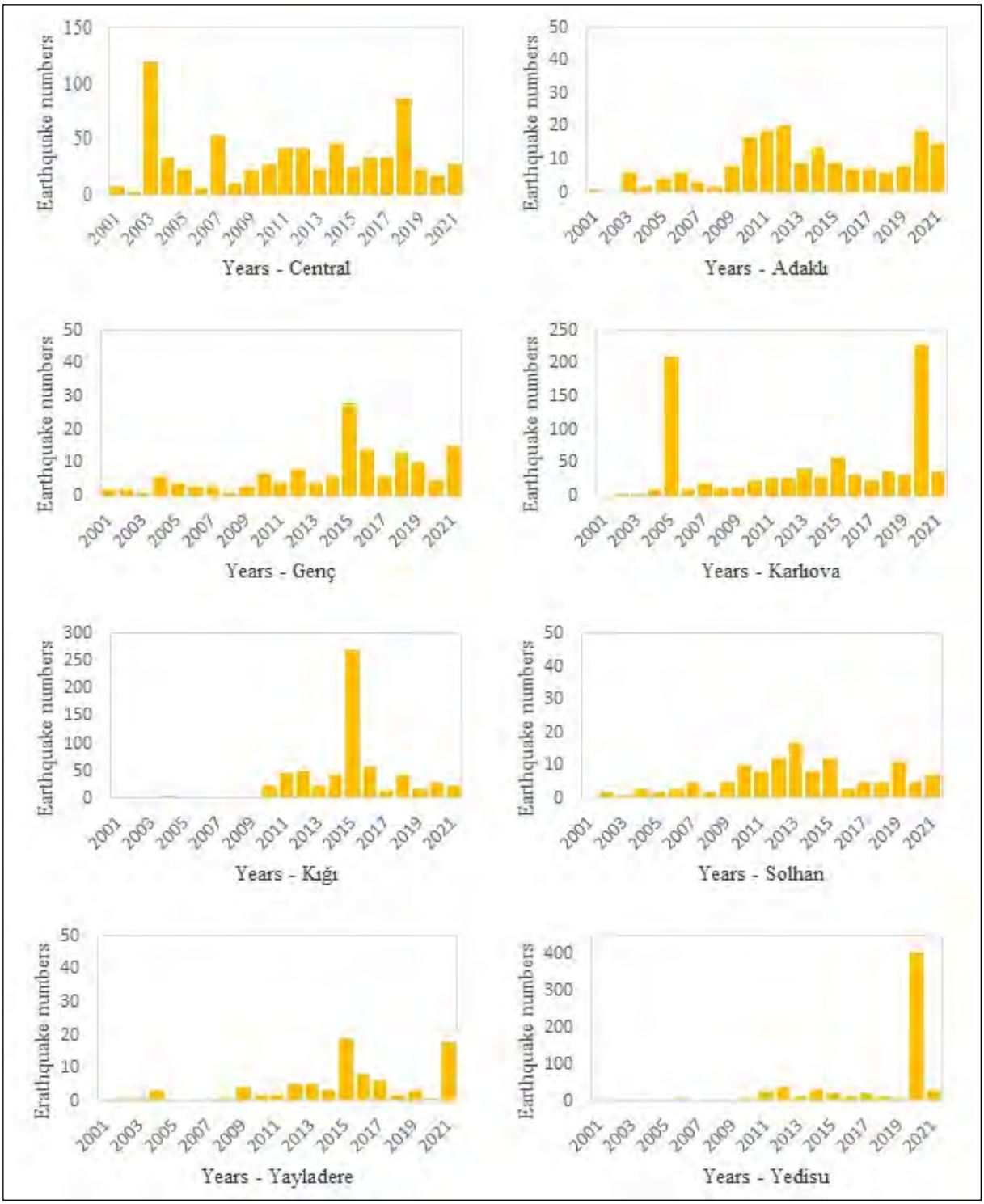

Figure 3- Numbers of $1 \leq M < 3$ earthquakes occurred between 2001 and 2020 in the Districts of Bingöl.

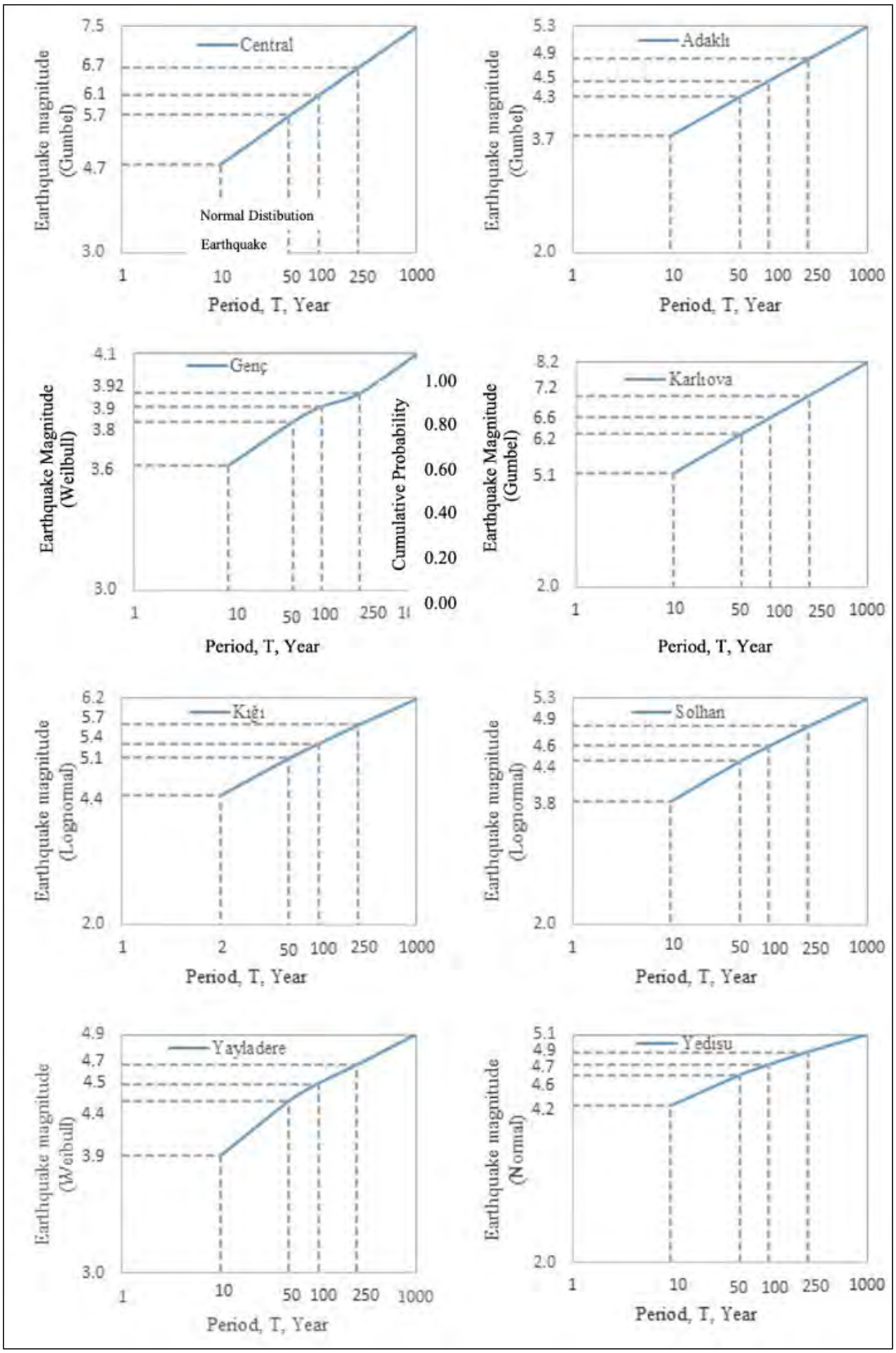

Figure 4- The maximum annual earthquake magnitudes according to return periods for each district of Bingöl. The paleo-seismological trench study held along the SUFZ suggests at least two main events in the Holocene without giving a recurrence interval (Selçuk et al., 2021).

periods. The Karlıova District hosts the KTJ where the pieces of both the NAFZ and the EAFZ mapped. The previous studies suggest an earthquake recurrence interval of 200 to 250 along most of the length of the NAFZ (cf., Zabcı et al., 2017). Hence, it is safe to choose the maximum earthquake value corresponding the 250 return period which is 7.2 M (Figure 4) as the probable magnitude of the next big earthquake occurred on the NAFZ and EAFZ in the Karlıova District. This magnitude is also in good correlation with the maximum expected earthquake value (7.2 M) calculated by Zabcı et al (2017).

The maximum earthquake magnitudes seem to be 5.1 M for the 1000-year return period in Yedisu District, where some important segments of the NAFZ were mapped (Figure 4). This is not compatible with the paleo-seismological trench results and empirical calculations of Zabcı et al (2017). The reason for this inconsistency is attributed to low quality seismic data in this region.

For Kiğı and Solhan Districts, maximum earthquake magnitudes fit the Lognormal distribution, and the earthquake magnitudes are 6.2 and 5.3 for the 1000-year return period. Weibull distributed Yayladere District's maximum earthquake magnitudes are 4.9 for the 1000-year return period. For the Genç District, the least maximum earthquake magnitude is calculated as 4.1 for the same return period. If 10-year return periods are examined, maximum earthquake magnitudes are calculated between 3.6 and 5.1 in all districts. This shows that perceptible earthquakes will occur once every ten years.

5. Conclusions

Determination of the 5 time-dependent probability distributions (Normal, Lognormal, Gamma, Gumbel, Weibull) and return periods of earthquakes for all districts of Bingöl give the following results. The best probability fit arises from the Gumbel distribution for Central, Karlıova, and Adaklı Districts. For the Genç District, where the least maximum earthquake magnitude is reported, the Weibull distribution gives the best fit. For the Central and Karlıova Districts, along which maximum earthquake magnitudes were reported and important faults of NAFZ and EAFZ were mapped, every 250 years a 6.6 M, and a 7.2 M occurs respectively. These results are in good correlation with the results of paleo-seismological data reported along the NAFZ and the EAFZ. Earthquake magnitudes in the 250-year return period change among 3.9 (Genç), 4.9 (Adaklı), 4.9 (Solhan), 4.9 (Yedisu), 4.7 (Yayladere), 5.7 (Kiğı). Calculated maximum earthquake magnitudes show that buildings in Bingöl City and Karlıova district must be constructed more carefully than the other districts. For a 10-year return period, earthquake magnitudes reach to 3.6 and 5.1 in all districts suggesting that every decade a perceptible earthquake will occur in Bingöl. It is important to note that in the Yedisu District, the maximum earthquake magnitudes seem as 5.1 M for the 1000-year return period, incompatible with previously published findings. Significant changes in earthquake numbers in the Yedisu necessitate investigation of active faults, and seismicity in the zone.

Acknowledgement

We sincerely thank Kemal Kıranşan for supplying the elevation contours and city borders in Figure 1b, three anonymous reviewers, Editor-in-Chief Halim Mutlu, Associate Editors Şule Gürboğa, and Eren Pamuk for their valuable criticism and help during the review process.

References

AFAD (Disaster and Emergency Management Presidency). http:/www.afad.gov.tr (April 23,2021).

Akbayram, K., Kıranşan, K., Özer, Ç., Varolgüneş, S. 2021. The surface deformation of the 2020 Doğanyol-Sivrice earthquake (Mw 6.8) and the earlier events suggest Mw<7.0 earthquakes do not create significant surface slip along the East Anatolian Fault Zone (unpublished).

Akbayram, K., Bayrak, E., Pamuk, E., Özer, Ç., Kıranşan, K., Varolgüneş, S. 2022*a*. Dynamic sub-surface characteristic and the active faults of the Genç District locating over the Bingöl Seismic Gap of the East Anatolian Fault Zone, Eastern Turkey. Natural Hazards 114(1) ,825-847.

Akbayram, K., Kıranşan, K., Varolgüneş, S., Büyükakpınar, P., Karasözen, E., Bayık, Ç. 2022*b*. Multi-disciplinary analyses of the rupture characteristic of 2020 June 14 Mw 5.9 Kaynarpınar (Karlıova, Bingöl) earthquake reveals NE-SW trending active faulting along the Yedisu Seismic Gap of the North Anatolian Fault Zone towards Turkish-

Iranian Plateau. International Journal of Earth Sciences 1-21.

Akkar, S., Boore, D. M., Gülkan, P. 2008. An evaluation of the strong ground motion recorded during the May 1, 2003 Bingol Turkey, earthquake. Journal of Earthquake Engineering 9, 173–197.

Alkan, H., Bayrak, E. 2022. Coulomb stress changes and magnitude - frequency distribution for Lake Van region. Bulletin of the Mineral Research and Exploration 168, 141-156.

Altuncu P. S., Aksarı, D., Ergün, T., Teoman, U. M., Pınar, A. 2019. The December 2nd, 2015 Bingöl, Eastern Anatolia-TURKEY, earthquake (Mw = 5.3): A rupture on optimally oriented fault plane. Journal of Asian Earth Science 173, 88–97.

Ambraseys, N. 1970. Some characteristic features of the Anatolian fault zone. Tectonophysics 9, 143–165.

Ambraseys, N. 1975. Studies in historical seismicity and tectonics. Geodynamics.

Ambraseys, N. 1989. Temporary seismic quiescence: SE Turkey. Geophysical Journal International 96, 311–331.

Ambraseys, N., Jackson, J. 1998. Faulting associated with historical and recent earthquakes in the Eastern Mediterranean region. Geophysical Journal International 133, 390–406.

Anagnos, T., Kiremidjian, A. 1988. A review of earthquake occurrence models for seismic hazard analysis. Probabilistic Engineering Mechanics 3, 3–11.

Arpat, E., Şaroğlu, F. 1972. The East Anatolian Fault System: thoughts on its development. Bulletin of the Mineral Research And Exploration 78, 33–39.

Bak, P., Christensen, K., Danon, L., Scanlon, T. 2002. Unified scaling law for earthquakes. Physical Review Letters 88, 178501.

Balun, B., Nemutlu, Ö.F., Sarı, A. 2020. Estimation of probabilistic hazard for Bingol province, Turkey. Earthquakes and Structures 18 (2), 223-231.

Barka, A., Toksöz, M., Kadinsky-Cade, K., Gülen, L. 1987. The segmentation, seismicity and earthquake potential of the eastern part of the North Anatolian Fault Zone. Bulletin of Earth Science 14, 337–352.

Campbell, K., Thenhaus, P., Bamhard, T., Hampson, D. 2002. Seismic hazard model for loss estimation and risk management in Taiwan. Soil Dynamic Earthquake Engineering 22, 743–754.

Çetin, H., Güneyli, H., Mayer., L. 2003. Paleoseismology of the Palu-Lake Hazar segment of the East Anatolian fault zone, Turkey. Tectonophysics 374, 163-197.

Çoban, K. H., Sayil, N. 2020*a*. Different probabilistic models for earthquake occurrences along the North and East Anatolian fault zones. Arabian Journal of Geosciences 13 (18), 1-16.

Çoban, K. H., Sayil, N. 2020*b*. Conditional Probabilities of Hellenic Arc Earthquakes Based on Different Distribution Models. Pure and Applied Geophysics 177 (11), 5133–5145.

Çobanoğlu, İ., Bozdağ, Ş., Dinçer, İ., Erol, H. 2006. Statistical Approaches to Estimate the Recurrence of Earthquakes in the Eastern Mediterranean Region. İstanbul Yerbilimleri Dergisi 19, 91–100.

Demirtaş, R. 2019. 12 Mart 2005 (M=5.6), 14 Mart 2005 (M=5.9) ve 24 Mart 2005 (M=5.4) Karlıova (Bingöl) Depremleri. Ankara.

Dewey, J., Şengör, A. 1979. Aegean and surrounding regions: complex multiplate and continuum tectonics in a convergent zone. Geological Society of America Bulletin 84–92.

Duman, T. Y., Emre, Ö. 2013. The East Anatolian Fault: geometry, segmentation and jog characteristics. Geological Society, London, Special Publications 495–529.

Emre, Ö., Duman, T., Özalp, S., Elmacı, H., Olgun, Ş., Şaroğlu, F. 2013. Active Fault Map of Turkey with an Explanatory Text 1:1.250.000 scale, Special Publication Series 30. General Directorate of Mineral Research and Exploration (MTA), Turkey.

Eyidoğan, H., Guclu, U., Utku, Z., Degirmenci, E. 1991. Türkiye Büyük Depremleri Makro-Sismik Rehberi (1900–1988). ITU Maden Fakültesi Jeofizik Mühendisliği Bölümü, İstanbul.

Gumbel, E. J. 1941. The Return Period of Flood Flows. Annals of Mathematical Statistics 12, 163-190.

Gürboğa, Ş. 2016. The termination of the North Anatolian Fault System (NAFS) in Eastern Turkey. International Geological Review 58, 1557–1567.

Hagiwara, Y. 1974. Probability of earthquake occurrence as obtained from a Weibull distribution analysis of crustal strain. Tectonophysics 23, 313–318.

Hainzl, S., Scherbaum, F., Beauval, C. 2006. Estimating Background Activity Based on Interevent-Time Distribution. Bulletin of the Seismological Society of America 96, 313–320.

Herece, E. 2008. Atlas of East anatolian fault. MTA Special Publication Series 13.

Hubert-Ferrari A., Lamair, L., Hage, S., Schmidt, S., Çağatay, M. N., Avşar, U. 2020. A 3800 yr paleoseismic record (Lake Hazar sediments, eastern Turkey): Implications for the East Anatolian Fault Seismic Cycle. Earth and Planetary Science Letters 538, 116-152.

Kalafat, D., Kekovalı, K., Güneş, Y., Yılmazer, M., Kara, M., Deniz, P., Berberoğlu, M. 2009. A catalogue of source parameters of moderate and strong earthquakes for Turkey and its surrounding area (1938–2008). Boğaziçi University, Kandilli Observatory and Earthquake Research Institute.

Kıranşan, K., Akbayram, K., Avci, V. 2021. Effects of Active Tectonism on Geomorphological Structure in Bingöl Basin and Its Surroundings. Gümüşhane Üniversitesi Sosyal Bilimler Enstitüsü Elektronik Dergisi 12, 1110–1129.

KOERI (Kandilli Observatory and Earthquake Research Institute). http://koeri.boun.edu.tr (May 12, 2022).

Kottegoda, N. T., Rosso, R. 2008. Applied Statistics for Civil and Environmental Engineers, Engineering.

Köküm, M., Özçelik, F. 2020. An example study on re-evaluation of historical earthquakes: 1789 Palu (Elazığ) earthquake, Eastern Anatolia, Turkey. Bulletin of the Mineral Research and Exploration. 161, 157-172.

McKenzie, D. 1972. Active tectonics of the Mediterranean region. Geophysics Journal International 30, 109–185.

Nalbant, S., McCloskey, J., Steacy, S., Barka, A. 2002. Stress accumulation and increased seismic risk in eastern Turkey. Earth Planetary Science Letters 195, 291–298.

Nishenko, S., Buland, R. 1987. A generic recurrence interval distribution for earthquake forecasting. Bulletin of the Seismological Society of America 77, 1382–1399.

Öztürk, S., Bayrak, Y., Çınar, H., Koravos, G. C., Tsapanos, T. M. 2008. A quantitative appraisal of earthquake hazard parameters computed from Gumbel I method for different regions in and around Turkey. Natural Hazards 47 (3), 471–495

Öztürk, S. 2011. Characteristics of seismic activity in the Western, Central and Eastern parts of the North Anatolian Fault Zone, Turkey: Temporal and spatial analysis. Acta Geophysica 59, 209–238.

Öztürk, S., Bayrak, Y. 2012. Spatial variations of precursory seismic quiescence observed in recent years in the eastern part of Turkey. Acta Geophysica 60, 92–118.

Parvez, I. A., Ram, A. 1999. Probabilistic Assessment of Earthquake Hazards in the Indian Subcontinent. Pure and Applied Geophysics 154, 23–40.

Pasari, S., Dikshit, O. 2015. Earthquake interevent time distribution in Kachchh, Northwestern India. Earth Planet and Space 67, 1-17.

Pasari, S., Dikshit, O. 2018. Stochastic earthquake interevent time modeling from exponentiated Weibull distributions. Natural Hazards 90, 823–842.

Polat, O., Gök, E., Ylmaz, D. 2008. Earthquake hazard of Aegean Extension Region, Turkey. Turkish Journal of Earth Science 17, 593–614.

Rikitake, T. 1974. Probability of earthquake occurrence as estimated from crustal strain. Tectonophysics 23, 299–312.

Sançar, T., Zabcı, C., Akyüz, H., Karabacak, V., Altunel, E. 2009. Late Holocene Activity of Kargapazari Segment, Eastern Part of the North Anatolian Fault Zone, Bingöl, Turkey. EGU General Assembly, Vienna, 7710.

Sançar, T., Zabci, C., Akyüz, H., Sunal, G., Villa, I. 2015. Distributed transpressive continental deformation: The Varto Fault Zone, eastern Turkey. Tectonophysics 661, 99–111.

Sançar, T., Zabcı, C., Akcar, N., Karabacak, V., Yeşilyurt, S., Yazıcı, M., Akyüz, H., Öztüfekçi Önal, A., Ivy-Ochs, S., Christl, M., Vockenhuberf, C. 2020. Geodynamic importance of the strike-slip faults at the eastern part of the Anatolian Scholle: Inferences from the uplift and slip rate of the Malatya Fault. Jounal of Asian Earth Science 188, 104091.

Selçuk, A., Erturaç, M., Karabacak, V., Sançar, T., Kul, A., Yavuz, M. 2021. Active Tectonic Setting and Paleoseismicity of the Sancak-Uzunpazar Fault Zone. Turkish Jornal of Earthquake Research 3, 75–91.

Şahin, Ş., Öksüm, E. 2021. The relation of seismic velocity and attenuation pattern in the East Anatolian fault zone with earthquake occurrence: Example of January 24, 2020 Sivrice Earthquake. Bulletin of the Mineral Research and Exploration 165, 141-161.

Şengör, A., 1979. The North Anatolian transform fault: its age, offset and tectonic significance. Journal of Geological Society of London 136, 269–282.

Şengör, A. 1980. Türkiye neotektoniğinin esasları. Türkiye Jeoloji Kurumu Konferans Serisi 2. Ankara, 40.

Şengör, A., Görür, N., Şaroğlu, F. 1985. Strike-slip faulting and related basin formation in zones of tectonic escape: Turkey as a case study, in: Biddle, K., Christie-Blick, N. (Eds.), Strike-Slip Deformation, Basin Formation and Sedimentation. Society of Economic Paleontologists and Mineralogists, Tulsa, OK, 227–264.

Seyitoğlu, G., Esat, K., Kaypak, B., Moosarreza, T., Bahadır, A. 2019. Internal Deformation of Turkish-Iranian Plateau in the Hinterland of Bitlis-Zagros Suture Zone. Developments in Structural Geology and Tectonics 3, 161–244.

Shelly, D., Beroza, G., Ide, S. 2007. Non-volcanic tremor and low-frequency earthquake swarms. Nature 446, 305–307.

Tan, O., Tapirdamaz, M., Yörük, A. 2008. The Earthquake Catalogues for Turkey. Turkish Journal Earth Science 17, 405–418.

Tan, O., Pabucu, Z., Taprdamaz, M. C., Nan, S., Ergintav, S., Eyidoğan, H., Aksoy, E., Kuluöztürk, F. 2011. Aftershock study and seismotectonic implications of the 8 March 2010 Kovanclar (Elazğ, Turkey) earthquake (MW = 6.1). Geophysical Research Letters 38.

Taymaz, T., Eyidoğan, H., Jackson, J. 1991. Source parameters of large earthquakes in the East Anatolian Fault Zone (Turkey). Geophysical Journal International 106, 537–550.

Tripathi, J. 2006. Probabilistic assessment of earthquake recurrence in the January 26, 2001 earthquake region of Gujrat, India. Journal of Seismology 10, 119–130.

Ulusay, R., Aydan, Ö. 2005. Characteristics and geo-engineering aspects of the 2003 Bingöl (Turkey) earthquake. Journal of Geodynamics 40, 334–346.

USGS (United States Geological Survey). http://usgs.gov. June,2022.

Utkucu, M., Budakoğlu, E., Çabuk, M. 2018. Teleseismic finite-fault inversion of two M w = 6.4 earthquakes along the East Anatolian Fault Zone in Turkey: the 1998 Adana and 2003 Bingöl earthquakes. Arabian Journal of Geoscience 11, 1–14.

Utsu, T. 1984. Estimation of parameters for recurrence models of earthquakes. Bulletin of Earthquake Research Institute 59, 53–55.

Wu, C., Shelly, D., Gomberg, J., Peng, Z., Johnson, P. 2013. Long-term changes of earthquake inter-event times and low-frequency earthquake recurrence in central California. Earth Planetory Science Letters 368, 144–150.

Yadav, R., Tripathi, J., Rastogi, B., Das, M., Chopra, 2010. Probabilistic assessment of earthquake recurrence in northeast India and adjoining regions. Pure Applied Geophysics 167, 1331–1342.

Zabcı, C., Akyüz, H. S., Sançar, T. 2017. Palaeoseismic history of the eastern part of the North Anatolian Fault (Erzincan, Turkey): Implications for the seismicity of the Yedisu seismic gap. Journal of Seismology 21, 1407–1425.

Bulletin of the Mineral Research and Exploration

http://bulletin.mta.gov.tr

Noise attenuation of a 3D marine seismic reflection dataset - a case study in the Southwest Black Sea region

Hamza BİRİNCİ[a*], Kürşat ERGÜN[a], Aslı Zeynep YAVUZOĞLU[a], Korhan KÖSE[a], Güniz Büşra YALÇIN[a], Mustafa Berkay DOĞAN[a], Fatma Betül KARCI[a], Murat EVREN[a], Ayşe GÜNGÖR[a] and Bahri Serkan AYDEMİR[a]

[a]*General Directorate of Mineral Research and Exploration, Department of Marine Research, Ankara, Türkiye.*

Research Article

Keywords:
Seismic Noise Attenuation, Swell Noise, Cavitation Noise, Bird Noise, Geovation 2.0.

ABSTRACT

Noises in marine seismic data are one of the biggest obstacles in seismic imaging. The most significant step in seismic data processing is the removal of seismic noise, which can be classified as instrument and background noise. Noise attenuation usually results in improved seismic interpretation by increasing the signal-to-noise ratio. In this study, we will focus on attenuating these seismic noises with several data processing techniques. A number of denoising examples describing swell, strumming/tugging, and cavitation, which are background-type noises, and streamer-mounted device noise (Nautilus), which is an instrument-type noise, were illustrated by analysing a marine 3D seismic dataset recorded by Oruç Reis Research Vessel in Black Sea project of Mineral Research and Exploration (MTA). This study was achieved by implementing an f-x prediction filter (SPARC, DENOISE3D) and f-k filter (DWATT) in the t-x domain, and radon filter (RADATT) in Tau-P domain by the use of Geovation 2.0 software.

Received Date: 29.03.2022
Accepted Date: 26.09.2022

1. Introduction

It is well known that noises in marine seismic are one of the biggest obstacles in seismic imaging. These noises can mask primary data and thus degrade the imaging which may lead to misinterpretation. In seismic exploration and processing, which are the main phases of determining the well location in oil and gas exploration (McConnell, 2000), such an inaccuracy that may result can cause millions of dollars in losses for companies when it comes to the interpretation stage. Therefore, it is very important to carefully eliminate the noise while preserving the underlying data.

Seismic noise can be distinguished on the basis of its seismic characteristic into coherent and random noise (Schoenberger and Mifsud, 1974; Dondurur, 2018). To better understand the origin of the seismic noise, Elboth et al. (2010) classified the noise as background, instrument, and source-generated type noise. However, source-generated noise will not be covered in this paper. One of the fundamentals of seismic data processing is eliminating noises originating from various sources. Although there are several attenuation techniques that have been exemplified in various studies (Yılmaz, 2001; Guo and Lin, 2003; Gülünay et al., 2004; Gülünay, 2008; Elboth et al., 2009; Elboth et al., 2010; Zhang and

Citation Info: Birinci, H., Ergün, K., Yavuzoğlu, Z. A., Köse, K., Yalçın, G. B., Doğan, M. B., Karcı, F. B., Evren, M., Güngör, A., Aydemir, B. S. 2023. Noise attenuation of a 3D marine seismic reflection dataset – A case study in the Southwest Black Sea region. Bulletin of the Mineral Research and Exploration 172, 31-39. https://doi.org/10.19111/bulletinofmre.1180869

**Corresponding author: Hamza BİRİNCİ, hamzabirinci01@gmail.com*

Wang, 2015), the methods most suitable for the dataset was applied and presented here.

In addition, preserving the primary signal (target reflections) plays a pivotal role in noise attenuation (Elboth et al., 2009). Filter parameters and time windows should be carefully designed so as not to damage the primary signal. Therefore, filters should be applied gently to the frequencies containing the primary signal. In this study, the application of noise attenuation was employed in order; swell noise, tugging/strumming noise, seismic interference, and bird noise.

The dataset presented here was collected by Oruc Reis R/V with acquisition parameters shown in Table 1. This study will firstly focus on methods of suppressing seismic noises that are swell, operational, strumming/tugging, streamer positioning instrument, and cavitation noise by applying f-x prediction filter and f-k filter in the t-x domain, radon filter in Tau-P domain, respectively. Then, the results of this study will be presented.

2. Common Noises in Marine Seismic

2.1. Background Noise

Background noises are types of ambient noises which are not generated by the seismic operation but uncontrollable external sources (Hlebnikov et al., 2021). Background noise types frequently encountered in marine seismic are swell noise, tugging/strumming noise, and cavitation noise. Below part, the results of these attenuation methods are shared.

2.1.1. Swell Noise

The swell noise is one of the most common and dominant noise types encountered in marine seismic, which can be classified as non-coherent background noise.

Two mechanisms have been proposed that can generate swell noise. According to this, the first mechanism is Bulge waves in the sea due to aggressive weather conditions, which cause a hydrostatic pressure difference on the streamer and the second mechanism is the ocean currents creating cross flow effect on the streamer (Dondurur, 2018).

Swell noise generally produces a high amplitude signal with a frequency range of 1-10 Hz, which can be observed as blobs on shot gathers in Figure 1a (Elboth et al., 2009). While the most common way to remove the swell noise is to apply a band-pass filter, this method is not only inadequate but also may cause data loss. Instead of this, an f-x projective filter was applied by processing for each frequency range belonging to different components of the swell noise with proper threshold values. F-x projection filtering is a statistical noise attenuation method in which the noise is eliminated by filtering the data with an auto-deconvolved prediction error filter (Soubaras, 1994, 1995).

F-x projection filter (SPARC) could be implemented into different time windows considering where the primaries are dominant in order to avoid affecting primary data. Therefore, the filter can be applied harshly with low threshold values and a broad frequency range in which primaries cannot be observed while it can be applied more moderately with high threshold values and a narrow frequency range in the primary zone time window.

Figure 1a shows a shot gathered heavily contaminated by the swell mostly in the middle. The effect of swell noise can be observed continuously throughout the shot gather. After the application of the projection filter, the swell noise is almost completely removed from the data while the primary reflections remain preserved thanks to the sensitive parameter and window design. (Figures 1b, c). F-k plots indicate that low-frequency content delineating swell energy has been successfully attenuated from the data (Figures 1d, e, f).

2.1.2. Tugging/Strumming Noise

Another challenge in marine seismic data processing is to remove tugging/strumming noise

Table 1- Acquisitions parameters of processed data.

No. of Receivers	No. of Cables	Nominal Fold	Record Length	Shot Interval	Receiver Interval	Near / Far Offset	Source Type	Receiver Depth / Source Depth
1920	4	60	10050 ms	25 m (flip/ flop)	12.5 m	~120 m / 6050 m	Bolt 1900 LLXT airgun 3480 cu^3	7 m / 6 m

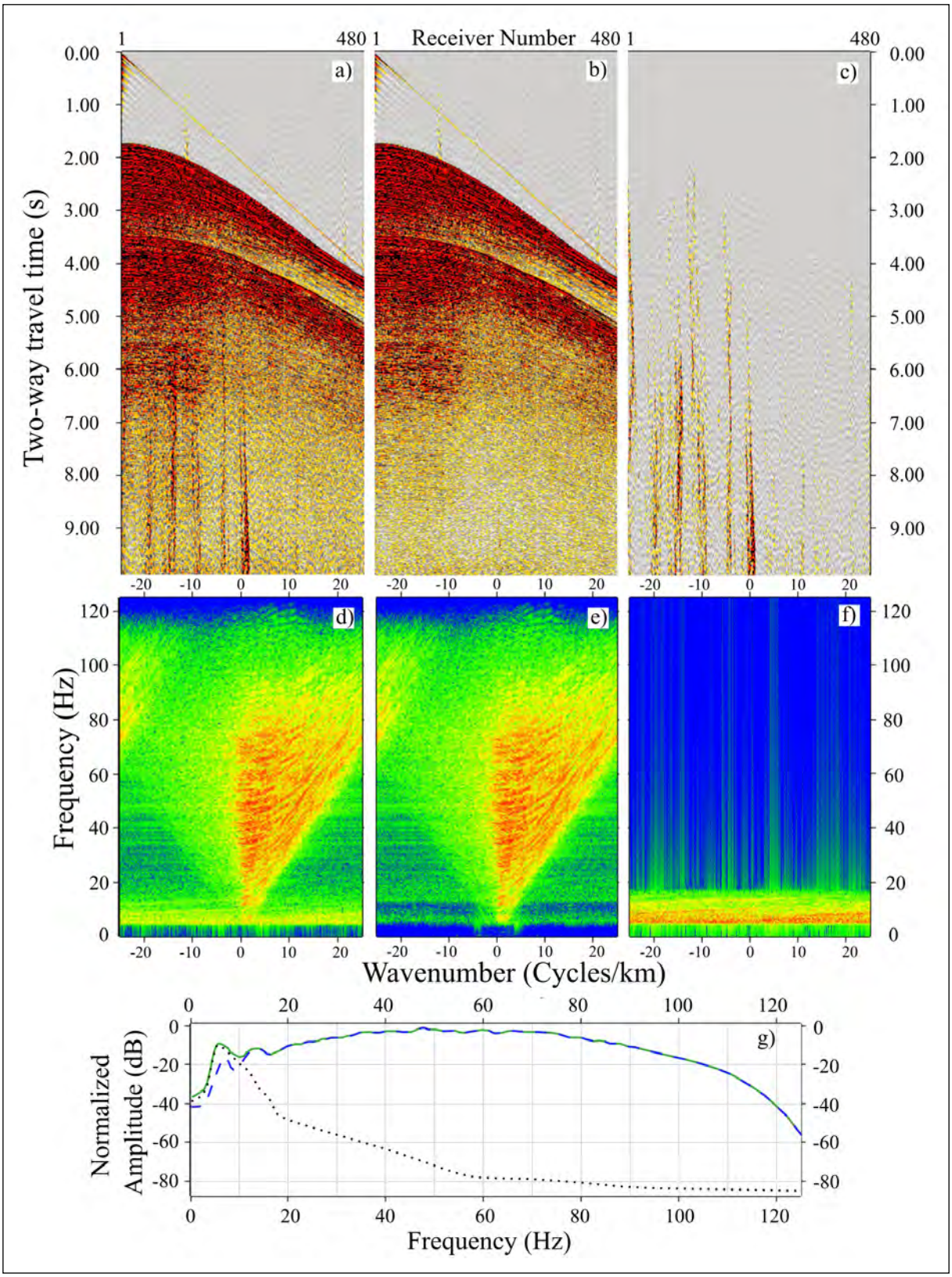

Figure 1- Swell noise attenuation; a) before SPARC application, b) after SPARC application, c) difference, d), e), f) f-k spectrum – before, after, difference, respectively, and g) amplitude spectrum before SPARC (green/straight line), after SPARC (blue/dashed line), difference (black/dotted).

which can be classified as coherent background noise (Hlebnikov et al., 2019). This noise type originated from longitudinal vibrations along the streamer. During the acquisition of seismic data, a vibration occurs on the streamer because of the tension between the vessel and towed streamer. In addition, the tension between the streamer and a tail buoy causes tugging/strumming noise (Parrish, 2005; Hlebnikov et al., 2019).

Since the tension is more dominant on the outer streamers in 3D projects, tug/strum noise is more evident and easily distinguishable in the shot gathers of these streamers. The vibrations created by the tows connecting the streamer to the ship and paravanes as a result of the ship movement appear in the gathers as linear events (head-to-tail) with a frequency range of 1-10 Hz (it can be observed up to 20 Hz), usually affecting near traces whereas the noise caused by the tail buoy has a negative moveout linear characteristic (tail-to-head) in far traces.

Linear noise can be removed by filtering the noise as a fan of apparent velocities in the f-k domain (Dondurur, 2018; Hlebnikov et al., 2021). A fan filter was designed that covers the velocities of tug noises in the t-x domain. Subsequently, using the DWATT module in Geovation 2.0, this fan filter in the t-x domain was transformed into the f-k domain, and then the filtered and modelled part was subtracted from the data.

Figure 2a demonstrates that near traces of the shot gather are dominated by tug noise while strum noise from the tail to head appears very weak in far traces. In Figures 2b, c, linear events are almost completely eliminated without damaging primary reflections with the help of a carefully designed fan filter. As can be seen in f-k spectra, linear noises with a frequency of up to 18 Hz, with 11-18 Hz being weak, have been discarded from the data (Figures 2d, e, f, g).

2.1.3. Cavitation Noise

Cavitation noise is a type of seismic interference (SI) caused by propellers of ships passing close to the streamer during the acquisition of seismic data (Elboth et al., 2009). This type of noise is quite common, especially in study areas where marine traffic is intense, and it is highly unlikely to avoid this noise during the towed-streamer acquisition.

Depending on the position of the noise-generating ship relative to the streamer, cavitation noise can be observed as either a linear or hyperbolic event in shot gathers with a broad frequency content. The cavitation noise repeats itself throughout the recording until the noise-generating vessel is outside the sensitivity range of the streamer. Our streamer recorded this noise (Figure 3a) for about 200 shots, generated by a passing vessel. Firstly, defining the frequency, move-out, and dipping of the noise in the shot gather is important to design the filter to properly eliminate the noise from the dataset. The noise for this case in the study has a frequency range of 40 Hz to 125 Hz. When the motion of the noise in the shooting pattern is examined, it appears as tail-to-head in shot gathers, becomes hyperbolic due to the relative motion between the two ships, then becomes head-to-tail and fades away from gather.

Although many approaches to eliminating cavitation noise have been proposed, two effective methods will be focused here. Firstly, Tau-P transformation in which it is possible to mute the p values related to the move outs of the propeller noise, which has different move outs from primaries in Tau-P domain was used (RADATT). In addition, in this stage, a frequency-limited filter was applied in order to preserve primary reflections.

Another SI attenuation algorithm presented by Gülünay et al. (2004) is a useful method based on FX prediction filters. Basically, this tool (SINAT module on Geovation 2.0) compares the contaminated shots with the adjacent shots in particular time and space windows to detect and flag the differences among them. However, in this shot-to-shot comparison, there are no differences (near to zero) within primary reflections. Thus, primaries are likely to be preserved in the dataset with this method. SINAT may require some conditions to work properly. These are:

- Amplitude of the noise should be higher than the underlying amplitude of the signal.
- Noise should be incoherent with the adjacent shots in designated time windows.
- Primaries and the SI noise should be monodip (Brittan et al., 2008; Gülünay, 2008).

Figure 3a shows that semi-symmetrical hyperbolas caused by the propeller of a close passing vessel

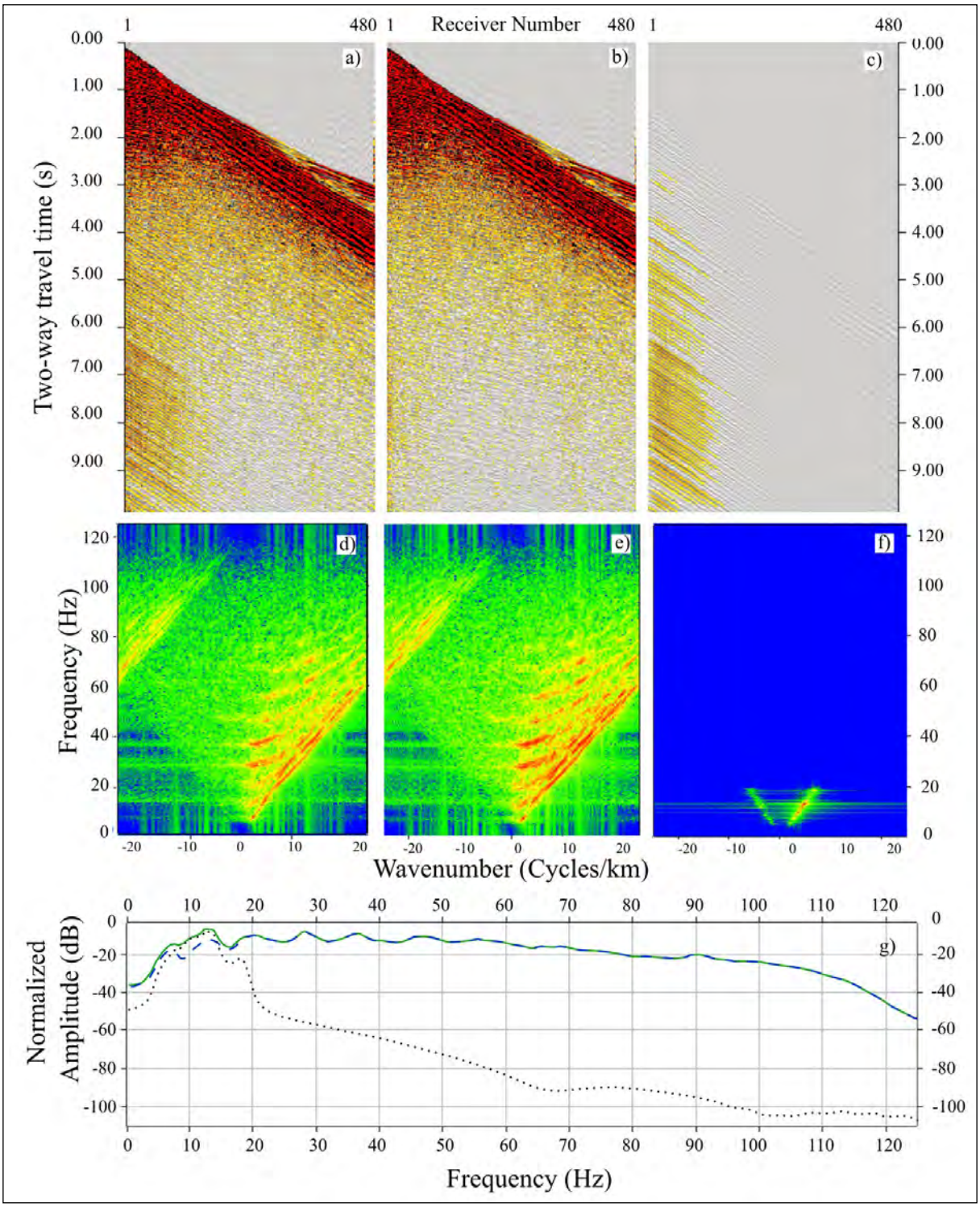

Figure 2- Tugging/strumming noise attenuation; a) before DWATT application, b) after DWATT application, c) difference, d), e), f) f-k spectrum – before, after, difference, respectively, and g) amplitude spectrum before DWATT (green/straight line), after DWATT (blue/dashed line), difference (black/dotted). Please note that the amplitudes in the f-k spectra are not balanced.

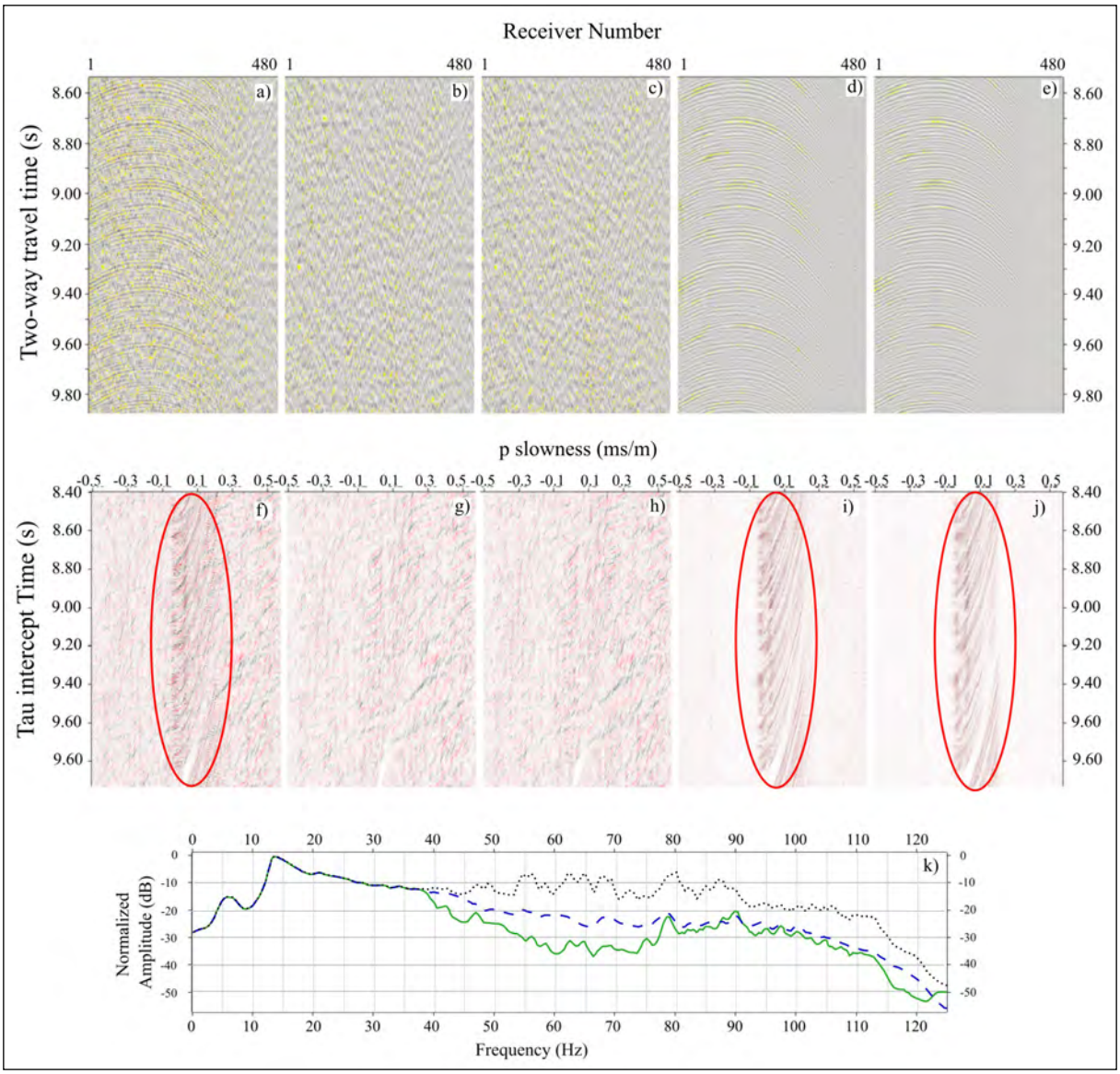

Figure 3- Seismic Interference Noise Attenuation; a) raw data, b) after RADATT application, c) after SINAT application, d) difference between RADATT and raw data, e) difference between SINAT and raw data, f), g), h), i) and j) Tau-P plots – raw data, RADATT applied, SINAT applied, the difference between raw data and RADATT, difference between raw data and SINAT, respectively. Red circles denote the hyperbolas of the cavitation noise, k) amplitude spectrum indicating raw data (black/dotted), RADATT (green/straight line), SINAT (blue/dashed line). Note that since the hyperbolas in the shot domain appear as inverted hyperbolas in the Tau-P domain, the Tau-P scale is given wider in the upward direction.

contaminate all the traces in the shot gather. These semi-symmetrical hyperbolas appear as upside hyperbolas in the Tau-P domain (Figure 3f). By the help of a Tau-P filter designed for the purpose, removing the cavitation noise without touching any other signal was managed (Figures 3b, d). A shot gathered in Tau-P domain focusing on the affected area clearly illustrates that the noise is no longer noticeable. The result of the FX prediction filter is also successful for the attenuation of the hyperbolas (Figures 3c, e, h, j). However, the Tau-P method gave a more satisfactory result specifically to the dataset used in this study (Figures 3b, d, g, i).

2.2. Instrument Noise

Instruments used in a seismic operation can cause unwanted noise due to malfunctions (electrical and mechanical errors) or operating principles such as steering and balancing of the streamer. The most

obvious type of instrument noise is bird noise, which is defined as streamer-mounted unit noise in this study.

2.2.1. Streamer-Mounted Unit Noise

One of the most significant noises in marine seismic data is caused by streamer positioning and controlling devices (NAUTILUS), commonly called bird noise (Dondurur, 2018). This noise, which is non-coherent, is observed on the near traces where the devices are mounted on the streamer. These devices, causing stress on the streamer in their mounting locations (on and around the channel), create noise at a velocity of less than 1500 m/s.

The general characteristic of bird noise can be described as inverted v-shaped, with frequency content up to 18 Hz, regularly distributed over shot gathers (Figure 4a). Despite its simply recognizable character

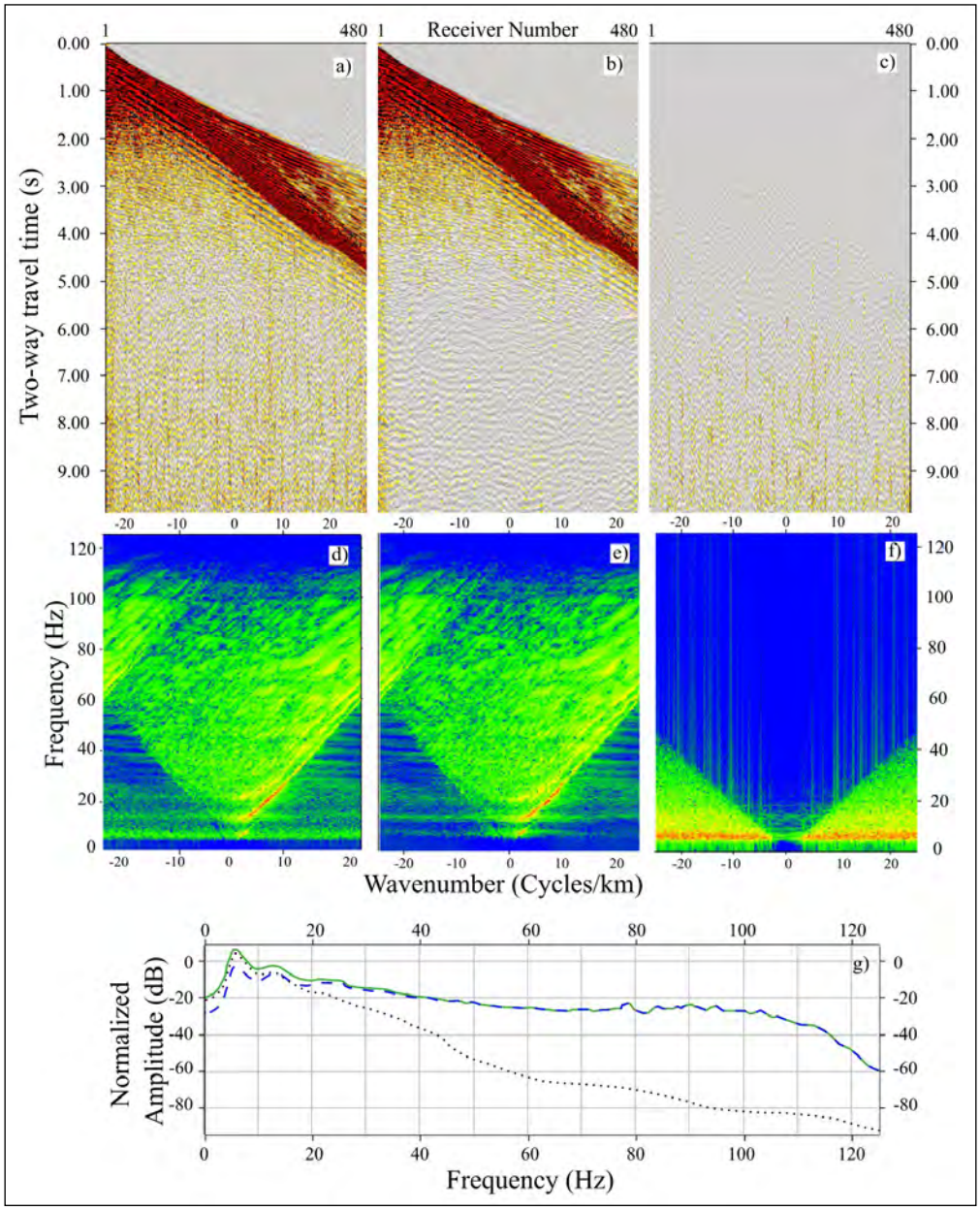

Figure 4- Bird Noise Attenuation; a) before BRDEN application, b) after BRDEN application, c) difference, d) to f) f-k spectrum – before, after, difference, respectively and g) amplitude spectrum before BRDEN (green/straight line), after BRDEN (blue/dashed line), difference (black/dotted).

in the record, it may be difficult to attenuate this noise from the signal. However, an f-k method filter (BRDEN-which was developed by CGG specifically to eliminate this noise) was applied to this data.

Figure 4a demonstrates that noise appearing at regular intervals generated by birds mounted on the streamer is clearly visible on the shot gather and the RMS amplitude map (Figure 5a). The filter is designed for the bird-related linear events which correspond to about 1300 m/s in the f-k domain. In order to avoid overlapping of linear events, it is suggested that the dataset is prepared in such a way that swell and tugging/strumming noise is attenuated beforehand. Figures 4b, c show that the bird noise is successfully discarded from the data. Figures 4d, e, f also reveal the attenuation of low-frequency bird noise in the f-k spectra of the corresponding gathers.

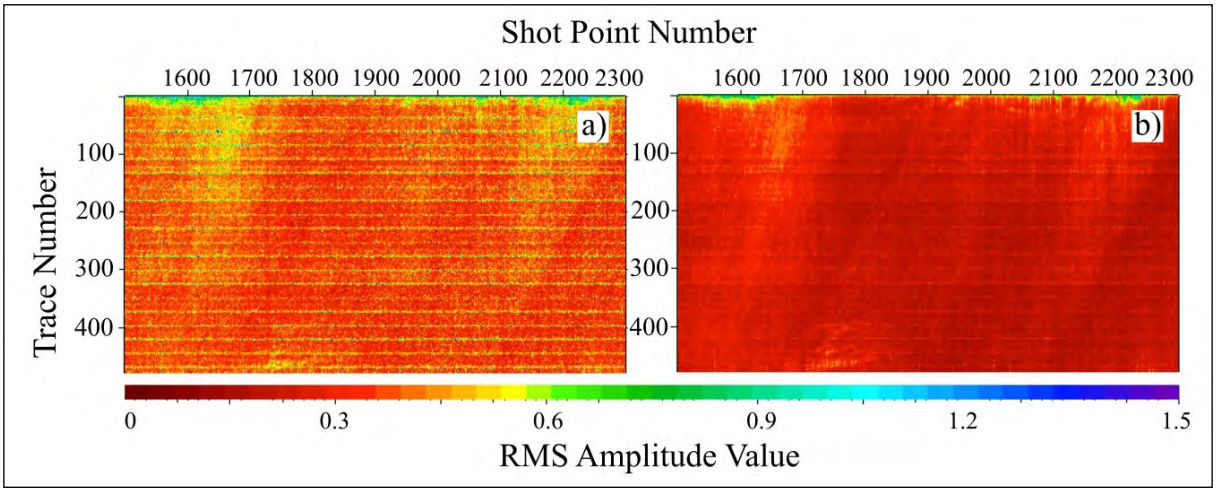

Figure 5- RMS Amplitude maps; a) before BRDEN application, b) after BRDEN application. Please note that the remaining noise in the second figure can be easily removed with a footprint correction that can be applied in later stages.

3. Results

The results of a series of marine seismic noise attenuation methods on a seismic dataset collected in the Southwest Black Sea are presented. Various specific methods were applied for the noises encountered in this study. When the results are evaluated, the noises are eliminated satisfactorily without damaging the primary reflections. However, one of the most essential points not to forget in seismic noise attenuation is that every type of noise is unique for every project dataset. Therefore, noise filtering is suggested to be designed uniquely for each project dataset. Furthermore, these illustrated methods might work for different circumstances but reaching perfection in noise attenuation requires numerous parameter tests, significant labour, a great deal of time, and computing capacity, all of which may be costly for companies. For that reason, the aim of the studies, the demands of the clients, and the deadline of the projects should be carefully assessed by the seismic data processing team to design cost-effective and optimum processing flows.

Acknowledgements

As the team that carries out the work, we are sincerely grateful to the General Directorate of Mineral Research and Exploration which we are a part and worker of for providing us the 3D dataset and the instruments to process the data. We thank all those involved during the acquisition of the dataset on R/V Oruç Reis. We would also like to thank the anonymous reviewers who took the time to review this article.

References

Brittan, J., Pidsley, L., Cavalin, D., Ryder, A., Turner, G. 2008. Optimizing the removal of seismic interference noise. Leading Edge 27(2), 166–175.

Dondurur, D. 2018. Acquisition and Processing of Marine Seismic Data. Elsevier.

Elboth, T., Geoteam, F., Hermansen, D. 2009. Attenuation of Noise In Marine Seismic Data. 2009 SEG Annual Meeting SEG-2009, 3312.

Elboth, T., Reif, B. A. P., Andreassen, Ø. 2009. Flow and swell noise in marine seismic data. Geophysics 74(2).

Elboth, T., Vik Presterud, I.,Hermansen, D. 2010. Time-frequency seismic data de-noising. Geophysical Prospecting 58(3), 441–453.

Guo, J., Lin, D. 2003. High-amplitude noise attenuation. SEG Technical Program Expanded Abstracts, Society of Exploration Geophysicists, 1893–1896.

Gülünay, N. 2008. Two different algorithms for seismic interference noise attenuation. Leading Edge 27(2), 176–181.

Gülünay, N., Magesan, M., Baldock, S. 2004. Seismic interference noise attenuation. SEG Technical Program Expanded Abstracts, 23(1), 1973–1976.

Hlebnikov, V., Elboth, T., Vinje, V., Gelius, L. J. 2019. Onboard de-noise processing for improving towed marine seismic acquisition efficiency. SEG Technical Program Expanded Abstracts 47–51.

Hlebnikov, V., Elboth, T., Vinje, V., Gelius, L. J. 2021. Noise types and their attenuation in towed marine seismic: A tutorial. Geophysics 86(2), 1–19.

McConnell, D. R. 2000. Optimizing deepwater well locations to reduce the risk of shallow-water-flow using high-resolution 2D and 3D seismic data. Offshore Technology Conference.

Parrish, J. F. 2005. Streamer string waves and swell noise. SEG Technical Program Expanded Abstracts, Society of Exploration Geophysicists 72–75.

Schoenberger, M., Mifsud, J. F. 1974. Hydrophone Streamer Noise. Geophysics 39(6), 781–793.

Soubaras, R. 1994. Signal-preserving random noise attenuation by the fx projection. SEG Technical Program Expanded Abstracts, Society of Exploration Geophysicists 1576–1579.

Soubaras, R. 1995. Prestack random and impulsive noise attenuation by fx projection filtering. SEG Technical Program Expanded Abstracts, Society of Exploration Geophysicists 711–714.

Yılmaz, Ö. 2001. Seismic Data Analysis: Processing, Inversion, and Interpretation of Seismic Data. Society of Exploration Geophysicists 10.

Zhang, Z., Wang, P. 2015. Seismic interference noise attenuation based on sparse inversion. SEG Technical Program Expanded Abstracts, Society of Exploration Geophysicists 4662–4666.

Bulletin of the Mineral Research and Exploration

http://bulletin.mta.gov.tr

Groundwater potential mapping using the integration of AHP method, GIS and remote sensing: a case study of the Tabelbala region, Algeria

Ahmed BENNIA[a, b*], Ibrahim ZEROUAL[a], Abdelkrim TALHI[a] and Lahcen Wahib KEBIR[b]

[a]*University Center Ali KAFI, Institute of Science and Technology, Laboratory of Environmental and Energy Systems, Tindouf, Algeria.*
[b]*Agence Spatiale Algérienne, Centre des Techniques Spatiales, Arzew, Algeria.*

Research Article

Keywords:
Remote Sensing, GIS, Hydrogeology, Tabelbala, Analytic Hierarchy Process.

ABSTRACT

Recently, groundwater resources are assessed and evaluated using Geographic Information System (GIS) and remote sensing technologies due to their effectiveness and wide spatial coverage. This work aims to identify groundwater potential areas in the Tabelbala region which lies in the Algerian desert in order to help for the solution of water resources shortages. GIS and remote sensing are employed in the preparation of the controlling factors such as lithology, lineaments, drainage network, slope, land use/land cover, topographic wetness index, and elevation. Statistical Analysis, as well as interpretation of remote sensing data, allow the extraction of important features about the study area and its characteristics. The prepared layers are combined with multicriteria analysis to identify the groundwater potential zones (GWPZs) based on their statistical weights. To validate the conducted work, 222 wells/boreholes are collected and prepared to assess the potential areas. Results reveal that the very good potentiality class covers approximately 8.81% of the total area while 6.47% shows very poor potentiality. In addition, the application of the ROC curve shows an AUC of 89% which reveals the effectiveness of the proposed approach. The final resulting map can be used for the identification of suitable sites for wells implantation.

Received Date: 04.04.2022
Accepted Date: 13.10.2022

1. Introduction

In arid regions, groundwater is one of the essential natural resources for agricultural, domestic, and industrial needs (Kumar et al., 2021). A significant part of the world's population uses groundwater as a source for their daily supply (Kemper, 2004). The Saharan region's development is related to the water-resource availability. Agriculture is the main activity in such regions and an important factor for stabilizing the population. Region development is not limited to enlarging the irrigated surfaces and extending the flow from the wells but mainly it is concerned with the improvement of agricultural productivity. The development success based on a coherent and appropriate definition of water-agriculture-environment policies implies the implementation of suitable technical and organizational actions so that the expected effects are not compromised by uncontrolled and inefficient management.

In the data-scarce region (well data, geophysical data, geomorphology, and geology), GIS and remote sensing techniques are considered effective for water resources prospection and evaluation of groundwater resources. Investigating water resources through

Citation Info: Bennia, A., Zeroual, İ., Talhı, A., Kebir, L. W. 2023. Groundwater potential mapping using the integration of AHP method, GIS and remote sensing: a case study of the Tabelbala region, Algeria. Bulletin of the Mineral Research and Exploration 172, 41-60. https://doi.org/10.19111/bulletinofmre.1188507

**Corresponding author: Ahmed BENNIA, abennia@cts.asal.dz*

classical methods (ex. geophysical, hydrogeological surveys, mapping of outcrops, and logging) is the most adopted approach but they remain expensive and time-consuming (Jha et al., 2010). Although remote sensing applications are numerous, the integration of satellite data with different groundwater layers remains a challenging problem in terms of results reliability. Thus, the integration of such data, as sources of information, in the Saharan region is an effective and promising solution provided that reliability is assured. On the other hand, groundwater prospection maps require the use of spatial techniques (GIS and remote sensing (RS) technique) as well as multi-decision criteria (ex. Analytical Hierarchy Process, AHP) as tools for identifying groundwater potential areas before detailed exploration based on drilling, geophysical techniques and hydrogeological data (Fenta et al., 2015). The created maps can be used for rational and sustainable management based on the estimated groundwater areas (Dar et al., 2011; Thapa et al., 2017; Nasir et al., 2018).

Examining the literature, several decision-making methods (heuristic, deterministic, statistic, index overlay …) allow the decision-maker to formalize the problem and explain the decisional context before proceeding to the evaluation and comparison of the solutions. The AHP aggregation method is one of the simplest to implement, it makes it possible to calculate a synthetic score on the basis of a hierarchy and a weighting of all the criteria relating to the process. Several studies delineate groundwater potential by the use of spatial techniques and conventional classical methods. Multi-Criteria Decision-Making (MCDM) techniques to assess groundwater potential zones is used for potentiality maps that are prepared by assigning weights to variables based on their calculated influences (Kaur et al. 2020). Other authors succeeded in evaluating the groundwater potential by showing the effectiveness of geology and geophysics through the extraction and analysis of the lineaments network and its role in identifying recharge areas (Mpofu et al. 2020). In Panipat (India), two multi-criteria analysis methods (AHP, CT catastrophe multi-criteria technique) are applied by Kaur et al. (2020) to delineate the groundwater potential where the obtained maps are validated using field data. To exploit the importance of remote sensing Saadi et al. (2021) delineated groundwater storage zones by using RS and GIS based on the integration of several influencing factors like geology, rainfall, slope and TWI. These works confirm the importance of remote sensing and GIS when combined with multi-criteria decision methods.

The conducted study aims at the identification of the groundwater potentiality areas by the integration of satellite data, GIS, as well as the AHP method. According to recent works, it can be seen that multi-criteria decision analysis is widely used for groundwater modelling (Islam et al., 2017) and groundwater storage evaluation (Jha et al., 2010; Nag and Kundu, 2018). The combination of information obtained by the processing and analysis of satellite data and conventional statistical data facilitates the elaboration of information related to groundwater potential areas (Rashid et al., 2012; Selvam et al., 2015; Nasir et al., 2018). It is, furthermore, useful for extracting morpho-structural information (lineaments, and drainage patterns) contributing to delineating the recharge areas (Magesh et al., 2012). In addition, the analysis of the controlling factors (ex. lithology, structures, slope, aspect and drainage density) in the GIS framework through the AHP can lead to better performance as all the factors are brought into consideration. To increase the reliability of the conducted study, field data (222 wells/boreholes) are collected and used to assess the obtained results based on the ROC curve. The final map has the objective of identifying sites for wells implementation to satisfy the water demands. For the first time, remote sensing and GIS technique is used in this Saharan region (Tabelbala) which has not known any hydrogeological study before. The result of the present study can give an idea about the potential zones in the Tabelbala region. The first part of this paper is to elaborate the influencing parameters (lithology, lineaments, LULC, drainage network, slope, elevation, and TWI) at an appropriate scale allowing a hydrogeological study, and update the lineament (structural study) and lithological maps from the interpretation of satellite images (optical images and DEM). The second part of this work presents the groundwater potential zone's locations, using the AHP technique as an illustration of how to use the digital maps created as part of this study and it is the first method to delineate the groundwater potential zones in this region (Tabelbala).

2. Description of the Study Area

The study area is situated in southern west Algeria and lies between 3° to 4° W longitude and 29° to 30°N latitude (Figure 1). Its elevation varies from 398 m to 909 m above mean sea level. The Tabelbala region borders the Marocain Anti Atlas in the North, the Réguibat shield in the South, the Ougarta range in the East and the Tindouf basin in the West. It has an area of 10705.09 km^2, an average temperature of 25°C and an arid continental climate.

The geological structures of the region are characterized by different geological domains that are: Erg Er Raoui in the North-East, Djebel Kahal Tabelbala in the East, Djebel Ben Tadjine in the South, and Erg El Atchane in the South.

The precipitation is very low as reported by the average monthly precipitation distribution data acquired from Data Access Viewer-Nasa Power (DAV) in the period 1981 to 2020 (https://power.larc.nasa.gov/data-access-viewer/). Figure 2 shows that the Tabelbala region is located in the areas of isohyets which have values below 10 mm. In addition, the average monthly precipitation histogram shows clearly that the rainiest month is October (0.4 mm) whereas July is the driest month (0.02 mm).

The drainage network characterizing the study area seems well developed in the landscape, dry for the most part, the main river in the region is that of the Daoura (Oued Daoura) in the North coming from Morocco (Figure 3).

Except for some existing reliefs (Djebel Kahal Tabelbala in the East, Djebel Ben Tadjine in the South-West), the Tabelbala region consists of Erg Erraoui, Erg El Atchane, Erg Atimine and Hamada of Manda. The geological structures characterizing the considered area are of medium complexity, noting the complexity of the Lower Cambrian deposits. This entity as it appears to us today is actually infinitely more complex than the presented maps. Indeed, each new cycle modifies the state of the previous cycle. The sediments of the recent cycle partly mask the oldest deposits and each orogenic phase partially deforms and breaks the pre-existing architectures and structural pre-dispositions that guide the new structures. Based on the previous work (Menchikoff, 1930; Mekkaoui et al., 2017), it appears that the mountains of the

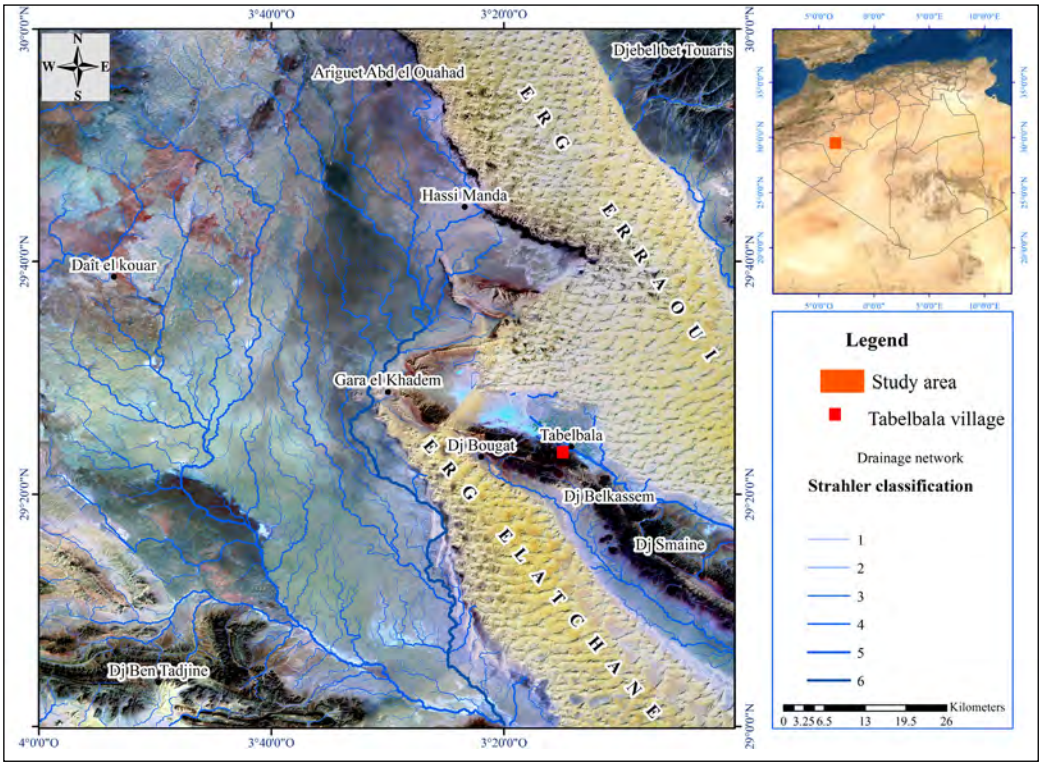

Figure 1- Study area location.

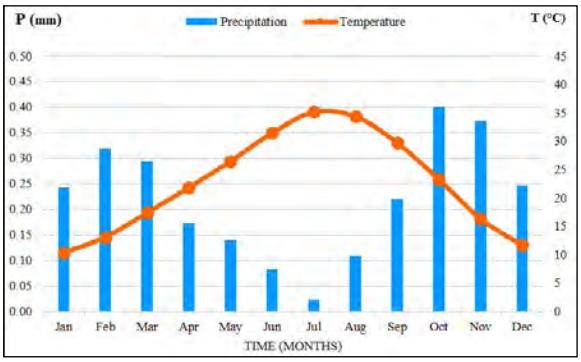

Figure 2- The average monthly precipitation and temperature from 1981 to 2020.

considered area (Tabelbala) form a succession of anticlines and synclines of NW-SE direction and they are sometimes intersected by accidents of the same direction (Ougartian accident), as well as by major accidents of direction NE-SW (main tectonic accidents). The age of the folding's cannot be specified (Menchikoff, 1930) but the author explains that by their tectonic style, the mountains of Tabelbala would be linked well to the Hercynian folding's of Morocco, which does not appear in the south of the region. The drainage pattern of the study area is controlled by the second direction NW-SE.

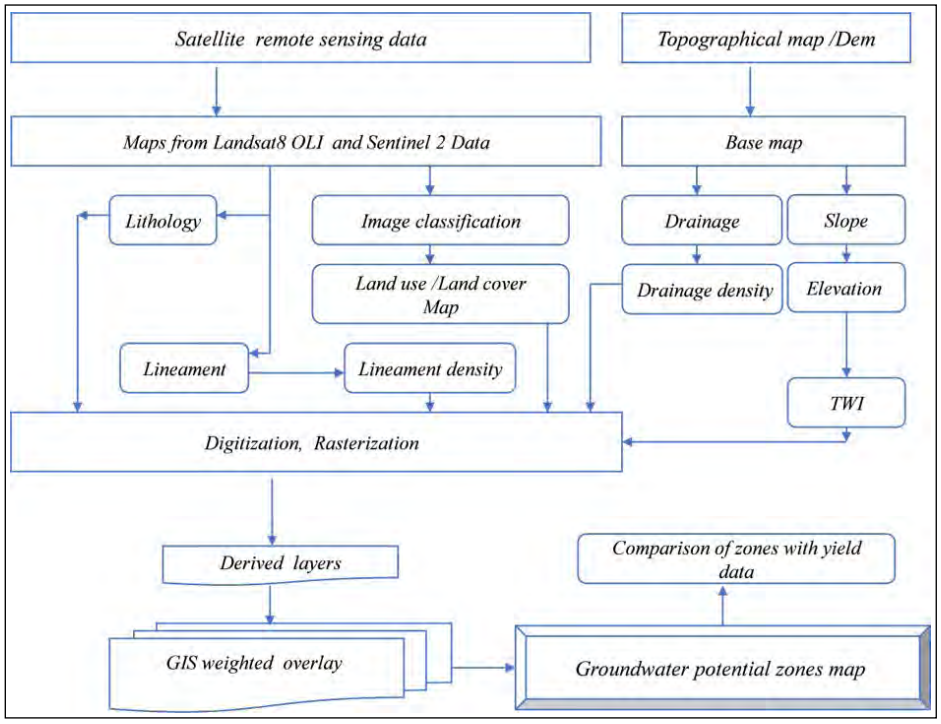

Figure 3- Conceptual framework of the proposed method.

3. Methodology

The proposed approach is summarized in Figure 3. For achieving the desired goal, multitemporal and multiresolution images are used for the characterization of lithological and structural outcrops. Satellite data required for the conducted work include Landsat 8 (OLI) images provided by the United States Geological Survey (USGS) acquired the 13th October 2021 and the 20th October 2021 where four scenes located by paths (199 to 200) and row (39 to 40) are use.

3.1. Overview and Contributions

AHP is the most popular method used for the preparation of groundwater prospect maps. During this work, seven thematic layers are prepared: lithology, drainage density, lineaments density, slope, elevation, topographic wetness index, and land use/ land cover. These maps are elaborated based on the processing, analysis, and interpretation of satellite images (Figure 4). In order to highlight geological features (lithological and structural information) and

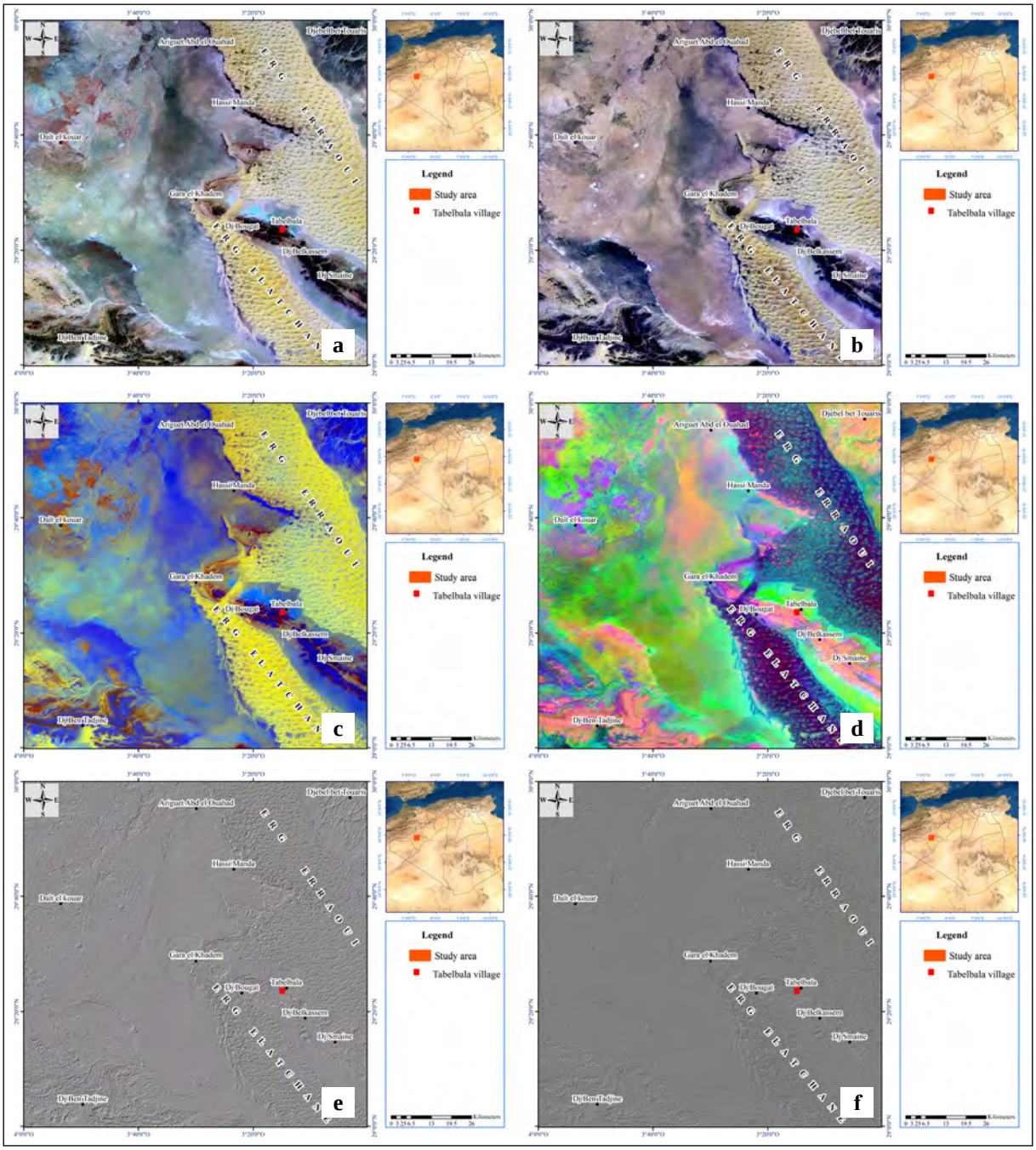

Figure 4- a) Landsat 8 OLI false color composite 7(R)5(G)4(B), b) Sentinel 2 false color composite 8(R)4 (G)3(B), c) Landsat 8 OLI bands ratios 7/3(R), 5/2 (G), 4/7 (B), d) Landsat 8 OLI principal component analysis (P1P2P3), e) Landsat 8 OLI filter 45° and f) Sentinel filter 45°.

update the geological map of the region at 1/200.000 scale, several digital images processing techniques are applied: color composite, enhancements, filtering, principal component analysis, and band ratio. These techniques include Landsat 8 OLI in false color composite (Bands: 754), Sentinel 2 in false color composite (Bands:843), Landsat 8 OLI bands ratios (7/3, 5/2, 4/7) and Landsat8 OLI principal component analysis. The usefulness of such information is considered in many studies as an efficient tool for lithological discrimination, especially in arid zones (Scanvic, 1997; Prost, 1994; Rencz and Ryerson, 1999; Prost, 2013; Nemmour-Zekiri and Oulebsir, 2020). In order to extract and highlight the linear

network and structural discontinuities (dykes, faults, lineaments and fractures), directional filters are carried out on Landsat 8 OLI (Bands:754) and Sentinel 2 images (Bands:843) which have suitable spatial and spectral resolutions. In our study area, 414 lineaments are extracted using the semi-automatic extraction tool (Figure 4) in different directions N0°, N45°, N90°, and N135° (Scanvic, 1997; Rencz and Ryerson, 1999; Prost, 2013; Gupta, 2017; Nemmour-Zekiri and Oulebsir, 2020).

To model the complex terrain of Tabelbala, a specific type of raster data (DEM) is used which has an important role in terms of spatial analysis and their integration in the GIS network. The drainage density, slope, elevation, and the Topographic Wetness Index are generated automatically from the Shuttle Radar Topography Mission (SRTM) Digital Elevation Model (30m of spatial resolution).

The land use/land cover map is prepared using the supervised classification of Landsat 8 OLI images.

3.2. The Proposed GIS-Based AHP Method

The AHP method is developed by Saaty (1980) and becomes the widely used method for calculating the weights and rates for the input factors based on their importance to the relative criteria (Kousalya et al., 2012; El abidine and Abdelmansour, 2019). The AHP method is used generally to facilitate decisions, reduce the complexity of different problems, find priorities (Punniyamoorty et al., 2012), planning and distinguish resources. In this work, weight assignment of controlling factors is carried out based on the opinion of experts' judgement, and knowledge, the literature review and field experience (Table 1) in order to increase the precision and reliability of the results. The judgement matrix is established based on pairwise comparison according to a 9-level scale to affect the decision of the parameters (Saaty, 2003) (Table 2).

Several consecutive steps are performed to compute the Consistency Ratio (CR) and evaluate the normalized weights:

1) Pairwise comparison matrix (PCM) conception:

$$P=\begin{pmatrix} P_{11} & P_{12} & \dots & P_{1n} \\ P_{21} & P_{22} & \dots & P_{2n} \\ \dots & \dots & \dots & P_{3n} \\ P_{n1} & P_{n2} & \dots & P_{4n} \end{pmatrix} \quad (1)$$

Where *Pij* is the n^{th} indicator unit and *Pnn* represents the judgement matrix factor.

2) Normalized weight computation:

$$W_n=GM_n/\sum_{n=1}^{N} GM_n \quad (2)$$

Where the *W* represents the weight vector and *GMn* is the geometric mean related to the i^{th} row.

3) Judgement's coherence calculation:

$$CR=CI/RCI \quad (3)$$

Where CR denotes the Consistency Ratio, CI represents the Consistency Index and RCI stands for the Random Consistency Index of Saaty's classification (Saaty, 1990). The RCI value depends on the number of parameters which is estimated to be 1.32 in our case.

4) Consistency Index is computed using the Equation 4:

$$CI=(\lambda_{max}-N)/(N-1) \quad (4)$$

Where λ signifies the Eigen value of the judgement matrix and it is computed using Equation 5.

5) Eigen value of the X matrix:

$$\lambda=\frac{\sum_{i=1}^{n}(P_iW)_n}{N*W} \quad (5)$$

The assigned weights as well as the values of the comparison matrix are reported in Tables 1, 2, 3.

The Consistency Ratios (CR) related to the pairwise comparisons were less than 0.1. The values of λ_{max} and the CR values of criterion CI and RI are shown in Table 4.

For groundwater potential mapping, the weighted index overlay is widely used as mentioned in the literature. It is based on human judgements as well as the combination of multiple thematic maps (Boobalan

Table 1- Weights of the controlling factors and their classification.

Factor/class	Subclass	Rating	weight	Normalized rate	Weighting
Lit	Quaternary	5	38.9	0.294	11.441
	Neogene	4		0.235	9.153
	Silurian	3		0.176	6.865
	Ordovician	2		0.118	4.576
	Cambrian	2		0.118	4.576
	Proterozoic	1		0.059	2.288
LD	Very low	1	23.7	0.067	1.580
	Low	2		0.133	3.160
	Moderate	3		0.200	4.740
	High	4		0.267	6.320
	Very high	5		0.333	7.900
LULC	Runoff zone	5	15.4	0.192	2.962
	Sandy deposits	4		0.154	2.369
	Sandy veil	3		0.115	1.777
	ERG	2		0.077	1.185
	Hilly area	1		0.038	0.592
	Valley	5		0.192	2.962
	Settlement	1		0.038	0.592
	Agricultural zone	4		0.154	2.369
	Reg & Hamada zones	1		0.038	0.592
DD	Very low	5	8.7	0.333	2.900
	Low	4		0.267	2.320
	Moderate	3		0.200	1.740
	High	2		0.133	1.160
	Very high	1		0.067	0.580
S	0°-3°	5	5.3	0.333	1.767
	3°-6°	4		0.267	1.413
	6°-12°	3		0.200	1.060
	12°-25°	2		0.133	0.707
	25°-50°	1		0.067	0.353
E	398m-500m	5	4.9	0.333	1.633
	500m-600m	4		0.267	1.307
	600m-700m	3		0.200	0.980
	700m-800m	2		0.133	0.653
	800m-909m	1		0.067	0.327
TWI	03-06	1	3.1	0.067	0.207
	06-10	2		0.133	0.413
	10-14	3		0.200	0.620
	14-18	4		0.267	0.827
	18-22	5		0.333	1.033

Table 2- AHP's comparison matrix.

	Lit	LD	LULC	DD	S	E	TWI
Lit	1.00	2.00	3.00	4.00	6.00	7.00	9.00
LD	0.50	1.00	2.00	3.00	4.00	5.00	7.00
LULC	0.33	0.50	1.00	2.00	3.00	4.00	5.00
DD	0.25	0.33	0.50	1.00	2.00	3.00	4.00
S	0.17	0.25	0.33	0.50	1.00	1.00	2.00
E	0.14	0.20	0.25	0.33	1.00	1.00	2.00
TWI	0.11	0.14	0.20	0.25	0.50	0.50	1.00

Lit: lithology, LD: lineament density, LULC: land use/land cover, DD: drainage density, S: slope, E: elevation, TWI: topographic wetness index.

Table 3- The Normalized AHP matrix.

	Lit	LD	LULC	DD	S	E	TWI	Norm Weight
Lit	0.399	0.451	0.411	0.360	0.342	0.325	0.300	0.370
LD	0.199	0.225	0.274	0.270	0.228	0.232	0.233	0.237
LULC	0.133	0.113	0.137	0.180	0.171	0.186	0.166	0.155
DD	0.099	0.075	0.068	0.090	0.114	0.139	0.133	0.103
S	0.066	0.056	0.045	0.045	0.057	0.046	0.066	0.054
E	0.057	0.045	0.034	0.030	0.057	0.046	0.066	0.048
TWI	0.044	0.032	0.027	0.022	0.028	0.023	0.033	0.030
Sum	**1.000**	**1.000**	**1.000**	**1,000**	**1.000**	**1.000**	**1.000**	**1.000**

CR= 0.02 < 0.1 acceptable, CI= 0.03, λ_{max}= 7.209.

Table 4- Theme quantity (n), highest Eigen value of judgement matrix (λ_{max}), Random Consistency Index (RI), Consistency Ratio (CR) and Consistency Index (CI) of the considered layers.

Themes	N	λ_{max}	CI	RI	CR
Lithology (Lit)	6	6.277	0.109	1.24	0.088
Lineament density (LD)	5	4.73	0.01	1.12	0.01
Land use/land cover (LULC)	9	9.58	0.13	1.45	0.09
Drainage density (DD)	5	5.27	0.06	1.12	0.059
Slope (S)	5	5.25	0.103	1.12	0.092
Elevation (E)	5	5.22	0.10	1.12	0.08
Topographic wetness index (TWI)	5	5.22	0.08	1.12	0.075

and Gurugnanam, 2016). To identify the potential zones for Tabelbala region, a multi-criteria approach was applied after assigning the corresponding rates and weights to all controlling factors. The GWPZ is calculated as shown in the Equation 6 (Das et al., 2019):

$$GWPZ= \sum_{i}^{n} (Litw*Litr)+(LDw*LDr)+(LU\&LCw* LU\&LCr)+(DDw*DDr)+(Sw*Sr)+(Ew*Er)+(TWIw*TWIr) \quad (6)$$

Where *GWPZ*: groundwater potential zones, *r:* rating, *w*: factor weightage *Lit*: lithology, *LD*: lineament density, *LULC*: land use/land cover, *DD*: drainage density, *S*: slope, *E*: elevation and *TWI*: topographic wetness index.

3.3. Lithology

For groundwater studies, lithology is one of the important parameters in determining the permeability of the different formations. The Tabelbala region is part

of the marginal (intra-cratonic) depression of the West African platform (Kurek and Preidl, 1987; Ennih and Liégeois, 2001). It is made up of volcano-sedimentary formations of the Proterozoic (lower structural stage), sedimentary deposits (sandstone, sandstone-clay, and sandstone-carbonate) of the Paleozoic (middle structural stage) and Cenozoic deposits of various genesis (Menchikoff, 1930). The lower structural stage is represented by basic and neutral volcanites, tuffs, greywackes, and acidic volcanites. The middle structural stage is formed of Paleozoic rocks (Mekkaoui et al., 2017). The Quaternary formation occupies an important part in the study area and it's made of sand, silt, and alluvial deposits. It has been assigned the highest weight due to its favorable infiltration characteristics. The oldest formation is related to the Proterozoic which is formed of rhyolite, ignimbrite, dacitic porphyry, sandstone, basalt, andesitic basalt, andesitic tuffs, andesitic porphyry tuffs, greywackes, and conglomerate (Figure 5). For this formation, the lowest weight has been assigned due to the low infiltration capability. The Cambrian, the Ordovician sedimentary as well as the Quaternary deposits (alluvium, torrential and aeolian deposits) are the most developed in this region while the Silurian is characterized by a fairly limited extension.

3.4. Lineament Density

Linear structures are straight linear features that appear on the earth's surface as meaningful landscape lines (Hobbs, 1904). Lineaments are indicators of an area of weakness in bedrocks and are defined as curvilinear or linear structures on the surface of the earth. Lineament density is one of the important factors in groundwater delineation as high lineament density indicates high groundwater productivity (Hatefi and Ekhtesasi, 2016). Lineament density is prepared using the following equation (Mandal et al., 2016).

$$\text{Lineament density (LD)} = \sum_{i=1}^{n} \text{Li/S} \qquad (7)$$

Where LD stands for the lineament density, Li defines the lineament length, *i* is the lineament number and S signifies the unit area.

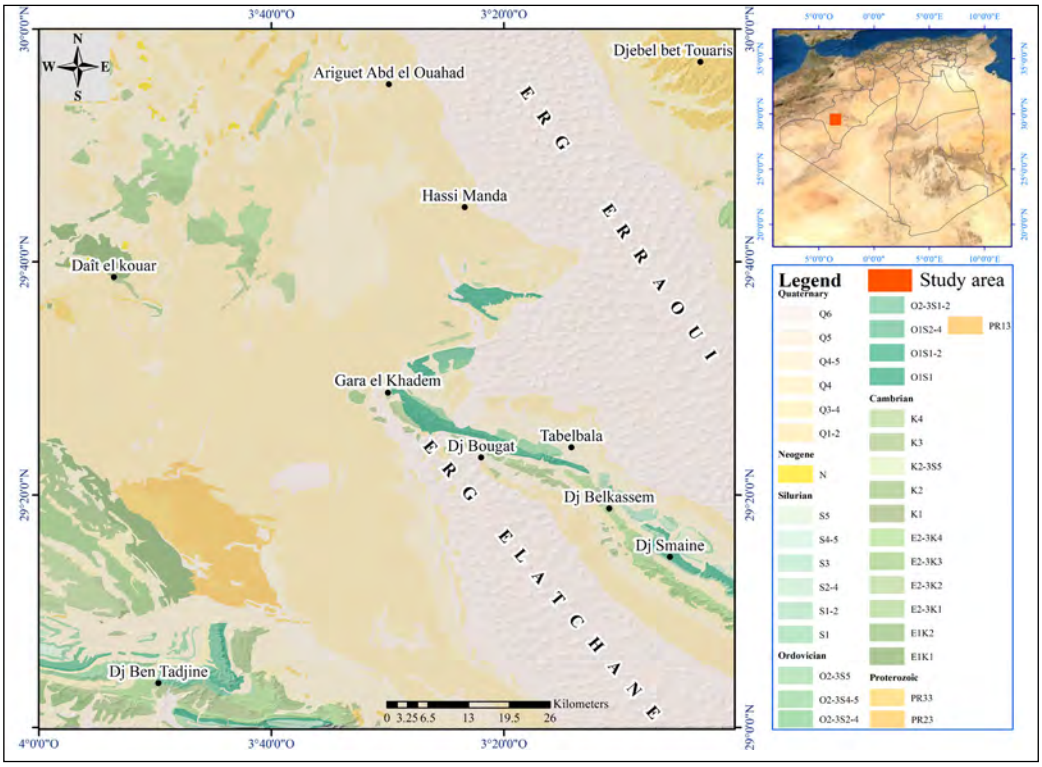

Figure 5- Lithological map of Tabelbala (Rabah et al., 2016).Quaternary: sand, silt, and alluvial deposits; Neogene: sandy-clay, conglomerate, sandstone, and limestone; Silurian: clay-shale, sandstone, and limestone; Ordovician: Quartzite, sandstones, clay-shale, and conglomerate; Cambrian: Quartzite-sandstone, sandstone, copper-sandstone, and intraformational conglomerate; Proterozoic: rhyolite, ignimbrite, dacitic-porphyry, sandstones, basalt, andesitic-basalt, andesitic-tuffs, andesitic-porphyry tuffs, greywackes, and conglomerate.

The lineaments are extracted and mapped from two sources: Geological Survey of Algeria at 1/200000 scale and satellite data. Their length ranges from 0.12 to 24.79 km whereas their directions are interpreted by using rose diagrams. It is found that the majority of lineaments are oriented towards the NE-SW direction followed by the other directions (Figure 7).

In the study area, the lineament density ranges from 0 to 0.00083 km/km^2 and it was arranged into five classes: 0-0.00017, 0.00017-0.00034, 0.00034-0.00051, 0.00051-0.00068, 0.00068-0.00085 with a real percentage of 80.15, 13.62, 4.56, 1.26, 0.38 respectively. The highest lineament density (0.00068-0.00085 km/km^2) has a good groundwater potential while the lowest lineament density (0-0.00017 km/km^2) is characterized by a poor groundwater potential (Figure 6).

The directional statistical analysis of the different lineaments shows two preferential directions. They are generally oriented NE-SW and NW-SE. The histogram of relative frequencies (Figure 7) confirms the same linear classes.

3.5. Drainage Density

The drainage network is prepared and updated using DEM (SRTM) and Landsat 8 OLI images. It is categorized up to the fifth order. Once the network is prepared, the drainage density map can be calculated as it is considered a vital factor for groundwater assessment where it is inversely proportional to the permeability (Shekhar and Pandey, 2015). It is the ratio of total stream length and the total area of the region of interest (Yeh et al., 2016) as shown in the Equation 8:

$$DD=L/S \qquad (8)$$

Where *DD* defines the drainage density, *L* is the length of the stream, and *S* stands for the unit area (Tarboton et al., 1992).

Areas with high groundwater potential are often characterized by a fairly high infiltration rate as well as a sparse and sparsely drained drainage network (Dinesh Kumar et al., 2007). For this reason, we assign the lowest weight value to the highest drainage density and vice versa. As shown in (Figure 8), Tabelbala demonstrates a wide range of density values ranging from 0 to 0.0012 km/km^2.

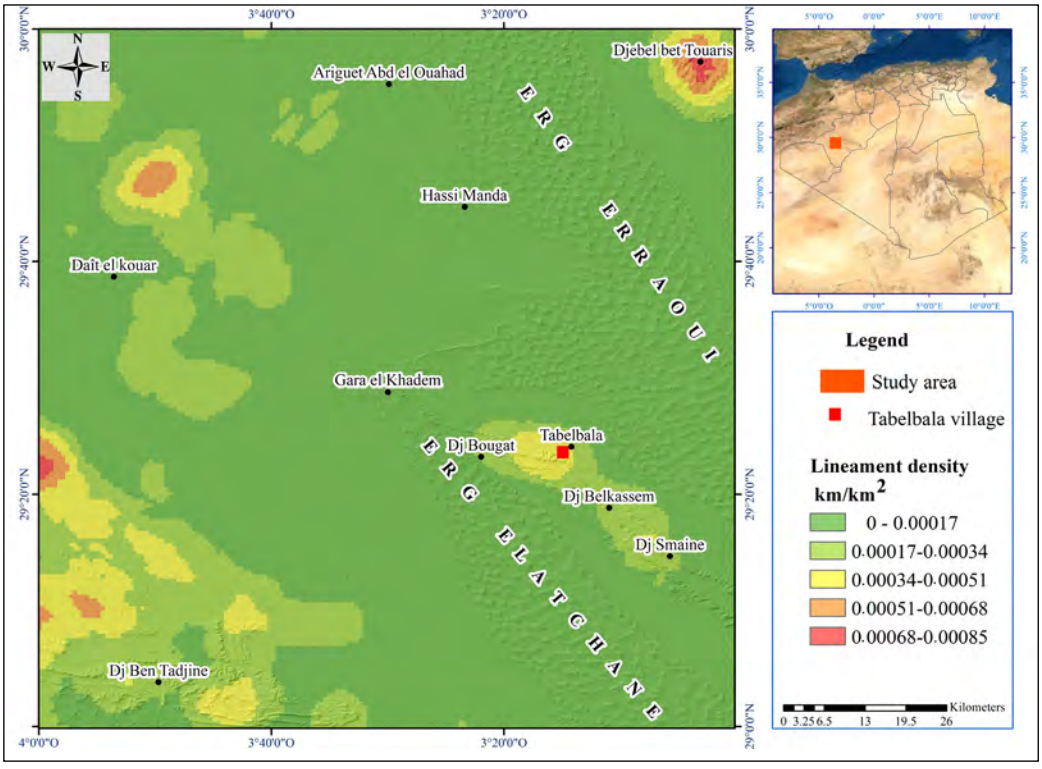

Figure 6- Lineament density.

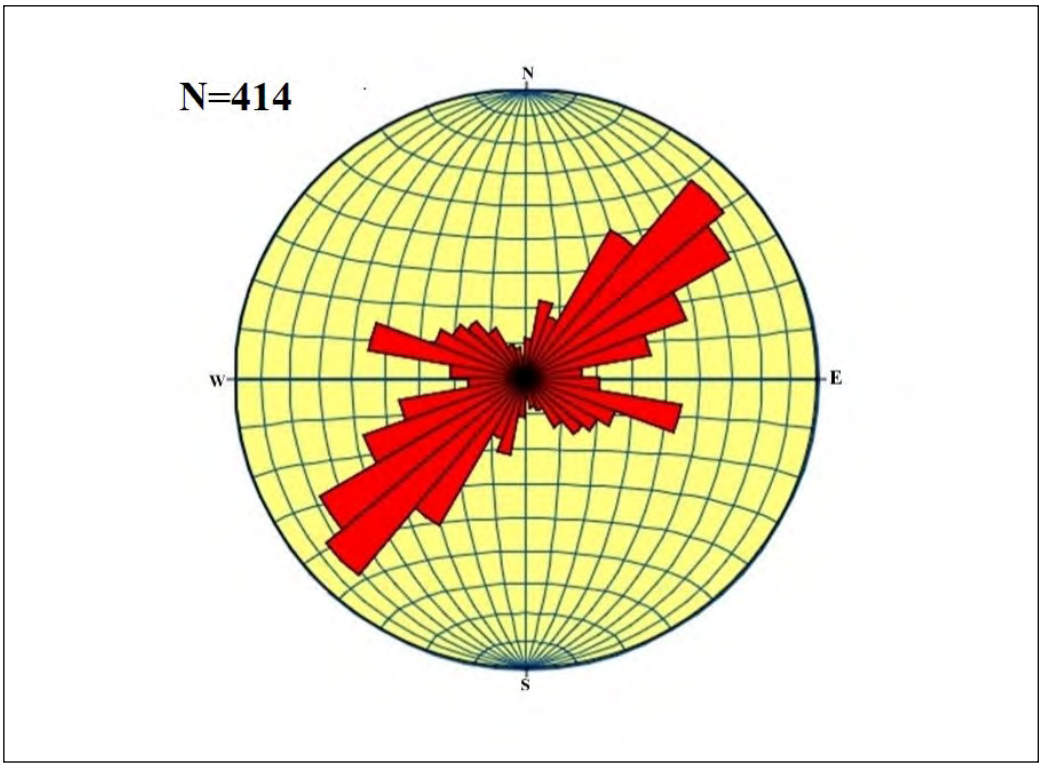

Figure 7- Rose diagram of the lineament orientation.

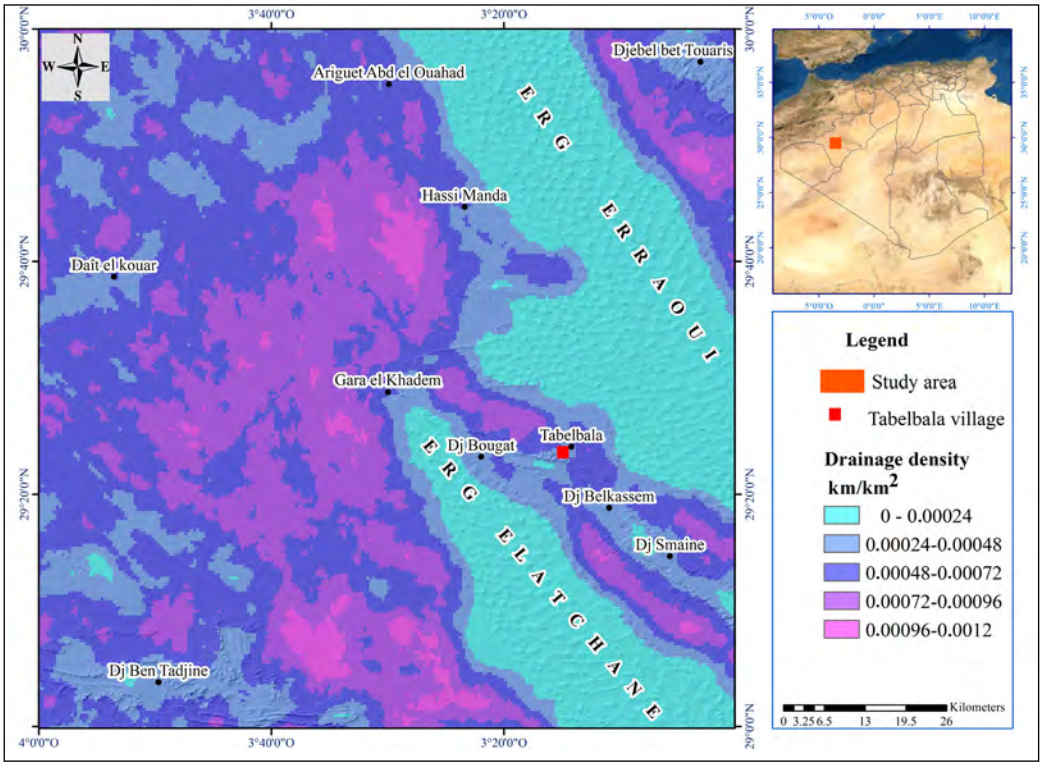

Figure 8- Drainage density of Tabelbala.

3.6. Slope

In groundwater investigation, the slope is a significant factor which has a direct effect on water retention and the infiltration amount (Tanvir Rahman et al., 2012). In Dait el Kouar, Ariguet Abd el Ouahad and Hassi Maanda, the slope is very gentle to nearly flat (0-3°) while it ranges from 6 to 50° on the right side (Djebel bet Touaris, Erg Erraoui, Erg El Alatchane, Gara El Khadem, Djebel Bougat, Djebel Belkassem, Djebel Smaine, and Djebel Ben Tadjine). The hilly, moderate and high elevated areas are characterized generally by a low infiltration rate while the plain areas have high infiltration. (Thapa et al., 2017). The slope map is generated based on the DEM SRTM-30m spatial resolution and it ranges between 0 and 55°. The plain area has high priority while high and moderate elevated points have low priority. Five slope classes are characterized in our study area: 0°-3°, 3°-6°, 6°-12°, 12°-25°, 25°-50° (Figure 9).

3.7. Elevation

For groundwater estimation, elevation is considered one of the most important elements. Generally, the plain zones are characterized by a high rate of infiltration as well as a long retention time in terms of groundwater recharge. On steep slopes, the runoff surface is quite large while the infiltration rate is almost low (Adeyeye et al., 2019). In our region, the elevation value varies from 398 m to 909 m (above mean sea level). The elevation value is subdivided into five classes: 398-500 m (20.20%), 500-600 m (64.34%), 600-700 m (14.52%), 700-800 m (0.84%), 800-909 m (0.07%), respectively (Figure 10).

3.8. Land Use/Land Cover (LULC)

The land use/land cover is one of the most determining factors in hydrogeological prospecting. It has a direct effect on hydrologic parameters, surface runoff zone, infiltration and evapotranspiration (Jasrotia et al., 2016; Thapa et al., 2017; Berhanu and Hatiye, 2020). Land use/land cover of the study area (Figure 11) is composed of runoff zones (35.01%), Oued (0.27%), reg and Hamada zones (27.65%), relief (10.26%), Erg (26.56%), sandy veil (0.002%), sandy deposits (0.13%), agricultural areas (0.106%) and settlements (0.008%). The importance order is given in Table 1. The highest rate is given for a runoff zone and Oued while the lowest rate is assigned to the settlements and relief.

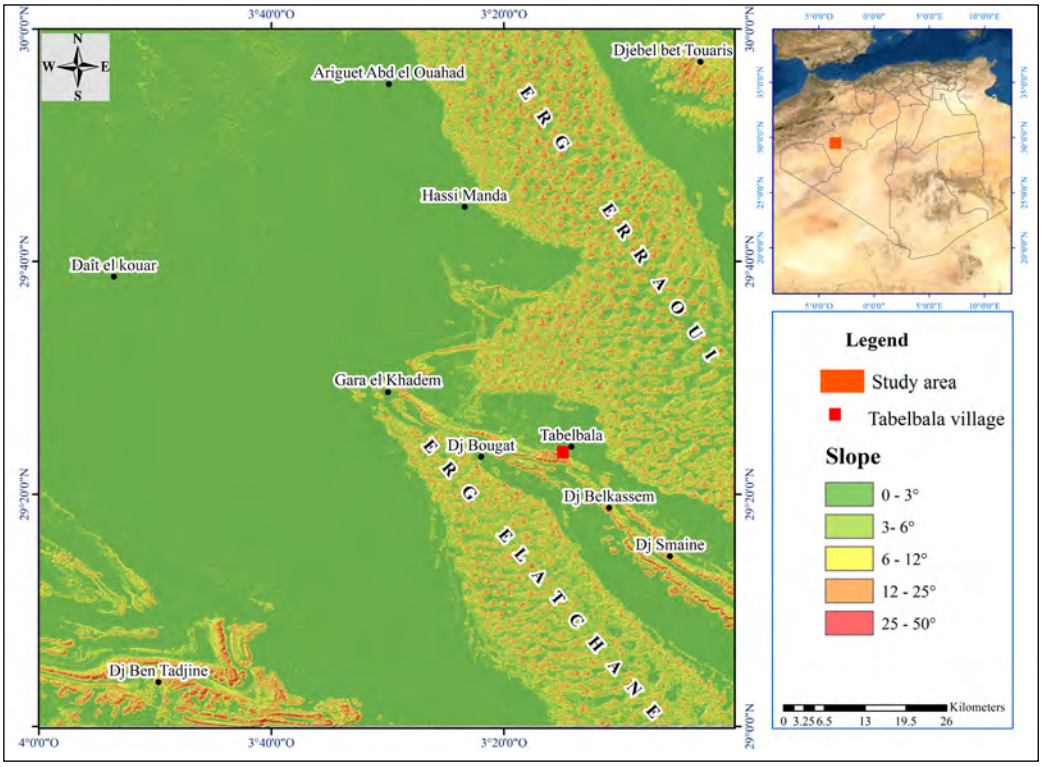

Figure 9- Slope map of the concerned area.

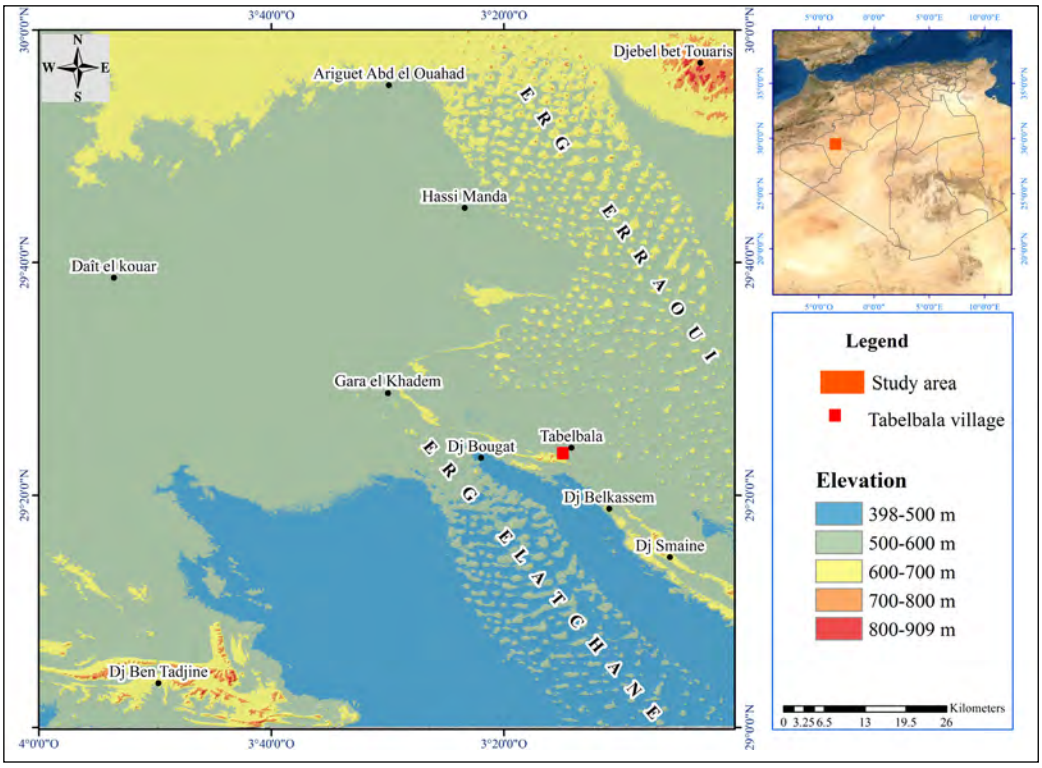

Figure 10- Elevation map of the study area.

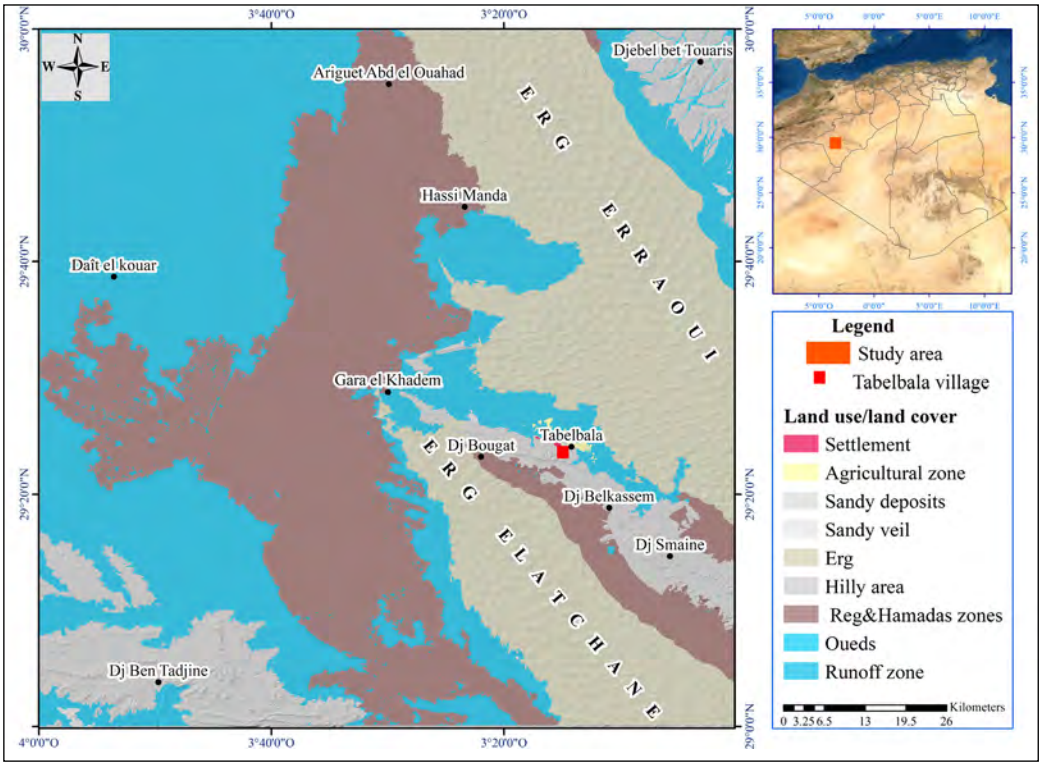

Figure 11- Land use/land cover map of Tabelbala.

3.9. Topographic Wetness Index TWI

Topography is known to have an influence on the different hydrological processes related to permeability, infiltration, runoff and land productivity. The amount of groundwater infiltration of the study area (Kousalya et al., 2012; Nithya et al., 2019) is measured by elaborating the TWI factor and its topographical conditions.

By using the GIS environment, the TWI is prepared and used to trigger the hydrological flow in the watershed (Vadrevu et al., 2006; Bevan and Lake, 2016). TWI can be calculated using the following equation:

$$TWI=\ln \alpha/\beta \qquad (9)$$

where α = slope of the studied area and β = topographic gradient.

The high weight is attributed to the high topographic wetness index value. The TWI value of the study area varies from 3 to 22 (Figure 12), the higher TWI value corresponds to high groundwater potentiality and vice versa. The visual interpretation of the TWI map shows that the high to medium sites favorable to wetlands are situated along the watercourses, Oued, runoff zones, and agricultural zones while the dry areas are located in the Reg and Hamada Zones, Erg, sandy veil, and deposits.

4. Discussion

4.1. Groundwater Prospects Zones

Several studies attempt to analyze Algeria's groundwater resources although these assessments have mostly focused on the country's north region. Based on the available information, this study intends to assess the groundwater resources of the Tabelbala region (Desert area). In the case of the lesser-known aquifers in southwestern Algeria, the used methodology has proven to be effective in a number of data-scarce studies. It is based on the integration of layers that influence potentiality and have been incorporated into a GIS environment. By integrating consistent influencing layers of lineament density, lithology, drainage density, land use/land cover, slope, elevation, and topographic wetness index which were weighed and categorized in a GIS, a multi-criteria analysis was established. The groundwater potential zones map is created by combining (rate*weight)

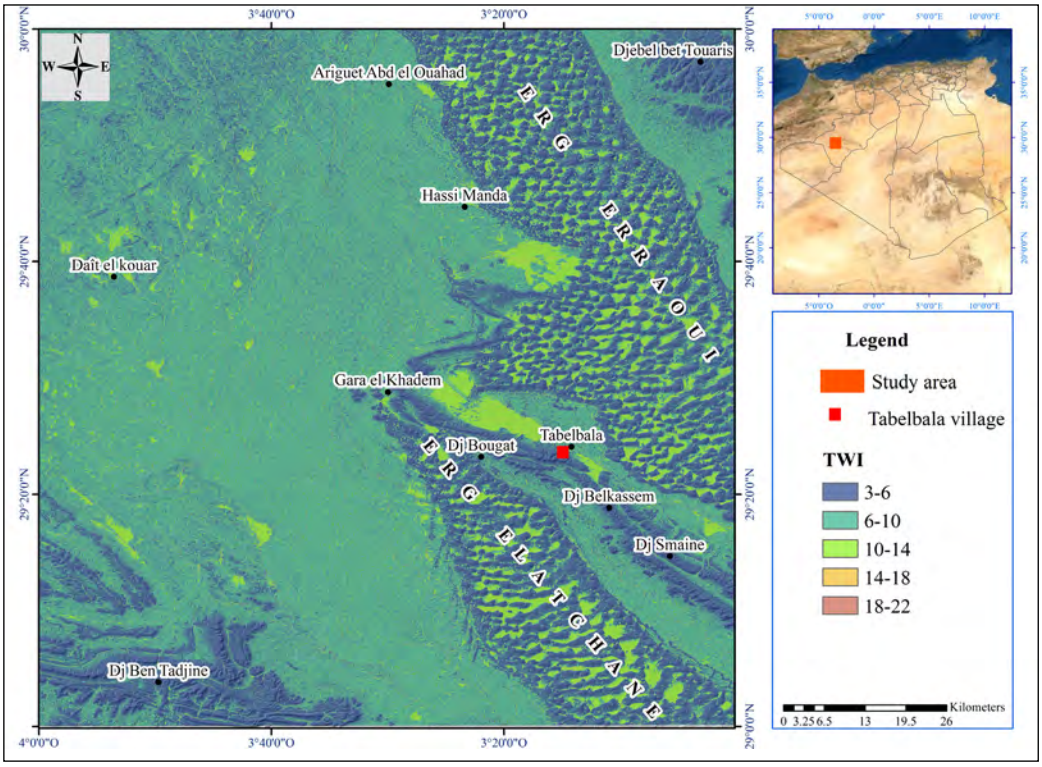

Figure 12- Topographic wetness index map of the study area.

of the layers indicated above with each layer being assigned a weight ranging from 1 to 9 depending on the relevance and value of each factor in groundwater prospects and assessment. The pairwise comparison matrix is created using the techniques outlined in the preceding section. Weights and rates are chosen based on the work of numerous researchers (Kerzabi et al., 2021).

The obtained results provide an assessment of each factor's influence and an estimate of its rate of contributions to the determination of prospective groundwater areas. These results are presented as follows (Figure 13): lithology (38.9%) is the most influential component, followed by lineaments (23.7%), Lu/Lc (15.4%), drainage density (8.7%), slope (5.3%), elevation (4.9%) and TWI (3.1%). It should be highlighted that the CR value (used to aggregate the multiple criteria) is estimated at 0.02 which indicates that our simulation is very consistent (rates and weighs) (Figure 14 and 15).

Figure 16 shows the groundwater potential zones obtained. According to the conducted research, the very high potentiality class accounts for 8.81% of the total area and it is related to a moderate slope, low elevation values, and lithology of sands, conglomerates, and alluvium deposits. It can be found in the South-West of Djebel Ben Touaris, in Tabelbala, in the South-East and North of Dait El Kouar and Djebel Ben Tadjine.

The high potentiality zone (20.53%) is located in the south-west of Erg El Atchane, Erg Er Raoui and Djebel Bet Touaris with an altitude ranging from 500 to 600 meters. It contains a high lineament density and a gentle slope whereas the moderate potentiality zone (58.25%) occupies a good part of the study area and is mainly confined to relatively moderately sloping areas with minor lineaments. It corresponds to the lower part of the upper pediment and relief whose lithological character is composed of an eolian sand at elevations ranging from 398 to 550m and a medium to low TWI rate. The zones of low potentiality (5.94%) are located in the upper part of the pediment (recharge zones) with low lineament density, low elevation, and covered by a Proterozoic formation. The high potentiality near Dait El Kouar, is explained by the high lineament density (main fault). It corresponds to the lower part of the upper pediment and relief whose lithological character is composed of quaternary deposits (sand, silt, and alluvial deposits) at elevations ranging from 398 to 550m.

On the other side, the hilly areas are grouped into runoff areas with a very steep slope and low infiltration. They are characterized by a very low potentiality (6.47%) where groundwater is limited to narrow valleys and belongs to faults and fractures (lineaments). For the well locations, most of them are concentrated on Erg Er Raoui which is known

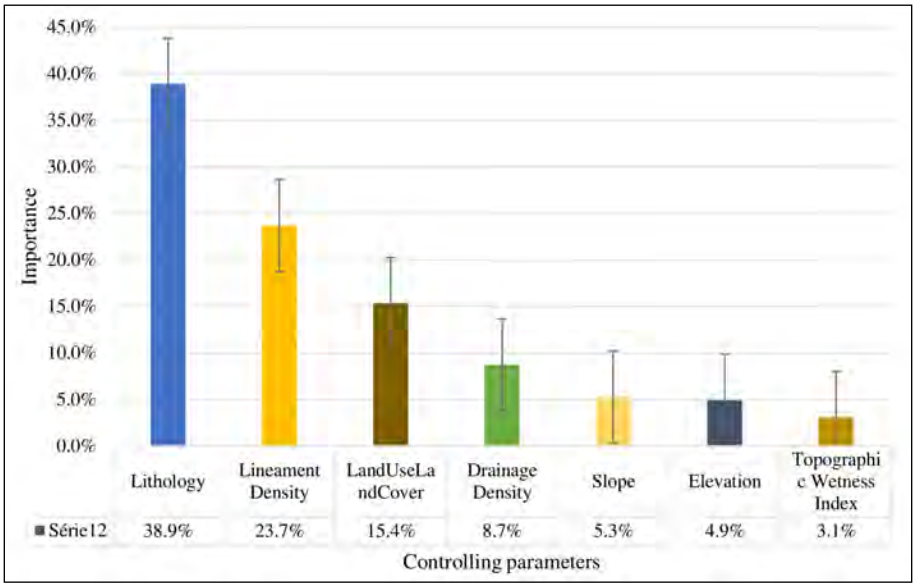

Figure 13- Weights assigned in AHP method (Lit: lithology, LD: lineament density, LULC: land use/land cover, DD: drainage density, S: slope, E: elevation and TWI: topographic wetness index).

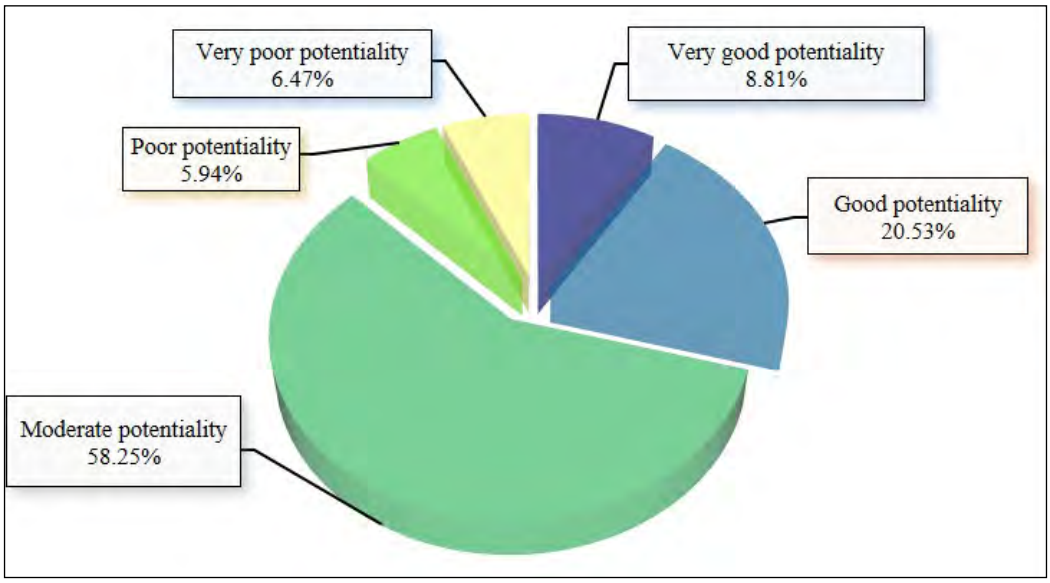

Figure 14- Percentage of different spatial potentiality zones of the study area.

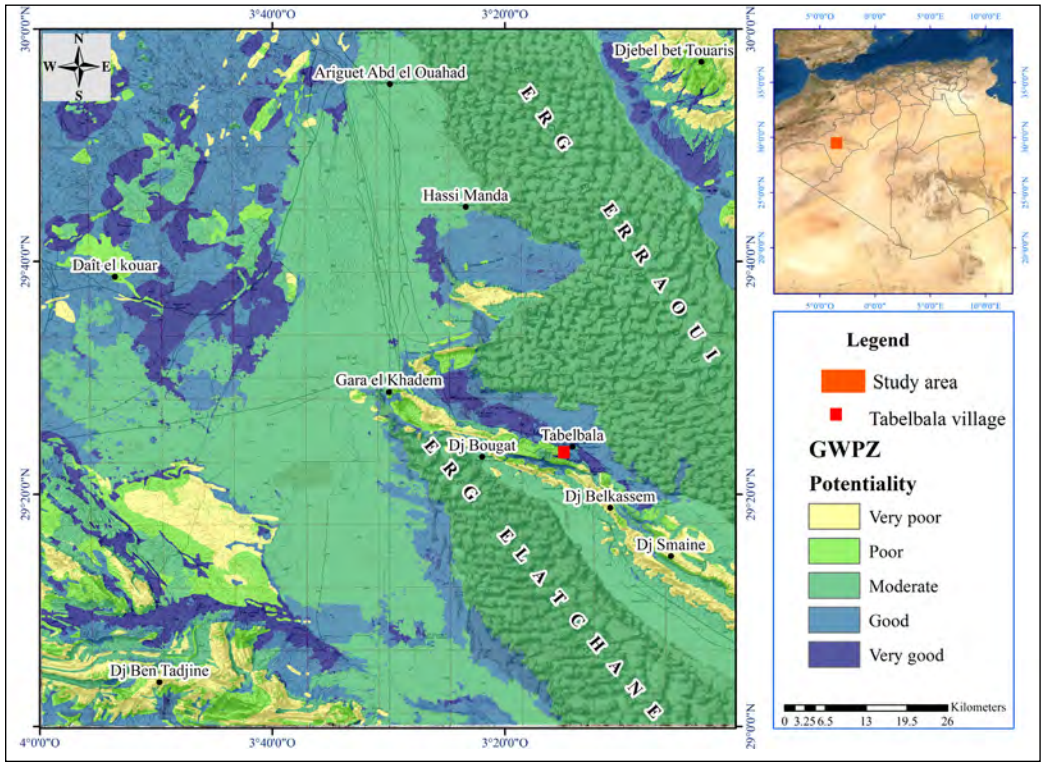

Figure 15- The groundwater potential zones map of the Tabelbala region.

as a drinking-water reservoir. The most famous are Hassi El Hariga, Hasi Aouissia and Hassi El Kheîl (Mekkaoui, 2015).

4.2. Groundwater Validation

The evolution of GIS and RS allowed for substantial advancement, however, filed verification and validation is still required due to the huge margins of error associated with automated algorithms applied to satellite imagery. In this section, we will evaluate the obtained results achieved in this arid zone against a field collected data to provide a global approach accuracy. In order to offer a reliable evaluation, field measurements from well-distributed drilling flows are employed over the whole study region. It is also important to illustrate the accuracy of the different prepared maps. The receiver operating characteristic (ROC) curve analysis and area under curve (AUC) are used to assess the locations of the different wells (222 wells and boreholes got from the National Agency for water resources) with the prepared potential zones map.

The spatial distribution of the wells reveals that 24.32% (54 wells) and 71.62% (159 wells) are in locations with very high and high groundwater potentialities, respectively, while 1.80% (4 wells) and 2.25% (5 wells) are in regions with moderate and low potentialities. The area under curve AUC is 0.89 which indicates good performance (Figure 16). This precision demonstrates that the AHP method is efficient in the study area and it can be used for groundwater delineation in isolated areas**.**

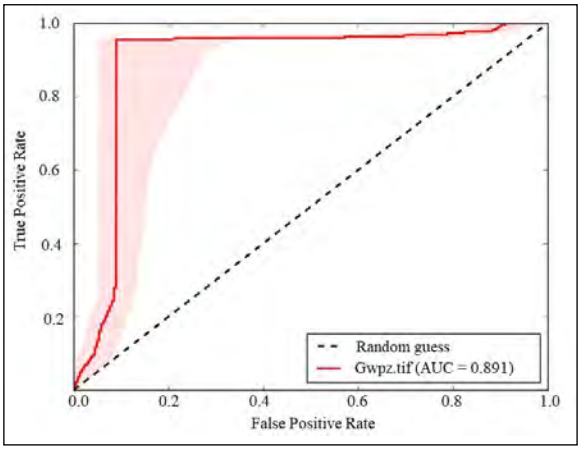

Figure 16- The ROC curve diagram corresponding to the study area.

The research yielded valuable new hydrogeological data that can be used in groundwater fluctuation studies to better understand the behaviour of aquifers in the area. It can also give adequate facilities for better natural resource management, usage, and secure supply, as well as sustainable development.

4.3. Material

During this work, different GIS and image processing software is used. ENVI and ERDAS Imagine are used to process satellite data through color composite, bands ratios, principal component analysis, and filtering. This processing is the key for updating lithological units, extracting lineaments and the preparation of the land use/land cover map. ArcGIS software is used to prepare the drainage density, slope, elevation and TWI maps. Stereonet software is used for the elaboration of the rose diagram which is related to the lineament orientation.

5. Results

Groundwater mapping has become extremely important in the Algerian desert region due to the country's rapid population development, which has increased the requirement for water supplies for the area's population and agricultural operations. The identification and spatial classification of promising areas from a hydrogeological point of view, requires a detailed examination of data from preliminary studies (geomorphological, geological, structural… etc.). In this study, a GIS database was gathered and prepared for the Tabelbala region using seven predictive factors then the AHP approach was applied. The analysis of potentiality was initiated with the combination and integration of controlling factors. The combination that brings together the predictive factors lithology, land use/land cover, lineament density, slope, drainage density, elevation, and topographic wetness index turns out to be the best possible combination for our area. It makes it possible to predict about 80% of water points. This study shows that the approach adopted using GIS can provide promising results in the analysis of field-oriented data. Lithology, land use/land cover, lineament density, slope, drainage density, elevation, and topographic wetness index are prepared to characterize the region. The results show that the groundwater potential map can be divided into five categories: very good potentiality (943.34 km^2), good potentiality (2197.36 km^2), moderate potentiality

(6236.47 km^2), poor potentiality (635.70 km^2), and very bad potentiality (692.88 km^2). More than 29.34% of the study area has extremely good groundwater potential according to the findings. It can be noted that the zone covered by Oued under sedimentary deposits (sandstone, sandstone-clay, and sandstone-carbonate) has a moderate slope, high lineament density, and low drainage density, is defined as a very high groundwater potential zone with a 943.34 km^2 area. We also observe that the area made up of volcano-sedimentary formations of the Paleozoic and Cenozoic deposits of various genesis which has a very low lineament density, high drainage density, very high slope, and is covered by runoff zones, is characterized by a very poor groundwater potential zone (692.88 km^2). The accuracy of the obtained map is validated using the ROC curve analysis and the AUC by taking into account the location of the field collected wells (222 boreholes and wells). Results show that AUC is 0.89 which demonstrates that the proposed method can be used as a high-precision investigation tool for groundwater resources particularly in data-scarce areas. It can also be confirmed that in the absence of field data, remote sensing and GIS techniques are one of the most effective tools for determining groundwater potential zones. This work will provide a digital and an update digital information (digital database) of the different influencing factors which will be used and increase the general knowledge and digital database of the Tabelbala region. Thus, applying this method might be beneficial for saving money and time.

This multi-criteria approach has nevertheless certain limits, particularly in relation to the working scale, due to the coarse resolution of the available data; DEM (30 m), Landsat (30 m), and Sentinel 2 (10 m), indeed the drilling operation management must be supported by ground reconnaissance or other parallel support (electrical sounding). As future work, it is therefore planned to improve the scale of processing, in particular via optical satellite imagery (Alsat2 at 2.5m in pansharpened mode), and also with a digital terrain model of better resolution (based on topographic campaign), while prospecting other emerging approaches including machine learning and microwave remote sensing SAR.

References

Adeyeye, O. A., Ikpokonte, E. A., Arabi, S. A. 2019. GIS-based groundwater potential mapping within Dengi area, North Central Nigeria. The Egyptian Journal of Remote Sensing and Space Science 22, 175–181.

Berhanu, K. G., Hatiye, S. D. 2020. Identification of groundwater potential zones using proxy data: Case study of Megech watershed, Ethiopia. Journal of Hydrology: Regional Studies 28, 100676.

Bevan, A., Lake, M. 2016. Intensities, interactions, and uncertainties: some new approaches to archaeological distributions. International Computational Approaches to Archaeological Spaces 27–52.

Boobalan, C., Gurugnanam, B. 2016. Mapping of groundwater potential zones in Sarabanga Sub-basin, Cauvery River, South India using remote sensing and GIS techniques. Indian Journal of Applied Research 6, 364–369.

Dar, I. A., Sankar, K., Dar, M. A. 2011. Deciphering groundwater potential zones in hard rock terrain using geospatial technology. Environmental Monitoring and Assessment 173, 597–610.

Das, B., Pal, S. C. 2019. Combination of GIS and fuzzy-AHP for delineating groundwater recharge potential zones in the critical Goghat-II block of West Bengal, India. HydroResearch 2, 21–30.

DAV (Data Access Viewer-Nasa Power). https://power.larc.nasa.gov/data-access-viewer/. September 20, 2021.

Dinesh Kumar, P., Gopinath, G., Seralathan, P. 2007. Application of remote sensing and GIS for the demarcation of groundwater potential zones of a river basin in Kerala, southwest coast of India. International Journal of Remote Sensing 28, 5583–5601.

El Abidine, R. Z., Abdelmansour, N. 2019. Landslide susceptibility mapping using information value and frequency ratio for the Arzew sector (North-Western of Algeria). Bulletin of the Mineral Research and Exploration 160, 197–211.

Ennih, N., Liégeois, J.-P. 2001. The Moroccan Anti-Atlas: the West African craton passive margin with limited Pan-African activity. Implications for the northern limit of the craton. Precambrian Research 112, 289–302.

Fenta, A. A., Kifle, A., Gebreyohannes, T., Hailu, G. 2015. Spatial analysis of groundwater potential using remote sensing and GIS-based multi-criteria evaluation in Raya Valley, northern Ethiopia. Hydrogeology Journal 23, 195–206.

Gupta, R. P. 2017. Remote sensing geology, Springer.

Hatefi, A. A. H., Ekhtesasi, M. R. 2016. Groundwater potentiality through analytic hierarchy process (AHP) using remote sensing and geographic information system (GIS). Geopersia 6(1).

Hobbs, W. H. 1904. Lineaments of the Atlantic border region. Bulletin of the Geological Society of America 15, 483–506.

Islam, A. T., Shen, S., Bodrud-Doza, M., Rahman, M. A., Das, S. 2017. Assessment of trace elements of groundwater and their spatial distribution in Rangpur district, Bangladesh. Arabian Journal of Geosciences 10, 95.

Jasrotia, A., Kumar, A., Singh, R. 2016. Integrated remote sensing and GIS approach for delineation of groundwater potential zones using aquifer parameters in Devak and Rui watershed of Jammu and Kashmir, India. Arabian Journal of Geosciences 9, 304.

Jha, M. K., Chowdary, V., Chowdhury, A. 2010. Groundwater assessment in Salboni Block, West Bengal (India) using remote sensing, geographical information system and multi-criteria decision analysis techniques. Hydrogeology Journal 18, 1713–1728.

Kaur, L., Rishi, M. S., Singh, G., Thakur, S. N. 2020. Groundwater potential assessment of an alluvial aquifer in Yamuna sub-basin (Panipat region) using remote sensing and GIS techniques in conjunction with analytical hierarchy process (AHP) and catastrophe theory (CT). Ecological Indicators 110, 105850.

Kemper, K. E. 2004. Groundwater from development to management. Hydrogeology Journal 12, 3-5.

Kerzabi, R., Mansour, H., Yousfi, S., Marín, A. I., Navarro, B. A., Bensefia, K. E. 2021. Contribution of Remote Sensing and GIS to mapping groundwater vulnerability in arid zone: case from Amour Mountains-Algerian Saharan Atlas. Journal of African Earth Sciences 104277.

Kousalya, P., Reddy, G. M., Supraja, S., Prasad, V. S. 2012. Analytical hierarchy process approach–an application of engineering education. Mathematica Aeterna 2, 861–878.

Kumar, A., Taxak, A., Mishra, S., Pandey, R. 2021. Long term trend analysis and suitability of water quality of River Ganga at Himalayan hills of Uttarakhand, India. Environmental Technology and Innovation 22, 101405.

Kurek, S., Preidl, M. 1987. Le Precambrien des chaines d'Ougarta (Sahara Algerien), sa place dans la structure de l'Afrique du Nord-Ouest. In Colloquium on African Geology 14, 61–64.

Magesh, J. P., Nochyil S. et Chandrasekar, Nainarpandian et Soundranayagam. 2012. Délimitation des zones potentielles d'eaux souterraines dans le district de Theni, Tamil Nadu, à l'aide de techniques de télédétection, SIG et MIF. Frontières Géoscientifiques 3, 189–196.

Mandal, U., Sahoo, S., Munusamy, S. B., Dhar, A., Panda, S. N., Kar, A., Mishra, P. K. 2016. Delineation of groundwater potential zones of coastal groundwater basin using multi-criteria decision making technique. Water Resources Management 30, 4293–4310.

Mekkaoui, A. 2015. Le magmatisme basique de l'axe Damrane-Kahal Tabelbala (Daoura, Monts de l'Ougarta, Sud-Ouest, Algérie): Géologie, Pétrologie, Géochimie et Contexte Géodynamique. PhD Thesis. Université d'Oran 2 Mohamed Ben Ahmed.

Mekkaoui, A., Remaci-Bénaouda, N., Graïne-Tazerout, K. 2017. Mafic dikes at Kahel Tabelbala (Daoura, Ougarta Range, south-western Algeria): New insights into the petrology, geochemistry and mantle source characteristics. Comptes Rendus Geoscience 349, 202–211.

Menchikoff, N. 1930. Recherches géologiques et morphologiques dans le Nord du Sahara occidental. PhD Thesis. University of Paris.

Mpofu, M., Madi, K., Gwavava, O. 2020. Remote sensing, geological, and geophysical investigation in the area of Ndlambe Municipality, Eastern Cape Province, South Africa: Implications for groundwater potential. Groundwater for Sustainable Development.

Nag, S., Kundu, A. 2018. Application of remote sensing, GIS and MCA techniques for delineating groundwater prospect zones in Kashipur block, Purulia district, West Bengal. Applied Water Science 8, 1–13.

Nasir, M. J., Khan, S., Zahid, H., Khan, A. 2018. Delineation of groundwater potential zones using GIS and multi influence factor (MIF) techniques: a study of district Swat, Khyber Pakhtunkhwa, Pakistan. Environmental Earth Sciences 77, 1–11.

Nemmour-Zekiri, D., Oulebsir, F. 2020. Application of remote sensing techniques in lithologic mapping of Djanet Region, Eastern Hoggar Shield, Algeria. Arabian Journal of Geosciences 13, 1–10.

Nithya, C. N., Srinivas, Y., Magesh, N., Kaliraj, S. 2019. Assessment of groundwater potential zones in Chittar basin, Southern India using GIS based AHP technique. Remote Sensing Applications: Society and Environment 15, 100248.

USGS EarthExplorer. (United States Geological Survey). https://earthexplorer.usgs.gov/. October 13, 2021.

Prost, G. L. 1994. Remote sensing for geologists: a guide to image interpretation. CRC Press.

Prost, G. L. 2013. Remote sensing for geoscientists. CRC Press, New York.

Punniyamoorty, M., Mathiyalagan, P., Lakshmi, G. 2012. A combined application of structural equation modeling (SEM) and analytic hierarchy process (AHP) in supplier selection. Benchmarking: An International Journal 19(1), 70-92.

Rabah, Nimour, Briedj, Tamani, Aouabed. 2016. Carte minute géologique de Tabelbala (Algérie: ASGA).

Rashid, M., Lone, M. A., Ahmed, S. 2012. Integrating geospatial and ground geophysical information as guidelines for groundwater potential zones in hard rock terrains of south India. Environmental Monitoring and Assessment 184, 4829–4839.

Rencz, A. N., Ryerson, R. A. 1999. Manual of remote sensing, remote sensing for the earth sciences. John Wiley and Sons.

Saadi, O., Nouayti, N., Nouayti, A., Dimane, F., Elhairechi, K. 2021. Application of remote sensing data and geographic information system for identifying potential areas of groundwater storage in middle Moulouya Basin of Morocco. Groundwater for Sustainable Development 14, 100639.

Saaty, T. L. 1980. The analytic hierarchy process: planning. Priority setting. Resource Allocation, MacGraw-Hill, New York. International Book Company, 287.

Saaty, T. L. 1990. Decision making for leaders: the analytic hierarchy process for decisions in a complex world. RWS publications.

Saaty, T. L. 2003. Decision-making with the AHP: Why is the principal eigenvector necessary. European Journal of Operational Research 145, 85–91.

Scanvic, J.-Y. 1997. Aerospatial remote sensing in geology. CRC Press.

Selvam, S., Magesh, N., Chidambaram, S., Rajamanickam, M., Sashikkumar, M. 2015. A GIS based identification of groundwater recharge potential zones using RS and IF technique: a case study in Ottapidaram taluk, Tuticorin district, Tamil Nadu. Environmental Earth Sciences 73, 3785–3799.

Shekhar, S., Pandey, A. C. 2015. Delineation of groundwater potential zone in hard rock terrain of India using remote sensing, geographical information system (GIS) and analytic hierarchy process (AHP) techniques. Geocarto International 30, 402–421.

Tanvir Rahman, M.A., Rahman, S. H., Majumder, R. K. 2012. Groundwater quality for irrigation of deep aquifer in southwestern zone of Banglades. Songklanakarin Journal of Science and Technology 34.

Tarboton, D. G., Bras, R. L., Rodriguez-Iturbe, I. 1992. A physical basis for drainage density. Geomorphology 5, 59–76.

Thapa, R., Gupta, S., Guin, S., Kaur, H. 2017. Assessment of groundwater potential zones using multi-influencing factor (MIF) and GIS: a case study from Birbhum district, West Bengal. Applied Water Science 7, 4117–4131.

Vadrevu, K. P., Eaturu, A., Badarinath, K. 2006. Spatial distribution of forest fires and controlling factors in Andhra Pradesh, India using spot satellite datasets. Environmental Monitoring and Assessment 123, 75–96.

Yeh, H., Cheng, Y., Hung-I, L., Lee, C. 2016. Mapping groundwater recharge potential zone using a GIS approach in Hualian River, Taiwan. Sustainable Environment Research. Elsevier Ltd. 26, 33–43.

Bulletin of the Mineral Research and Exploration

http://bulletin.mta.gov.tr

Caves in clastic rocks (Muğla, SW Türkiye)

Mutlu ZEYBEK[a], Murat GÜL[a, b*], Fikret KAÇAROĞLU[a], Ergun KARACAN[a] and Ahmet ÖZBEK[c]

[a]*Muğla Sıtkı Koçman University, Department of Geological Engineering, 48100, Kötekli-Menteşe, Muğla, Türkiye*
[b]*Muğla Sıtkı Koçman University, Department of Civil Engineering, 48100, Kötekli-Menteşe, Muğla, Türkiye*
[c]*Kahramanmaraş Sütçü İmam University, Department of Geological Engineering, Kahramanmaraş, Türkiye*

Research Article

Keywords:
Cave, Conglomerate, Mudstone, Late Miocene-Pliocene.

ABSTRACT

Caves evolution is controlled by lithological properties, discontinuities, water, climate, and physico-mechanical properties of soluble rocks, vegetation and human impact. This study investigates the cave formation in Upper Miocene-Pliocene clastic rock in Menteşe town of Muğla. The lithology, physico-mechanical properties and hydrogeologic factors of host rocks and morphology of the caves in Asar Hill and Damlam Stream valley were examined. The caves are 1.47-9.71 m long, 2.24-19.36 m wide and 1.38-27 m high. Four joint sets and bedding planes affect the clastics in the Asar Hill area. Mudstones (low plasticity clay, sandy clay) are in soft-very soft rock, while conglomerate is in moderate-hard rock class. The mudstone removal has started the formation of the caves. The vegetation roots act as groundwater circulation paths in the Damlam Stream area. Water has eroded mudstone and muddy matrix of conglomerate following cracks and led to the formation of the caves. Water infiltration may have led to stalactite, flowstone and travertine formation in Damlam Stream caves. Possible cave collapse could threaten life and property in the Asar Hill area, and may cause the destruction of internal structures of the caves in the Damlam Stream. Thus, precautionary measures such as continuous monitoring and protection must be taken in both cave areas.

Received Date: 15.04.2022
Accepted Date: 03.08.2022

1. Introduction

Karst features especially develop on soluble rocks such as limestone, marble, and gypsum (Ekmekçi, 2005; Ford and Williams, 2007). In addition to soluble rocks, soluble grains-clast or matrix bearing clastic rocks (conglomerate, sandstone, mudstone) may also show karstification (Busche and Sponholz, 1992; Bergada et al., 1997; Ferrarese and Sauro, 2005; Kranjc, 2005; Aubrecht et al., 2008; Breitenbach et al., 2010; Lipar and Ferk, 2011; Grimes, 2012). Caves in sandstone and conglomerate are scattered widely in many small areas across the world, but they are insufficiently studied (Dunkley et al., 2017).

Karstification in all rocks are controlled by strength, energy gradient, gravity, heat flow, micro bacteriology, discontinuities, climatic and environmental conditions, weathering, topography, grain size, and grain types, etc. (Palmer, 1991; Bergada et al., 1997; Kranjc, 2005; Breitenbach et al., 2010; Awadh et al., 2013). Active karst regions are usually associated with humid climate regimes. In karst regions precipitation and organic material in soils produce carbonic acid which dissolves karstified rocks at and below the surface over time. A wide range of international literature is available on the karst and cave studies in carbonate and evaporitic rocks (Palmer, 1991; Ford and Williams, 2007). However, the karstification in clastic rock is little studied in comparison to soluble carbonate and evaporitic rocks.

Citation Info: Zeybek, M., Gül, M., Kaçaroğlu, F., Karacan, E., Özbek, A. 2023. Caves in clastic rocks (Muğla, SW Turkey). Bulletin of the Mineral Research and Exploration 172, 61-79. https://doi.org/10.19111/bulletinofmre.1154017

**Corresponding author: Murat GÜL, muratgul@mu.edu.tr*

Caves in various conglomerates which have diverse underground morphology (vertical, horizontal, circular, tectonic discontinuity controlled) have been reported and described worldwide (Değirmenci et al., 1994; Bergada et al., 1997; Lapaire et al., 2006; Lipar and Ferk, 2011; Ferk and Lipar, 2012). Caves represent ground where rock strength and bearing capacity is significantly reduced. The critical dimensions are the width of the cave and the thickness of the rock cover (Waltham, 2002).

The caves in the Pleistocene conglomerate in Slovenia were studied in detail by Ferk and Lipar (2012). Based on the literature review and field work, the caves were grouped into four different types: 1) linear stream caves, 2) shelter caves, 3) breakdown caves, and 4) vadose shafts.

Tauride Mountains in southern Türkiye composed of Palaeozoic to recent carbonate rocks is the most important karstic region of Türkiye (Güldalı et al., 1984; Nazik, 1996; Özel et al., 1996; Tuncer et al., 2005; Günay et al., 2015). Muğla is located in western Taurides in SW Türkiye (Figure 1). The city centre and surrounding area contains Jurassic-Cretaceous carbonate rocks and post Neogene clastics (Göktaş, 1998). Upper Miocene-Pliocene clastics bearing Yatağan Formation forms a flat topped, step like exposure on carbonates (Göktaş, 1998; Gül, 2015; Gül et al., 2016). Some caves were reported in conglomerate and mudstone alternation of Yatağan Formation (Gül et al., 2016). One of the most significant cave areas is located north of the Muğla city centre (Asar Hill Caves - AHC) and there are some settlements on top of it (Figure 1). The other significant cave area is located 20 km southwest of the city centre (Damlam Stream Caves - DSC) and is used for recreational purposes (Figure 1).

Detailed studies on karstification on clastic rocks like Yatağan Formation are limited. Moreover, internal

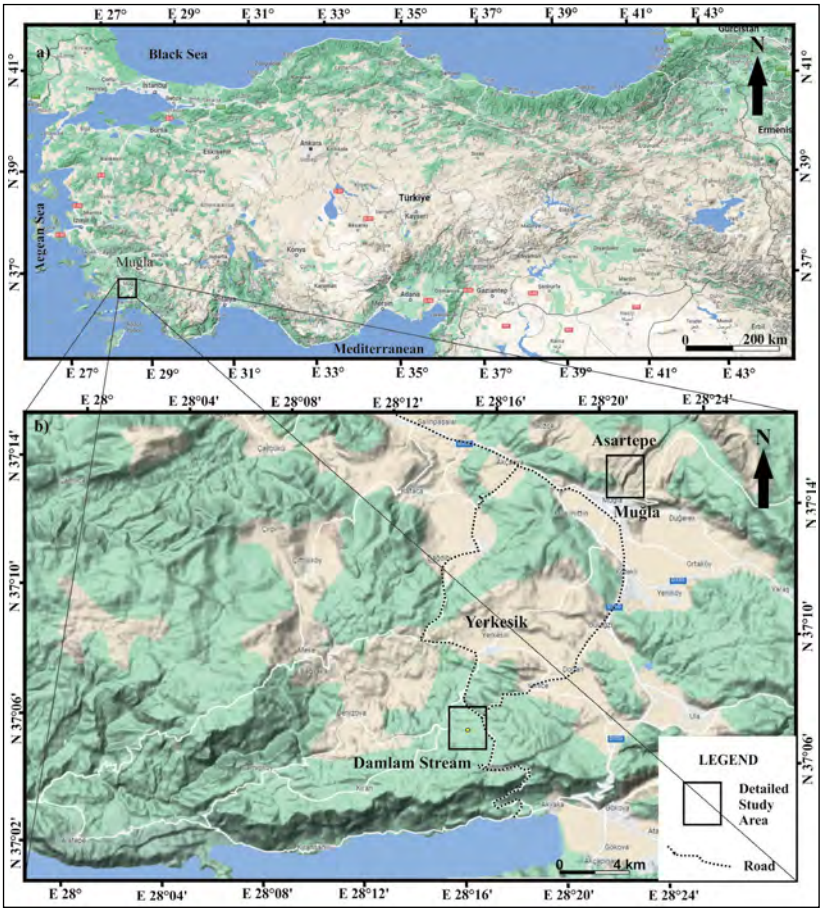

Figure 1- a) General location map of the study area, b) location map of the detailed study area (modified from Google 2022). Asartepe: Asar Hill Caves (AHC), Damlam Stream Caves (DSC).

structure differences in two significant cave areas of Yatağan Formation point to the importance of local factors. Thus, this study aims to describe the caves in Yatağan Formation, determine controlling factors of cave formation (karstification) in clastic rocks, and clarify related environmental issues. In this study physico-mechanical properties of the clastic rocks of the Yatağan formation in which caves are developed are also explained. Additionally, the formation and features of the caves are tried to be interpreted in relation with the rock properties.

2. Material and Methods

The Asar Hill and Damlam Stream, which are two significant areas with regard to cave occurrences were chosen for detailed studies (Figure 1). Each region contains numerous large and small caves. Height and width of cave mouth and length (depth through host rock interior) of cave were measured for each cave. Organic activities in caves, soil formation at the bottom of the caves and weathering were noted during the field analysis. Bed attitudes (strike-dip) and discontinuities were recorded during field studies. Two sedimentary sections were measured in both areas, and detailed lithological variations were noted. Moisture conditions of the ground, spring discharges were noted. Sieve analysis were applied to some loose samples, they classified according to Unified Soil Classification System (USCS; American Society for Testing and Materials (ASTM, 2000), D2487). Hand samples were collected during the section measurement in order to determine physico-mechanic properties of the rock material. During the office and laboratory studies, drainage network of both areas were drawn. Thin sections were prepared from fresh (limestone) and altered rocks for analysis of the petrographical properties of the rocks. Schmidt Hammer was applied to the rock for in situ rock strength determination. Schmidt Hammer was applied to stiff conglomerate part. Some geotechnical properties (porosity, density, point load, slake durability index etc.) of host rock were measured in the laboratory according to International Society for Rock Mechanics (ISRM, 2007) standard. The grain texture of studied rock was prevented from collecting standard samples during the field study. Irregular shaped block samples (for example: 20 cm (width) * 30 cm (length) *20 cm (depth)) were taken as big as possible for laboratory tests. For the Slake Durability Index experiment, a total of ten aggregate samples, each weighing between 40 and 60 g, were selected.

3. Geological Setting

The oldest rocks of the study area form highland and outcrops are Menderes Massif (including Paleozoic-Upper Cretaceous limestone-marble, schist, phyllite) in the north, Lycian Nappes (including Paleozoic-Paleocene sediments, Upper Cretaceous ophiolite-ophiolitic melange), Kuyucak Formation (Lower Miocene-Upper Oligocene conglomerates, sandstone-mudstone alternations) and Akyaka Formation (Lower Miocene-Upper Oligocene conglomerate and fossiliferous limestone) in the south (Figure 2; Konak et al., 1987; Aktimur et al., 1996; Göktaş, 1998;

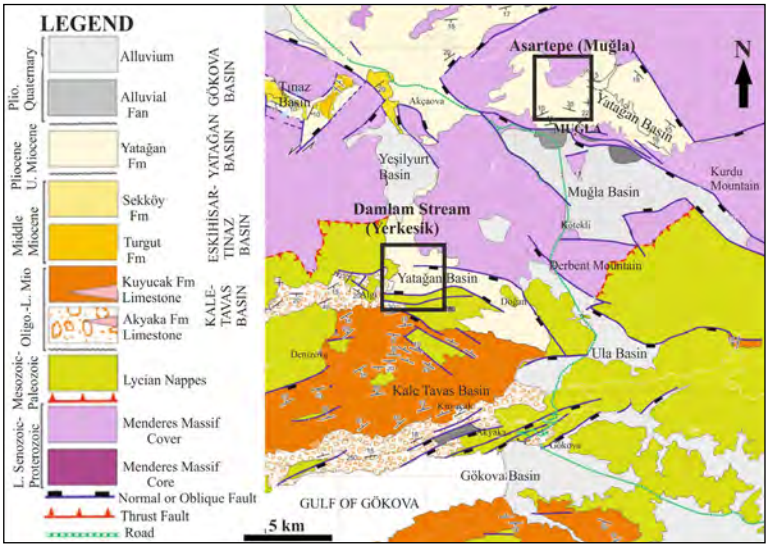

Figure 2- Geological map of the Muğla region in southwestern Anatolia (Gürer et al., 2013). Asartepe: Asar Hill Caves (AHC), Damlam Stream Caves (DSC).

MTA, 2002; Gürer et al., 2013). The Turgut Formation (Middle Miocene conglomerate, sandstoe, mudstone, marl, claystone with coal) and the Sekköy Formation (Middle Miocene limestone and marl) are exposed in Tınaz Basin (Figure 2; Gürer et al., 2013).

The Gereme Formation (Liassic carbonates), belonging to the Lycian Nappes, constitutes the higher mountains around Muğla (Figure 2) (Göktaş, 1998; MTA, 2002; Gül, 2015; Gül et al., 2021). The Yatağan Formation is reliable with the flat topography and (containing marl-limestone at the bottom, conglomerate-sandstone-mudstone at the top with caves) unconformably overlies the older formations (Konak et al., 1987; Göktaş, 1998; MTA, 2002; Gürer et al., 2013; Gül, 2015; Gül et al., 2021). This formation includes older limestone fragments (Gül et al., 2013; Gül, 2015; Gül et al., 2021), and calcite-quartz-kaolinite based on XRD test results (Gül et al., 2021). The Quaternary colluviums (breccia, mudstone) and alluviums (including conglomerates, sandstone, mudstone) filled the Muğla polje and unconformably overlie older formations (Gül, 2015; Küçükuysal et al., 2018).

The Yatağan Formation is bounded by active normal faults (Gürer et al., 2013). These faults had previously produced 4-5 magnitude earthquakes (Sezer, 2003). Tectonic history of the region locally has led to 4 different joint sets development (Gül et al., 2016).

Subtropical climate conditions are active in Muğla with average annual precipitation between 1928-2021 years was measured as 1209.1 mm (MGM, 2022). The lowest temperature is -12.6°C (04.01.1942), while the highest temperature is 42.1°C (27.07.2007), average monthly temperature varies between 5.3°C (January) and 26.4°C (July) based on 1928-2021 period measurements (MGM, 2022).

4. Caves of the Yatağan Formation

4.1. Asar Hill Caves (AHC)

4.1.1. Location, Morphology, Internal Structures

The Asar Hill is located just 500 m north of the Muğla city centre (Figure 3). The height of Asar Hill

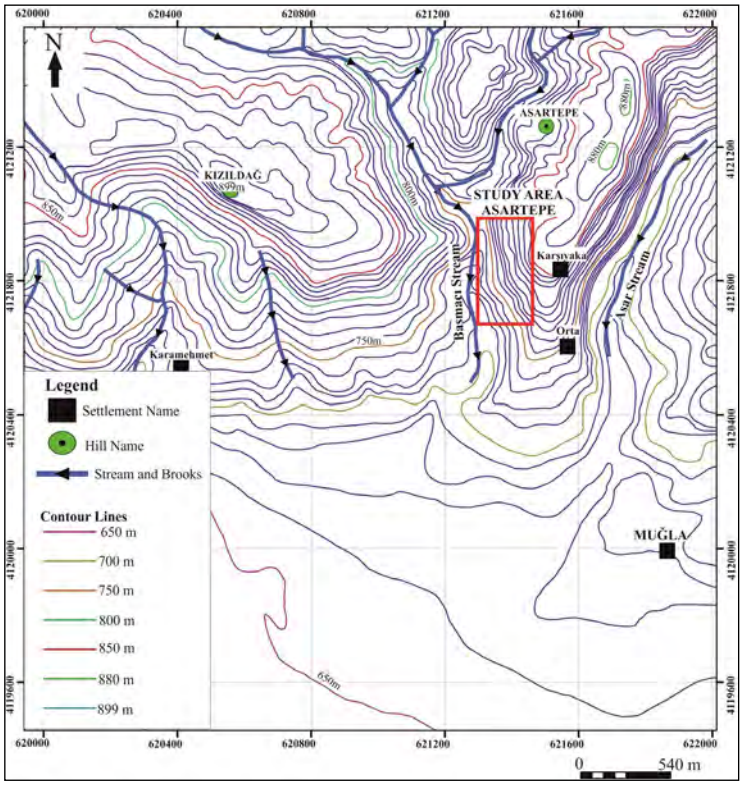

Figure 3- Topographical map and drainage network of the Asar Hill caves area was drawn from topographic raster map of Muğla province (The map is modified from a basemap of General Command of Mapping (HGK, 2016)).

is 830 m. It has 75-80° slope, and is surrounded by Basmacı or Asartepe streams. Eleven large and small caves were identified in southern skirt of the Asar Hill (Figures 4, 5; Table 1). However, number of caves is higher than this value. Some caves are inaccessible because they are either located in private property, used as barn or dense maquis. The caves in Asar Hill area differ in size, with length between 1.47 and 9.71 m, width between 2.24 and 14.89 m, and height between 1.38 and 15.88 m (Table 1). One or two storey houses

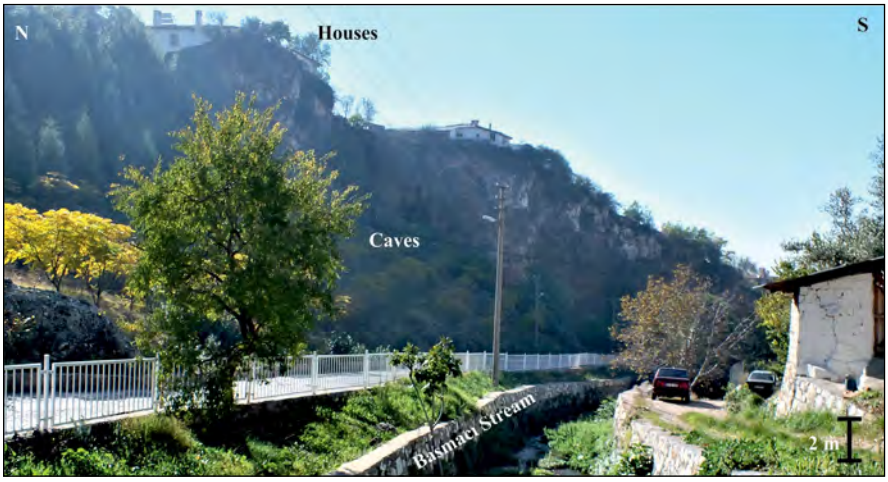

Figure 4- General field view of the Asar Hill caves (AHC) and Basmacı Stream (1-2 storey houses are on top of the caves, used for settlement and barn).

Figure 5- a) General field view of the caves on skirts of the Asar Hill, b) there are two-storey houses above the levels where the caves are located (man for scale in circle: 1.8 m), c) caves are observed in mudstone and muddy conglomerates of the Yatağan Formation (man for scale in circle: 1.8 m), d) some caves have been used as a barn for small animals.

Table 1- Dimensions of caves in Asar Hill caves area.

	Geometric Parameters		
Occurence Name	**Length (m)**	**Width (m)**	**Height (m)**
Cave 1	4.98	13.34	7.68
Cave 2	3.38	4.21	2.69
Cave 3	2.12	3.39	2.78
Cave 4	6.83	2.88	2.18
Cave 5	5.51	8.85	15.8
Cave 6	9.71	14.89	15.88
Cave 7	2.72	3.15	1.82
Cave 8	6.58	4.96	2.96
Cave 9	1.47	2.55	2.35
Cave 10	1.58	2.35	1.64
Cave 11	5.74	2.24	1.38
Statistical Evaluations			
Minimum	1.47	2.24	1.38
Maximum	9.71	14.89	15.88
Average	4.60	5.71	5.20
Standard Deviation	2.60	4.57	5.53

are located on top of the formation containing caves (Figure 4). There are no significant internal structures in AHC. Only local white coloured calcite bearing flowstone as a thin plastering were observed on host rocks. Some caves contain one or two step structures, which may have evolved due to weathering and/or human impact.

4.1.2. Local Geological Properties (Lithology, Structural Properties, Petrography)

Lithology of the Yatağan Formation on skirts of the Asar Hill is quite variable. Lower part and upper part of the section consist of poorly sorted, moderately-well indurated, cobbly, pebbly, and granule bearing muddy conglomerates, and coarse to very coarse grained sandstone alternations. The middle part of the section contains durable moderately-well sorted, pebble-granule size muddy conglomerates and coarse to very coarse grained sandstone and mudstone alternations (Figure 6). Clasts are generally Jurassic-Cretaceous Gereme Formation limestone fragments. Those

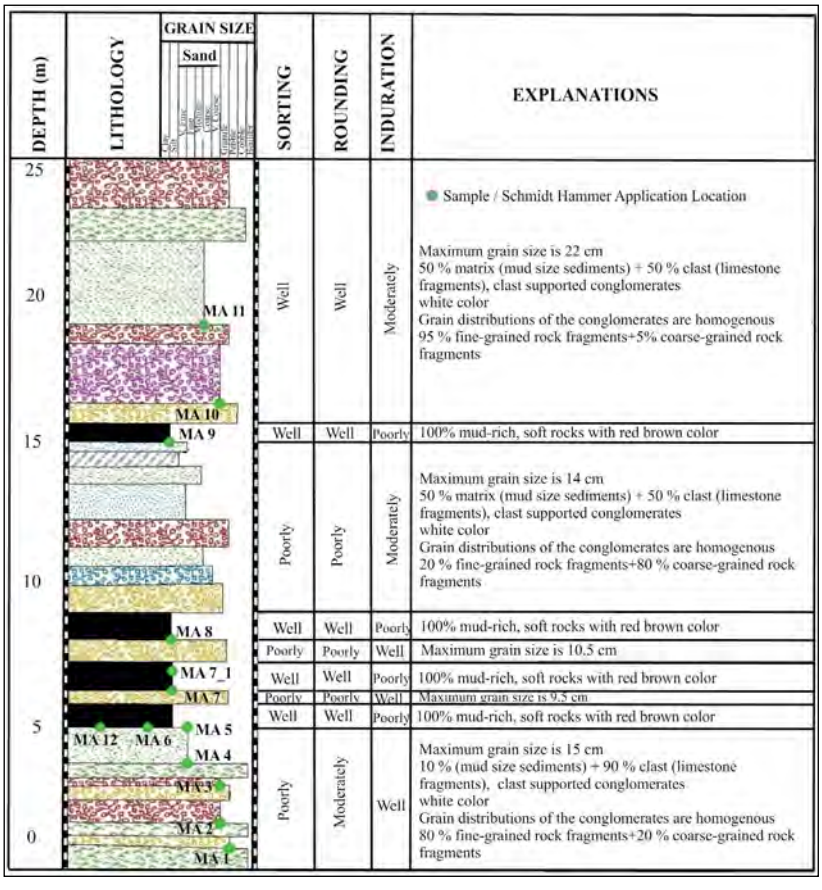

Figure 6- Detailed stratigraphic section of Asar Hill Caves (Zeybek, 2017).

fragments were binded with mud size sediments. Clast ratio (from 50 % to 90 %) and maximum clast size (from 9.5 cm to 22 cm) is highly variable along section (Figure 6). Four different joint sets in profile that comprised the caves (Gül et al., 2016) (Dip/dip direction, 60°/160°, 72°/197°, 72°/8°, 74°/331°, slope orientation 80°/257°, and bed orientation N60°E/25°-35°NW). The continuation of joints was determined as about 20 m (Gül et al., 2016). N15°-35°W/ 75°-80°SW directed joints were determined in the caves given in Figure 5c (Şahin, 2015). Their traces were also observed inside of some caves. Alignment of some joints are restricted by the caves. The joints generally have rough surfaces. Some joints are filled by clay minerals, after raining these joints show damp surfaces or water dripping occurs through them.

4.1.3. Hydrogeological Conditions

The Basmacı Stream flow west of the Asar Hill and collect water from a 5.5 km^2 drainage area. The stream is generally dry during the summer time. The caves are usually dry and hydrologically inactive. However, some small springs, and droplets were identified in some caves. The discharge of the perennial springs was 0.125 l/s (29.09.2016) and 0.143 l/s (20.01.2017). These springs reflect the current circulation of the groundwater in the karstified conglomerate which is characterized by a limited storage capacity. Şahin (2015) measured the discharge as 1.2 l/s in one fountain during the spring period. Damp areas and temporary springs were identified in caves mostly along cracks. Along those groundwater path, thin white coloured carbonate cover was formed.

4.1.4. Physico-Mechanical Properties

The dry densities of conglomerate samples from Asar Hill area fall between the 2.55 and 2.75 g/cm^3 and classified as moderate-high density class rock (Anon, 1979). Porosity values of the conglomerates are lower than 1 % and classified as very low porous rock (Anon, 1979). The strength of the examined materials (conglomerates) were classified as hard (1-3 MPa, point load strength) and mostly very hard rock (3-10 MPa, point load strength) (Broch and Franklin, 1972). The samples are in medium (60-85), medium-high (85-95) and high (95-98) durable rock classes based on Slake Durability Index after second cycle (Gamble, 1971, Sivakugan et al., 2013).

The Schmidt Hammer was applied to stiff part of the conglomerate. They have highly variable clast size from granule (2-4 mm) to cobble (64-256 mm), clast ratio, and supporting mechanism (matrix or clast supported). Moreover, application rock surface of the Schmidt Hammer is generally rough. For this reason, highly variable Schmidt Hammer rebound values were obtained even in very close areas during this study. The Schmidt Hammer rebound mumbers of the conglomerates are varying between 6.63 and 30.22. The calculated uniaxial compressive strength (UCS) values of the conglomerates from Schmidt Hammer rebound value based on the method proposed by Minaeian and Ahangari (2013) are varying from 4.5 to 20.5 MPa. Thus, one sample (MA2) was classified as very low strength (1-5 MPa) and others was classified as a low strength rock (5-25 MPa) based on ISRM (1978). Moreover, three samples (MA1, MA2, MA8) were classified as low strength (4-8 MPa), two samples (MA7, MA3) were classified as a high strength (16-32 MPa) rock, while others were classified as a medium strength (8-16 MPa) rock according to Deere and Miller (1966) classification system (Table 2). The highest strength values were obtained from the clast supported (clast ratio>80%) level. One sample from fine-grained level was classified as a SM (silty sand, 74 % sand, 26% mud) according to USCS.

Table 2- Physico-mechanical properties of conglomerate samples collected in Asar Hill area.

Sample Number	Occurrence Name	Schmidt Hammer Rebound Value	UCS = 0.678*SCH MPa	Porosity (%)	Dry Density (g/cm^3)	Point Load Strength Index (Is_{50}) (Is_{50}=Px1000/ De^2) (De=50mm) (MPa)	Slake Durability Index (2nd Cycle) Id(2)=[(C-D)/(A-C)]x100	Slake Durability
MA1	**Cave 1**	9.23	6.3	0.64	2.65	7.31	90.60	Medium-High Slake Durability
MA2	**Cave 2**	6.63	4.5	0.27	2.66	4.9	89.70	Medium-High Slake Durability
MA3	**Cave 3**	25.69	17.4	0.76	2.60	4.64	86.40	Medium- High Slake Durability
MA4	**Cave 4**	12.36	8.4	0.49	2.68	8.56	95.50	High Slake Durability
MA5	**Cave 5**	17.31	11.7	0.62	2.64	5.58	89.80	Medium-High Slake Durability
MA6	**Cave 6**	20.17	13.7	0.64	2.67	4.86	90.80	Medium-High Slake Durability
MA7	**Cave 7**	30.22	20.5	0.69	2.63	4.68	88.60	Medium-High Slake Durability
MA8	**Cave 8**	11.37	7.7	0.54	2.64	4.41	92.50	Medium-High Slake Durability
MA9	**Cave 9**	21.72	14.7	0.76	2.55	1.07	74.90	Medium Slake Durability
MA10	**Cave 10**	17.56	11.9	0.99	2.61	4	87.80	Medium-High Slake Durability
MA11	**Cave 11**	17.74	12.0	0.26	2.59	2.92	79.50	Medium Slake Durability
MA12	**Cave 12**	17.31	11.7	0.81	2.58	3.73	84.20	Medium Slake Durability
Statistical Evaluations								
Minimum		6.63	4.5	0.26	2.55	1.07	74.90	
Maximum		30.22	20.5	0.99	2.68	8.56	95.50	
Average		17.74	11.7	0.62	2.62	4.72	87.52	
Standard Deviation		6.96	4.8	0.21	0.03	1.91	5.68	

4.2. Damlam Stream Caves (DSC)

4.2.1. Location, Morphology, Internal Structures

The DSC is located 20 km southwest of the Muğla city centre (Figure 1). The N-S oriented walls of the caves, with slope angles ranging between 70-85°, are composed of muddy conglomerates (Figures 7, 8 and 9). The caves in Damlam Stream area differ in size, with length between 2.01-4.73 m, width between 4.16-19.36 m, and height between 2.83-27.00 m (Table 3). The capillary root vessels of the pine and other trees hang down from cave ceiling (Figure 9). The internal structures (speleothems) of DSC are composed of stalactite, flowstone and travertine formations (Figure 9). Stalactites, which grow down from the cave ceiling, are in 1-2 cm diameter, 10-12 cm long, and hanging down ceiling. Their growth generally

Table 3- Dimensions of caves in Damlam Stream valley.

	Geometric Parameters		
Occurence Name	**Length (m)**	**Width (m)**	**Height (m)**
Cave 1	2.10	6.80	3.90
Cave 2	3.73	14.70	15.16
Cave 3	4.73	19.36	27.00
Cave 4	2.01	4.16	2.83
Cave 5	3.46	6.66	4.50
Statistical Evaluations			
Minimum	2.01	4.16	2.83
Maximum	4.73	19.36	27.00
Average	3.20	10.33	10.67
Standard Deviation	1.15	6.41	10.39

follows capillary root vessels, and they are formed by percolation and dripping of dissolved carbonate mineral loaded water from cave ceiling. Most of the flowstone covers ceiling and sidewalls of caves as a gray colored, 5 mm thick layer. The water flowing on muddy conglomerate and mudstone leads to formation of flowstone. Flowstone has low resistance against erosion and can easily be crumbleb by hand. Some thick flowstone accumulations were observed in the caves. These accumulations may be interpreted as travertine formation (Figure 9).

4.2.2. Local Geological Properties (Lithology, Structural Properties. Petrography)

The DSC area contains cobbly, pebbly, and granule bearing conglomerates with mud matrix (Figure 10). The conglomerates contain generally well sorted, well rounded and moderately and well durable sediments. The clast of the conglomerates are older limestone fragments. Those fragments were bounded with mud size sediments. Compared to the Asar Hill section, the Damlam Stream section includes thicker mudstone

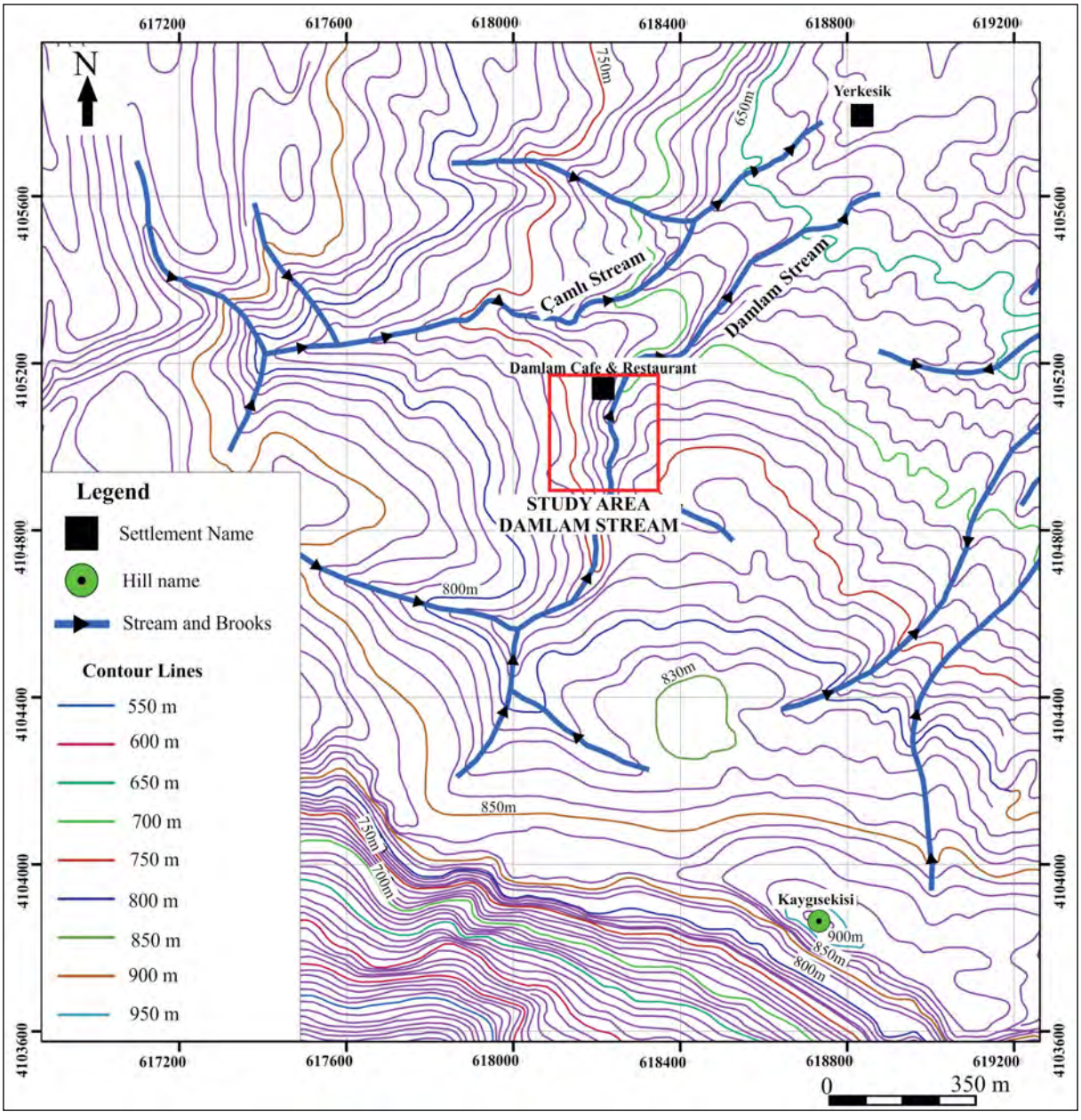

Figure 7- Topographical map and drainage network of the Damlam Stream caves was drawn from topographic raster map of Muğla province (The map is modified from a basemap of General Command of Mapping (HGK, 2016)).

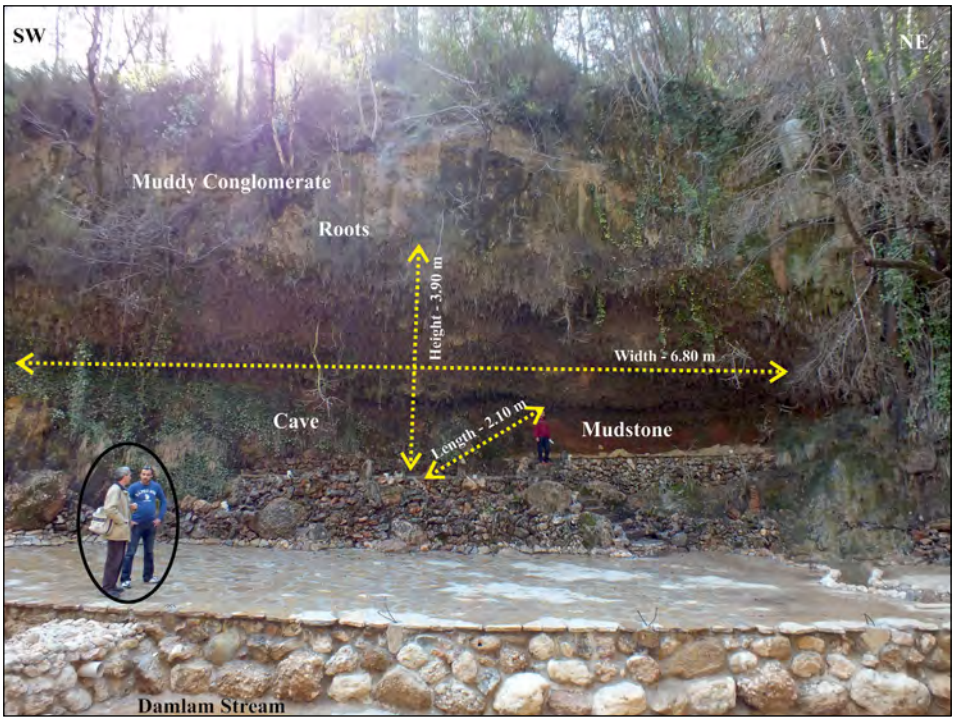

Figure 8- General field view of the cave in Damlam Stream valley. Partially interior part and in front of caves have arranged for recreation (man for scale: 1.80 m).

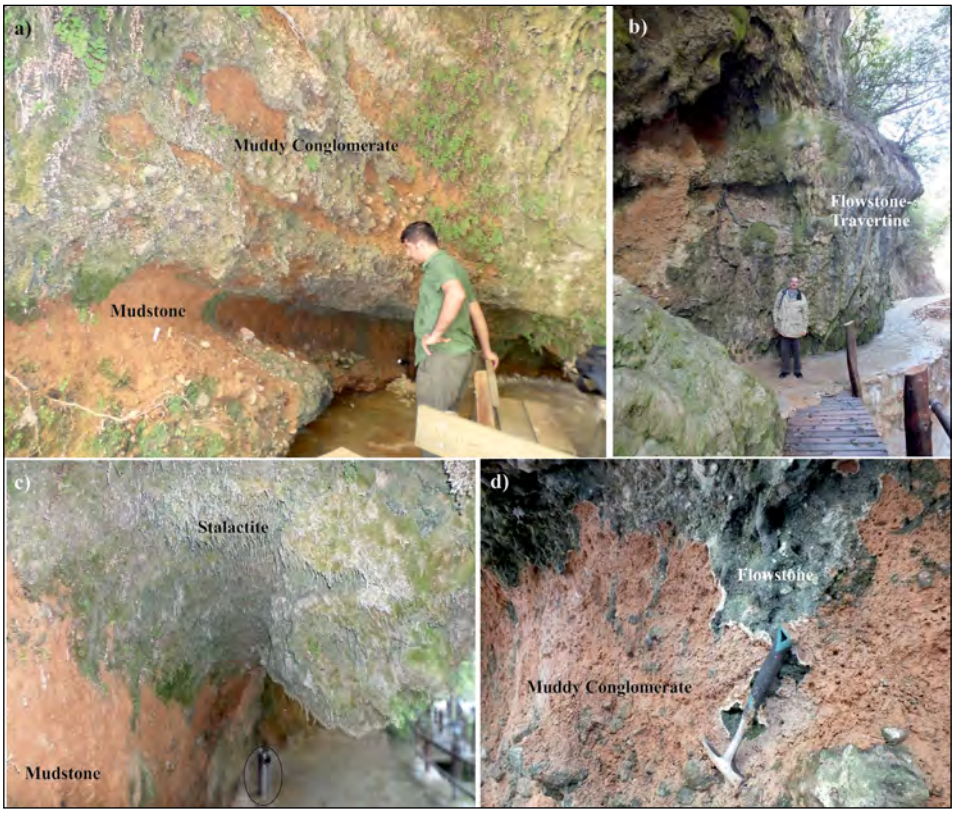

Figure 9- a) General field view of the Damlam Stream cave (man for scale in circle: 1.8 m), b) flowstone and travertine can observe on cave wall and valley side (man for scale in circle: 1.8 m), c) stalactite develop following the roots in the cave (dustbin for scale in circle: 60 cm), d) very thin flowstone cover can observe on muddy conglomerate in cave (hammer for scale: 33 cm).

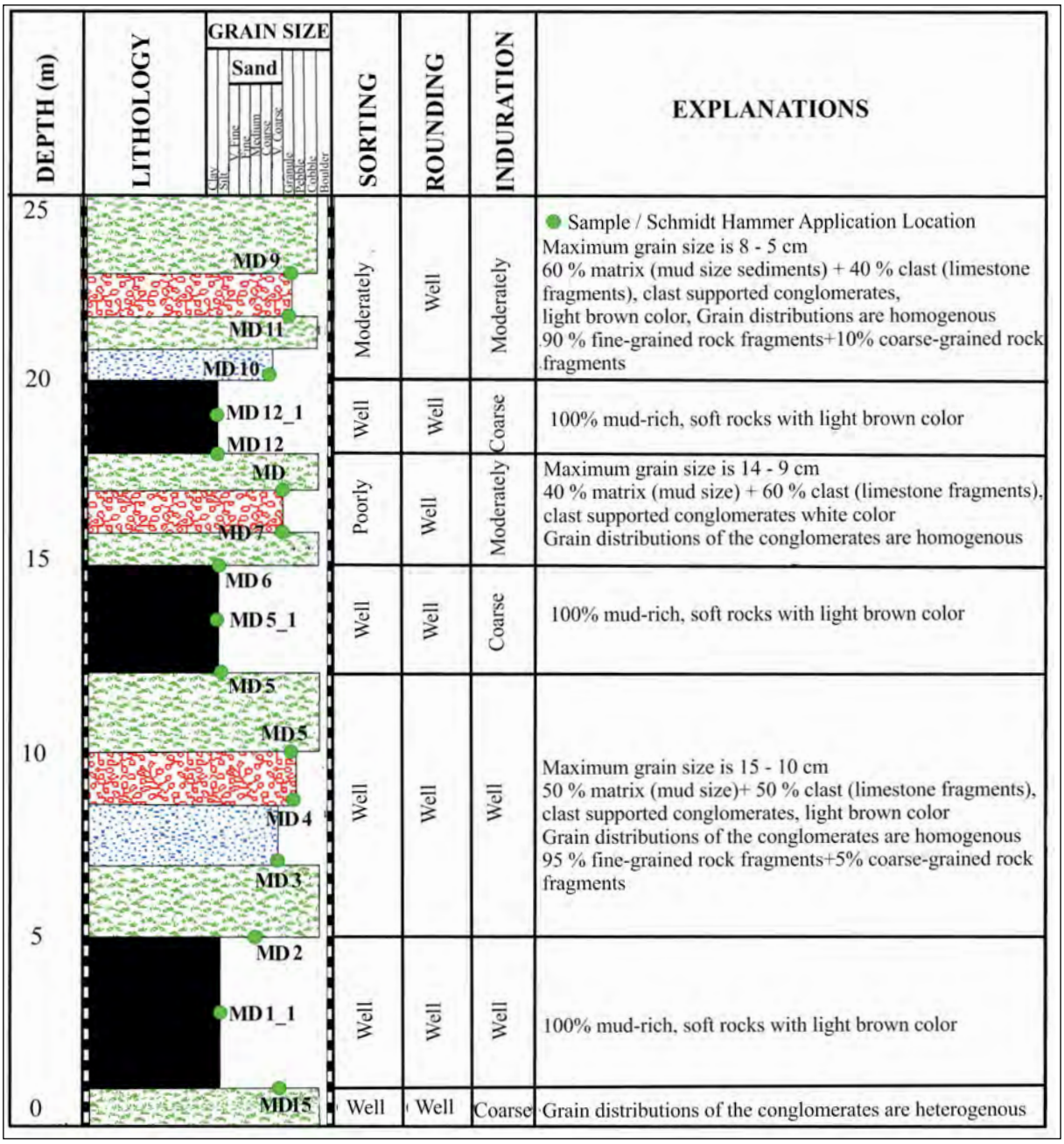

Figure 10- Detailed stratigraphic section of Damlam Stream caves area (DSC, Zeybek, 2017).

levels, and clast ratio of this region is less than the Asar Hill. Roundness and sorting of this region is better than the Asar Hill region. The maximum clast size of the Damlam Stream conglomerates is smaller than the Asar Hill conglomerates. There are no significant discontinuities determined in DSC area. The bedding plane of the conglomerate (N75°E / 18°SE) acts as weakness zone (Figure 8).

4.2.3. Hydrogeological Conditions

The DSC area has similar climatic and precipitation conditions with Asar Hill area. Damlam Stream valley is colder than Asar Hill area during the summer time due to the presence of dense vegetation and stream. Damlam Stream has a 4.8 km^2 dendritic drainage area (Figure 7), and a discharge rate of 0.5 l/s. There are permanent and temporary water leakage observed in the caves. Drippings have been observed at the edges

of stalactites. The surface of cave ceilings and walls are always damp which indicates that the rock of the cave (conglomerate) is saturated to water.

4.2.4. Physico-Mechanical Properties

The dry densities of the samples from Damlam Stream area drop into the 1.83-2.62 g/cm^3 range and are classified as low-moderate-high density rock class. The porosity values vary between 1.56 and 8.26 % and they are classified as a low – medium porous rock (Anon, 1979). The point load strength index of the examined materials ranges between 0.84 and 7.78 MPa and classified as a moderate (0.3-1 MPa) - hard (1-3 MPa, point load strength) and very hard rock (3-10 MPa, point load strength) (Broch and Franklin, 1972). The samples are medium (60-85), and medium high (85-95) durable rock based on Slake Durability Index after second cycle (Gamble, 1971; Sivakugan et al., 2013).

The difficulties encountered during the Schmidt Hammer application at Asar Hill were also experienced in this field. The Schmidt Hammer rebound numbers of the conglomerates vary between 8.53 and 24.48. The calculated uniaxial compressive strength values from Schmidt Hammer rebound value based on the method proposed by Minaeian and Ahangari (2013) are varying from 5.78 to 16.60 MPa, so they are classified as low strength (5-25 MPa) based on ISRM (1978). One sample (MD5) was classified as low strength (4-8 MPa), three samples (MD1, MD2, MD4) were classified as a medium strength (8-16 MPa) and one sample was classified (MD3) high strength (16-32 MPa) according to Deere and Miller (1966) classification system (Table 4). Those conglomerates are in medium strength characteristic. Four samples were collected from mudstone, and are classified as a CL (low to medium plasticity inorganic clays) and SC (sandy clay) based on USCS (Table 5). The mudstone, observed in the lower part of the cave in the measured section is very soft, and it is easily crumbled with finger. The Schmidt Hammer test was not applied to the mudstone due to its very soft character.

Table 4- Physico-mechanical properties of conglomerate samples collected in Damlam Stream area.

Sample Number	Occurrence Name	Schmidt Hammer Rebound Value	UCS = 0.678*SCH MPa	Porosity (%)	Dry Density (g/cm^3)	Point Load Strength Index (Is_{50}) (Is_{50}=Px1000/De^2) (De=50mm) (MPa)	Slake Durability Index (2nd Cycle) Id(2)=|(C-D)/(A-C)|x100	Slake Durability
MD1	**Cave 1**	21.49	14.57	1.56	2.62	7.54	86	Medium-High Slake Durability
MD2	**Cave 2**	18.49	12.54	7.25	2.31	1.56	77.10	Medium Slake Durability
MD3	**Cave 3**	24.48	16.60	8.26	2.38	2.54	72.40	Medium Slake Durability
MD4	**Cave 4**	15	10.17	3.95	1.83	0.84	90.40	Medium-High Slake Durability
MD5	**Cave 5**	8.53	5.78	3.79	2.57	7.78	86	Medium-High Slake Durability
Statistical Evaluations								
Minimum		8.53	5.78	1.56	1.83	0.84	72.40	
Maximum		24.48	16.60	8.26	2.62	7.78	90.40	
Average		18.23	11.93	4.96	2.34	4.05	81.47	
Standard Deviation		5.26	4.18	2.74	0.31	3.34	8.19	

Table 5- Laboratory results of soil samples collected in Damlam Stream area.

Sample Number	Occurrence Name	Moisture Content W_n (%)	Natural density ρ (g/cm^3)	Specific Gravity G_s	Atterberg Limits			Grain Size Distribution (Sieve Analysis)			Unified Soil Classification System (USCS)
					LL (%)	PL (%)	PI (%)	Gravel (%)	Sand (%)	Mud (Silt + Clay) (%)	
MD1_1	**Cave 1**	27.90	1.76	2.63	37.50	24.40	13.10	0	27.01	72.90	CL
MD5_1	**Cave 5**	26.60	1.80	2.67	40.10	24.70	15.40	0	21	79	CL
MD7	**Soil 7**	20.90	1.83	2.62	36.20	23.80	12.50	8.20	22.40	69.40	CL
MD10	**Soil 10**	16.40	1.86	2.60	32.30	22.40	9.90	5.70	50.40	43.90	SC
Statistical Evaluations											
Minimum		16.40	1.76	2.60	32.30	22.40	9.90	0	21	43.90	
Maximum		27.90	1.86	2.67	40.10	24.70	15.40	8.20	50.40	79	
Average		22.95	1.81	2.63	36.52	23.82	12.72	3.47	30.20	66.30	
Standard Deviation		5.32	0.04	0.02	3.25	1.02	2.26	4.14	13.70	15.45	

5. Discussion

Large and small caves have been determined in various outcrops of the Yatağan Formation. The formation mostly consists of mudstone and conglomerate alternations, which have variable thickness. It is mostly surrounded by Jurassic-Cretaceous limestone. Combined effects of structural properties, lithological variation, strength differences, groundwater and surface water, and vegetation have created favourable conditions and led to the formation of the caves. AHC and DSC areas are composed of very soft mudstone and relatively durable conglomerate packages. The Upper Miocene-Pliocene Yatağan Formation conglomerate is the example of oligomict-single type grain bearing (only Jurassic-Cretaceous limestone fragments) conglomerates. Mudstone layers of the Yatağan Formation, especially wet parts, which are very soft, can easily be crumbled with finger. The conglomerate levels of this formation are more durable, however the strength of the matrix including mud size sediments of the conglomerate are lower than that of the clasts.

When the water circulates in the formation, especially by following the cracks, weakening of mudstone and matrix of the conglomerate occures. While the muddy material is disintegrated, they are washed away and removed from the caves. These processes then cause release of the conglomerate clasts. Increase of precipitation amount and infiltrating water may accelerate this processes and lead to enlargement of the caves. Kayan (1979) reported that Early Pliocene represented by semi-arid climatic conditions and significant erosion, and during Late Pliocene wetter climatic conditions were present in the study area that led to north directed rivers, later period under the effect of the faults uplifted and fragmented, river erosion fastened. Jiménez-Moreno et al. (2015) point out that the climatic conditions of region in south of the study area was arid and warmer than today during late Pliocene and early Pleistocene time. Early-to mid Holocene time show oscillations between aridity and humidity, whereas second half of the Holocene point out the drier conditions, recent aridity conditions started approxiamately 1300 years ago based on isotopic record from Gölhisar in SE of the study area (Eastwood et al., 2007). In the geological time period ranging between Early Pliocene and recent, in general semi-arid to arid climatic conditions were valid in the study area according to the studies of Kayan (1979), Jiménez-Moreno et al. (2015) and Eastwood et al. (2007).

There are some similarities and differences in the properties of the Asar Hill and Damlam Stream caves. Comparison of features and controlling factors of cave development in Yatağan Formation given in Table 6.

The strength of the karstic cave rocks may be reduced substantially in a short period of time by dissolution and other weathering processes mainly acting along discontinuity planes (Parise and Lollino, 2011). The Asar Hill rocks have highly variable lithology and contain weakness zones including bed planes and fractures. Water following these fractures cause to weakening, weathering and removing of mudstone and muddy matrix of the conglomerate.

Table 6- Comparison of features and controlling factors of cave development in Yatağan Formation (modified from Zeybek, 2017).

Controlling Factors and Features of Cave Occurrences	Asar Hill Caves (AHC)	Damlam Stream Caves (DSC)
Size variation ranges of caves	Length: 1.47-9.71 m, Width: 2.24-14.89 m, Height:1.38-15.88 m	Length: 2.01-4.73 m, Width: 4.16-19.36 m, Height:2.83-27 m
Internal Structure(s)	Flowstone, step	Stalactite, flowstone, travertine
Usage purpose(s)	Barn, warehouse	Recreation
Hydrogeological Condition	Temporary-seasonal (ephemeral) river, spring at the base of cave, damp ground during wet season	Permanent (perennial) river, dripping from cave roof, moist ground inside cave, surface water flowing traces on sidewall of cave.
Vegetation effect	Rare, only bushes and their roots observed at outer edge of caves	Plenty of the roots of trees (Water follows capillary cracks caused by the roots of trees)
Lithological similarities and differences	Mudstone-muddy conglomerate alternations (Maximum grain size is 22 cm), cave formations were observed in different layers.	Mudstone-muddy conglomerate alternation (Maximum grain size is 15 cm), general cave formation observed along thick muddy layer.
Structural Properties	3-4 joint sets in different direction and bedding. Active normal fault is also cut the cave bearing formation.	A few fractures were observed in cave in addition to bedding. Active normal fault is bounded the Yatağan Formation.
Strength of rocks	Without cave parts are more durable than within cave parts. Mudstone has not any strength value that means “zero” by Schmidt Hammer due to a too soft rock that can be easily crumble by finger. Mud matrix strength of conglomerate is significantly lower than clast of conglomerate (Gül et al., 2016).	Without cave parts are more durable than within cave parts. Mudstone has not any strength value that means “zero” by Schmidt Hammer due to a too soft rock that can be easily crumble by finger. Mud matrix strength of conglomerate is significantly lower than clast of conglomerate (Gül et al., 2016).
Clay type(s) (according to the Unified Soil Classification System (USCS)	SM (silty sands, sand-silt mixtures)	CL (Inorganic clays of low to medium plasticity, gravelly / sandy / silty / lean clays) and SC (Clayey sands, sand-clay mixtures)
Environmental Impact	Enlargement of cave due to both anthropogenic and natural factor cause to decrease of overburden thickness of cave so collapsing risk are increasing day by day. This risk threatens to people just settled at top of cave. The sewage system of those settlers may reach the groundwater circulating inside the cave and may lead to contamination of groundwater and spring. Continuous monitoring of cave and groundwater and spring, relocation of houses on top cave must take into consideration.	Enlargement of cave occurrences may cause to collapsing risk. Collapsing and increasing human impact due to recreation increase destruction risk of special cave structures (stalactite, flowstone, travertine, etc.). For protection of recent situation of those structures, continuous monitoring, restriction of human impact and protection of vegetation and water circulation must supply.

The clasts of the conglomerate, which are composed of Jurassic-Cretaceous limestone fragments are disintegrated by means of dissolutional weathering processes. Active weathering processes may promote progressive rock mass weakening and break down in the cave. Sometimes large rock blocks (30- 40 cm wide) fall down to the road parallel to the Basmacı Stream.

The Muğla province which is a part of the SW Türkiye, is one of the most seismically active region of the country. Seismic activities led to formation of additonal joints and rock fall in caves. Possible collapse of cave ceiling constitutes a threaten to inhabitants in AHC area. Thus, regular monitoring of caves must be made, further excavation of caves and additional settlements on top of cave area must be prohibited, and relocation of these settlements may be taken into consideration. Dewatering of the cave area must be applied with suitable drainage system to ensure the stability of the caves.

The AHC area contains numerous caves. In general, the caves of Asar Hill are isolated and have

not developed a network of cave pattern. The rocks in which the caves developed are conglomerate with mud size sediment bearing matrix and mudstone alternation. Bedding planes and four joints sets are the structural features that affect those rock units. UCS values obtained from Schmidt Hammer rebound value indicate that in-situ strength of rock is largely classified as low to medium strength rock based on ISRM (1978) and Deere and Miller (1966). Laboratory tests on rock samples point out slightly porous, high density, hard rock, with medium-high slake durability. Both surface and ground water including springs, as well as damp ground were observed in the AHC area during the field studies.

Gül et al. (2016) reported that conglomerate in upper part of Asar Hill as low density (1.9 g/cm^3) and moderately porous (6.4 %) rock, while, mudstone as moderately dense (2.5 g/cm^3) and slightly porous (4.0%) rock based on Anon (1979) classification. Muddy conglomerate (matrix supported) in upper part of Asar Hill was classified as soft rock, clast supported conglomerate as hard rock and mudstone was classified as very soft rock based on insitu Schmidt Hammer Rebound Value (Gül et al., 2016).

In Asar Hill area, caves can be followed in several mudstone levels (Figure 5), while the caves follow one thick mudstone layer in the Damlam Stream area (Figure 8). The initiation of the cave formation was probably in fine-grained level of mudstones due to their relatively low resistance against weathering. Later, enlargement occured through the upper level coarse-grained muddy conglomerates. Both areas are under the effect of active normal faults. The tectonic history of the region revealed four joint sets and bedding planes have occured in Asar Hill area. However, these features (joints) are not much visible in Damlam Stream caves, because they are untraceable due to occurrence of the flowstone coverage on the cave walls.

AHC resemble shelter caves. Shelter type caves has been investigated and described by Ferk and Lipar (2012) developed in Pleistocene carbonate conglomerate in Slovenia. The authors have stated that shelter cave usually form on the edge walls of terraces or side walls of valleys or canyons. They also claim that physical weathering and corrosion are the processes that lead the formation of shelter caves in conglomerate. The length (depth) of the shelter caves of Asar Hill into the conglomerate varies from 1.5 m to about 10 m. Their width and height are usually greater than their length (Table 1). Ferk and Lipar (2012) claim that physical weathering and corrosion are the processes that form shelter caves throughout the world and these processes play a great role on the later evolution of shelter caves in conglomerate.

DSC area contains five caves. The rocks in which caves formed are conglomerate with mud matrix and mudstone alternations. Major joint sets were not detected during the field study. UCS values obtained from Schmidt Hammer rebound value indicate that insitu strength of rock is largely classified as low to medium strength rock based on ISRM (1978) and Deere and Miller (1966). Laboratory tests point out slight to moderate porous, low to high density, hard rock, with medium-high slake durability of conglomerate. The finer-grained parts of the Yatağan Formation are composed of mostly CL (low plasticity inorganic clay based on USCS) type clays.

The caves in DSC area resemble shelter caves, which were described by Ferk and Lipar (2012) in detail, developed in Pleistocene carbonate conglomerate in Slovenia. These shelter caves in DSC area have formed on the side walls of the valley. The length (depth) into the conglomerate of the shelter caves in DSC area varies from 2 m to 4.7 m. Their width and height are usually greater than their length (Table 3).

The Yatağan Formation in DSC area has highly variable lithology. Groundwater and/or surface water is quite active in this area. Water input increase into the karst rock enhances dissolution and transport of the mineral matter and may adversely modify the mechanical strength of the rock (Gutierrez et al., 2014). In DSC area, dense vegetation is present on top of the caves. The capillary root vessels of trees have penetrated into the Yatağan Formation at different places. The water follows those vessels during infiltration, and this causes weakening and disintegration of the host rock. The processes of weathering and removing of the mudstone of the Yatağan Formation, have started the formation of the caves. Then, water weakening the muddy matrix of conglomerate led to disintegration of clast, and enlargement of the caves. After the cave formation, dripping of the water along the root vessel led to the saturation of the water to calcium carbonate and formation of the stalactites, where it emerged on

the ceiling of the cave. The groundwater seeping from the cave walls and flowing downwards resulted in occurrence of the flowstone as a plaster and travertine.

Human activities, such as excavation of caves for barn, storage and other purposes cause enlargement of the caves in Asar Hill area. Moreover, sewage system of the settlements on top of cave area also increase the dissolutional capacity of the water moving along fractures in AHC. Leakages from sewage may contaminate the groundwater circulating in the conglomerate of AHC. Enlargement of caves by dissolution, weakening and drop out of the rock material causes decrease in cap rock thickness (overburden thickness) in time. Recently DSC area is used as a recreation place with a restaurant. Thus human activities are threatening natural state of the caves. Continuous monitoring of the caves is necessary in DSC area. The movement of groundwater and surface water under natural conditions have to be continued and vegetation cover above the caves must be protected. Otherwise caves and their special textures may be damaged and irreversibly disappear.

The strength values of the AHC and DSC areas are very close. However, the porosity of the DSC samples is significantly higher than the AHC samples (Tables 2 and 4). The density values of the DSC samples are lower than the AHC samples (Tables 2 and 4). These features, with the contribution of groundwater and plant roots, ensured the formation of the largest cave in the DSC (Cave 3, Table 3).

Clastic rocks with various age and thickness host caves with different size in different part of world (Busche and Sponholz, 1992; Bergada et al., 1997; Kranjc, 2005; Aubrecht et al., 2008; Breitenbach et al., 2010; Lipar and Ferk, 2011; Awadh et al., 2013). Those caves are permanently or temporarily used for recreation and supplying shelter for both human and animal (Busche and Sponholz, 1992; Bergada et al., 1997; Kranjc, 2005; Aubrecht et al., 2008).

The Asar Hill and the Damlam Stream caves have some similarities and dissimilarities with the aforementioned caves. For example, Awadh et al. (2013) reported that the caves in Upper Miocene-Pliocene Injana Formation in Najaf-Karbala-Iraq area clastics. They mentioned that water circulation following the cracks led to softening, weakening and disintegration of claystone and formation of claystone balls, which are not observed in the Yatağan Formation.

Lipar and Ferk (2011) studied conglomerate caves in Udin Boršt in Slovenia which developed depending on physical weathering that evolved under the effect of karstification after deposition, thus they classified as eogenetic origin. They defined four different type of caves in conglomerates; linear stream caves (mouth of cave has 1 m high and a few meter-wide entrance, controlled by discontinuties formed as a result of temporary or permananent streams on terrain surface), shelter caves (formed in carbonate rocks, cave entrance has a few meter height and 10 m width, <10 m length (depth), matrix porosity and physical weathering is important), breakdown caves (formed as a result of collapse of previous cave), and vadose shaft (single, vertical tubular form, evolved as a result of the vertical water movement). Similar shaft occurences and enderheic plataeu collapse (doline, uvala) and small karren structures reported in Niger sandstone in Niger (Busche and Sponholz, 1992). Bergada et al. (1997) also reported vertical potholes development in Palaeocene conglomerates in Catalonia (Spain).

The caves in clastic rocks of the Yatağan Formation are example of the shelter cave (due to development in carbonate clast enriched conglomerate). Vadose shaft and other karstic structures were not detected in the study area. Absence of these structures may be explained with age (youth) of the formation and/or they may have been destroyed due to loose lithology of the Yatağan Formation. Permanent and temporary streams are located below the bottom level of the caves, so direct effects of them to cave formation were not observed.

Karst terrains may be affected by severe ground instability problems. Natural and human-induced static and dynamic loadings may trigger the collapse of the caves under marginal stability conditions (Gutierrez et al., 2014). The load imposed by heavy vehicles, drilling rigs, dumped material and engineered structures may cause dangerous sinkhole collapse events (Gutierrez et al., 2014). Impacts and hazards associated with karst are rapidly increasing as development expands upon these areas without proper planning taking into account the peculiarities of these environments (Gutierrez et al., 2014). The roof of a cave may collapse either in its natural state

or under an imposed load from engineering activity. Natural collapse is by progressive failures of roof rock units, which may eventually reach the ground surface. Imposed loading may either accelerate or precipitate the natural processes of cave roof failure (Waltham, 2002).

Caves are very fragile geological occurences. Continuous monitoring of the caves, groundwater circulation, vegetation and structures are necessary for the protection of caves. Enlargement of caves and decreasing of overburden thickness may increase the collapse risk of the cave roofs. The possibility of collapse may threaten the property and human life in Asar Hill area, while in Damlam Stream valley, this may result in destruction of the specific cave structures.

6. Results

In the clastic rocks (conglomerates mainly composed of limestone pebbles) of the Yatağan Formation several caves with various size were observed in two areas. The caves in the study area differ in size, with length between 1.47-9.71 m, width between 2.24-19.36 m, and height between 1.38-27 m. The caves in the study area have the characteristics which are similar to that of shelter caves described by Ferk and Lipar (2012).

Joint sets, bedding planes and tree roots constitute the routes for water percolation and circulation that weaken the muddy matrix of the thick and relatively low resistant conglomerate bed and mudstone. Matrix dissolution and weathering in conglomerates, results in clast-after-clast release and grain-by-grain disintegration. After the disintegration of the conglomerate, fragments have been washed. In addition to these general structural and lithologic properties, some local factors also play role in the development of the caves, (for example human impact in the Asar Hill caves and vegetation affect in the Damlam Stream caves). Human activities promote enlargement of caves in Asar Hill caves, while groundwater percolation along main and capillary vessels of the roots led to formation of small scale stalactites, flowstone and travertine deposits in Damlam Stream cave.

Surface and subsurface karstic features pose some potential hazards which must be considered for land use planning, construction, and water resource management. Caves and sinkholes present a hazard for construction processes and settlement areas. These karstic features may potentially impact the load-bearing capacity of the karstified rock. Thus, engineers and planners have to be interested in understanding the behavior of these karstic features and the potential geological hazards they may cause.

Acknowledgements

The authors thank to reviewers Dr. Hüseyin KARAKUŞ and Dr. İbrahim ÇOBANOĞLU, and editors for their valuable contribution for increasing the scientific quality of the paper.

References

Aktimur, H. T., Sarıaslan, M. M., Sönmez, M., Keçer, M., Uysal, Ş., Özmutaf, M. 1996. Muğla ilinin (merkez ilçe) arazi kullanım potansiyeli. Maden Tetkik ve Arama Genel Müdürlüğü, Rapor No: 9853, 33, Ankara (unpublished).

Anon, O. H. 1979. Classification of rocks and soils for engineering geological mapping: part 1- rock and soil materials. Bulletin of Engineering Geology and the Environment 19(1), 364–71.

ASTM (American Society for Testing and Materials). 2000. D2487 standard practice for classification of soils for engineering purposes (Unified Soil Classification System, USCS).

Aubrecht, R., Lánczos, T., Šmída, B., Brewer-Carías, C., Mayoral, F., Schlögl, J., Audy, M., Vlček, L., Kováčik, Ľ., Gregor, M. 2008. Venezuelan sandstone caves: a new view on their genesis. hydrogeology and speleothems. Geologica Croatica 61(2-3), 345-362.

Awadh, S. M., Abood, Z. S., Eisa, M. J. 2013. Chemical and physical control processes on the development of caves in the Injana Formation, Central Iraq. Arabian Journal of Geoscience 6, 3765–3772.

Bergada, M. M., Cervello, J. M., Serrat, D. 1997. Karst in conglomerates in Catalonia (Spain): morphological forms and sedimentary sequence types recorded on archaeological sites. Quaternaire 8(2-3), 267-277.

Breitenbach, S. F. M., Donges, J. F., Daly, B. K., Kohn, T., Kohn, T. 2010. Two sandstone caves on the southern edge of the Meghalaya Plateau, India. Cave and Karst Science, Transactions of the British Cave Research Association 37(2), 49-52.

Broch, E., Franklin, J. A. 1972. The point-load strength test. International Journal of Rock Mechanics and Mining Sciences 9, 669-697.

Busche, D., Sponholz, B., 1992. Morphological and micromorphological aspects of the sandstone karst of eastern Niger. Zeitschrift für Geomorphologie 85, 1-18.

Deere, D. U., Miller, R. P. 1966. Engineering classification and index properties of rock. Technical Report No: AFWL-TR-65-116, Urbana, Illinois, 327.

Değirmenci, M., Bayarı, C. S., Denizman, C., Kurttas, T. 1994. Caves in conglomerate, Köprüçay Basin, Western Taurids-Türkiye. National Sculpture Society Bulletin 56, 14–22.

Dunkley, J., Ellis, M., Bolger, T. 2017. Unusual caves and karst-like features in sandstone and conglomerate in Thailand. Helictite 43, 15-31.

Eastwood, W. J., Leng, M. J., Roberts, N., Davis, B. 2007. Holocene climate change in the easternMediterranean region: a comparison of stable isotope and pollen data from Lake Gölhisar, southwest Türkiye. Journal of Quaternary Science 22(4), 327–341.

Ekmekçi, M. 2005. Karst in Turkish thrace: compatibility between geological history and karst type. Turkish Journal of Earth Science 14, 73–90.

Ferk, M., Lipar, M. 2012. Eogenetic caves in the Pleistocene carbonate conglomerate in Slovenia. Acta Geographica Slovenica 52(1), 7–33.

Ferrarese, F., Sauro, U. 2005. The Montello hill: The classical karst of the conglomerate rocks. Acta Carsologica 34(2), 439-448.

Ford, D. C., Williams, P. W. 2007. Karst Hydrogeology and Geomorphology. John Wiley and Sons, 562.

Gamble, J. C. 1971. Durability-Plasticity classification of shales and other argillaceous rocks. PhD Thesis, University of Illinois at Urbana-Champaign.

Google, 2022. www.google.com.tr/map. 06 May 2022.

Göktaş, F. 1998. Muğla çevresi (GB Anadolu) Neojen tortullaşmasının stratigrafisi ve sedimantolojisi. Maden Tetkik ve Arama Genel Müdürlüğü, Rapor No: 10225, 181, Ankara (unpublished).

Grimes, K. G. 2012. Karst and paleokarst features involving sandstones of the Judbarra / Gregory National Park. Northern Territory, Australia. Helictite 41, 67-73.

Gutierrez, F., Parise, M., DeWaele, J., Jourde, H. 2014. A review on natural and human-induced geohazards and impacts in karst. Earth-Science Reviews 138, 61–88.

Gül, M. 2015. Lithological properties and environmental importance of the Quaternary colluviums (Muğla, SW Türkiye). Environmental Earth Sciences, 74, 4089–4108.

Gül, M., Karacan, E., Aksoy, M. 2013. Muğla kenti yerleşim alanı ve yakın çevresinin genel jeolojik ve mühendislik jeolojisi özelliklerinin araştırılması. Muğla Sıtkı Koçman Üniversitesi, Bilimsel Araştırma Fonu, Proje No: 12/54, 25, (unpublished).

Gül, M., Özbek, A., Karacan, E. 2016. Rock fall hazard assessment in Asar Hill, ancient Mabolla City, Muğla—SW Türkiye. Environmental Earth Sciences 75, 1310, 16.

Gül, M., Çetin, E., Küçükuysal, C., Gülcan, M., Kahveci, Y. 2021. Recent alluvial fan developments in Muğla (SW Türkiye). Arabian Journal of Geosciences 14, 819.

Güldalı, N., Nazik, L., Soylu, C., Aksoy, B. 1984. Fethiye-Köyceğiz-Marmaris ve Muğla çevresinin doğal mağaraları. Maden Tetkik Arama Genel Müdürlüğü, Rapor No: 7586, Ankara (unpublished).

Günay, G., Güner, N., Törk, K. 2015. Turkish karst aquifers. Environmental Earth Sciences 74(1), 217-226.

Gürer, Ö. F., Sanğu, E., Özburan, M., Gürbüz, A., Sarıca-Filoreau, N. 2013. Complex basin evolution in the Gökova Gulf region: implications on the Late Cenozoic tectonics of southwest Türkiye. International Journal of Earth Science (Geologische Rundschau) 102, 2199–2221.

HGK (General Command of Mapping). 2016. http://www.hgk.msb.gov.tr. 25 August 2016

ISRM (International Society for Rock Mechanics). 1978. International society for rock mechanics commission on standardization of laboratory and field tests: Suggested methods for the quantitative description of discontinuities in rock masses. International Journal of Rock Mechanics and Mining Sciences and Geomechanics Abstracts 15(6), 319-368.

ISRM (International Society for Rock Mechanics). 2007. The complete ISRM suggested methods for rock characterization, testing and monitoring: 1974-2006.

Jiménez-Moreno, G., Alçiçek, H., Alçiçek, M., Van den Hoek Ostende, L., Wesselingh, F. 2015. Vegetation and

climate changes during the late Pliocene and early Pleistocene in SW Anatolia, Türkiye. Quaternary Research 84(3), 448-456.

Kayan, İ. 1979. Muğla-Yatağan Neojen havzalarının jeomorfolojisi. Türkiye Bilimsel ve Teknolojik Araştırma Kurumu, Proje No: TBAG-189, 272, Ankara (unpublished).

Konak, N., Akdeniz, N., Öztürk, E. M. 1987. Geology of the south of Menderes Massif: IGCP Project No.5: Correlation of Variscan and Pre-Variscan Events of the Alpine-Mediterranean Mountain Belt. Field Meeting, Türkiye, Sept. 13-19, 1987a, Guide Book for the Field Excursion Along Western Anatolia, Türkiye, 42-53, Ankara.

Kranjc, A. 2005. Conglomerate karst in Slovenia: history of cave knowledge and research of Udin Boršt (Gorenjsko). Acta Carsologica 34(2), 521-532.

Küçükuysal, C., Gül, M., Aghayev, T. 2018. Muğla polyesi kırmızı Akdeniz toprakları (Terra Rossa): mineralojik, mikromorfolojik, jeokimyasal ve pedolojk özellikleri. Türkiye Bilimsel ve Teknolojik Araştırma Kurumu, Proje No: 116Y027, 74, Ankara (unpublished).

Lapaire, F., Becker, D., Christe, R., Luetscher, M. 2006. Karst phenomena with gas emanations in Early Oligocene conglomerates: risks within a highway context (Jura, Switzerland). Bulletin of Engineering Geology and the Environment 66, 237–250.

Lipar, M., Ferk, M. 2011. Eogenetic caves in conglomerate: an example from Udin Boršt. Slovenia. International Journal of Speleology 40(1), 53-64.

MGM (Turkish State Meteorological Service). 2022. https://www.mgm.gov.tr/veridegerlendirme/il-ve-ilceler-istatistik.aspx?k=undefined&m=MUGLA. 31 May 2022.

MTA (General Directorate of Mineral Research and Exploration). 2002. 1/500.000 ölçekli jeoloji haritası, Aydın, N20 paftası, Maden Tetkik ve Arama Genel Müdürlüğü, Ankara.

Minaeian, B., Ahangari, K. 2013. Estimation of uniaxial compressive strength based on P-wave and Schmidt hammer rebound using statistical method. Arabian Journal of Geosciences 6, 1925–1931.

Nazik, L. 1996. Gökçeler Manisa ve Yerküpe Menteşe Kavaklıdere mağaralarinin ön araştırma raporu. Maden Tetkik ve Arama Genel Müdürlüğü, Rapor No: 9896, Ankara (unpublished).

Özel, E., Nazik, L., Mengi, H., Kutlay, H., Derici, Ş., Törk, K., Aksoy, B. 1996. Yerküpe mağarası Kavaklıdere Muğla araştırma raporu mimari ve elektrifikasyon uygulama projesi. Maden Tetkik ve Arama Genel Müdürlüğü, Rapor No: 10048, Ankara (unpublished).

Palmer, A. N. 1991. Origin and morphology of limestone caves. Geological Society of America Bulletin 103, 1-21.

Parise, M., Lollino, P. 2011. A preliminary analysis of failure mechanisms in karst and man-made underground caves in Southern Italy. Geomorphology 134, 132–143.

Sezer, İ. L. 2003. Muğla yöresinde deprem aktivitesi ve riski. Kuvaterner Çalıştayı IV. İTÜ Avrasya Yerbilimleri Enstitüsü 111-120.

Sivakugan, N., Shukla, S. K., Das, B. M. 2013. Rock Mechanics: An Introduction. CRC Press Taylor and Francis Group, 234.

Şahin, E. 2015. Karstification of Asartepe, Merkez, Muğla. Bsc Thesis, Muğla Sıtkı Koçman University, 35 (unpublished).

Tuncer, K., Törk, K., Nazik, L., Kutlay, H., Özel, E., Acar, C. 2005. Gökçeler-Muğla, İntepe-Milas, Gelme-Çingerek-Marmaris ve Girmeler-Fethiye mağaralari değerlendirme ve öneriler raporu. Maden Tetkik ve Arama Genel Müdürlüğü, Rapor No: 10172, Ankara (unpublished).

Waltham, T. 2002. The engineering classification of karst with respect to the role and influence of caves. International Journal of Speleology 31(1, 4), 19-35.

Zeybek, M. 2017. Geological factors controlling cave occurrences within clastic sediments of Yatağan Formation (Upper Miocene-Pliocene, SW Türkiye). MSc Thesis, Muğla Sıtkı Koçman University, 89 (unpublished).

Bulletin of the Mineral Research and Exploration

http://bulletin.mta.gov.tr

TÜBİTAK 1MV Accelerator Mass Spectrometer Designed for ^{14}C, ^{10}Be, ^{26}Al, ^{41}Ca, ^{129}I

Turhan DOĞAN[a*], Erhan İLKMEN[a] and Furkan KULAK[a]

[a]*TÜBİTAK, Marmara Research Center, Gebze, Kocaeli, Türkiye,*

Research Article

Keywords:
Radiocarbon, Radiocarbon Dating, Accelerator Mass Spectrometer, Accelerated Mass Spectroscopy.

Received Date: 10.05.2022
Accepted Date: 02.01.2023

ABSTRACT

A 1 MV Accelerator Mass Spectrometer (AMS) was established at TÜBİTAK, MRC Türkiye in December 2015. The 1MV TÜBİTAK AMS system is based on a Pelletron tandem accelerator, operating up to 1.1MV. Built by National Electrostatics Corporation (NEC), its design was unique at time of production. The TÜBİTAK 1MV AMS is based on the design of an XCAMS 0.5MV AMS also produced by NEC, but with a higher energy tandem accelerator. The higher energy accelerator features better precision (1% or less) for ^{10}Be measurements. This new AMS also has larger magnets than the XCAMS. Larger magnets make it possible to measure ^{41}Ca and ^{129}I at the two-anode gas-ionization detector. In this article, the technical features; the parameters of ion source, terminal and other operations, and measurement quality are explained for accomplished performance of the five isotopic ratios, $^{14}C/^{12}C$, $^{10}Be/^{9}Be$, $^{26}Al/^{27}Al$, $^{41}Ca/^{40}Ca$, $^{129}I/^{127}I$. This article also presents five years of data for $^{14}C/^{12}C$ ratio measurement quality control are represented as well.

1. Introduction

The first AMS facility in Türkiye was established in 2016 at The Scientific and Technological Research Council of Türkiye, (TÜBİTAK), Marmara Research Center, (MRC). The laboratory is called (Türkiye) National 1 MV Accelerated Mass Spectroscopy Laboratory (Doğan et al., 2021). Since 2016, the laboratory has been providing international commercial radiocarbon analysis making it one of only two AMS laboratories in the Middle East and the Balkans. Considering the high demand for radionuclide analysis in the fields of archeology, earth science, environmental science, and criminology in Türkiye and the region, Türkiye‘s first and only AMS laboratory is aiming to address both domestic and international requests. The establishment of the laboratory which includes the 1MV AMS system is financed with national resources by the Ministry of Development, Republic of Türkiye.

The TÜBİTAK 1MV AMS system is designed and produced by National Electrostatic Corporation (NEC) using their Pelletron tandem accelerator technology. The Universal AMS system is the first 1MV AMS from NEC designed for multi species measurements. In this paper, the unique design of the UAMS system, the 1MV Accelerator Mass Spectrometer capable of detecting ^{14}C, ^{10}Be, ^{26}Al, ^{40}Ca as well as ^{129}I, is explained. An overview of the system’s components is also featured. The technical features: The parameters of ion source, terminal and other operations, and measurement quality are explained for accomplished performance of the five isotopic ratios, $^{14}C/^{12}C$, $^{10}Be/^{9}Be$, $^{26}Al/^{27}Al$, $^{41}Ca/^{40}Ca$, $^{129}I/^{127}I$. The five years

Citation Info: Doğan, T., İlkmen, E., Kulak, F. 2023. TÜBİTAK 1MV Accelerator Mass Spectrometer Designed for ^{14}C, ^{10}Be, ^{26}Al, ^{41}Ca, ^{129}I. Bulletin of the Mineral Research and Exploration 172, 81-91. https://doi.org/10.19111/bulletinofmre.1228878

**Corresponding author: Turhan DOĞAN, turhandogan@hotmail.com*

of data for $^{14}C/^{12}C$ ratio measurement quality control are represented as well.

1.1. AMS System Room

The AMS System room is a crucial aspect for providing smooth operation of AMS. If the room where the AMS system is installed is not adequate, it may directly affect the quality of measurement. The AMS system room was thoroughly prepared for installation before the AMS was dispatched for installation: The room floor was checked to be less than ±1 cm slope and ground concrete was prepared to handle the heavy AMS weight. We did not observe any subsidence of the floor in the past 5 years. Any slope forming on the ground would affect the alignment of the AMS. Both the AMS system and the cooling water chiller unit have a stable dedicated AC power setup including a diesel generator and 160KVA UPS which feeds electricity with minimum noise. High electrical noise may lead to defects on AMS parts or shorten their life. Other essential things needed to operate stable AMS are clean compressed air, filtered cooling water, controlled air temperatures, and a low dew point of the room. Fluctuations in humidity and temperature of the room can cause unstable AMS measurements. The TÜBİTAK AMS room is equipped to provide a stable room temperature around 20±1 degrees Celsius and a dew point less than 15. These parameters are continuously monitored at 8 points around the room. After five years of operations, all the parameters mentioned above are strictly maintained.

The room is also large enough to accommodate and service the TÜBİTAK 1MV AMS system which has an outline of 7.4 m x 4 m. (Figure 1)

2. Development of AMS Systems and the TÜBİTAK 1MV AMS System

AMS systems have gone under significant transformations in the last four decades. After showing that rare isotopes can be measured with AMS, some existing accelerator systems were modified, and measurements were made. Measurements were mostly focused on radiocarbon, which was in high demand. During the 1980's, high energy accelerators were used with the capability to measure more than one isotope (Synal and Wacker, 2010). Following this initial phase, lower energy models with an accelerator 1MV or less dedicated for radiocarbon

Figure 1- The AMS system in TÜBİTAK AMS laboratory room.

measurement were introduced (Synal et al., 2000). Commercial availability of AMS systems became more widespread. Now, there are carbon dedicated 0.2 MV AMS systems (Schroeder et al., 2004; Synal et al., 2007). Furthermore, AMS systems with low energy accelerators proved to be sufficient for multi-isotope systems including ^{10}Be, ^{14}C, ^{26}Al and ^{41}Ca (Klein et al., 2006; Zondervan et al., 2015; Macková et al., 2021). Recently, systems with low energy accelerators have become more preferred for routine measurements. Certain minor additions to AMS systems enabled development of techniques that allow measurement by eliminating isobars at lower energies. An important example is the introduction of Si_3N_4 energy degrader foil to measure rare Beryllium isotopes as low as 0.5 MV terminal voltages (Müller et al., 2008). Therefore, Türkiye's first AMS system is conceptualized and designed on this model to be able to measure multiple isotopes and is intended to be further developed in future. The TÜBİTAK 1MV AMS system model is a NEC 3SDH-1 UAMS. The UAMS is a more advanced system based on the XCAMS design which in turn was based on NEC's radiocarbon dedicated compact AMS systems (CAMS) (Southon et al., 2004).

When comparing the TÜBİTAK 1MV AMS hardware features with XCAMS, the first noticeable ones are the 1MV accelerator and larger magnets. Apart from radiocarbon, the TÜBİTAK 1MV AMS can measure rare beryllium, aluminum, and calcium isotopes as well as iodine 129. The 1MV accelerator provides a significant improvement in the precision for Beryllium measurements compared to XCAMS (Zondervan et al., 2015). Also, the larger magnets allow measurements of calcium and iodine isotopes. In fact, the TÜBİTAK 1MV AMS system was ordered to measure only the species mentioned above. However, during production, we requested to add iodine measurement capability to the system. The TÜBİTAK 1MV AMS can be modified to measure more species as future technological developments in isobar separation filters emerge. For instance, AMS systems with 5 MV or higher terminal voltage can measure ^{36}Cl, however recent attempts to extend efficient isobar separation is promising it to be measured in lower energies (Martschini et al., 2011).

The layout of the 1MV AMS system and the details of the components are given in Figure 2.

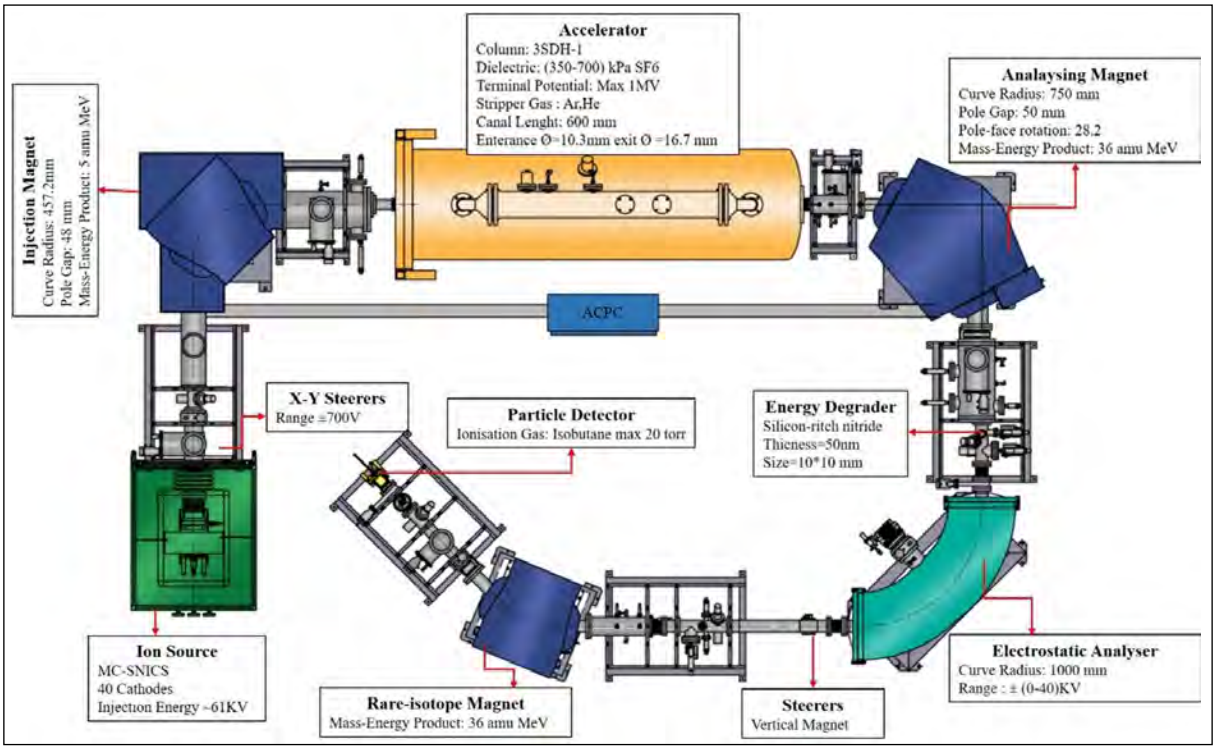

Figure 2- The layout of the 1MV AMS system and the details of the components.

2.1. Ion source

The TÜBİTAK 1MV AMS Multi-Cathode Negative Ion Source (MC-SNICS) holds up to 40 solid samples. The negative ions are accelerated through a potential of 61 kV. The ion source produces up to 100 microampere currents measured in the first Faraday cup, located just after the ion source. Ion source parameters for each isotope are given in Table 1.

2.2. Injection Line Section

An X/Y steerer is located after the ion source, and just before the first Faraday cup. These isotope specific steerers are used to tune the beam along the injection line section with the help of the first beam profile monitor (BPM), which displays the shape of the beam in the X and Y direction. This is the first BPM in the UAMS system and is placed following the Faraday cup before the insulating gap. The insulating gaps are at the image and object point of the magnet. The magnet bias supply (MBS) coupled to the 90° bending magnet does the sequential injection. In the case of Carbon analysis, abundant ^{12}C and ^{13}C ions are integrated at the Faraday cups every 1800 ms and 10000 ms respectively, whereas the rare ^{14}C ions are injected into the Gas Ionization Detector for 90000µs (Doğan et al., 2021). This cycle continues with a repetition rate of roughly 10 Hz. The injection times for each ion species are given in Table 2.

After the magnet, the beam of one ion is injected at once through the Pelletron accelerator. Between the magnet and the mass accelerator are offset Faraday cups to measure the abundant isotope(s). The injection magnet, or low energy magnet, has a radius of 457mm. After the magnet there are two off axis Faraday cups. The first one is used for ^{12}C, ^{13}C, ^{9}Be, ^{40}Ca, and ^{127}I while the other one is used for ^{27}Al. Slits are placed just before the entrance to the accelerator tank.

The sequential injection brings advantages to the AMS system. The average current from the abundant isotopes in the 3SDH accelerator remains small. This allows the use of substantial abundant isotope currents, maximizing throughput and measurement precision, but at the same time minimizes accelerator loading.

2.3. 1MV Accelerator

The one charge state ion's beam is accelerated to a maximum of 2.2 MeV to achieve the necessary energy dispersion through the high energy part of the mass spectrometer. An Einzel lens is placed in the acceleration tank just before the acceleration tubes. Interlocks are incorporated for safe operations. A chain stop was also installed in this system (Figure 3). It gives an opportunity to stop the chain motor if the chain stretches too much. Excess and unexpected stretch of the chain can cause damage to mechanical parts in the tank. 50 psi of SF_6 gas is sufficient for accelerator operation at 0.5MV. However, 80 PSI is required for operation at full gradient at 1.1 MV terminal voltage. The SF_6 gas is circulated in the tank so that it is continuously filtered to keep the gas as pure as possible and cooled with a heat exchanger.

The molecular dissociation is achieved by the accelerator via the stripper gas that can be selected among Helium and Argon from the two bottles placed inside the high voltage terminal. The stripper gas

Table 1- Ion source parameter for each isotope is given.

Isotope Ratio	$^{10}Be/^{9}Be$	$^{14}C/^{12}C$	$^{26}Al/^{27}Al$	$^{41}Ca/^{40}Ca$	$^{129}I/^{127}I$
Cathode	6.00 kV	6.00 kV	6.00 kV	6.00 kV	4.00 kV
Immersion Lens	5.65 kV	5.60 kV	5.60 kV	5.77 kV	3.33 kV
Extractor	15.00 kV	15.00 kV	15.00 kV	15.00 kV	18.00 kV
Focus	0.96 kV	0.8 kV	0.8 kV	0.00 kV	0.96 kV
Bias	41 kV	41 kV	52 kV	42 kV	37 kV
Ionizer	23 A	23 A	22 A	23 A	23 A

Table 2- The injection times for each ion species are given.

Species Measured	^{14}C	^{13}C	^{12}C	^{10}Be as (BeO^-)	^{9}Be as (BeO^-)	^{26}Al	^{27}Al	^{41}Ca as (CaF_3^-)	^{40}Ca as (CaF_3^-)	^{129}I	^{127}I
Injection time (millisecond)	90	10	1.8	1	99	1	99	100	1	1	99

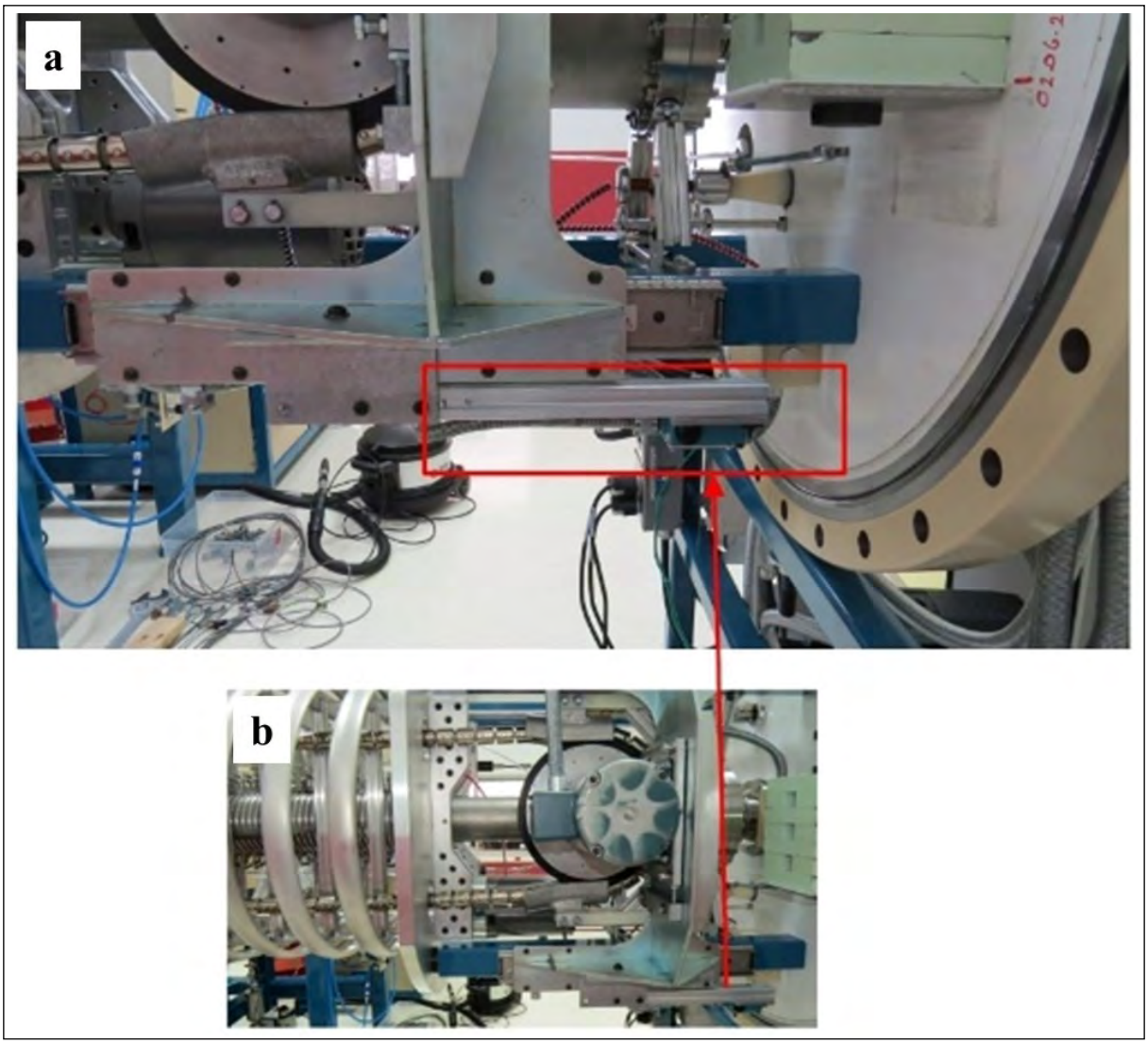

Figure 3- a) A chain stopper mechanism is installed to prevent damage in accelerator tank in case of excessive chain stretching and b) the position of the chain stopper mechanism in accelerator tank.

supply is configured to manually switch between Helium and Argon with a selector knob placed outside the tank. The stripper pressure is remotely adjusted with a metering valve in the high voltage terminal that is connected to a stepper motor on the tank head through a long lucite rod. Argon is used during carbon and aluminum measurements while Helium is chosen for Beryllium, Calcium, and Iodine (Doğan et al., 2021). The Stripper canal is differentially pumped and recirculates argon or helium with the two 300 l/min turbo pumps.

On each side of the terminal there are two 22 gap acceleration tubes. Voltage grading is achieved by 550 MOhm resistors across each gap.

The terminal stability is better than 0.05% of the terminal potential which indicates less than a 500V variation of the terminal voltage at 1 MV. Lost charge is stable below 0.4 micro ampere. Two VFDs were placed outside the accelerator tank to control the charging chain and generator motor. A glass viewport was placed at the top of the tank to monitor any stretching of the chain or sparking from the outside.

Focus adjustments are possible by changing the electric field gradient inside the accelerator with a shorting rod. With this the 3SDH Pelletron Accelerator can be operated at terminal potentials from 0.2 MV to 1.1 MV. The optimum terminal energy at the terminal

and the parameters specific to isotopes being measured are given in Table 3.

2.4. Analyzing Magnet

A Faraday cup is placed after the exit of the accelerator which is utilized during beam tuning. Due to design limitations, this beam line cup does not have a suppressor. This feature is different from other Faraday cups in the system. There is also an electrostatic quadrupole triplet before the analyzing magnet which is used for beam shaping and focusing.

The analyzing magnet has a 75cm radius, 50mm pole gap and ME/Z^2=36amu-MeV. This allows bending higher masses than Carbon and Beryllium. Thus, heavy isotopes such as ^{41}Ca and ^{129}I can reach the gas ionization detector.

After acceleration, the analyzing magnet separates the isotopes of interest, sending the abundant reference isotopes to the off-axis Faraday cups at the image point of the analyzing magnet. Furthermore, the rare isotopes travel down the rare isotope beamline. Fast, precision, gated current integrators with digital sampling circuitry measure the abundant isotopes currents.

There are 3 off-axis Faraday cups where 12C, ^{13}C, ^{9}Be, ^{40}Ca, ^{27}Al are measured. For ^{10}Be measurements a 75 nm energy degrader Silicon Nitride foil is inserted via an actuator. Due to slightly different stopping powers, the ^{10}B isobar counts at the detector can be separated from the ^{10}Be counts.

For the abundant isotope ^{127}I, measurement is done in the low energy side Faraday cup. Since it does not have any isobar, it is possible to use measurement data from the low energy side.

2.5. Electrostatic Analyzer

The second BPM along the UAMS is placed before the ESA, which makes it possible to check the shape and orientation of the beam after the high energy magnet. The ESA has a 100 cm radius which provides a longer flight path compared to the XCAMS. The ESA elements are kept at around +40 kV and –40 kV respectively for carbon measurements. The electrostatic analyzer discriminates ions based on energy and prevents unwanted ions from reaching the final rare isotope detector. The third filter, a 45° magnet in combination with a thin stopper foil before the ESA, is necessary for separating the isobar ^{10}B from ^{10}Be. A magnetic steerer is placed after the ESA

Table 3- The optimum terminal energy and the parameters specific to each element are given.

Rare Isotope	**^{10}Be**	**^{14}C**	**^{26}Al**	**^{41}Ca**	**^{129}I**
Source Output (A) (Species)	1.034×10^{-06}	5.234×10^{-05}	4.143×10^{-07}	1.685×10^{-07}	4.581×10^{-06}
Terminal Voltage (MV)	1.10	0.46	0.57	1.10	0.50
Charge State	1	1	1	5	3
Transmission	56.300%	41.050%	21.190%	0.002%	Not measured
Blank Measured	9.88×10^{-16}	2.50×10^{-16}	2.12×10^{-15}	1.72×10^{-11}	8.68×10^{-15}
Blank Material	Blank	Phtalic Anhydride	Blank	Blank	Woodward
Standard Material	NIST	NIST SRM 4990C (Ox-II)	KN-4-1	Nishiizumi et al., 2000	n/a
Standard Ratio	2.6775×10^{-12}	1.4202×10^{-12}	6.5727×10^{-11}	9.291×10^{-09}	1.5578×10^{-12}
Standard Deviation (%)	0.535%	0.080%	0.226%	0.705%	0.573%
Rare Isotope (Injected)	^{10}Be+(BeO^-)	^{14}C+(C^-)	^{26}Al+(Al^-)	^{41}Ca+5(CaF_3^-)	^{129}I ($129I^-$)

which makes it possible to tune up the beam in the Y direction. The third BPM in the UAMS makes it possible to monitor and tune the beam after the ESA and steerer magnet. There is also a Quadrupole located just before the 45° Degree Magnet.

2.6. 45° Degree Magnet

A 45° double focusing magnet is crucial to measure $^{10}Be/^{9}Be$ ratios precisely. In addition to a 45° magnet before the detector, a thin, removable, stripper foil is placed before the ESA. Some species traveling through this foil lose one more electron resulting in double charged $^{10}Be^{2+}$ ions to have a slightly higher energy than the interfering $^{10}B^{2+}$ ions (Figure 4). Finally, it is possible to separate these isobars in the gas ionization detector.

2.7. Rare Isotope Detector

The final BPM is placed just before the detector and serves to monitor and tune the final abundant beam trajectory before the detector.

The TÜBİTAK 1MV UAMS system employs a compact GIC (gas ionization counter) with two plates to separate the rare isotopes from remaining interferences, which can be "gated" out from the counts.

The detector connects to preamplifiers which connect to NIM amplifiers for pulse shaping and amplification. The output is sent to a XIA Pixie-4 4 channel analog-digital converter to minimize background from interference ions. Timing signals from the jumping beam system are typically used to gate the output signal along with the coincidence signal. This eliminates the possibility of counting artifacts during the short periods when the abundant isotopes are being accelerated and measured.

2.8. Control Deck

Like all NEC AMS systems, the AccelNET control system PCs are running on Scientific Linux. A second computer on Scientific Linux is running the offline analyzing software ABC software for normalization and evaluation of the results.

3. System Performance

Operation parameters of TÜBİTAK 1MV AMS for routine Carbon measurement are given in Table 4. Systematic testing of all five isotopes was performed in site acceptance tests. All acceptance requirements for the five isotopes were met. Since the system will be used predominantly for carbon measurements several IAEA standards were measured and compared to their consensus value (Table 5). Plotting the measured pMC values over the IAEA consensus values has a 0.99587 agreement.

Radiocarbon measurements have routinely continued since the laboratory was established. The five years of data for $^{14}C/^{12}C$ ratio measurement quality control are represented in Figures 5, 6, 7, 8 and 9 which illustrates times series graph for standard reference materials SRM 4990C (Ox-II), IAEA-C7, IAEA-C8 as well as processed (Phthalic anhydride $C_8H_4O_3$, Sigma Aldrich 320064) and unprocessed blank (Alfa Aesar graphite powder natural, briquetting grade 100 mesh, 99,9995%). It is an attempt to measure standard reference materials with a less than 1 % uncertainty. Providing a low uncertainty level has been the most important parameter for the TÜBİTAK measurement condition. Chemistry of graphite

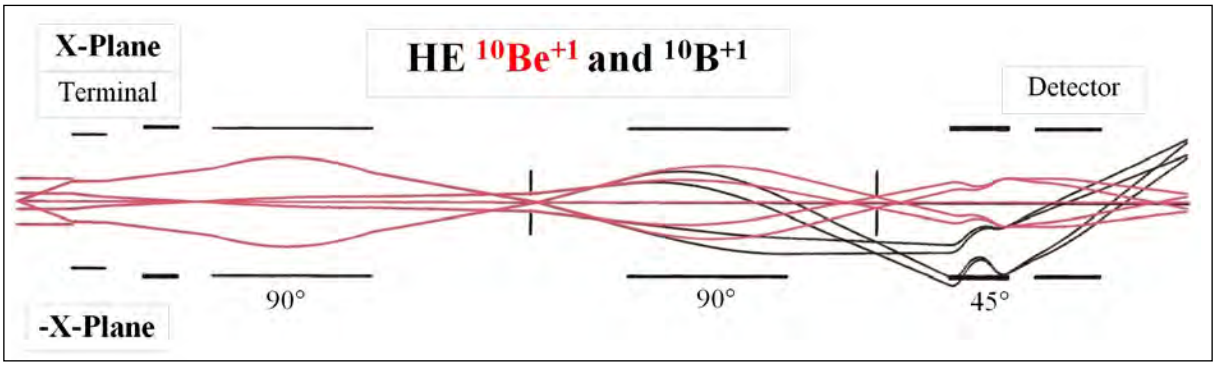

Figure 4- The ion beam profile in double focusing magnet.

Table 4- Operation parameters of TÜBİTAK 1MV AMS for routine Carbon measurement.

Section of AMS	Parameter	Value
Ion Source	Beam Current Energy of the Beam	50-60 µA 61 keV
Injection Magnet	Field MBS	0.29T 10.683 kV 5.090 kV 0.200 kV
Accelerator	Terminal Voltage Argon Stripper Gas Pressure	0.460 MV 0.06 mbar
Analyzing Magnet	Field	0.72T
Faraday Cups	^{12}C Beam ^{13}C Beam	2.149x10-05 A 2.341x10-07 A
Electrostatic Analyzer	Plate Voltage	39.78 kV, -39.78 kV
^{14}C Detector	OXII count rate	~ 10000 cpm

Table 5- Carbon Agreement with IAEA Standards are given for the preliminary measurements done during acceptance tests in 2015. *It is improved to closer to consensus value as 0.00-0.05pMC with eliminating contamination from graphite production in the last five years. **It is measured as 0.22±0.03 pMC when treated with acid base acid (ABA) before measurement (Doğan et al., 2023).

Standard Reference Material	Consensus Value (pMC)	Measured Value (pMC)
IAEA C1	0±0.02	0.136*±0.08
IAEA C2	41.14	41.61±0.22
IAEA C3	129.41	128.95±0.51
IAEA C4	0.20 - 0.44	0.30±0.07
IAEA C5	23.05	23.05±0.12
IAEA C7	49.53	49.51±0.17
IAEA C8	15.03	15.01±0.07
IAEA C9	0.12 - 0.21	0.39**±0.03

production process and keeping ion source clean have been the most important impacts in uncertainty values. After operating for a total of 15 days (360 hours), the ion source has to be cleaned. Ionizer, immersion lens, and other components in this part of the AMS must be disassembled in order to clean the ion source. Typically, it is cleaned with Kimwipe™ and pure water and ethanol. Depending on the amount of crust developed on the surface of the ionizer, a sandblaster can be used with an ionizer and an immersion lens.

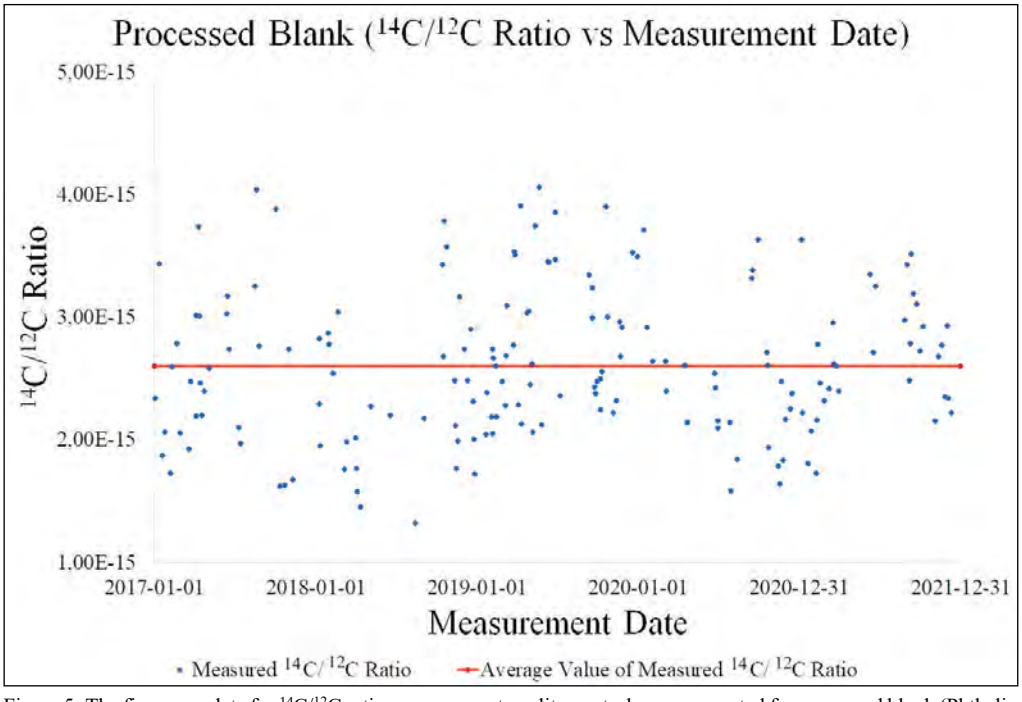

Figure 5- The five years data for ^{14}C/^{12}C ratio measurement quality control are represented for processed blank (Phthalic anhydride $C_8H_4O_3$, Sigma Aldrich 320064). The average value of ^{14}C/^{12}C ratio is measured to be 2.60x10^{-15}. The increase in this value is considered a contamination from the process in the chemistry laboratory.

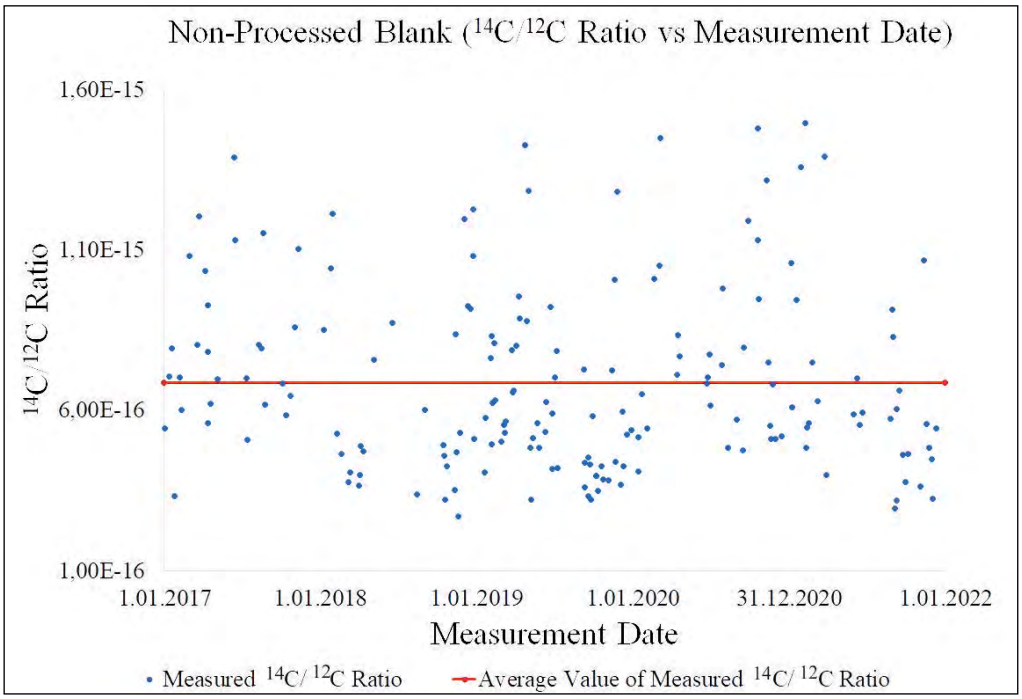

Figure 6- The five years data for $^{14}C/^{12}C$ ratio measurement quality control are unprocessed blank (Alfa Aesar graphite powder natural). The average value of $^{14}C/^{12}C$ ratio is measured to be $6.85x10^{-16}$. The increase in this value is considered rise in the background ^{14}C in the AMS usually because of contaminated ion source.

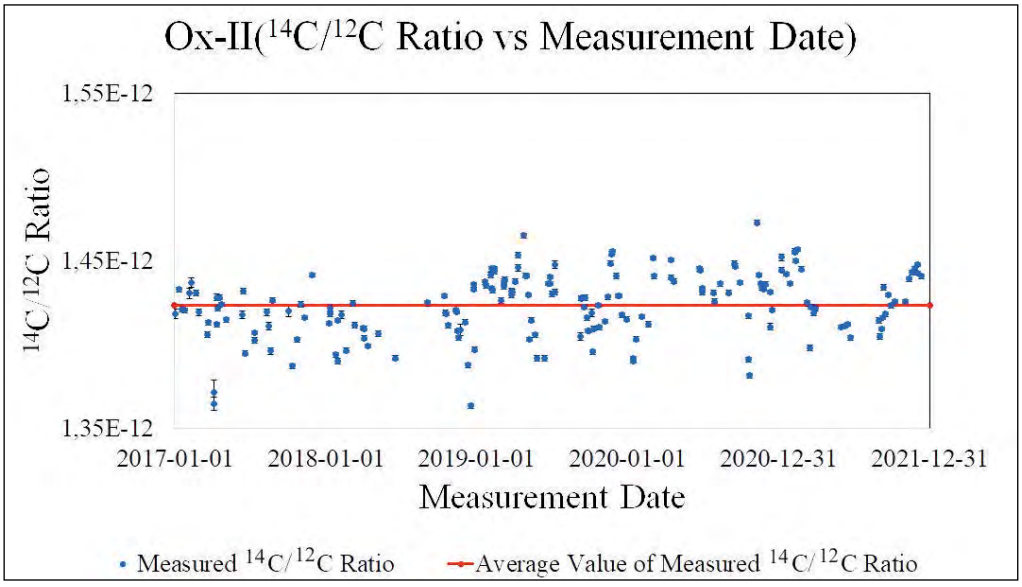

Figure 7- The five years data for $^{14}C/^{12}C$ ratio measurement quality control are represented for the standard reference material SRM 4990C (Ox-II),). The average value of $^{14}C/^{12}C$ ratio is measured to be $1.42x10^{-15}$. The cause change in this value is observed to be associated with replacement of ion source parts.

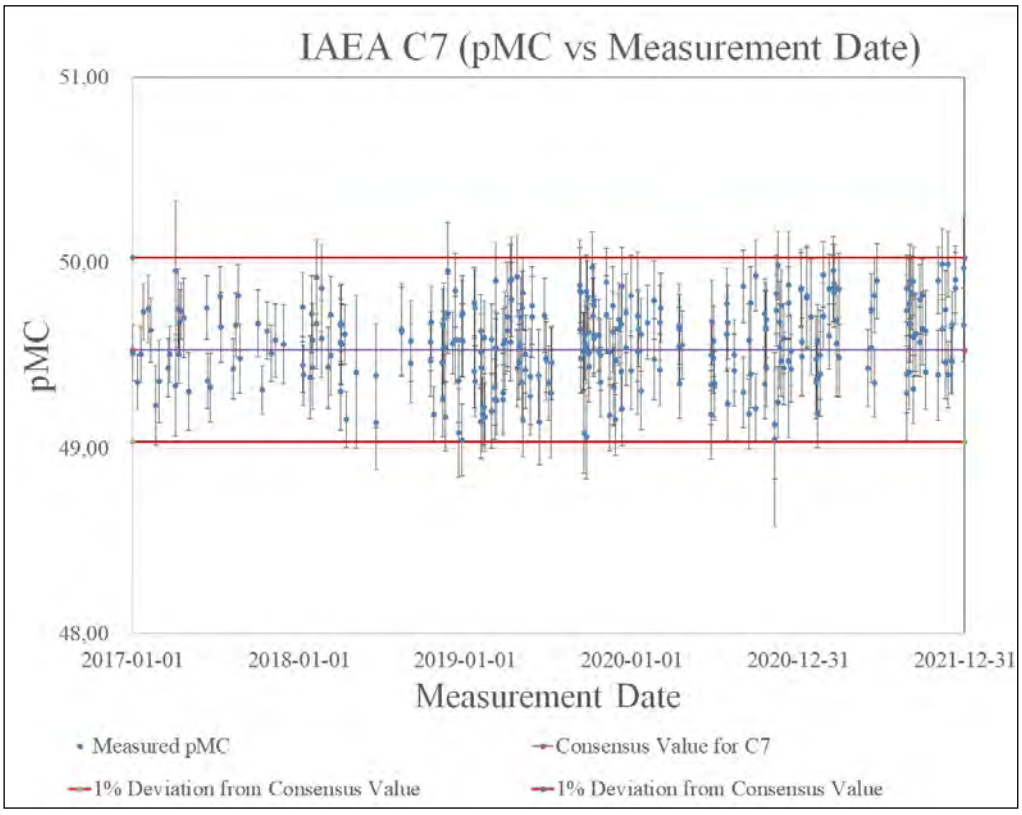

Figure 8- The five years data for $^{14}C/^{12}C$ ratio measurement quality control are represented for the standard reference material IAEA-C7. The average value of $^{14}C/^{12}C$ ratio is measured to be 49.57 pMC which is very close to consensus value 49.53 pMC. IAEA-C7 is measured to be maximum 1% deviation to be accepted; the overall measurement pass the quality control.

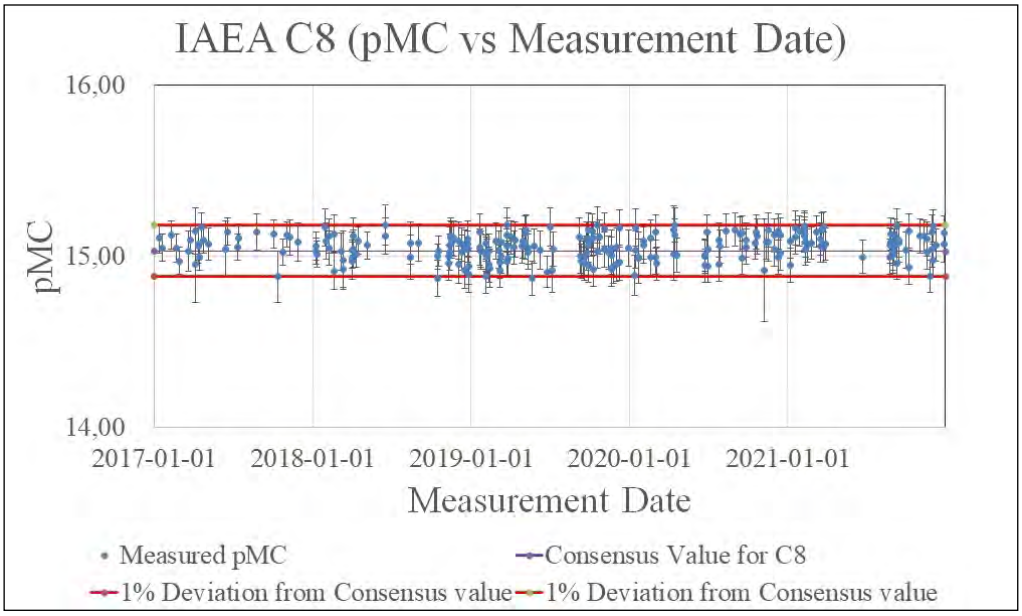

Figure 9- The five years data for $^{14}C/^{12}C$ ratio measurement quality control are represented for the standard reference material IAEA-C8. The average value of $^{14}C/^{12}C$ ratio is measured to be 15.05 pMC which is very close to consensus value 15.03 pMC. IAEA-C8 is measured to be the maximum 1% deviation to be accepted; the overall measurement passes the quality control.

4. Conclusion

A new AMS system based on a 1 MV tandem Pelletron was installed and accepted in December 2015. This UAMS was designed and built to measure five different isotopes. All standard and background isotopic ratios agreed with consensus values. After the system was validated and approved, regular operation procedures were implemented. The laboratory is now performing routine measurements on samples that have been brought in from across the world. The TÜBTAK AMS Laboratory is very significant for its work and support for scientific study in this region because it is one of the only three AMS laboratories in the entire Middle East and the Balkans (Doğan et al., 2023).

References

Doğan, T., İlkmen, E., Kulak, F. 2021. A new national 1 MV AMS laboratory at TÜBİTAK MRC in Türkiye. Nuclear Instruments and Methods in Physics Research Section B: Beam Interactions with Materials and Atoms 509, 48-54.

Doğan, T., İlkmen, E., Kulak, F. 2023. Radiocarbon Analysis And Status Report From Türkiye: 1MV National AMS Laboratory (TÜBİTAK-AMS). Radiocarbon (accepted).

Klein, M. G., Mous, D. J. W., Gottdang, A. 2006. A compact 1MV multi-element AMS system. Nuclear Instruments and Methods in Physics Research Section B: Beam Interactions with Materials and Atoms 249, 764-767.

Macková, A., Malinský, P., Cutroneo, M., Havránek, V., Voseček, V., Flaks, J., Semián, V., Vonka, L., Zach, V., Bém, P., Běhal, R., Čihák, M., Mrázek, J., Krist, P., Poklop, D., Štefánik, M., Štursa, J., Olšanský, V., Chvátil, D., Kučera, J., Němec, M., Světlík, I., Kameník, J., Tecl, J. 2021. Small accelerators and their applications in the CANAM research infrastructure at the NPI CAS. The European Physical Journal Plus 136, 558.

Martschini, M., Forstner, O., Golser R., Kutschera W., Pavetich S., Priller, A., Steier P., Suter M., Wallner A. 2011. Recent advances in AMS of ^{36}Cl with a 3-MV-tandem. Nuclear Instruments and Methods in Physics Research Section B: Beam Interactions with Materials and Atoms 269 (24), 3188-3191.

Müller, A. M., Christl, M., Döbeli, M., Kubik, P. W., Suter, M., Synal H. A. 2008. 10Be AMS measurements at low energies (E<1MeV). Nuclear Instruments and Methods in Physics Research Section B: Beam Interactions with Materials and Atoms 266 (10), 2207-2212.

Nishiizumi, K., Caffee, M. W., DePaolo D. J. 2000. Preparation of 41Ca AMS standards. Nuclear Instruments and Methods in Physics Research Section B: Beam Interactions with Materials and Atoms 172 (1–4), 399-403.

Schroeder, J., Hauser, T., Klody, G., Norton, G. 2004. Initial Results with Low Energy Single Stage AMS. Radiocarbon 46 (1), 1-4.

Southon, J. R., Santos dos, G. M., Druffel-Rodriquez, K. C., Druffel, E. R. M., Trumbore, S., Xu, X., Maya Mazo M., Ali S., Mazon M. 2004. The Keck Carbon Cycle AMS Laboratory, University of California, Irvine; initial operation and a background surprise. Radiocarbon 46, 41–49.

Synal, H. A., Wacker, L. 2010. AMS measurement technique after 30 years: Possibilities and limitations of low energy systems. Nuclear Instruments and Methods in Physics Research Section B: Beam Interactions with Materials and Atoms 268, (7–8) 701-707.

Synal, H. A., Jacob, S., Suter, M. 2000. The PSI/ETH small radiocarbon dating system. Nuclear Instruments and Methods in Physics Research Section B: Beam Interactions with Materials and Atoms 172, 1–7.

Synal, H. A., Stocker, M, Suter, M. 2007. MICADAS: A new compact radiocarbon AMS system. Nuclear Instruments and Methods in Physics Research Section B: Beam Interactions with Materials and Atoms 259 (1),7-13.

Zondervan, A., Hauser, T. M., Kaiser, J., Kitchen, R. L., Turnbull, J. C., West J. G. 2015. XCAMS: The compact 14C accelerator mass spectrometer extended for 10Be and 26Al at GNS Science, New Zealand. Nuclear Instruments and Methods in Physics Research Section B: Beam Interactions with Materials and Atoms 361, 25-33.

Bulletin of the Mineral Research and Exploration

http://bulletin.mta.gov.tr

Supplemental skeleton revision of Pseudorbitoididae M.G. Rutten, 1935 from mainly Tethyan and partly American provinces

Ercüment SİREL[a] and Ali DEVECİLER[b*]

[a]*Ankara University Department of Geological Engineering, Ankara, Türkiye.*
[b]*General Directorate of Mineral Research and Exploration, Department of Geological Researches, Ankara, Türkiye.*

Research Article

Keywords:
America, Foraminiferida, Pseudorbitoididae, Tethyan.

Received Date: 25.05.2022
Accepted Date: 01.02.2023

ABSTRACT

The nine genera here described from the Tethyan and four genera from the American and Caribbean provinces have previously been placed within different families of Foraminifera by various authors, namely, *Arnaudiella* DOUVILLÉ, *Sirtina* BRÖNNIMANN and WIRZ, *Vanderbeekia* BRÖNNIMANN and WIRZ, *Helicorbitoides* MacGILLAVRY, *Dizerina* MERİÇ, *Sirelella* ÖZGEN-ERDEM and *Cideina* SİREL were shown in Lepidorbitoitidae VAUGHAN; *Postorbitokathina* SİREL and *Orbitokathina* HOTTINGER in Rotaliidae EHRENBERG; *Helicolepidina* TOBLER, *Helicosteginopsis* CAUDRI, *Eulinderina* BARKER and GRIMSDALE and *Helicostegina* BARKER and GRIMSDALE in Lepidocyclinidae SCHEFFEN, in spite of the fact that all of them have characteristics of both rotaliid early and orbitoidal adult stages. Thus the growth stages such as rotaloid early and orbitoidal adult stages of the aforementioned general correspond with the known family Pseudorbitoididae RUTTEN and its type genus *Pseudorbitoides* DOUVILLÉ. Therefore the thirteen genera found in great abundance in the Tethyan, American and Caribbean provinces have been transferred to Pseudorbitoididae RUTTEN.

1. Introduction

The main purpose of this study is to revise the family Pseudorbitoididae RUTTEN and some of the genera from the Tethyan and American provinces (Figure 1).

The Maastrichtian foraminiferal genus *Cideina* SİREL has been placed originally within the family Lepidorbitoididae VAUGHAN; however, due to the both rotaliid and orbitoidal stages, Sirel (1991, Plates I, II) proposed it has typical trochospiral early chambers with pillars and radial canals (funnels).

Sirel (1991) proposed a new family for the new genus *Cideina* SİREL, as well as the known genera *Sirtina* BRÖNNIMANN and WIRZ, *Vanderbeekia* BRÖNNIMANN and WIRZ, and *Orbitokathina* HOTTINGER. This insight gives us an opportunity to find, in particular, a suitable family for the genera (Plates I-VI). As a result of this investigation, the family Pseudorbitoididae RUTTEN (type species *Pseudorbitoides trechmanni* DOUVILLÉ in Plate I) was choosen as the proper family for the here described and figured genera (Plate I-VI) through the common characters such as rotaloid early and orbitoidal adult stage.

So, the following nine genera *Arnaudiella* DOUVILLÉ (Plate I, Figures 1, 3), *Sirtina* BRÖNNIMANN and WIRZ (Plate II, Figures 4, 8),

Citation Info: Sirel, E., Deveciler, A. 2023. Supplemental skeleton revision of Pseudorbitoididae M.G. Rutten, 1935 from mainly Tethyan and partly American provinces. Bulletin of the Mineral Research and Exploration 172, 93-117. https://doi.org/10.19111/bulletinofmre.1245807

**Corresponding author: Ali DEVECİLER, alideveciler@gmail.com*

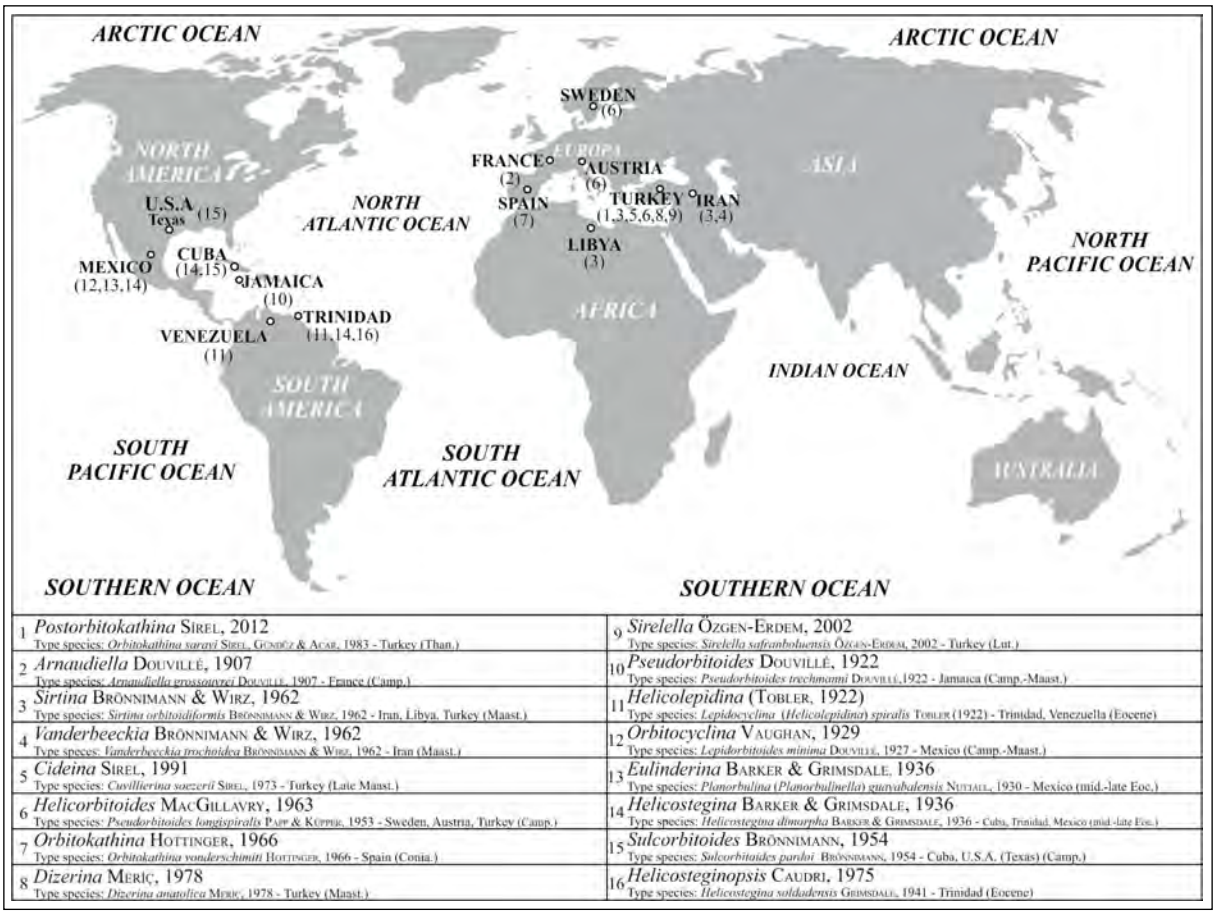

1 *Postorbitokathina* SIREL, 2012 Type species: *Orbitokathina sarayi* SIREL, GÖNDÜZ & ACAR, 1983 - Turkey (Than.)	9 *Sirelella* ÖZGEN-ERDEM, 2002 Type species: *Sirelella safranboluensis* ÖZGEN-ERDEM, 2002 - Turkey (Lut.)
2 *Arnaudiella* DOUVILLÉ, 1907 Type species: *Arnaudiella grossouvrei* DOUVILLÉ, 1907 - France (Camp.)	10 *Pseudorbitoides* DOUVILLÉ, 1922 Type species: *Pseudorbitoides trechmanni* DOUVILLÉ,1922 - Jamaica (Camp.-Maast.)
3 *Sirtina* BRÖNNIMANN & WIRZ, 1962 Type species: *Sirtina orbitoidiformis* BRÖNNIMANN & WIRZ, 1962 - Iran, Libya, Turkey (Maast.)	11 *Helicolepidina* (TOBLER, 1922) Type species: *Lepidocyclina* (*Helicolepidina*) *spiralis* TOBLER (1922) - Trinidad, Venezuella (Eocene)
4 *Vanderbeeckia* BRÖNNIMANN & WIRZ, 1962 Type species: *Vanderbeeckia trocholdea* BRÖNNIMANN & WIRZ, 1962 - Iran (Maast.)	12 *Orbitocyclina* VAUGHAN, 1929 Type species: *Lepidorbitoides minima* DOUVILLÉ, 1927 - Mexico (Camp.-Maast.)
5 *Cideina* SIREL, 1991 Type species: *Cuvillierina soezerii* SIREL, 1973 - Turkey (Late Maast.)	13 *Eulinderina* BARKER & GRIMSDALE, 1936 Type species: *Planorbulina* (*Planorbulinella*) *guayabalensis* NUTTALL, 1930 - Mexico (mid.-late Eoc.)
6 *Helicorbitoides* MACGILLAVRY, 1963 Type species: *Pseudorbitoides longispiralis* PAPP & KÜPPER, 1953 - Sweden, Austria, Turkey (Camp.)	14 *Helicostegina* BARKER & GRIMSDALE, 1936 Type species: *Helicostegina dimorpha* BARKER & GRIMSDALE, 1936 - Cuba, Trinidad, Mexico (mid.-late Eoc.)
7 *Orbitokathina* HOTTINGER, 1966 Type species: *Orbitokathina vonderschmitti* HOTTINGER, 1966 - Spain (Conia.)	15 *Sulcorbitoides* BRÖNNIMANN, 1954 Type species: *Sulcorbitoides pardoi* BRÖNNIMANN, 1954 - Cuba, U.S.A. (Texas) (Camp.)
8 *Dizerina* MERİÇ, 1978 Type species: *Dizerina anatolica* MERIÇ, 1978 - Turkey (Maast.)	16 *Helicosteginopsis* CAUDRI, 1975 Type species: *Helicostegina soldadensis* GRIMSDALE, 1941 - Trinidad (Eocene)

Figure 1- Location map, showing the geographic distribution of the genera in the Tethyan and American provinces.

Vanderbeekia BRÖNNIMANN and WIRZ (Plate II, Figure 9), *Helicorbitoides* MacGILLAVRY (Plate III, Figures 1-4), *Orbitokathina* HOTTINGER (Plate III, Figures 5, 8), *Dizerina* MERİÇ (Plate III, Figures 9, 11), *Cideina* SİREL (Plate IV, Figures 1, 4), *Sirelella* ÖZGEN-ERDEM (Plate IV, Figures 5, 7) and *Postorbitokathina* SİREL (Plate IV, Figures 8, 11) from the Tethys region and five genera viz, *Helicolepidina* TOBLER (Plate V, Figures 1, 4), *Orbitocyclina* VAUGHAN (Plate V, Figures 5, 6), *Eulinderina* BARKER and GRIMSDALE (Plate V, Figures 7, 10), *Helicostegina* BARKER and GRIMSDALE (Plate VI, Figures 1, 3), *Sulcorbitoides* BRÖNNIMANN (Plate VI, Figures 4, 7) and *Helicosteginopsis* CAUDRI (Plate VI, Figures 8, 11) from the American province were transferred from the improper old families to the Pseudorbitoididae RUTTEN.

2. Systematic Palaeontology

The suprageneric classification is based particularly on Loeblich and Tappan (1987) and BouDagher-Fadel (2008). The genera are arranged in the text in chronological order, except for the type genus *Pseudorbitoides* DOUVILLÉ, 1907. The following diagnostic characters of the family Pseudorbitoididae and its genera have been compiled largely from the Plates I-VI.

Superfamily: Rotalioidea EHRENBERG, 1829

Family: Pseudorbitoididae RUTTEN, 1935

Type genus: *Pseudorbitoides* DOUVILLÉ, 1907

Type species: *Pseudorbitoides trechmanni* DOUVILLÉ, 1907

Description of Pseudorbitoididae RUTTEN: Test free, inflated lenticular-discoidal, ornamented with pustulates (Plate I, Figures 6, 7; Plate II, Figure 7; Plate III, Figure 6), the rotaliid spiral chambers coiling planispiral-involute (Plate II, Figure 5; Plate VI, Figure 10) or trochospiral-evolute in patterns (Plate II, Figure 8; Plate III, Figures 7, 8; Plate IV, Figures

2, 5, 6, 8; Plate 6, Figure 5); the spiral chambers sometimes become uncoiled or from a helicolepidine string towards the periphery (Plate 2, Figures 1, 2; Plate III, Figure 1; Plate V, Figure 1), the well-developed orbitoidal equatorial chamberlets occur in the median plane (Plate I, Figures 3, 6), the smaller secondary orbitoidal chamberlets appear between the equatorial chamberlets (Plate III, Figures 1, 4; Plate VI), the lateral orbitoidal chamberlets occur on both sides (Plate I, Figures 1, 5, 8; Plate II, Figures 3, 5, 8, 9; Plate III, Figures 2, 3; Plate V, Figures 2, 6; Plate VI, Figures 3, 5, 10), or only on the dorsal side of the test (Plate II, Figures 5, 8, 9; Plate IV, Figure 1, 2).

In consequence of these analyses, all representative genera here illustrated in Plate I-VI of Pseudorbitoididae have characteristic common rotaliid and orbitoidal chambers and chamberlets in the early and late stages respectively. Therefore, they are collected in the aforementioned family.

*Remarks***:** The name of Pseudorbitoididae was translated from the subfamily Pseudorbitoidinae RUTTEN by Brönnimann (1958). The family Orbitocyclinidae without description established by van Gorsel (1972) instead of Pseudorbitoididae is not available according to the International Code of Zoological Nomenclature (ICZN). Recently, the family Pseudorbitoididae RUTTEN was adopted by Loeblich and Tappan (1987) and BouDagher-Fadel (2008). In this study, the revision of the family was realized by means of the shared rotaliid and orbitoidal growth stages described here sixteen Tethyan and American genera (Plate I-VI). Brönnimann (1955, p. 63) and Loeblich and Tappan (1987, p. 652-653) already reported the spirally enrolled chambers in early stage, followed by orbitoidal chamberlets of adult stage. Besides some of the genera such as *Pseudorbitoides* DOUVILLÉ, *Arnaudiella* DOUVILLÉ, *Helicorbitoides* MacGILLAVRY and maybe *Dizerina* MERİÇ have rods (radiating rowes/ radial plates) appearing in the equatorial sections just as mentioned in previous studies (Vaughan 1929, p. 294; Rutten 1935, p. 543-544; Brönnimann 1955, p. 58; Loeblich and Tappan 1987, p. 652-653).

Seven Tethyan genera such as *Arnaudiella* DOUVILLÉ (Plate II, Figures 1, 3), *Sirtina* BRÖNNIMANN and WIRZ (Plate II, Figures 4, 8), *Vanderbeekia* BRÖNNIMANN and WIRZ (Plate II, Figures 9), *Helicorbitoides* MacGILLAVRY (Plate III, Figures 1, 4), *Dizerina* MERİÇ (Plate III, Figures 9, 11), *Sirelella* ÖZGEN-ERDEM (Plate IV, Figures 5-7) which have come from Lepidorbitoitidae VAUGHAN in Loeblich and Tappan (1987) and BouDagher-Fadel (2008), were transferred to the family Pseudorbitoididae RUTTEN. In the same way, *Cideina* SİREL (Plate IV, Figures 1, 4) was transferred from the Lepidorbitoitidae in Sirel (1991) to the foregoing family by having a rotaliid early stage; in that Lepidorbitoitidae differs from Pseudorbitoididae in its characteristic bilocular embryonic apparatus consisting of the spherical protoconch and reniform deuteroconch, whereas the latter family has a rotaliid early stage with planispiral-trochospiral chambers (Plate I, III, IV).

Two genera *Orbitokathina* HOTTINGER and *Postorbitokathina* SİREL which have previously been included within Rotaliidae EHRENBERG by Loeblich and Tappan (1987) and Sirel (2012) respectively, are here included in the Pseudorbitoididae RUTTEN, in that they differ from the Rotaliidae in possessing well developed equatorial orbitoidal chamberlets in the adult stage of the microspheric forms (Plate III, Figure 5; Plate IV, Figures 9, 11).

The four American genera, viz, *Helicolepidina* TOBLER *Helicosteginopsis* CAUDRI, *Eulinderina* BARKER and GRIMSDALE and *Helicostegina* BARKER and GRIMSDALE have previously been placed in the subfamily Helicolepidininae TAN, 1936 within the Lepidocyclinidae SCHEFFEN by Loeblich and Tappan (1987) and BouDagher-Fadel (2008), but are here transferred to Pseudorbitoididae, in that Lepidocyclinidae differs from Pseudorbitoididae in having a bilocular embryonic apparatus instead of the rotaloid early stage with planispiral-trochospiral chambers (Plates I, III, IV).

Earlier, other three genera, the herein described type genus *Pseudorbitoides* DOUVILLÉ, *Orbitocyclina* VAUGHAN and *Sulcorbitoides* BRÖNNIMANN had been included within the family Pseudorbitoididae RUTTEN by Loeblich and Tappan (1987, p. 611) and BouDagher-Fadel (2008, p. 356-357).

Additionally, *Radiorbitoides* KRIJNEN, *Vaughanina* PALMER and *Clypeorbis* DOUVILLÉ need to be examined regarding some generic characteristics. The figures of *Radiorbitoides* KRIJNEN do not reflect clearly rotaliid early chambers of Pseoudorbitoididae (Krijnen, 1993,

pl. 1, 2). Numerous annular chambers with small subrectangular chamberlets of *Vaughanina* PALMER are apparently similar to that of discocylinid type (Palmer, 1934; Krijnen, 1972; Vaughan and Cole, 1943) therefore, the aforementioned genera are out of scope of the present study. The morphometric and evolutionary study as regards to radial foraminifera (*Pseudorbitoides* DOUVILLÉ, *Vaughanina* PALMER) have been analyzed in detail through the figures of Krijnen (1972) by Drooger (1993). In contrast to the original description, *Clypeorbis* DOUVILLÉ has a lepidorbitoid embryonic stage (Hottinger and Caus, 2007, pl. 8, Figure 5) consisting of protoconch, deuteroconch and adauxiliary chambers rather than the trochoid early stage. Also Mitchell et al. (2022) have established a new family Helicosteginidae including *Tremastegina* BRÖNNIMANN and *Helicostegina* BARKER and GRIMSDALE, however *Helicostegina* BARKER and GRIMSDALE already shows the chracteristics of the Pseudorbitodidae family.

Type genus ***Pseudorbitoides* DOUVILLÉ, 1922**

(Plate I, Figures 1-9)

*Description***:** The microspheric generation has a large inflated lenticular test with pointed peripheral margin (Plate I, Figures 1, 5, 8). External surface ornamented with small pustules (Plate I, Figures 6, 7); very small microsphere followed by small shapeless rotaliid chambers lining up in two whorls or may be more (Plate I, Figures 2, 9). Later arcuate-shapeless median orbitoidal chamberlets arranged in an irregular concentric row (Plate I, Figures 2, 9). The layer of rotaliid and median orbitoidal chambers and chamberlets completely covered by the lateral layers of the orbitoidal chamberlets on both sides of the test, in which the thick pillars occur between the lateral chamberlets (Plate I, Figures 1, 5, 8).

The megalospheric test has a large spheric protoconch followed by large spiral chambers then median orbitoidal shapeless chamberlets arranged irregularly (Plate I, Figure 4), Dimorphism distinct, Campanian-Maastrichtian of American province.

The aforementioned description of the type genus *Pseudorbitoides* DOUVILLÉ is based on the figures in Figure 2 of Brönnimann (1955), Vaughan and Cole (1943), and Krijnen (1972).

Plate I-VI have been compiled, in order to show common diagnostic characters of here described sixteen genera with regard to Pseudorbitoididae RUTTEN.

2.1. Tethyan Forms

The following genera that occur in the Tethys regions were interpreted to belong to the family Pseudorbitoididae RUTTEN in the light of the generic features in the sections of Plates II-IV.

***Arnaudiella* DOUVILLÉ, 1907**

(Plate II, Figures 1-3)

*Description***:** The megalospheric generation of the type species has a lenticular test with central thickening (Plate II, Figure 3). The external surface is ornamented with numerous small indistinct pustules (Plate II, Figure 1). An excellent equatorial section (Plate II, Figure 2) clearly shows that the spherical protoconch and small second chamber are followed by the subrectangular spiral chambers in one and half whorl, later spiral chambers are entirely uncoiled and become a helicolepidine string towards the periphery as in *Helicorbitoides* MacGILLAVRY and *Helicolepidina* TOBLER (Plate III, Figures 1-4; Plate V, Figures 1-4) respectively. The septal flaps are distinct in the last spiral chambers (Plate II, Figure 2). The layer of radial canals and rods occur in the median plane instead of the orbitoidal chamberlets (Plate II, Figures 1, 2). The spiral rotaliid chambers, radial canals and rods in the median plane are completely covered by the layer of lateral orbitoidal chamberlets with pillars (Plate II, Figure 3). Dimorphism unknown, Campanian.

The foregoing description of *Arnaudiella* DOUVILLÉ is based on the figures of van Gorsel (1975, 1978) and Loeblich and Tappan (1987, p. 649).

Remarks: *Arnaudiella* DOUVILLÉ (1907) has been placed in the family Lepidorbitoididae VAUGHAN by Loeblich and Tappan (1987, p. 649) and BouDagher-Fadel (2008). However the representatives of Lepidorbitoididae (particularly the type genus *Lepidorbitoides* SILVESTRI) differ from *Arnaudiella* in possessing bilocular embryonic apparatus consisting of protoconch and deuteroconch and two primary auxiliary and numerous auxiliary chambers. Due to the rotaliid spiral chambers and lateral orbitoidal chamberlets (Plate II, Figures

1-3) *Arnaudiella* DOUVILLÉ was transferred to Pseudorbitoididae RUTTEN.

Sirtina BRÖNNIMANN and WIRZ, 1962

(Plate II, figures 4-8)

Description: The inflated small specimens have unequally biconvex rotaliids test with pointed peripheral margin (Plate II, Figure 5). The external surface is covered by small central pustules (Plate II, figure 4). The ventral side is more convex than the dorsal side. The umbilical cavity is filled by thin radial canals (funnels) occuring between the thickened pillars (Plate II, Figure 5, 8). The dorsal side is covered by the layers of lateral orbitoidal chamberlets with pillars as known from typical orbitoids (Plate II, Figures 5, 8). The chambers of the rotaloid test are coiled in asymmetric planispiral-evolute pattern during the early ontogeny, but become trochospiral in the adult stage (Plate II, Figure 5). Maastrichtian of Iran, Libya, Oman (Özcan et al., 2022) and Türkiye.

The foregoing description of *Sirtina* BRÖNNIMANN and WIRZ is based on the figures of Brönnimann and Wirz (1962) and van Gorsel (1978).

Remarks: The classification of *Sirtina* BRÖNNIMANN and WIRZ (1962) is originally uncertain. It has been interpreted as a rotaliid genus with orbitoidal characters by Brönnimann and Wirz (1962. p. 519) and van Gorsel (1978, p. 91). This genus has been placed in Lepidorbitoididae VAUGHAN by Loeblich and Tappan (1987, p. 649) and BouDagher-Fadel (2008, p. 256), despite the fact that it has a typical early rotaliid stage with trochospiral chambers (Plate II, Figures 5-8). Therefore, it has been included here within the family Pseudorbitoididae RUTTEN.

Vanderbeekia BRÖNNIMANN and WIRZ, 1962

(Plate II, Figure 9)

Description: The following description of *Vanderbeekia* BRÖNNIMANN and WIRZ is based on the non-centered section illustrated in Plate II, Figure 9 from Brönnimann and Wirz (1962, Figure 7).

According to the section (holotype of *Vanderbeekia trochoidea* BRÖNNIMANN and WIRZ, 1962), the ventral side has thick pillars with intercalated umbilical radial canals (funnels) as in typical rotaliid forms. On the contrary, the dorsal side is covered by the large arcuate lateral orbitoidal chamberlets with intercalated pillars. The large equatorial orbitoidal chamberlets with thick wall line up from the early rotaliid stage to the periphery (Plate II, Figure 9).

Remarks: The type description of the genus is based only on a non-centered incomplete axial section that is drawn by hand in Brönnimann and Wirz (1962, Figure 7), therefore, the position of the early chambers, septa and aperture are uncertain. *Vanderbeekia* (type species *Vanderbeekia trochoidea* BRÖNNIMANN and WIRZ, 1962, Figure 7) has been included in the Lepidorbitoididae VAUGHAN by Loeblich and Tappan (1987) and BouDagher-Fadel (2008). Due to the rotaliid early chambers with thick pillars and radial canals (funnels) in the umbilical region and equatorial orbitoidal chamberlets well as developed lateral orbitoidal chamberlets (Plate II, Figure 9), the genus *Vanderbeekia* has been placed here in the family Pseudorbitoididae RUTTEN.

Vanderbeekia trochoidea BRÖNNIMANN and WIRZ 1962 was described from a cutting sample from the Maastrichtian in Iran. So far we did not meet this form in Turkey, although the marine Maastrichtian sediments with *Sirtina* BRÖNNIMANN and WIRZ occur most widespread in the territory of Türkiye.

Helicorbitoides MacGILLAVRY, 1963

(Plate III, Figures 1-4)

Description: The test is inflated lenticular (Plate III, Figures 2, 3). An excellent equatorial section clearly shows that the spherical protoconch is followed by the subrectangular rotaliid small chambers arranged in one symmetric planispiral involute/evolute whorl (Plate III, Figures 1, 3), later equatorial chambers are entirely uncoiled and form a helicolepidine string towards the periphery (Plate III, Figures 1, 4) as in *Helicolepidina* TOBLER. The secondary arcuate small chambers occur between successive spiral whorls at the equatorial layer (Plate III, Figures 1, 4). The equatorial orbitoidal chamberlets occur particularly at the periphery (Plate III, Figure 1). The structural elements at the median plane are covered completely by the layer of the arcuate orbitoidal chamberlets with pillars (Plate III, Figures 2, 3). The pillars extend from early whorls to the periphery (Plate III, Figures 2, 3), the wall at the periphery has numerous pores (Plate III, Figure 4), dimorphism indistinct, Campanian; Sweden, Austria and Türkiye.

Remarks: *Helicorbitoides* MacGILLAVRY (type species *Helicorbitoides longispiralis* (PAPP and KÜPPER, 1953) and other species *Helicorbitoides boluensis* SİREL have previously been placed in the family Lepidorbitoididae VAUGHAN by Loeblich and Tappan (1987, p. 650), Sirel (1995, p. 86) and BouDagher-Fadel (2008, p. 256). Because of the well-developed planispiral-involute early stage with thick pillars, orbitoidal chamberlets in the equatorial layer and lateral orbitoidal chamberlets (Plate III, Figures 1-4), *Helicorbitoides* MacGILLAVRY was transferred from Lepidorbitoididae to Pseudorbitoididae RUTTEN (Plate III, Figures 2, 3).

Orbitokathina HOTTINGER, 1966

(Plate III, Figures 5-8)

Description: The microspheric generation has a convexo-concave lenticular test with rounded peripheral margin (Plate III, Figure 8). The very small trochospiral early chambers are lined up in the very narrow two-three whorls (Plate III, Figure 5). This early stage is followed by a stage with orbitoidal chamberlets in the equatorial layer of the late ontogeny, where they are arranged in irregular concentric rows (Plate III, Figure 5). The dorsal side is covered by thick hyaline calcareous walls, on the contrary the ventral side has thin vertical canals (funnels) that occur between the thick pillars (Plate III, Figure 8).

The megalospheric generation (Plate III, Figure 7) resembles the microspheric form by the rotaloid stage with trochospiral chambers, but it has not a late stage with orbitoidal chamberlets as in *Postorbitokathina* SİREL (2012, Plate V, Figure 6).

Remarks: The Santonian genus *Orbitokathina* HOTTINGER (type species: *Orbitokathina vonderschmitti* HOTTINGER, 1966) has not been placed in any family in the original description. The microspheric and megalospheric forms of *Orbitokathina* have been interpreted as rotaliid genus with orbitoidal character by Hottinger (1966, p. 290).

The genus has been placed in Rotaliidae by Loeblich and Tappan (1987, p. 662), although it has well developed equatorial orbitoidal chamberlets in the adult stage (Plate III, Figure 5). It was included here within the Pseudorbitoididae RUTTEN in the light of the distinct rotaliid and orbitidal stages.

Dizerina MERİÇ, 1978

(Plate III, Figures 9-11)

Description: The megalospheric form has an inflated discoidal to elongated ovoid test with broadly rounded peripheral margin (Plate III, Figure 10). The spherical megalosphere is followed by the spiral chambers of the early stage arranged in two whorls which tend to uncoil (Plate III, Figure 11). The shapeless rotaliid chambers have a septal flap (Meriç, 1978, Plates II, IV). The equatorial sections clearly show the orbitoidal chamberlets occuring at the equatorial layer particularly near the periphery (Plate III, Figures 9, 11). The very small lateral orbitoidal chamberlets and pillars are recognizable in the well preserved axial sections (Plate III, Figure 10). Dimorphism indistinct, Maastrichtian of Türkiye.

Remarks: The Maastrichtian genus *Dizerina* MERİÇ has been placed originally in Lepidorbitoididae VAUGHAN by Meriç (1978, p. 97) and Loeblich and Tappan (1987, p. 650), in spite of the fact that it has developed rotaliid chambers of the early stage (Plate III, Figures 9-11). It has been placed here in Pseudorbitoididae RUTTEN because of the rotaliid, orbitoidal growth stages in the equatorial layer (Plate III, Figures 9, 11) and orbitoidal chamberlets in the lateral layers (Plate III, Figure 10).

Cideina SİREL, 1991

(Plate IV, Figures 1-4)

Description: The specimens have medium size, discoidal to low conical test with rounded peripheral margin (Plate IV, Figures 1, 2). The external surface of the test is ornamented with irregular reticular network and numerous pores (Sirel 1991, Plate I, Figure 12). Very small, spheric protoconch is followed by trochospiral early chambers in two-three whorls (Plate IV, Figures 1-4). Later adult spiral shapeless chambers with septal flap increase suddenly towards the periphery (Plate IV, Figures 3, 4). The coarsely perforated thick wall of the last chambers contains large vacuoles and marginal sutural canals (Plate IV, Figure 4). The dorsal side is covered by a few rows of arcuate orbitoidal chamberlets (Plate IV, Figures 1, 2). Thick pillars and radial canals (funnels) occur in the ventral region (Plate IV, Figures 1, 2). Dimorphism indistinct, late Maastrichtian in the Black Sea region, Türkiye.

Remarks: In the original description, *Cideina* has been placed in Lepidorbitoididae VAUGHAN by Sirel (1991), in spite of the fact that it has rotaliid early chambers with pillars and radial canals (Plate IV, Figures 1, 2). However, because of the existence of the common rotaliid and orbitoidal characters, a new family was proposed for *Cideina* SİREL, *Sirtina* BRÖNNIMANN and WIRZ and *Orbitokathina* HOTTINGER by Sirel (1991, p. 69). Therefore, the aforementioned genera which have two common growth stages were transferred to Pseudorbitoididae RUTTEN.

Sirelella ÖZGEN-ERDEM, 2002

(Plate IV, Figures 5-7)

Description: The diagnostic characters of the genus are interpreted from the megalospheric generation. The generation has low conical test with rounded peripheral margin (Plate IV, Figures 5, 6). The juvenile stage of the test is composed of an embryo (protoconch and second chamber) and large trochospiral chambers of the juvenile stages (Plate IV, Figure 6). The nepionic stage has large orbitoidal chamberlets in the equatorial layer (Plate IV, Figures 6, 7). The umbilical area is pierced by thick pillars and radial canals (funnels) that occur indistinctly among the pillars, Lutetian, Safranbolu town, N Türkiye.

Remarks: *Sirelella* ÖZGEN-ERDEM was not placed in any family in the original description by Özgen-Erdem (2002), However, she has proposed to introduce a new family for the genus, *Cideina* SİREL, *Sirtina* BRÖNNIMANN and WIRZ and *Orbitokathina* HOTTINGER as in Sirel (1991, p. 69). Recently, this middle Eocene genus was placed within the family Lepidorbitoididae VAUGHAN by BouDagher-Fadel (2008, p. 361). However, it differs from the representatives of Lepidorbitoididae VAUGHAN in possessing well developed trochospiral chambers of the early stage (Plate IV, Figures 5, 7). Therefore, it was included here within Pseudorbitoididae RUTTEN.

Postorbitokathina SİREL, 2012

(Plate IV, Figures 8-11)

Description: The microspheric test is discoidal, concave-convex or near the margin it curves up to meet the spiral side (Sirel, 2012, Plate V). The wall of the test is perforated, hyaline calcareous. The test of the genus is composed of rotaliid early and orbitoidal adult stages (Plate IV, Figures 8-11). The spherical, small microsphere is followed by subrectangular trochospiral chambers of the early stage arranged in the multiple spirals; duplication of spirals starts in the early ontogeny (Plate IV, Figures 9, 11). The septa with intraseptal canals of the trochospiral early chambers are very thin, they become bifurcate when they reach the latter whorl, producing the small intraseptal interlocular space (Plate IV, Figure 9). The numerous thick umbilical canals (funnels) occur among the thick pillars of the early rotaliid stage (Plate IV, Figure 8). The numerous orbitoidal chamberlets in the equatorial layer of the adult stage vary in shape and size and are arranged irregularly (Plate IV, Figures 9-11). The connection of the adjacent orbitoidal chamberlets is through basal stolons. Dimorphism distinct, occurs in the early Thanetian (*Glomalveolina primaeva* Reichel-*Vania anatolica* Sirel and Gündüz assemblage zone), Türkiye.

Remarks: The type species *Orbitokathina sarayi* SİREL, GÜNDÜZ and ACAR has not been placed any family of Foraminiferida EICHWALD in the original description, however it was hinted to belong to the family Rotaliidae (Sirel et al. 1983, p. 150) by trochospirally coiled early stage (Plate IV, Figure 8). Later on the new genus *Postorbitokathina* SİREL (type species *Orbitokathina sarayi* SİREL, GÜNDÜZ and ACAR) has been placed in the Rotaliidae EHRENBERG because of the rotaliid early stage by Sirel (2012, p. 277). However well preserved equatorial and superficial sections (Plate IV, Figures 9-11) clearly show numerous orbitoidal chamberlets to occur around the rotaliid stage, this structural characteristic does not correspond with the representatives of Rotaliidae EHRENBERG. For this reason, *Postorbitokathina* SİREL was included here within the Pseudorbitoididae RUTTEN in the light of the distinct rotaliid and orbitidal stages.

2.2. American and Caribbean Forms

The following genera occurring in the American and Caribbean provinces have been interpreted to belong in the family Pseudorbitoididae Rutten by means of the original figures of the authors.

Helicolepidina TOBLER, 1922

(Plate V, Figures 1-4)

Type species Lepidocyclina (*Helicolepidina*) *spiralis* TOBLER, 1922;

nomen translatum GALLOWAY, 1928 (=name transferred to a different rank)

Description: The microspheric generation has a very small microsphere with very small planispiral-trochospiral chambers arranged in two whorls, but helicolepidine string is unclear. The very small arcuate orbitoidal chamberlets in the equatorial layer are lined up irregularly from the early planispiral-trochospiral chambers to the periphery (Plate V, Figure 3).

The megalospheric generation has a small inflated lenticular test with rounded peripheral margin (Plate V, Figures 2, 4). The spheric megalosphere is followed by few rotaliid chambers that uncoil as from the first whorl and they become a helicolepidine string towards the periphery (Plate V, Figure 1). The very small shapeless equatorial orbitoidal chamberlets line up irregularly (Plate V, Figure 1). The early rotaliid and orbitoidal chambers in the median plane are completely covered by the lateral orbitoidal chamberlets on both sides of the test; rather thick pillars occur between lateral orbitoidal chamberlets (Plate V, Figures 2, 4). Dimorphism distinct, middle-late Eocene of North and South America.

Remarks: *Helicolepidina* TOBLER has previously been placed in the family Lepidocyclinidae SCHEFFEN by Loeblich and Tappan (1987, p. 611) and BouDagher-Fadel (2008, p. 356), whereas it differs from the representatives of Lepidocyclinidae SCHEFFEN in having early planispiral/trochospiral rotaliid and helicolepidine string adult chambers (Plate V, Figure 1). Therefore, *Helicolepidina* TOBLER was transferred from the family Lepidocyclinidae to Pseudorbitoididae RUTTEN.

Orbitocyclina VAUGHAN, 1929

(Plate V, Figures 5-6)

Description: The macrospheric generation has an inflated lenticular test with pointed peripheral margin and the surface of the test covered by numerous small pustules (Galloway 1928). Unclear early spiral rotaliid chambers followed by very small arcuate equatorial orbitoidal chamberlets arranged irregularly. Aforementioned early and adult chambers in Galloway (1928) are covered definitely by lateral orbitoidal chamberlets and pillars.

The megalospheric generation has an inflated lenticular test with pointed peripheral margin (Plate V, Figure 6). The small, spheric megalosphere and second chamber followed by small spiral rotaliid chambers of the early stage (Plate V, Figure 6), then the equatorial arcuate orbitoidal chamberlets are arranged irregularly (Plate V, figure 5). The rotaliid spiral chambers and arcuate orbitoidal chamberlets are completely covered by the lateral orbitoidal chamberlets with pillars (Plate V, Figure 6). Dimorphism distinct, Campanian-Maastrichtian of the American province.

Remarks: *Orbitocyclina* VAUGHAN, 1929 has previously been placed already in the family. Pseudorbitoididae RUTTEN because of the rotaliid and orbitoidal stages (Plate V, Figures 5, 6) by Loeblich and Tappan (1987, p. 656) and BouDagher-Fadel (2008, p. 260).

Eulinderina BARKER and GRIMSDALE, 1936

(Plate V, Figures 7-10)

Description: The microspheric generation has a lenticular to discoidal test with thick perforated outer wall (Plate V, Figure 9). Very small microsphere followed by small spiral chambers of the rotaliid early stage arranged in two whorls or maybe more later numerous small, shapeless orbitoidal chamberlets lined up irregularly (Plate V, Figure 8). Because of the thick outer wall, the lateral orbitoidal chamberlets are indistinct (Plate V, Figure 9).

The megalospheric generation has a small, inflated lenticular test with slightly rounded peripheral margin (Plate V, Figure 10). The large, spheric megalosphere followed by large rotaliid spiral chambers of the early stage that are arranged in one and half whorls (Plate V, Figure 7), later small median arcuate orbitoidal chamberlets line up regularly in concentric rows (Plate V, Figure 7). The equatorial orbitoidal chamberlets are completely covered by lateral orbitoidal chamberlets with pillars on both sides of the test (Plate V, Figure 10). Dimorphism distinct, middle-late Eocene of Mexico.

Remarks: *Eulinderina* has been placed originally in the family Orbitoididae SCHUBERT by Barker and Grimsdale (1936, p. 237), but *Eulinderina* differs from the representatives of Orbitoididae SCHUBERT in its spiral chambers in the early stage (Plate V, Figures 7, 8). Later *Eulinderina* BARKER and GRIMSDALE was included within the family Lepidocyclinidae SCHEFFEN by Loeblich and Tappan (1987, p. 611) and

BouDagher-Fadel (2008, p. 356). Also, *Eulinderina* differs from the representatives (particularly the type genus *Lepidocyclina* GÜMBEL) of Lepidocyclinidae in possessing early rotaliid chambers (Plate V, Figures 7, 8). The rotaliid early equatorial orbitoidal adult chambers and lateral orbitoidal chamberlets of *Eulinderina* are similar to the structural elements of the type genus *Pseudorbitoides* DOUVILLÉ of Pseudorbitoididae RUTTEN (Plate V, Figures 7, 10), therefore *Eulinderina* BARKER and GRIMSDALE, 1936 was transferred here to Pseudorbitoididae.

Helicostegina BARKER and GRIMSDALE, 1936

(Plate VI, Figures 1-3)

Description: Megalospheric *Helicostegina* has an inflated lenticular test with rounded peripheral margin (Plate VI, Figure 3). It has characteristic retrorse septa on the chamber floor (Plate VI, Figure 1). The external surface of the test is ornamented by coarse granules (Barker and Grimsdale, 1936). The equatorial section clearly shows that the test developed as large trochospiral early and orbitoidal equatorial adult chambers/chamberlets (Plate VI, Figures 1, 2). The large, spheric megalosphere is followed by large arcuate trochospiral chambers arranged in one and a half whorl (Plate VI, Figures 1, 2). Later shapeless orbitoidal equatorial chamberlets line up at around the periphery and few very small underdeveloped secondary median chamberlets occur among the successive spiral chambers (Plate VI, Figures 1, 2) according to Barker and Grimsdale (1936). The growth stages are covered by the lateral orbitoidal chamberlets (Plate VI, Figure 3), dimorphism unknown. Middle-late Eocene of Cuba, Trinidad and Mexico.

Remarks: *Helicostegina* BARKER and GRIMSDALE has previously been placed originally in the family Asterigerinidae D'ORBIGNY, but *Helicostegina* BARKER and GRIMSDALE differs from the representatives Asterigerinidae in possessing main orbitoidal equatorial chambers and lateral orbitoidal chamberlets and in lacking stellar chamberlets (Plate VI, Figures 1-3; Barker and Grimsdale, 1936, Plates 32, 34). Later it has been included in Lepidocyclinidae SCHEFFEN by Loeblich and Tappan (1987, p. 611) and BouDagher-Fadel (2008, p. 356), but it differs from the representatives (particularly the type genus *Lepidocyclina* GÜMBEL) of Lepidocyclinidae SCHEFFEN in having large trochospiral early chambers and smaller secondary equatorial chambers/chamberlets (Plate VI, Figures 1, 2). Therefore, it was transferred here to Pseudorbitoididae RUTTEN.

Sulcorbitoides BRÖNNIMANN, 1954

(Plate VI, Figures 4-7)

Description: Very inflated lenticular test has two growth stages (Plate VI, Figures 4-6), the trochospiral chambers of the early stage which follow the small protoconch increase towards the periphery (Plate VI, Figure 6). The shapeless equatorial orbitoidal chamberlets arranged irregularly around the trochospiral chambers (Plate VI, Figure 6); trochospiral early chambers and shapeless equatorial orbitoidal chamberlets are covered entirely by the 4-7 layers of the lateral orbitoidal chamberlets with pillars (Plate VI, figures 4, 5, 7). Campanian of the American province.

Remarks: The trochospiral early (Plate VI, Figure 5) and adult equatorial orbitoidal chambers (Plate VI, figure 6), as well the lateral orbitoidal chamberlets (Plate VI, Figures 5, 6) of *Sulcorbitoides* BRÖNNIMANN 1954 are virtually identical with that of the structural elements of the type genus *Pseudorbitoides* DOUVILLÉ of Pseudorbitoididae RUTTEN. Already, it has been placed in Pseudorbitoididae RUTTEN by Loeblich and Tappan (1987, p. 654) and BouDagher-Fadel (2008, p. 259).

Helicosteginopsis CAUDRI, 1975

(Plate VI, Figures 8-11)

Description: The megalospheric generation has inflated lenticular test with thick wall (Plate VI, Figure 10). The globular megalosphere is followed by characteristic numerous main rotaliid spiral chambers which are arranged in 2-3 involute whorls (Plate VI, Figures 8-11). The smaller secondary orbitoidal chambers occur among the rotaliid spiral chambers as in *Helicorbitoides* MacGILLAVRY, the equatorial orbitoidal chambers occur at the periphery and are small when compared with the rotaliid chambers (Plate VI, Figures 8, 9, 11). A central knob and weakly developed lateral orbitoidal chamberlets are present (Plate VI, Figure 10), dimorphism unknown, late Eocene of Trinidad.

Remarks: *Helicosteginopsis* CAUDRI 1975 has rotaliid early, main and secondary orbitoidal

median chambers/chamberlets and orbitoidal lateral chamberlets in common with *Helicostegina* BARKER and GRIMSDALE. It has previously been placed in the family Lepidocyclinidae SCHEFFEN by Loeblich and Tappan (1987, p.611) and BouDagher-Fadel (2008, p.357), It differs from the representatives (particularly the type genus *Lepidocyclina* GÜMBEL) of Lepidocyclinidae SCHEFFEN in possessing planispiral early chambers in four whorls (Plate VI, Figure 10) and the smaller secondary chamberlets among the spiral chambers (Plate VI, Figures 8, 9, 11). Thus, it was included with the family Pseudorbitoididae RUTTEN as *Helicostegina* BARKER and GRIMSDALE.

3. Conclusion

The main objective of this study is finding a suitable foraminiferal family for *Helicorbitoides* MacGILLAVRY species (*Helicorbitoides boluensis* SİREL), *Postorbitokathina* SİREL (type *Orbitokathina sarayi* SİREL, GÜNDÜZ and ACAR), *Dizerina* MERİÇ (type *Dizerina anatolica* MERİÇ), *Cideina* SİREL (type *Cuvillierina soezerii* SİREL), *Sirelella* ÖZGEN-ERDEM (type *Sirelella safranboluensis* ÖZGEN-ERDEM) which occur in Türkiye.

The here described and figured nine known genera from Tethyan and four genera from American and Caribbean provinces have been placed previously in different families in Loeblich and Tappan (1987. p. 654) and BouDagher-Fadel (2008, p. 259). Namely, *Arnaudiella* DOUVILLÉ, *Sirtina* BRÖNNIMANN and WIRZ, *Vanderbeekia* BRÖNNIMANN and WIRZ, *Helicorbitoides* MACGILLAVRY, *Dizerina* MERİÇ, *Sirelella* ÖZGEN-ERDEM and *Cideina* SİREL were included in the Lepidorbitoitidae VAUGHAN; *Postorbitokathina* SİREL and *Orbitokathina* HOTTINGER in Rotaliidae EHRENBERG, *Helicolepidina* TOBLER, *Helicosteginopsis* CAUDRI, *Eulinderina* BARKER and GRIMSDALE and *Helicostegina* BARKER and GRIMSDALE in Lepidocyclinidae SCHEFFEN, although all of them in Plates II-VI have characteristic both rotaliid early and orbitoidal adult stages. Owing to the structural elements such as rotaliid early and orbitoidal adult chamberlets, the known family Pseudorbitoididae RUTTEN (type genus *Pseudorbitoides* DOUVILLÉ, Plate I) is identified as the suitable family for the aforementioned genera. Thus the herein described and figured sixteen Tethyan, American and Caribbean genera have been included within Pseudorbitoididae RUTTEN.

Acknowledgements

The authors would like to thank Prof. Dr. Johannes Pignatti for his careful evaluation and valuable suggestions.

References

Barker, R. W. 1934. Some notes on the genus *Helicolepidina* Tobler. Journal of Paleontology 8, 344-351.

Barker, R. W., Grimsdale, T. F. 1936. A contribution to the phylogeny of the orbitoidal foraminifera with descriptions of new forms from the Eocene of Mexico. Journal of Paleontology 10, 231-247.

BouDagher-Fadel, M. K. 2008. Evolution and Geological Significance of Larger Benthic Foraminifera. Developments in Paleontology and Stratigraphy 21.

Brönnimann, P. 1954. Upper Cretaceous orbitoidal foraminifera from Cuba Part 1, *Sulcorbitoides* n.gen. Contributions from the Cushman Foundation for Foraminiferal Research 5, 91-105.

Brönnimann, P. 1955. Upper Cretaceous orbitoidal Foraminifera from Cuba. Part III, *Pseudorbitoides* H. Douvillé, 1922. Cushman Foundation for Foraminiferal Research 6, 57-76.

Brönnimann, P. 1958. New *Pseudorbitoididae* from the Upper Cretaceous of Cuba, with remarks on encrusting foraminifera. Micropaleontology 4, 165-185.

Brönnimann, P., Wirz, A. 1962. New Maastrichtian Rotaliids from Iran and Libya. Eclogae Geologicae Helvetiae 55, 519-528.

Caudri, C. M. B. 1975. Geology and paleontology of Soldado Rock. Trinidad (West Indies), part 2, The larger foraminifera. Eclogae Geologicae Helvetiae 68, 533-689.

Douvillé, H. 1907. Evolution et enchainements des foraminifères. Bulletin de la Société Géologique de France 4 (6), 588-602.

Douvillé, H. 1922. *Orbitoides* de la Jamaique *Pseudorbitoides trechmanni* nov.gen. n. sp., Compte Rendu des Séances. Société Géologique de France 1922, 203-204.

Drooger, C.W. 1993. Radial foraminifera: Morphometrics and evolution. Verhandelingen der Koninklijke Nederlandse Akademie van Wetenschappen, Afd. Natuurkunde, Eerste Reeks 41, 1-242.

Galloway, J. J. 1928. Notes on the genus *Polylepidina* and new species. Journal of Paleontology 1, 299-303.

Grimsdale, T. E. 1941. New species of *Helicolepidina* from Soldado Rock. In: Preliminary Report on the Cretaceous and Tertiary Larger Foraminifera of Trinidad, British West Indies (Eds. Vaughan, T. W. and Cole, W.S.). Special Papers of the Geological Society of America 30, 86-87.

Hottinger, L. 1966. Foraminifères rotaliformes et Orbitoïdes du Sénonien inférieur Pyrénéen. Eclogae Geologicae Helvetiae 59, 277-301.

Hottinger, L., Caus, E. 2007. Shell architecture in the late Cretaceous foraminiferal subfamily Clypeorbinae Sigal, 1952. Journal of Foraminiferal Research 37 (4), 372-392.

Krijnen, J. P. 1972. Morphology and phylogeny of pseudorbitoid foraminifera from Jamaica and Curaçao a revisional study. Scripta Geologica 8, 1-133.

Krijnen, J. P. 1993. A new genus and lineage of pseudorbitoid foraminifera in Jamaica. The Journal of the Geological Society of Jamaica 29, 41-48

Loeblich, A., Tappan, H. 1987. Foraminiferal genera and their classification, von Nostrand Reinhold, NewYork 970.

MacGillavry, H. J. 1963. Phylomorphogenesis and evolutionary trends of Cretaceous orbitoidal foraminifera, In Koenigswald, G. H. R. von, Emeis, J. D.,.Buning, W. L., Wagner, C. W. 1963. Evolutionary Trends in Foraminifera, Elsevier 160, 139-196.

Meriç, E. 1978. *Dizerina* a new genus from the upper Maastrichtian of northeastern Turkey. Micropaleontology 24 (1), 97-108.

Mitchell, S. F., Robinson, E., Özcan, E., Jiang, M. M., Robinson, N. 2022. A larger benthic foraminiferal zonation for the Eocene of the Caribbean and central American region. Carnets de Géologie 11, 409-563.

Nuttall, W. L. E. 1930. Eocene foraminifera from Mexico. Journal of Paleontology 4, 271-293.

Özcan, E., Abbasi, A. İ., Yücel, A.O., Aşçı, S. Y., Erkıza, L. S., El-Ghali, M. A. K., Çalışkan, D., Gültekin, M. N., Kayğılı, S. 2022. First record of the foraminiferal genera *Clypeorbis* Douvillé and *Ilgazina* Erdoğan from the Maastrichtian of the Arabian Peninsula (Simsima Formation, North of Oman): Paleobiogeographic implications. Cretaceous Research 138 (2022), 1-19.

Özgen-Erdem, N. 2002. *Sirelella safranboluensis* n. gen.n.sp., a foraminifer from the Lutetian of the Safranbolu Area (Northern Turkey). Micropaleontology 48 (1), 79-86.

Palmer, D. K. 1934. Some large fossil foraminifera from Cuba. Memorias de la Sociedad Cubana de Historia Natural 8, 235-264.

Papp, A., Küpper, K. 1953. Die Foraminiferenfauna von Guttaring und Klein St. Paul (Kärnten) III. Foraminiferen aus dem Campan von Silberegg. Sitzungsberichte der Österreichischen Akademie der Wissenschaften, Wien. Mathematisch-Naturwissenschaftliche Klasse 162, 345-357.

Rutten, M. G., 1935. Larger foraminifera of northern Santa Clara Province, Cuba. Journal of Paleontology 9, 527-545.

Sirel, E. 1991. *Cideina* a new Foraminiferal genus from the Maastrichtian limestone of the Cide Region (north Turkey). Bulletin of the Mineral Research and Exploration 112, 65-70.

Sirel, E. 1995. Occurrence of the genus *Helicorbitoides* MacGillavry (Foraminiferida) in Turkey. Revue de Paléobiologie 14 (2), 85-94.

Sirel, E. 2012. Seven new larger benthic foraminiferal genera from the Paleocene of Turkey. Revue de Paléobiologie 31 (2), 267-301.

Sirel, E., Gündüz, H., Acar, Ş. 1983. Sur la présence d'une nouvelle espéce d'*Orbitokathina* HOTTINGER dans le Thanétien de Van (Est de la Turquie). Revue de Paléobiologie 2 (2), 149-159.

Tobler, A. 1922. *Helicolepidina* ein neues Subgenus von *Lepidocyclina*. Eclogae Geologicae Helvetiae 20, 323-330.

Van Gorsel, J. T., 1972. *Orbitocyclina minima* (H. Douvillé) at its type locality, with remarks about its origin, evolution and systematic place. Proceedings of the Koninklijke Nederlandse Academic van Wetenschappen ser.B 77, 339-346.

Van Gorsel, J. T., 1974. Some complex Upper Cretaceous rotaliid foraminifera from the northern border of the Aquitaine Basin (SW France). Proceedings of the Koninklijke Nederlandse Academie van Wetenschappen, ser. B 77, 319-339.

Van Gorsel, J. T., 1975. Evulitionary trends and stratigraphic significance of the late Cretaceous *Helicorbitoides-lepidorbitoides* lineage. Utrecht Micropaleontology Bulletins 12, 1-99.

Van Gorsel, J. T., 1978. Late Cretaceous orbitoidal foraminifera, in R. H. Hedley and C. G. Adams ed. Foraminifera. London Academic Press 3, 31-120.

Vaughan, T. W. 1929. Studies of orbitoidal foraminifera: the subgenus *Polylepidina* of *Lepidocyclina* and *Orbitocyclina*, a new genus. Proceedings of National Academy of Sciences 15, 288-295.

Vaughan, T. W. 1936. *Helicolepidina nortoni* a new species of foraminifera from a deep well in St. Landry Parish, Louisiana. Journal of Paleontology 17, 97-100.

Vaughan, T. W., Cole, W. S. 1943. A restudy of the foraminiferal genera *Pseudorbitides* and *Vaughanina*. Journal of Paleontology 10, 248-252.

PLATES

PLATE I

Abbreviation for Figure 2-7: Equatorial orbitoidal chambers (eoc), Rotaliid early chambers (rch), Protoconch (pr), Pustules (pu), Lateral orbitoidal chamberlets (loc), Rotaliid stage (rs), Secondary equatorial chambers (sec), Pillar (pi), funnel (umbilical radial canals) (f), Vacuoles (vu), Radial canals and rods (rcr), septal flap (sf), retrorse septa (ret). Following figures show the structural elements of ***Pseudorbitoides*** DOUVILLÉ (type species ***Pseudorbitoides trechmanni*** DOUVILLÉ, 1922).

Figure 1: Axial section,

Figure 2: Incomplete median section, B form,

Figure 3: Incomplete median section B form,

Figure 4: Centered median section, A form,

Figure 5: Axial section,

Figures 6, 7: External views (topotypes),

Figure 8: Incomplete axial section,

Figure 9: Incomplete equatorial section, B form. The figures were compiled from the following authors: (Figure 2A, B) from Brönnimann (1955), (Figure 2C, F, G) from Vaughan and Cole (1943) and (Figure 2D, E, H, I) from Krijnen (1972).

PLATE I

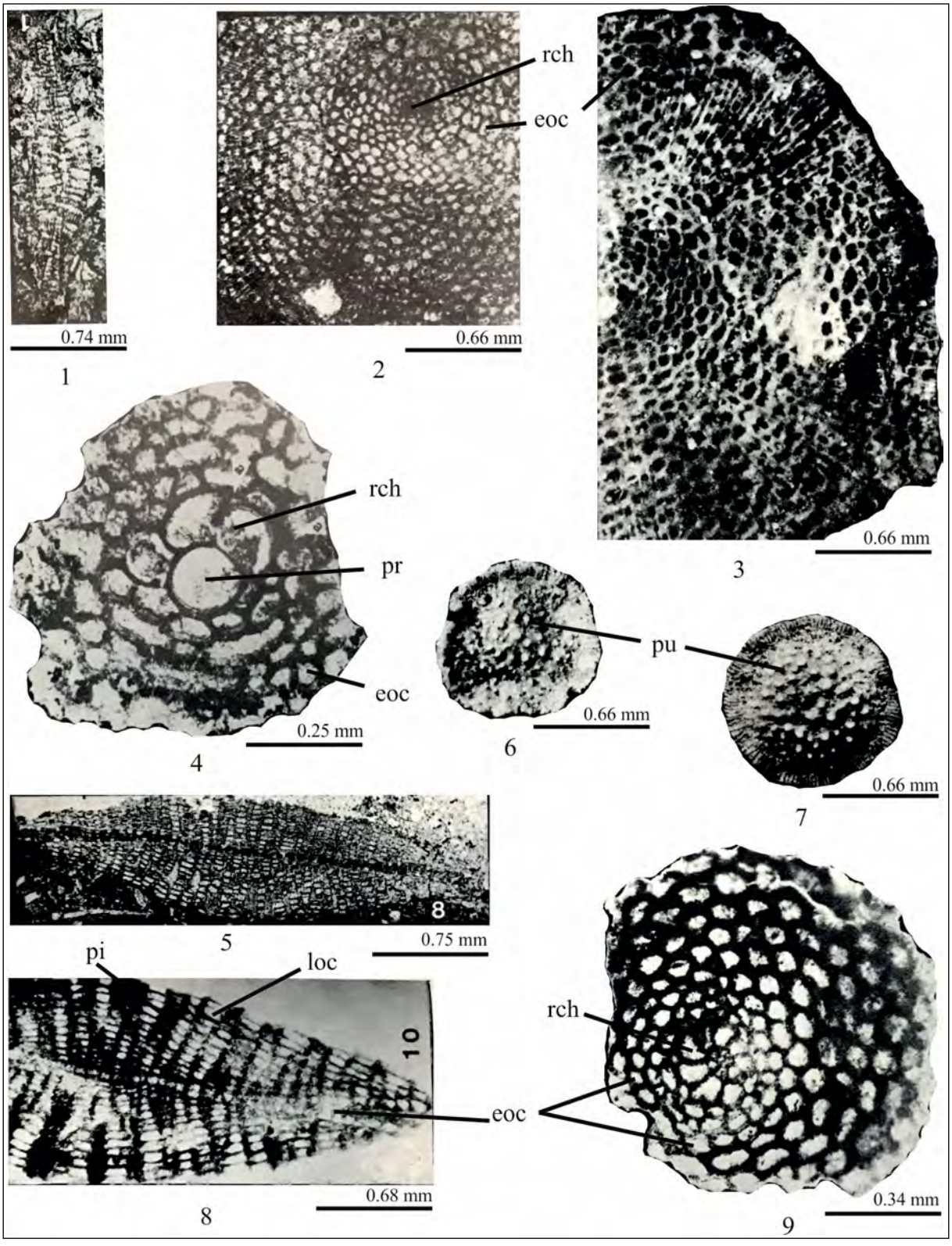
0.74 mm
1
rch
eoc
0.66 mm
2
0.66 mm
3
rch
pr
eoc
0.25 mm
4
pu
0.66 mm
6
0.66 mm
7
8
0.75 mm
5
pi
loc
10
eoc
0.68 mm
8
rch
0.34 mm
9

PLATE II

Arnaudiella DOUVILLÉ, 1907 (type species ***Arnaudiella grossouvrei*** DOUVILLÉ, 1907),

Figure 1: Almost equatorial section,

Figure 2: Equatorial section, A form,

Figure 3: Axial section, all figures from van Gorsel (1974, 1978); ***Sirtina*** BRÖNNIMANN and WIRZ, 1962 (type species ***Sirtina orbitoidiformis*** BRÖNNIMANN and WIRZ, 1962),

Figure 4: External view,

Figure 5: Axial section, A form,

Figure 6: Equatorial section, B form, all figures from Brönnimann and Wirz, (1962 Figure 2a, Figure 5); ***Sirtina granulata*** (RAHAGHI),

Figure 7: External view,

Figure 8: Axial section, B form, all figures from Van Gorsel, (1974 and 1978, Figure 27 b, c, f); ***Vanderbeekia*** BRÖNNIMANN and WIRZ 1962 (type species ***Vanderbeekia trochoidea*** BRÖNNIMANN and WIRZ 1962),

Figure 9**:** Subaxial section, from Brönnimann and Wirz (1962, Figure 7).

PLATE II

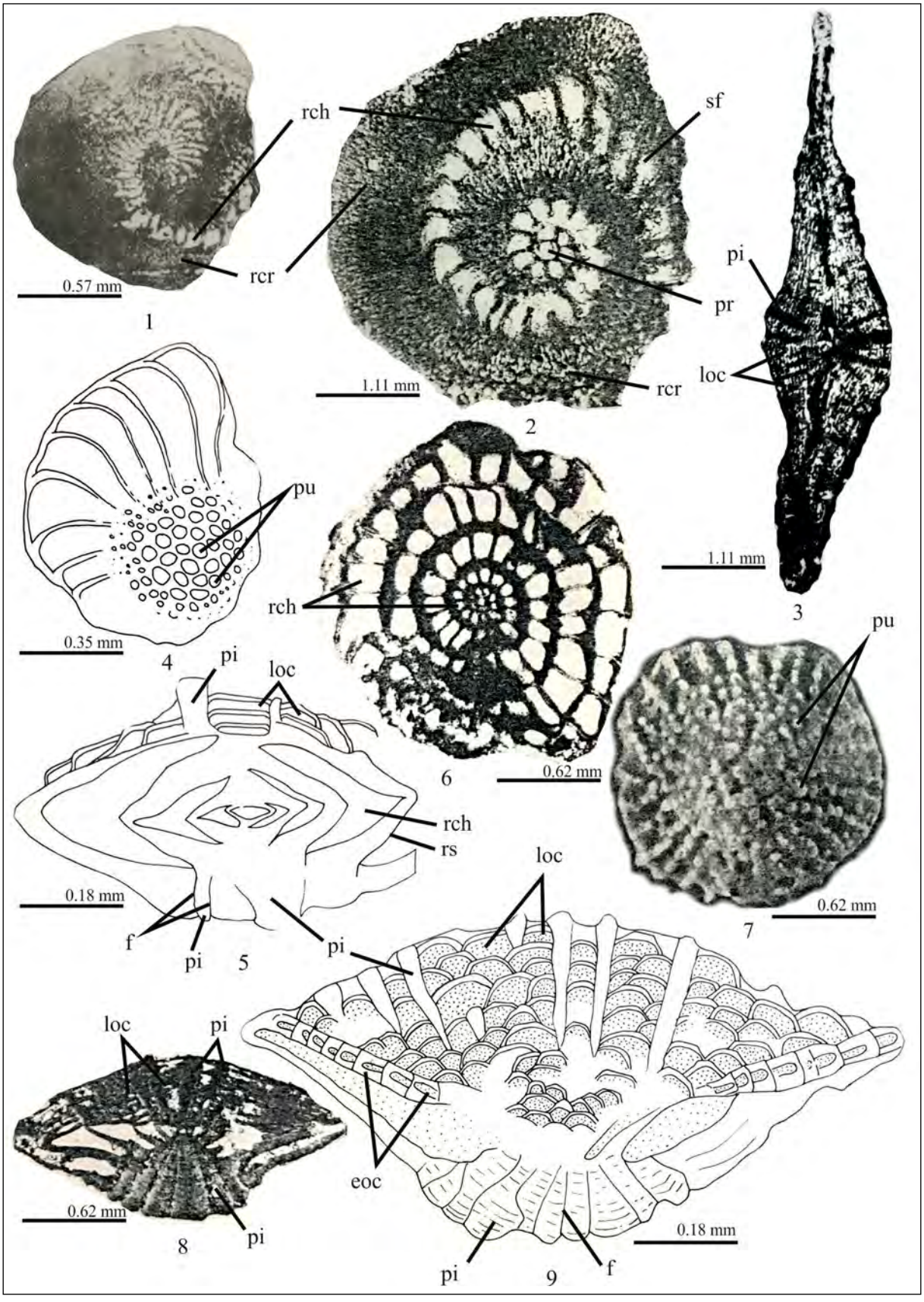
rch
rcr
0.57 mm
1
sf
pr
rcr
1.11 mm
2
pi
loc
1.11 mm
3
pu
0.35 mm
4
rch
6
0.62 mm
pi
loc
rch
rs
0.18 mm
f
pi
5
pu
0.62 mm
7
loc
pi
0.62 mm
8
pi
eoc
pi
f
0.18 mm
9

PLATE III

Helicorbitoides MacGILLAVRY, 1963 (type species ***Pseudorbitoides longispiralis*** PAPP and KÜPPER, 1953),

Figure 1: Equatorial section, A form,

Figure 2: Axial section, all from van Gorsel (1975); ***Helicorbitoides boluensis*** SİREL, 1995,

Figure 3: Axial section,

Figure 4: Equatorial section, A form, all figures from Sirel (1995); ***Orbitokathina*** HOTTINGER, 1966 (type species ***Orbitokathina vonderschmitti*** HOTTINGER, 1966),

Figure 5: Incomplete equatorial section, B form,

Figure 6: Superficial tangential section,

Figure 7: Incomplete subaxial section, A form,

Figure 8: Axial section, B form; all figures from Hottinger (1966); ***Dizerina*** MERİÇ, 1978 (type species ***Dizerina anatolica*** MERİÇ, 1978),

Figure 9: Equatorial section, A form,

Figure 10: Almost axial section,

Figure 11: Equatorial section, A form; all figures from Meriç (1978).

PLATE III

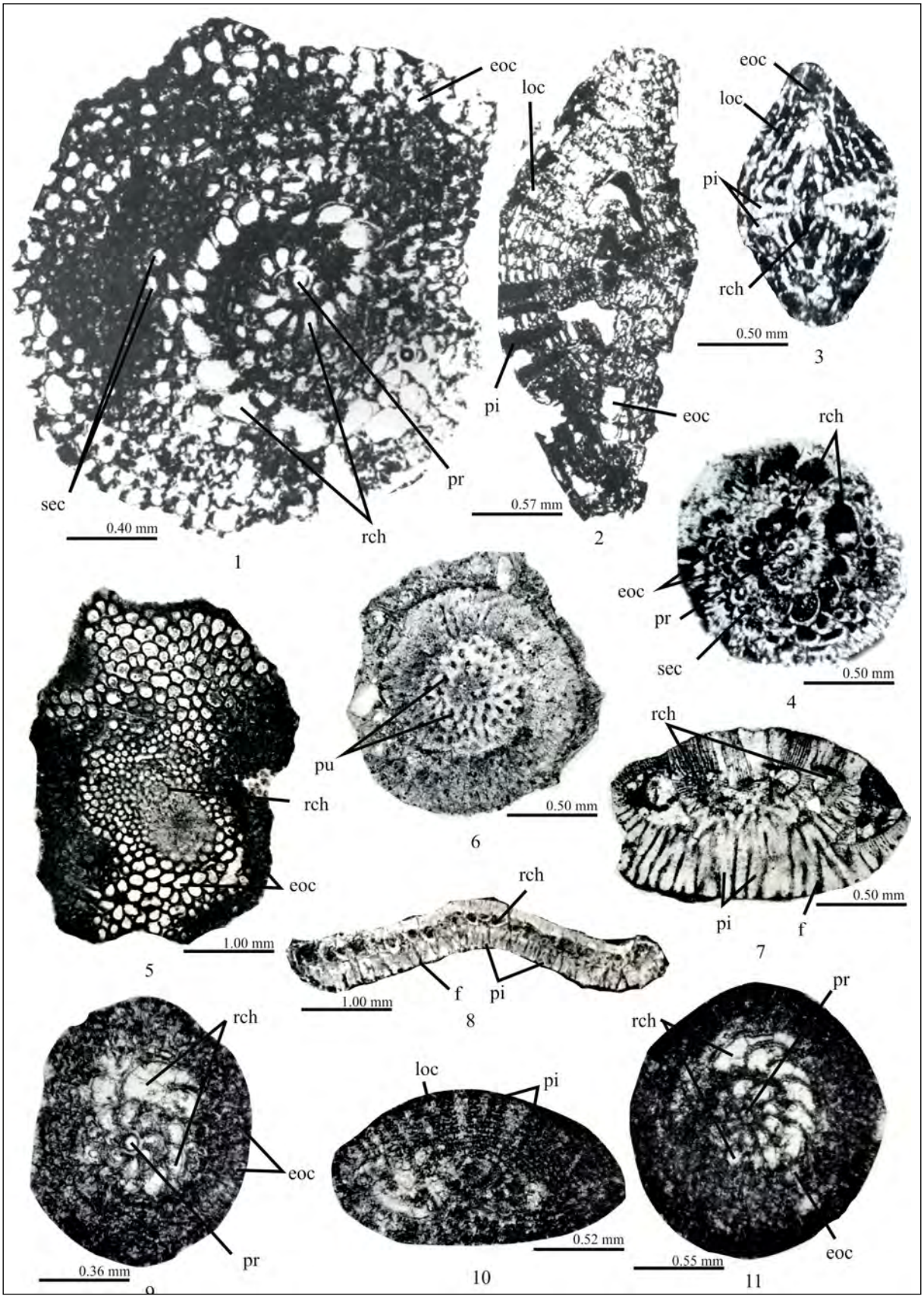
eoc
loc
pi
rch
0.50 mm
3
pi
eoc
0.57 mm
2
sec
pr
rch
0.40 mm
1
rch
eoc
pr
sec
0.50 mm
4
pu
0.50 mm
6
rch
eoc
1.00 mm
5
rch
0.50 mm
pi
f
7
rch
f
pi
1.00 mm
8
rch
eoc
pr
0.36 mm
9
loc
pi
0.52 mm
10
pr
rch
eoc
0.55 mm
11

PLATE IV

Cideina SİREL, 1991 (type species ***Cuvillierina sözerii*** SİREL, 1973),

Figure 1: Axial section (holotype), B form,

Figure 2: Incomplete axial section,

Figure 3: Equatorial section A form,

Figure 4: Equatorial section, A form; all figures from Sirel (1991); ***Sirelella*** ÖZGEN-ERDEM, 2002 (type species ***Sirelella safranboluensis*** ÖZGEN-ERDEM, 2002),

Figure 5: Axial section, A form,

Figure 6: Axial section, A form,

Figure 7: Incomplete equatorial section, A form; all figures from Özgen-Erdem (2002); ***Postorbitokathina*** SİREL, 2012 (type species ***Orbitokathina sarayi*** SİREL, GÜNDÜZ and ACAR, 1983),

Figure 8: Axial section, B form,

Figure 9: Incomplete equatorial section, B form,

Figure 10: Incomplete superficial view dorsally, B form,

Figure 11: Incomplete equatorial section, B form; all figures from Sirel et al. (1983) and Sirel (2012).

PLATE IV

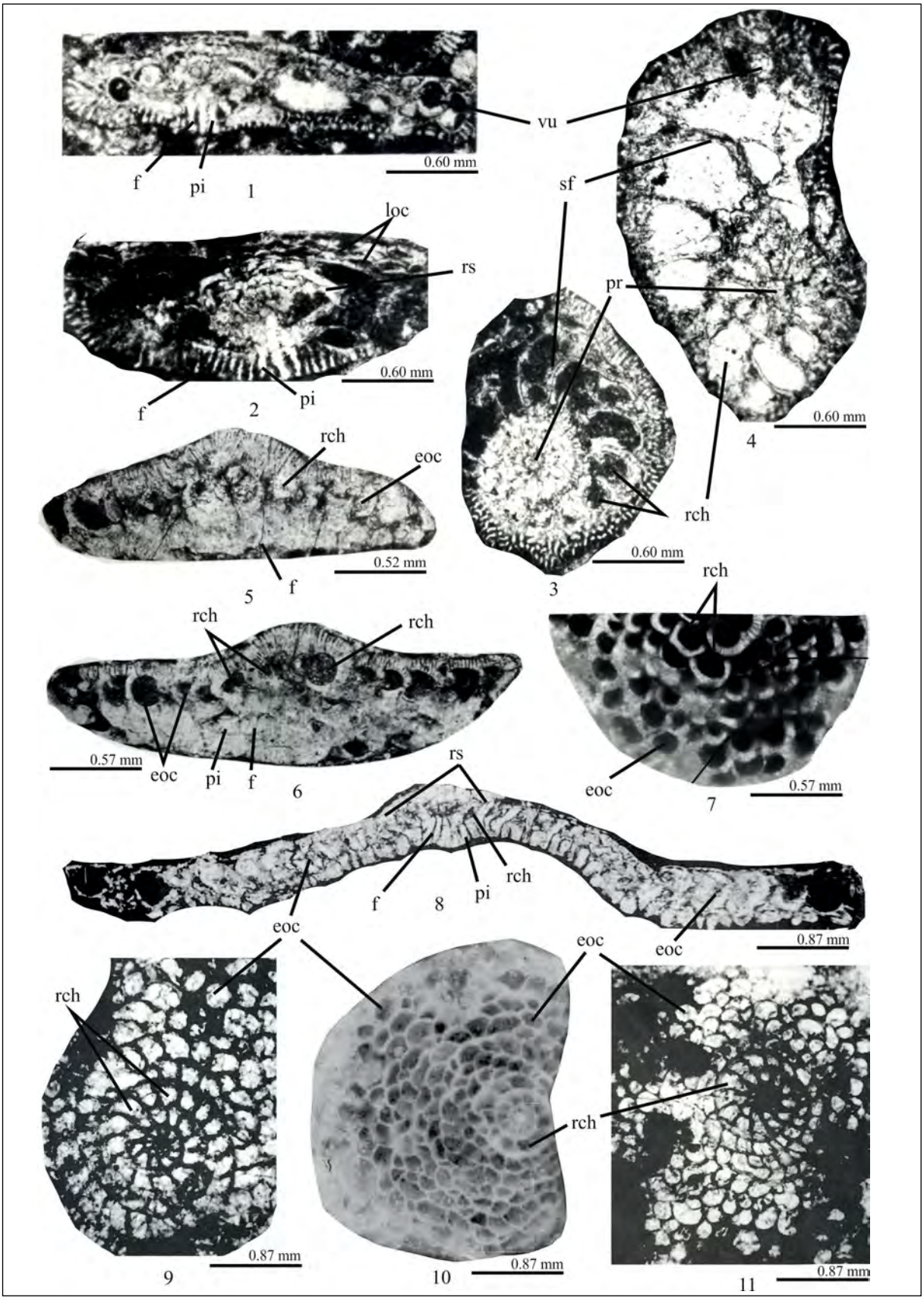
vu
f
pi
1
0.60 mm
loc
rs
f
pi
2
0.60 mm
sf
pr
rch
3
0.60 mm
4
0.60 mm
rch
eoc
f
5
0.52 mm
rch
rch
eoc
pi
f
6
0.57 mm
rch
eoc
7
0.57 mm
rs
f
pi
rch
8
eoc
eoc
0.87 mm
rch
9
0.87 mm
eoc
rch
10
0.87 mm
eoc
11
0.87 mm

PLATE V

Helicolepidina TOBLER, 1922 (type species ***Lepidocyclina* (*Helicolepidina*) *spiralis*** TOBLER, 1922),

Figure 1: Equatorial section, A form from Vaughan (1936),

Figure 2: Axial section, A form from Tobler (1922),

Figure 3: Equatorial section, B form from Barker (1934),

Figure 4: Axial section from Barker and Grimsdale (1936). ***Orbitocyclina*** VAUGHAN, 1929 (type species ***Lepidorbitoides minima*** DOUVILLÉ), ***Orbitocyclina americana*** (HANZAWA),

Figure 5: Equatorial section, A form,

Figure 6: Axial section, A form, both figures from Cole (1941); ***Eulinderina*** BARKER and GRIMSDALE, 1936 (type species ***Planorbulina* (*Planorbulinella*) *guayabalensis*** NUTTALL, 1930),

Figure 7: Equatorial section, A form,

Figure 8: Equatorial section, B form,

Figure 9: Axial section, B form,

Figure 10: Axial section, A form; all figures from Barker and Grimsdale (1936).

PLATE V

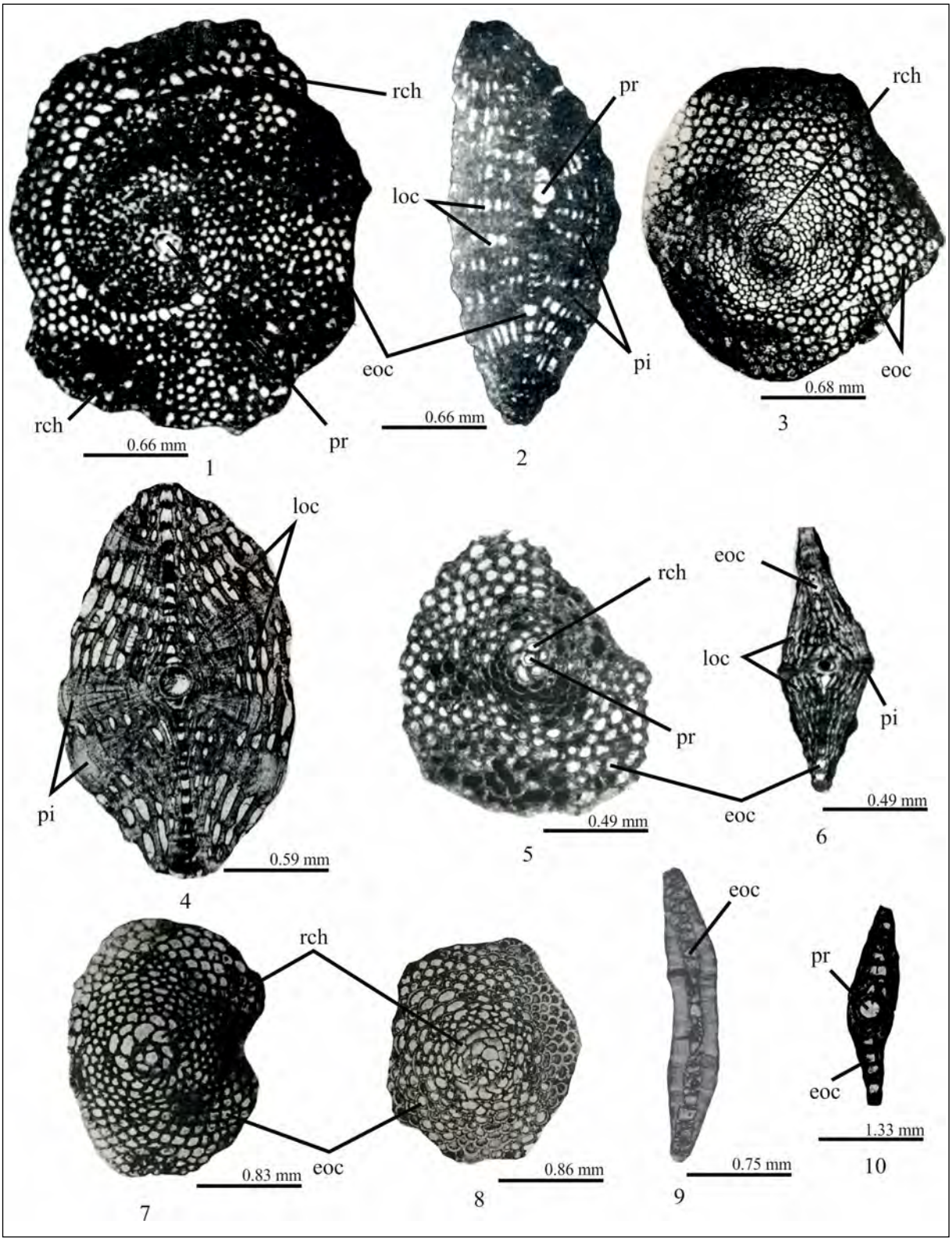
rch
rch
0.66 mm
pr
1
pr
loc
eoc
pi
0.66 mm
2
rch
eoc
0.68 mm
3
loc
pi
0.59 mm
4
rch
pr
0.49 mm
5
eoc
loc
pi
eoc
0.49 mm
6
rch
eoc
0.83 mm
7
0.86 mm
8
eoc
0.75 mm
9
pr
eoc
1.33 mm
10

PLATE VI

Helicostegina BARKER and GRIMSDALE, 1936 (type species ***Helicostegina dimorpha*** BARKER and GRIMSDALE, 1936),

Figure 1: Equatorial section, A form,

Figure 2: Equatorial section, A form,

Figure 3: Axial section, A form, all figures from Barker and Grimsdale (1936); ***Sulcorbitoides*** BRÖNNIMANN, 1954 (type species ***Sulcorbitoides pardoi*** BRÖNNIMANN, 1954),

Figure 4: Axial section, A form,

Figure 5: Axial section***,*** A form,

Figure 6: Equatorial section, A form,

Figure 7: Axial section, all figures from Brönnimann, (1954); ***Helicosteginopsis*** CAUDRI, 1975 (type species ***Helicostegina soldadensis*** GRIMSDALE, 1941),

Figure 8: Equatorial section, A form,

Figure 9: Equatorial section, A form,

Figure 10: Axial section, A form,

Figure 11: Equatorial section, A form, all figures from Grimsdale (1941).

PLATE VI

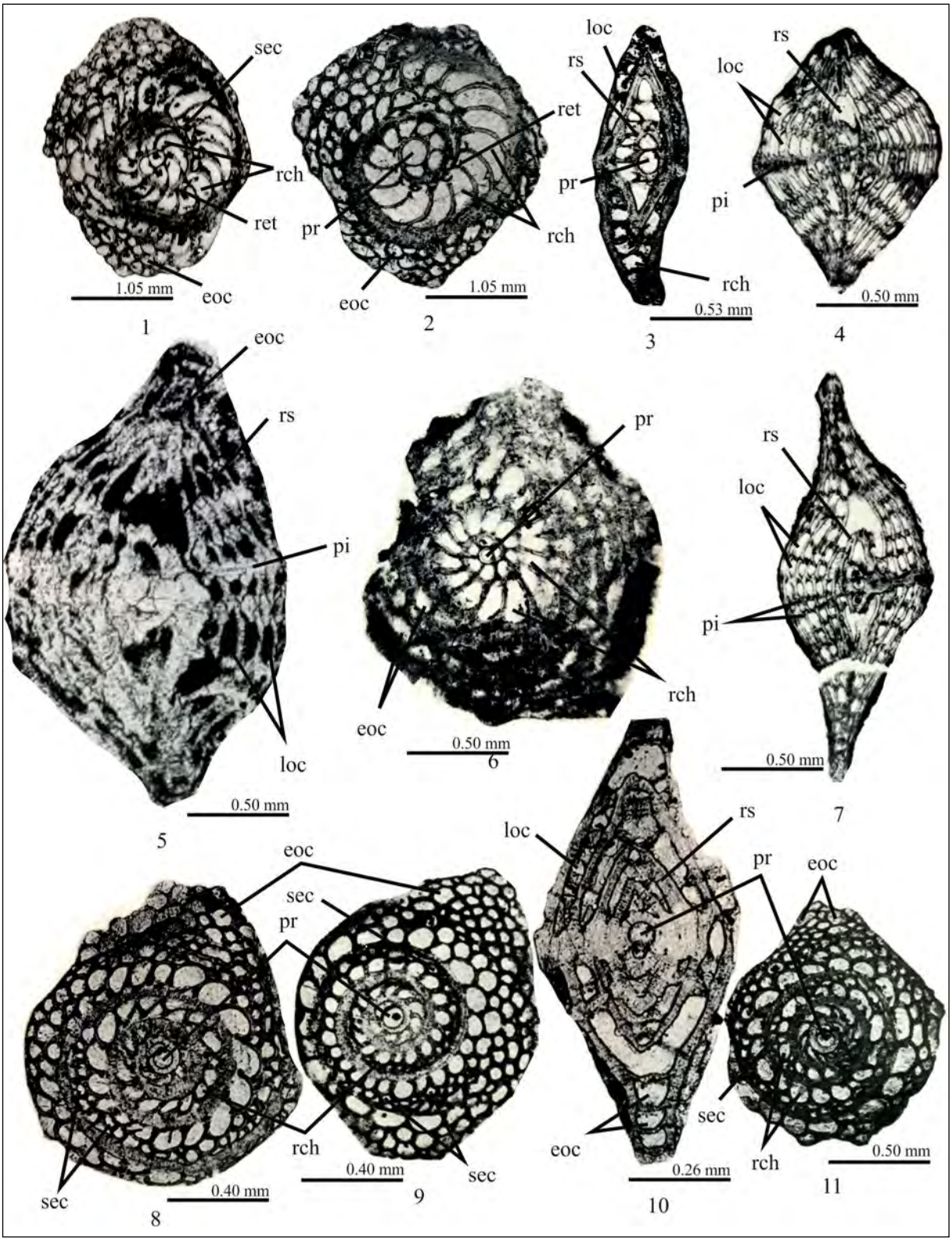
sec
rch
ret
eoc
1.05 mm
1
pr
ret
rch
eoc
1.05 mm
2
loc
rs
pr
rch
0.53 mm
3
rs
loc
pi
0.50 mm
4
eoc
rs
pi
loc
0.50 mm
5
pr
rch
eoc
0.50 mm
6
rs
loc
pi
0.50 mm
7
eoc
sec
pr
rch
sec
0.40 mm
8
sec
0.40 mm
9
loc
rs
pr
eoc
0.26 mm
10
eoc
sec
rch
0.50 mm
11

Bulletin of the Mineral Research and Exploration

http://bulletin.mta.gov.tr

Neotectonics of the Sarıköy-İnova and Çan-Bayramiç-Ezine fault zones: basin formation, age and slip rates, NW Anatolia-Türkiye

Ali KOÇYİĞİT[a]

[a]*Middle East Technical University, Department of Geological Engineering, Active Tectonics and Earthquake Research Laboratory, 06800, Ankara, Türkiye*

Research Article

Keywords:
North Anatolian Fault Zone, Biga Peninsula, Strike-Slip Neotectonic Regime, Pull-Apart Basin, Slip Rate.

ABSTRACT

The Sarıköy-İnova and the Çan-Bayramiç-Ezine fault zones (SIFZ, ÇBEFZ) comprise the southern strand of the North Anatolian Fault System in the Biga Peninsula. They are located in the area between Sarıköy to northeast and the Dalyan settlement around Bozcaada in the North Aegean Sea to southwest. Both of the fault zones are active. This is evidenced by the 6 March 1737 (Ms =7.0) İnova, 1st February 1809 Hurma (Ms = 6.1), and the 8 February 1826 Güllüce (Ms = 6.2) historical earthquakes resulted from these fault zones. Maximum lengths of fault segments comprising the SIFZ and the ÇBEFZ are 14 km and 15 km, respectively. Based on the maximum lengths of fault segments, the magnitude of the peak earthquakes to be originated from these faults are Mw = 6.3 and 6.6, respectively. Based on both the geological and geographic markers, the total right lateral offsets accumulated on the SIFZ and ÇBEFZ are 12 km and 20 km, respectively. These offset values imply to the slip rates of 4.6 mm/yr and 7.7 mm/yr, respectively. Five pull-apart basins were developed on both fault zones. These are the Sarıköy, İnova, Kazabat, Çan and Ezine-Bayramiç basins. The first three of them are pure strike-slip pull-apart basins, while the type of the rest basins is superimposed. The angular unconformity between the nondeformed basin fill of Quaternary age and the folded to thrust-faulted basement rocks of pre-Quaternary age reveals strongly that the pull-apart basins have formed during the Quaternary time. This relationship also reveals that the commencement age of the strike-slip neotectonic regime and formation of associated fault zones are the Early Quaternary. This work was dedicated to the retirement memory of Dr. Fuat Şaroğlu.

Received Date: 17.06.2022
Accepted Date: 20.01.2023

1. Introduction

The North Anatolian Fault System is divided into numerous fault zones around the Sea of Marmara and results in an active deformation zone wider than 120 km. Two of them are the Sarıköy-İnova and the Çan-Bayramiç-Ezine fault zones. They cut across the Biga Peninsula in the area between Ulukır village to northeast and Dalyan to the further southwest and are included in the southern strand of the North Anatolian Fault System (Figure 1). Based on aerial photograph study, seven fault segments within these two fault zones were previously identified and mapped by Barka and Kadinsky-Cade (1988). Later on, four single faults, which comprise these two fault zones, were also observed, mapped and renamed separately by Siyako et al. (1989). These are the Ezine-Bayramiç, Çan, Terzialan-Çomaklı and the İnova-Sarıköy single faults. They also reported that these faults have formed in a neotectonic period that commenced in

Citation Info: Koçyiğit, A. 2023. Neotectonics of the Sarıköy-İnova and Çan-Bayramiç-Ezine fault zones: basin formation, age and slip rates, NW Anatolia-Türkiye. Bulletin of the Mineral Research and Exploration 172, 119-140. https://doi.org/10.19111/bulletinofmre.1239900

**Corresponding author: Ali KOÇYİĞİT, alikocyigit45@gmail.com*

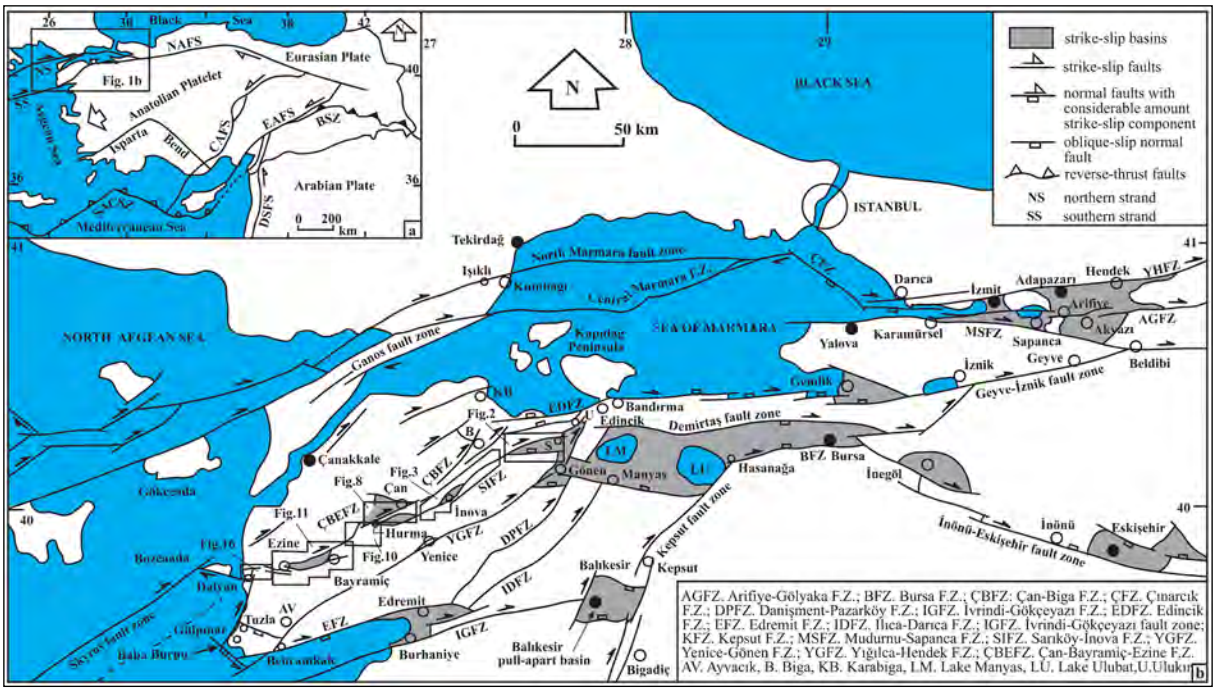

Figure 1- a) Simplified map illustrating plate tectonic configuration of Türkiye and location of study area, b) Simplified fault map illustrating major strands of the North Anatolian Fault system and fault zones comprising them around Sea of Marmara.

the Early-Middle Miocene. Additionally, some dextral offsets, such as the 1.5 km on the Çan fault and 8 km on the İnova-Sarıköy fault, were also determined and reported by the same authors. Later on, these two studies were followed by several researchers (Şaroğlu et al., 1992; Koçyiğit, 2006; Duru et al., 2007; Koçyiğit, 2011; Emre et al., 2011, 2012). Şaroğlu et al. (1992) named the same structures as the Etili fault, Çan-Biga fault zone and the Sarıköy fault, respectively. Duru et al. (2007) carried out a detailed geological map of the İnova area, divided the Sarıköy fault into two segments namely the Asmalı and Tahtalı segments, and then reported 12 km dextral offset on both fault segments. Lastly, same structures were also reevaluated and named as the Biga-Çan fault zone, Sarıköy fault and Gündoğan fault respectively by (Emre et al., 2011; 2012), who also redivided the Biga-Çan fault zone into three fault segments as Çan, Yuvalar, and Biga fault segments. Five pull-apart basins occur along these fault zones. From NE to SW these are the Sarıköy, İnova, Kazabat, Çan and the Ezine-Bayramiç basins. Except for the İnova basin, rest four basins have not been studied yet, whereas, these basins contain valuable stratigraphic and structural data about the commencement age of the neotectonic period, evolutionary history of faults and associated displacements accumulated on them. In terms of this study, some type localities, such as the Sarıköy, İnova, Kazabat, Çan-Etili, Bezirganlar, Ezine-Bayramiç and the Kurudere areas, were mapped in detail on 1/25.000 scale, and new findings were obtained. These new data were obtained by the usage of both the office and field methods. Office studies include computer program T-TECTO 3.0, satellite images and aerial photograph studies, whereas field studies focus on the detailed field geological mapping of rocks and faults carried out directly in the field. In the present day, the debate about the fault pattern, total displacement, and the commencement age of the neotectonic period in the study area is still lasting. This study aims to bring plausible solutions to these debates under the lights of both the newly obtained field data and national to international literature surveys.

2. Fault Zones

Both the Sarıköy-İnova and Çan-Bayramiç-Ezine fault zones are represented by the dextral strike-slip faulting caused by stress field state, in which the maximum principal compressive stress (σ_1) is operating in approximately E-W direction, while the least principal stress axis (σ_3) or extension direction is N-S (Koçyiğit and Gürboğa, 2021). Based on

the relationship between the strike of faults and the operation direction of the maximum principal compressive stress axis, the NE-striking faults are dextral strike-slip faults, NW-striking faults are sinistral strike-slip faults, the E-W striking faults are oblique-slip normal faults and the N-S striking faults are oblique-slip reverse faults. In general, as the strikes of the faults approach to the E-W direction, i.e., σ_1 direction, their normal components increase (Wilcox et al., 1973). Consequently, the Biga Peninsula and its neighborhood are being shortened in E-W direction, while it is expanded in N-S direction.

2.1. Sarıköy-İnova Fault Zone (SIFZ) and Related Basins

In general, the SIFZ is 0.2-5 km wide, totally 65 km long, and N45° to 70E°-trending active deformation zone dominated by the dextral strike-slip faulting. It is situated between Ulukır village to the northeast and Hurma village to the southwest (Figure 1b). It begins around Ulukır village and then runs southwestward across the Sarıköy, Armutlu, Geyikli, Tahtalı, Yolindi, Aşağıinova, Yukarıinova, Asmalı, Sameteli and Hurma settlements. Around Hurma village further southwest, it meets with the Çan-Bayramiç-Ezine fault zone (ÇBEFZ) and then terminates. Along the whole length, the SIFZ consists of numerous 0.3-3 km spaced, 0.1-14 km long and NE-, E-W- and NW-trending structural fault segments. In addition, it is divided into five major sections in the pattern of a fault set by the intervening some other strike-slip complexities and related pull-apart basins. These sections or fault sets are, from northeast to southwest, the Sarıköy-Geyikli, Hüseyinbey, Tahtalı-Aşağıinova, Yukarıinova-Asmalı, and the Kazabat fault sets, respectively (Figures 2 and 3). They are 18 km, 14 km, 17 km, 18 km and 12 km in length, respectively. The most diagnostic character of the SIFZ is the anastomosing pattern. The master fault bifurcates and rejoins frequently, divides the earth crust into a series of diverse-sized lensoidal blocks with long axes running more or less parallel to the general trend of the fault zone. Thus, it displays an anastomosing occurrence pattern peculiar to the strike-slip faulting (Figures 2 and 3). Fault segments, which comprise the SIFZ, cut across various rocks (Permo-Triassic Karakaya Complex, Liassic clastic rocks, Jurassic-Cretaceous Limestone and the Oligo-Miocene igneous to volcanic rocks) (Bingöl et al., 1973; Siyako et al., 1989; Okay et al., 1990; Koçyiğit, et al., 1991; Şahin et al., 2010) and tectonically juxtapose them with to each other, and also with the Quaternary basin fill. They also displace older rocks in both vertical and right-lateral directions. Various lithofacies of the Permo-Triassic Karakaya Complex are displaced up to 12 km in dextral direction by the Tahtalı-Aşağıinova section of the SIFZ (X-Y in Figure 4) (Engin et al., 2012). This is also confirmed by the offset drainage system. The Sarıköy Çay, Keçi Stream, Balıklı Çay and the Kaz Stream are fault-controlled drainage systems flowing within the SIFZ. In particular, the Balıklı Çay is offset up to 12 km in the dextral direction by the Tahtalı-Aşağıinova section of the SIFZ (X-Y in Figure 3). Same offset features were also previously reported by Siyako et al. (1989) and Emre et al. (2012). The longest segment of the SIFZ is the 14 km long Tahtalı fault, on which the total displacement accumulated until the present is 12 km. Based on the maximum length of this fault segment, the magnitude of the peak earthquake to be resulted from the Tahtalı fault is M_w = 6.4 based on formula introduced by Wells and Coppersmith (1994). There is a relationship among the slip rate (SR), total displacement (TD) and the age of the fault (A). In the same way, there is a relationship among the slip rate (SR), coseismic displacement (CD) and the return period (RP). It is explained by the equation (RP = CD/SR). Based on this equation, the amount of coseismic lateral displacement to be sourced from the Mw 6.4 earthquake is approximately 2.3 m or 2.5 m.

The SIFZ is a regional active structure. This is proven by two historical earthquakes. These are the 6th March 1737 İnova earthquake of Ms =7.0, and the first February 1809 Hurma earthquake of Ms = 6.1 (Figure 3) (Ambraseys, 2002; Tan et al., 2008). They were sourced from the Aşağıinova and Hurma sections of the SIFZ, respectively. The epicenter localities of these earthquakes are located on the strike-slip complexities, such as the İnova releasing step-over, a single contractional bend and the intersection of two fault zones, where motion on the fault is locked and causes to the accumulation of huge volume of elastic strain energy for the occurrence of earthquakes. However, the main bulk of the SIFZ still retains its seismic gap.

Three strike-slip basins have developed along the SIFZ owing to the strike-slip complexities. These are the Sarıköy, İnova and the Kazabat pull-apart basins. In the near southwest of Geyikli village, the SIFZ bifurcates into two sections such as the NE-trending

Sarıköy and the E-W-trending Hüseyinbey fault sets (Figure 2). This bifurcation results in an eastward widening fault-wedge type of pull-apart basin (Figures 2 and 5). It is bounded by the Sarıköy fault set to north and by the Hüseyinbey fault set to south (F1 and F2 in Figure 5). The 14 km long Hüseyinbey fault set consists of diverse-sized and northerly dipping several normal faults, and a single NW-trending sinistral strike-slip fault (Dereköy fault) (Figure 2). They display well-preserved normal and sinistral strike-slip fault slickensides. The stereographic plot of slip-plane data on Schmidt lower hemisphere stereonet indicates that the Sarıköy basin is under the effect of E-W shortening and N-S expansion (Figure 6). The Sarıköy basin is occupied by an approximately 85 m thick, weakly lithified to unconsolidated, and flat-lying fluvial sedimentary sequence of Quaternary age. This basin fill overlies with an angular unconformity on the erosional surface of the various rocks of pre-Quaternary age (Figure 2).

The second diagnostic structure included in the SIFZ is the İnova pull-apart basin. It occurs along both the Tahtalı-Aşağıinova and the Yukarıinova-Asmalı sections of the SIFZ. Around Aşağıinova village, the master fault of the SIFZ bends first toward left and then jumps to right, and so it results in a releasing type of stepover, which nucleates the İnova strike-slip basin (Figure 3). The southwestern and northeastern sections of the SIFZ were previously named as the Asmalı and Tahtalı segments respectively by Emre et al. (2012). However, this naming is not true, because it contradicts with the definition of structural fault segment, which is a single fault or a part of a single fault confined between two structural complexities, such as the step-over, bend and bifurcation. The İnova pull-apart basin is a 2.5 km wide and 7 km long depression occupied by 70 m thick, loose and non-deformed fluvial sediments of Quaternary age. The basin fill rests with an angular unconformity on the erosional surface of the Permo-Triassic Karakaya Complex (Bingöl et al., 1973).

Around Samateli the SIFZ bends at 25º towards north, bifurcates into several splay faults, and then results in an extensional horse-tail structure, namely the Sameteli horse-tail structure, where the third pull-apart basin occurs. It is the Kazabat depression located on the southwestern tip of the SIFZ (Figures 3 and 7). The Kazabat basin is a 2.5 km wide and 10 km long lense-shaped depression with an E-W trending long axis. It widens up to 2.5 km in the central section, while it narrows and wedges out in both east and west directions. It is bounded by the NE-trending Hurma fault to west, by the E-W to WNW-trending Çekiçler, Korualtı, Büyüktepeköy and Kalburcu fault segments to north, and by the E-W-trending Süleköy and Karakoca fault segments to south (Figure 7).

Both the northern- and southern margin-boundary fault segments gain a considerable amount of normal components greater than their strike-slip components

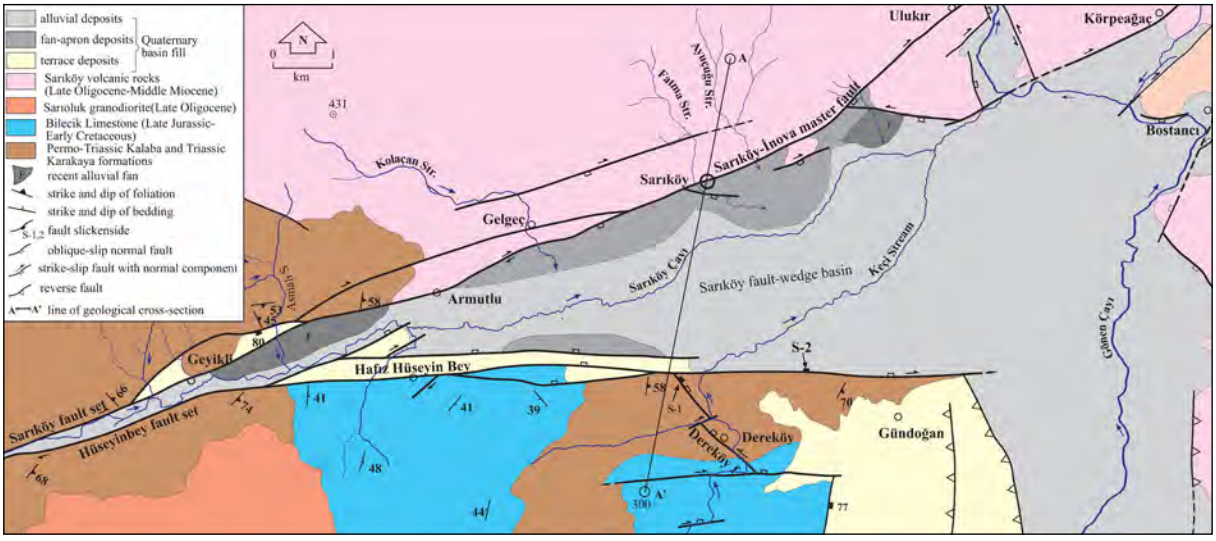

Figure 2- Geologic map of the Sarıköy fault-wedge basin and its near vicinity. Geological cross-section along line A-A' indicates the Sarıköy basin, its margin-boundary faults, fills and stratigraphical relationships with the pre-Miocene rocks.

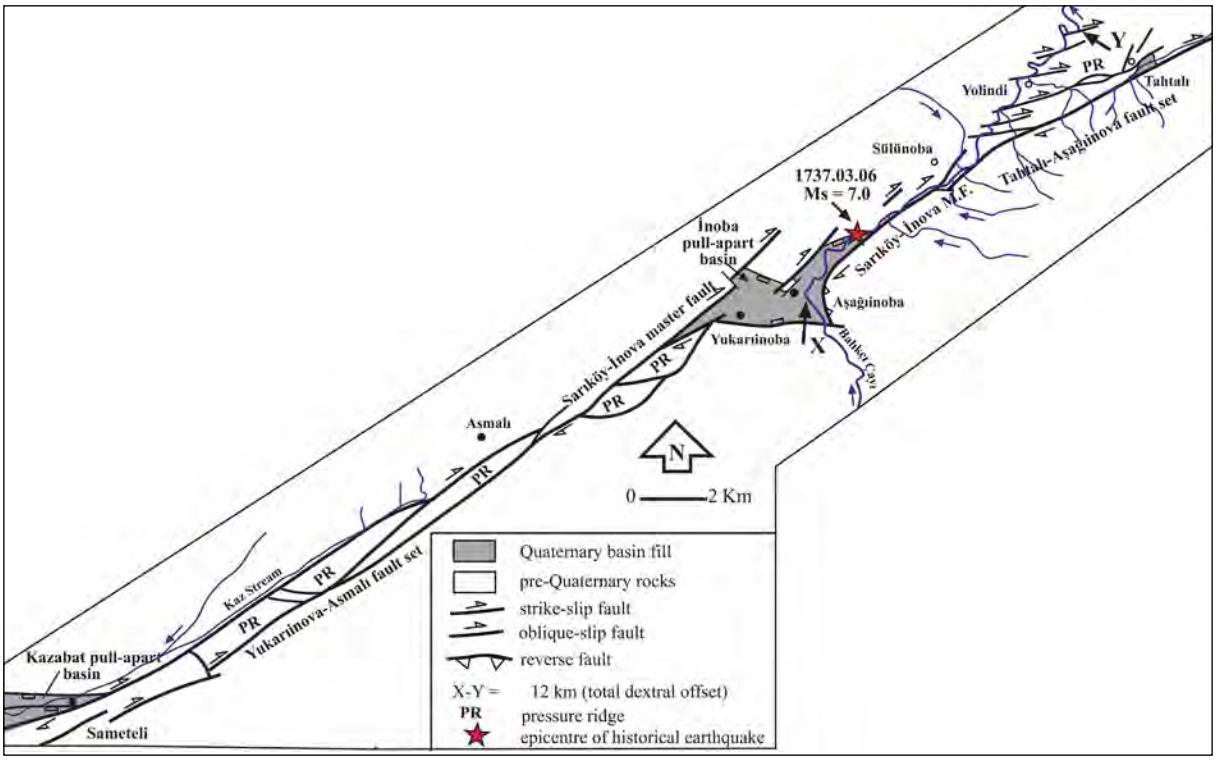

Figure 3- Neotectonic map of both the Tahtalı-Aşağıinova and the Yukarıinova-Asmalı sections of the Sarıköy-İnova fault zone (SIFZ).

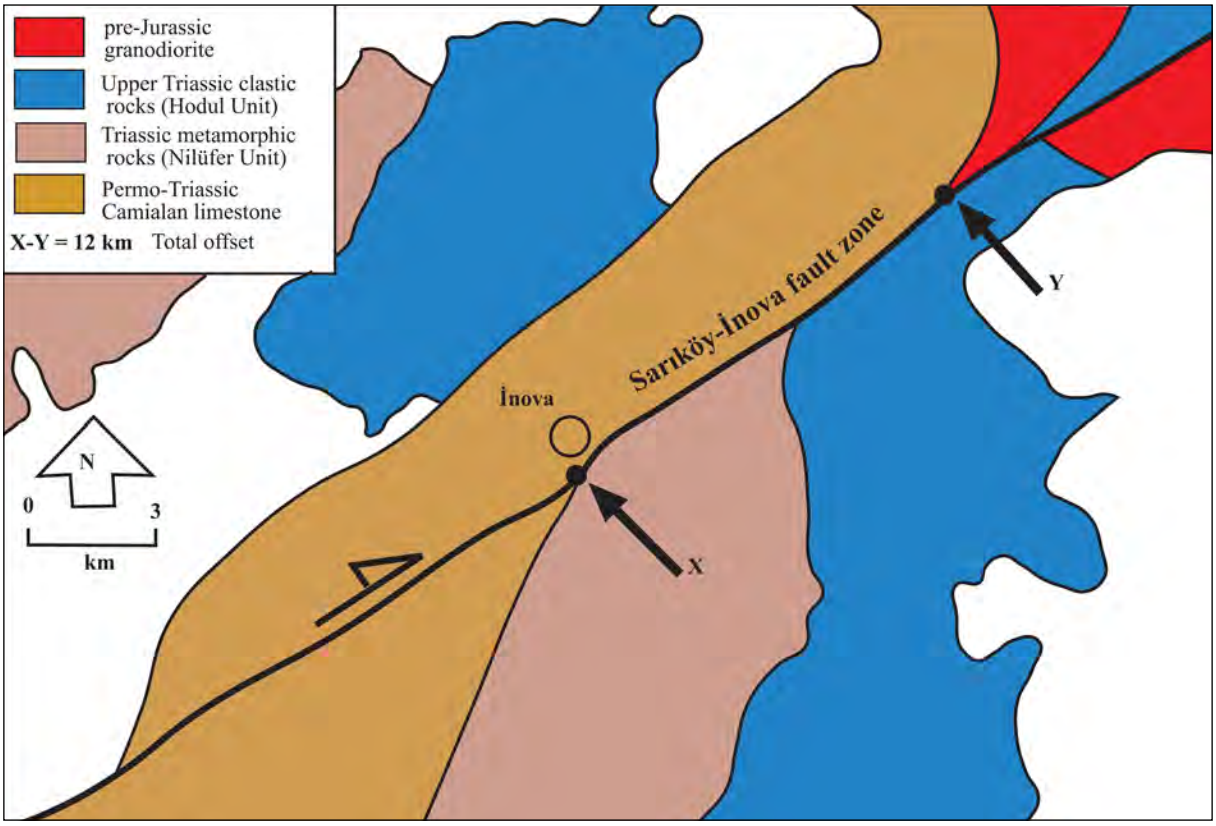

Figure 4- Map of various lithofacies of the Permo-Triassic Karakaya Complex displaced up to 12 km (X-Y = 12 km) in dextral direction by the SIFZ (modified from Appendix 3, Engin et al., 2012).

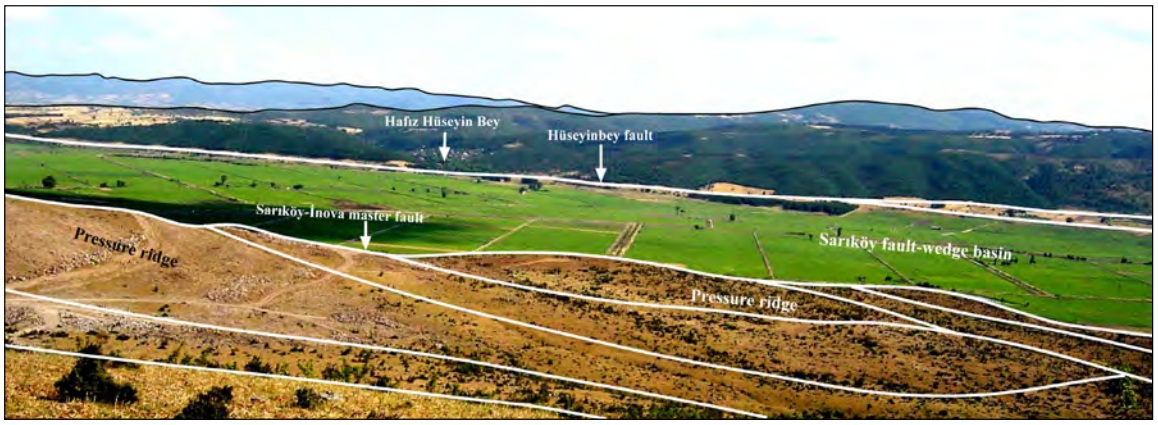

Figure 5- General view of the Sarıköy fault-wedge type of pull-apart basin (view to SSE).

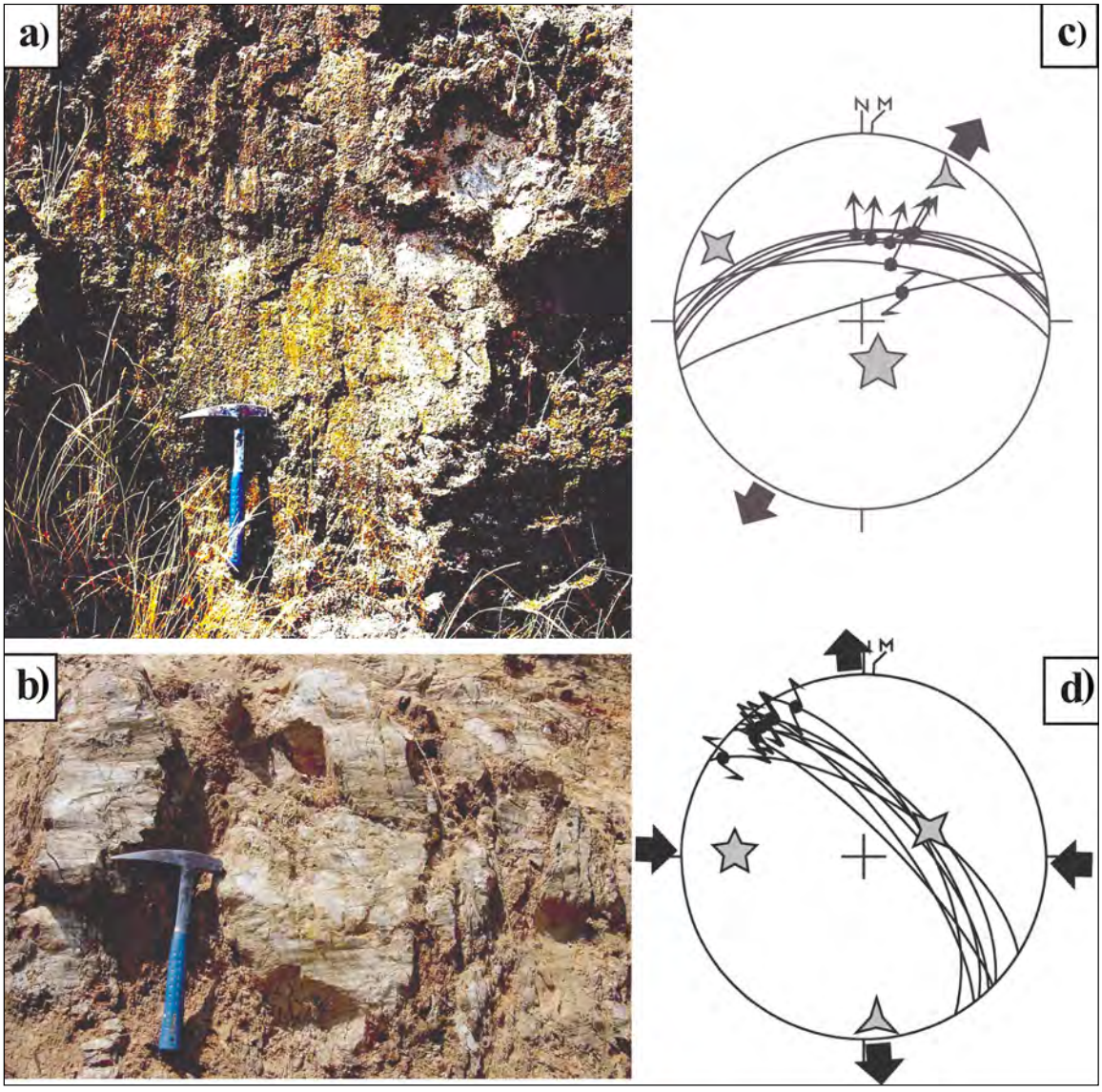

Figure 6- a) Field photographs of the Hüseyinbey oblique-slip normal fault and b) the Dereköy sinistral strike-slip fault slickensides, respectively, at stations S1 and S2 in Figure 2, c) and d) stereographic plots of slip-plane data on Schmidt lower hemisphere stereonet respectively (diverging and converging large arrows indicate expansion and shortening directions respectively.

owing to the kinematic character of the Sameteli horse-tail structure. This situation is also the main cause for the development of the Kazabat basin. This basin is occupied by 108 m thick fluvial to gravity-induced sedimentary fill (Kazabat formation) of Quaternary age (Figure 8). It rests with an angular unconformity on the erosional surface of various pre-Miocene rocks. The basin fill begins with well-bedded and weakly-sorted polygenetic basal conglomerates at the bottom, and then continues upwards with the alternation of weakly bedded to lose fluvial conglomerate, sandstone and siltstone. Towards the top, it is succeeded by both the coarse-grained marginal and finer-grained depocentral lithofacies such as slope-scree, fan-apron, fan and basin floor sedimentary deposits respectively. All the lateral and vertical gradations are observed among these lithofacies. Consequently, the stratigraphy of these pull-apart basins reveals strongly that the formation age of the SIFZ is Quaternary.

2.2. ÇBEFZ and Related Basins

In general, the ÇBEFZ is an 1.5-4.6 km wide, totally 80 km long and ENE- to NE-trending active deformation zone represented by mostly strike-slip faulting. It is situated between Helvacı village (Çan) to northeast and Dalyan Town (Bozcaada) to further southwest (Figure 1b). The ÇBEFZ begins around Helvacı village in the northeast and then runs in

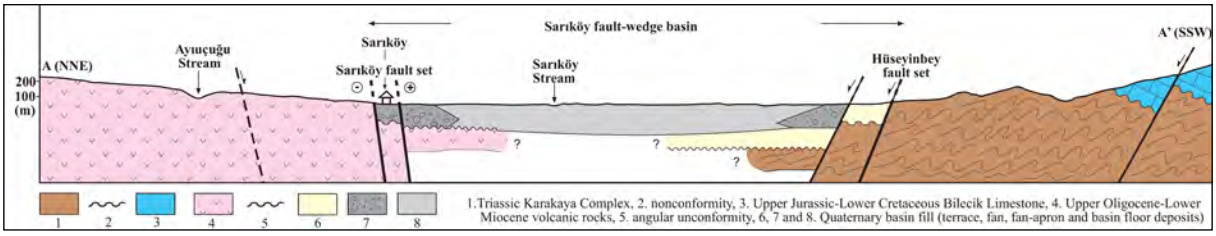

Figure 7- Geological cross-section along line A-A' (given in Figure 2) which illustrates the Sarıköy basin, its margin-boundary faults, fills and stratigraphical relationships with the pre-Miocene rocks.

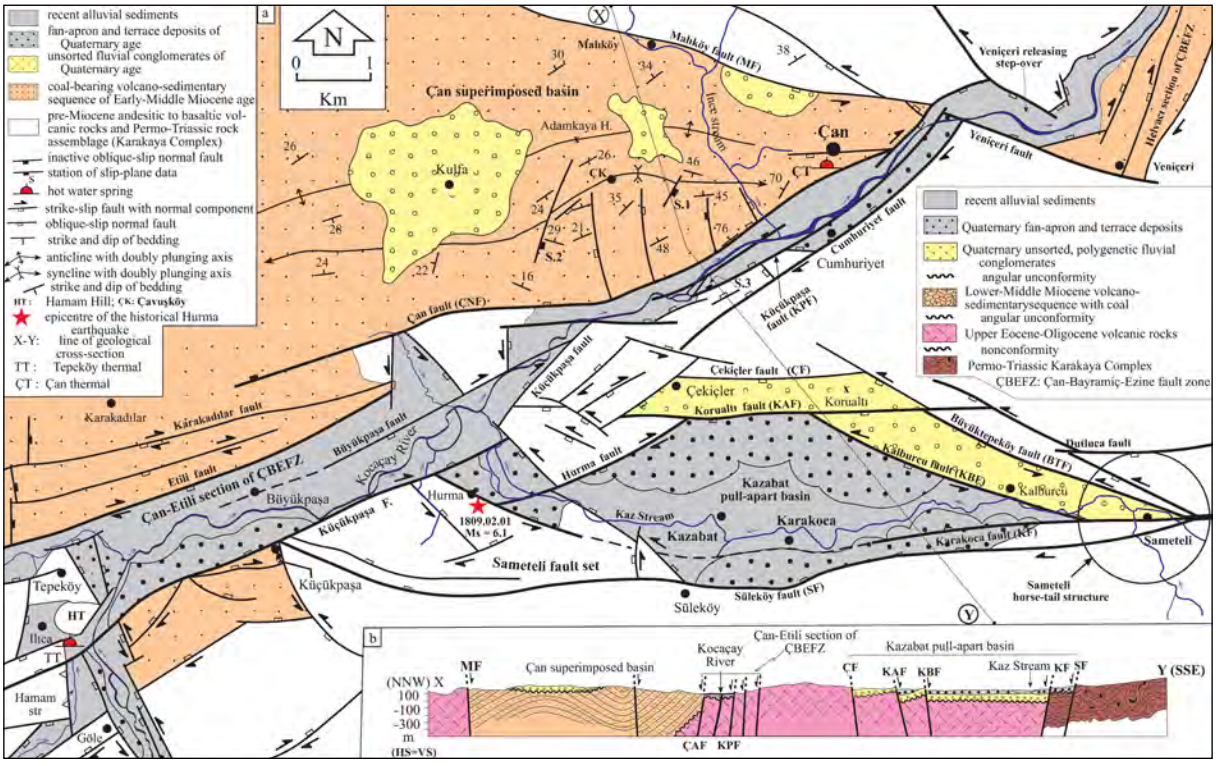

Figure 8- Geological map of both the Çan and Kazabat strike-slip basins, a) and the geological cross-section along line X-Y, b) showing their internal structures.

southwest direction along a series of settlements in the size of village, town and county. Based on some strike-slip complexities, such as the Yeniçeri and Etili releasing stepovers, bifurcation and the Doğancı bend, the ÇBEFZ is divided into five sections. These are, from northeast to southwest, the Helvacı, Çan-Etili, Bezirganlar, Ezine and the Bayramiç-Kurudere sections or fault sets (Figures. 7, 9 and 10).

These sections are 8 km, 16 km, 18 km, 21 km and 45 km in length, respectively. The ÇBEFZ consists of 0.4-15 km long, and E-W-, ENE, NW- to NE-trending numerous fault segments. They cut across various older rocks of different lithofacies, and the Quaternary neotectonic basin fill. These rocks are cut across, tectonically juxtaposed and offset in both lateral and vertical directions by the fault segments. The ÇBEFZ developed along a paleotectonic structure named previously as the Bayramiç and Etili grabens of Miocene age by Yılmaz et al. (2000), i.e., the younger strike-slip tectonic regime and related structures were overprinted on an earlier extensional tectonic regime and associated structures during the Quaternary time. For this reason, most fault segments comprising the

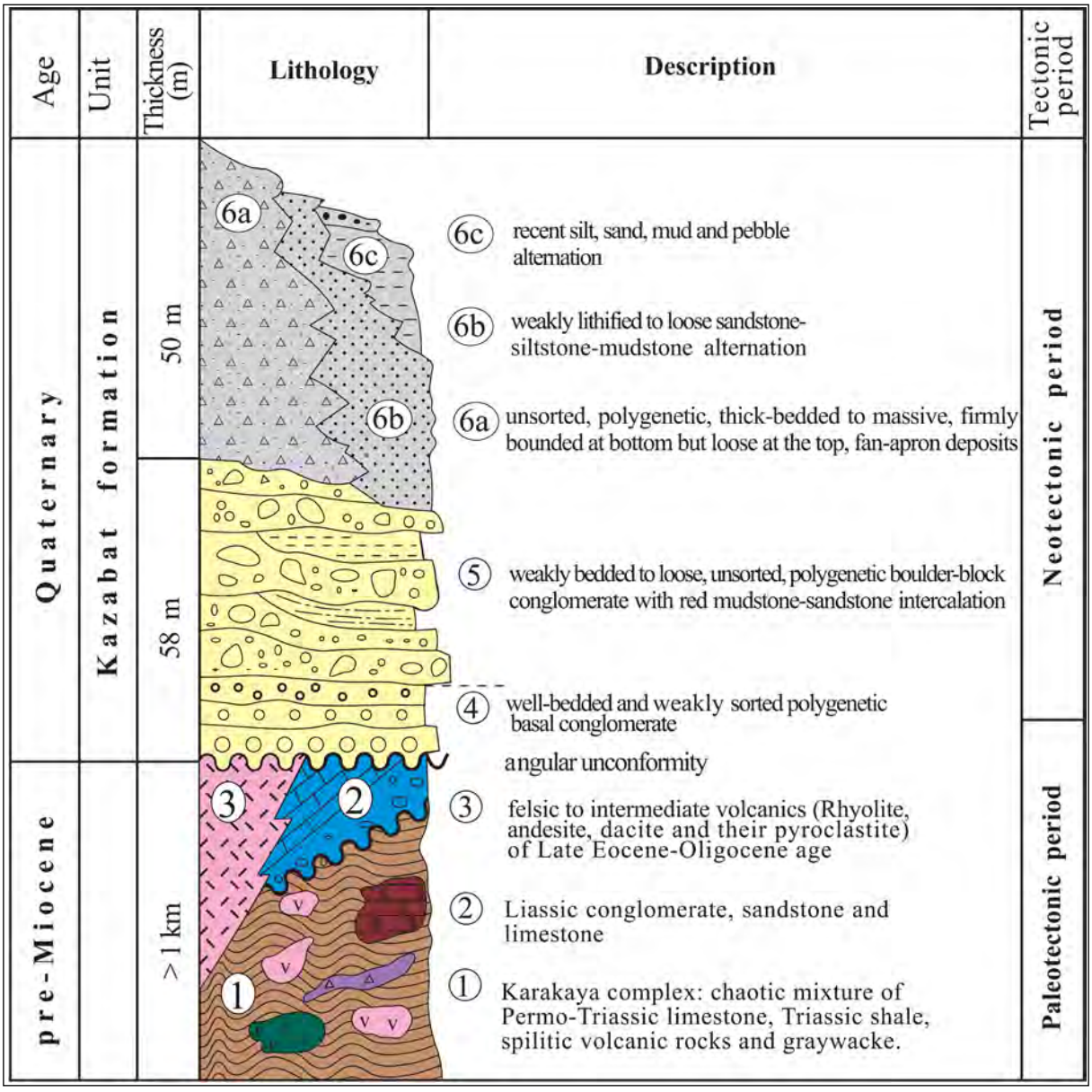

Figure 9- Generalized stratigraphical column of the pure strike-slip basins (Sarıköy, İnova and Kazabat basins).

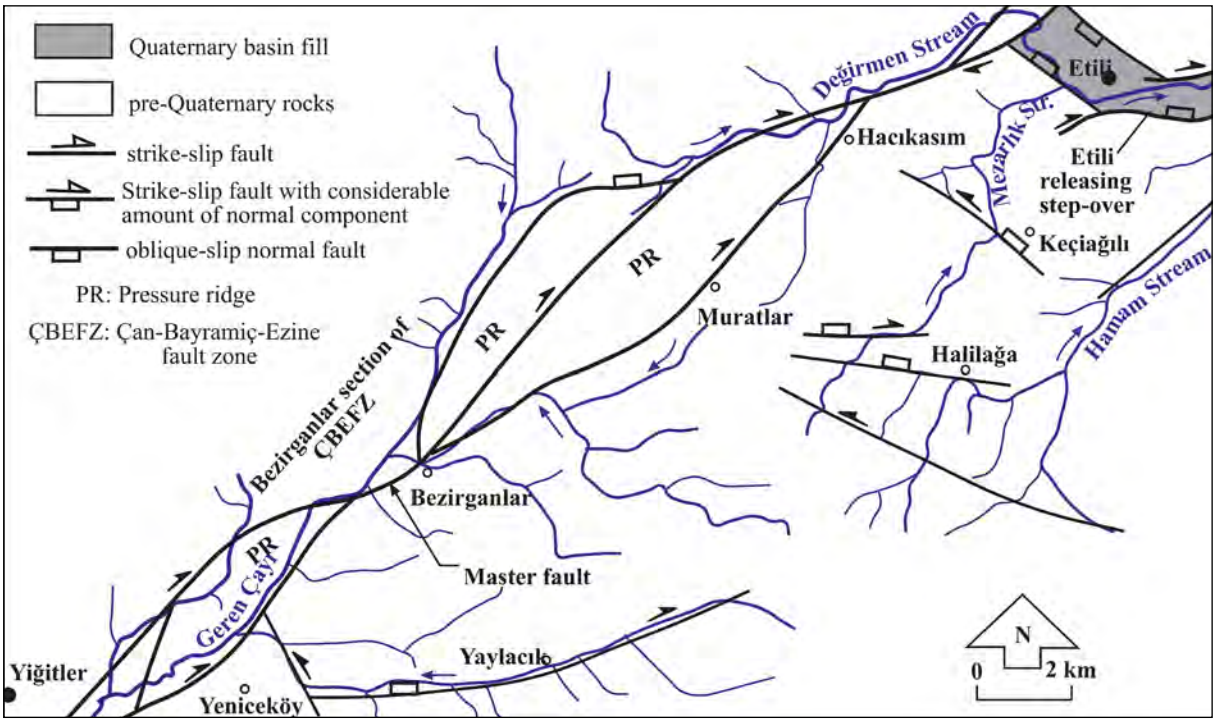

Figure 10- Simplified map illustrating the relationship of the Bezirganlar section of the Çan-Bayramiç-Ezine fault zone (ÇBEFZ) with the drainage system.

ÇBEFZ are reactivated older faults inherited from the Miocene extensional tectonic regime and related grabens. For instance, the Çan, Küçükpaşa and some intrabasinal fault segments in the Çan basin (Figure 7), and the Ezine and Bayramiç faults in the Ezine-Bayramiç basin (Figure 10) are originally reactivated older structures. This is also proven by the superimposed slip-plane features such as slip lines to fault steps and their kinematic analyses (Figure 11).

Both the Kocaçay and Karamenderes Çayı are two major fault-controlled drainage systems flowing in opposite directions within the ÇBEFZ. The Kocaçay River rises from the peak of Kazdağları pressure ridge to south and outside the study area, and then flows towards north. It changes its flow direction towards ENE and then is offset up to 20 km in dextral direction when it enters into the Çan-Etili section of the ÇBEFZ (X-Y in Figure 12). This dextral strike-slip displacement is also proven by a geologic marker, namely the offset formation boundary. The southern boundary of the Lower-Middle Miocene volcano-sedimentary sequence is crossed and displaced up to 30 km in right lateral direction (Figure 7 in Yılmaz et al., 2000). These total dextral offsets indicate the slip rates of 11.6 mm/yr. and 7.7 mm/yr., respectively, and the return period of approximately 400 years for the occurrence of a peak earthquake with the Mw = 7.0. Total geological offsets that have developed in NAF System within last 4-5 million years are compatible with GPS data and explain that the slip rate on Northern strand is about 4 times higher than Southern strand (Sipahioğlu and Matsuda, 1986; Şaroğlu et al., 1987; Koçyiğit, 1988; Emre et al., 1998; Armijo et al., 2002; Meade et al., 2002; Emre and Awata, 2003). The amount of coseismic lateral displacement is about 3-3.5 m. The longest segment of the ÇBEFZ is the 15 km long Güllüce fault. Based on the maximum length of this fault segment, the magnitude of the peak earthquake to have originated from the Güllüce fault is about Mw = 6.5 (Wells and Coppersmith, 1994). The ÇBEFZ is an active regional structure. This is indicated by both a series of morphotectonic structures and the 8th February 1826 Güllüce historical earthquake with the Mw = 6.2 (Tan et al., 2008). This earthquake was sourced from the Güllüce fault (Figure 10). Despite these earthquakes, the main bulk of the ÇBEFZ still retains its nature of seismic gap.

Two basins developed on the ÇBEFZ. These are the Çan and the Ezine-Bayramiç basins (Figures 7 and 10). Both of them are superimposed in nature,

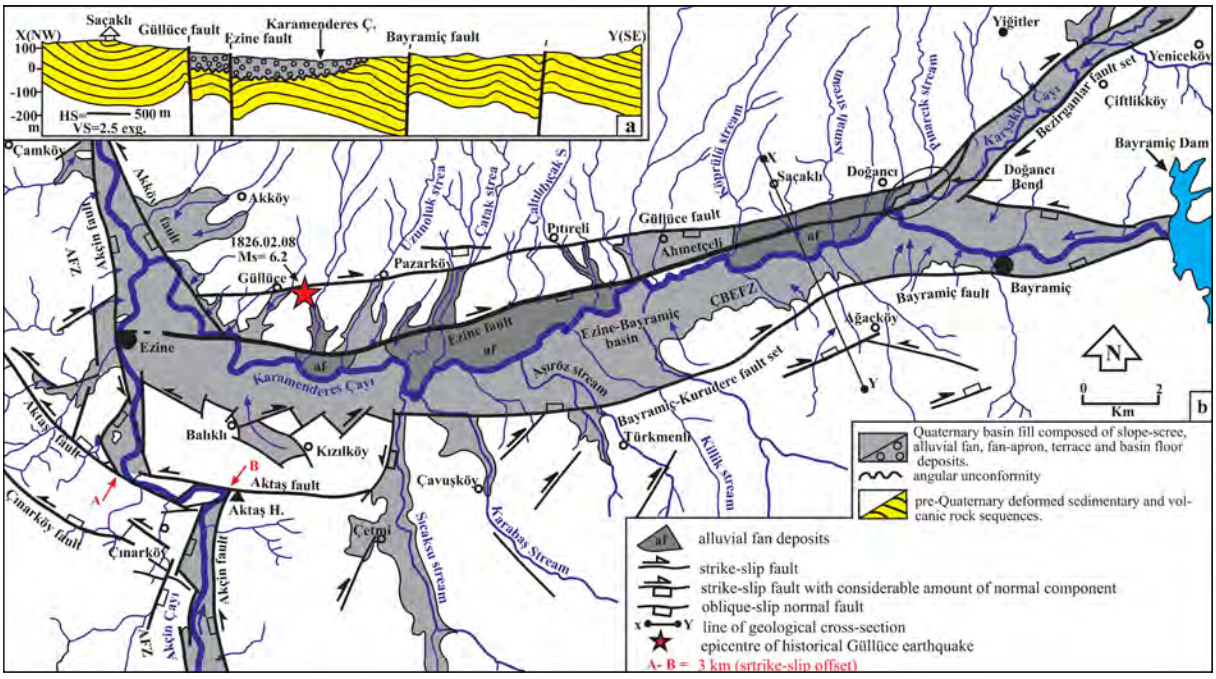

Figure 11-a) Geological cross section along line X-Y and b)neotectonic map of the Ezine and Bayramiç-Kurudere fault sets of the Çan-Bayramiç-Ezine fault zone (ÇBEFZ).

because they have two different infills separated by an intervening regional angular unconformity (Figure 13).

The Çan basin begins from the intersection of both the NE-trending Çan-Etili dextral fault set and the NW-trending Malıköy sinistral strike-slip fault, and then widens up to 5.5 km in westward direction, i.e., it is a fault-wedge basin outlined by these two structures along its southern and northeastern margins, respectively (Figures 7, 12 and 14).

The Ezine-Bayramiç basin is a 4 km wide, 30 km long and ENE-trending rectangular depression. It is bounded by the Ezine and Güllüce faults to the north, and by the Bayramiç fault set to south (Figure 10). In the west, it is outlined by the NNW-trending Akçin fault zone, which is an active deformation zone dominated by mostly the sinistral strike-slip faults with a considerable amount of reverse component. Conversely, in the west, the basin is divided into two arms and they wedge out to the further east. The southern margin of the Ezine-Bayramiç basin is outlined and controlled by the Bayramiç-Kurudere fault set. It consists of diverse-sized, and NE-, NW-, ENE- and WNW-trending numerous fault segments in the nature of both dextral to sinistral strike-slip faults and the oblique-slip normal faults. Some of them are the Bayramiç, Aktaş, Çınarköy and Kurudere faults (Figures 10 and 15).

The totally 45 km long Bayramiç fault set or section begins around Bayramiç Dam to the east and then runs wastwards up to south of Ezine County, where it cuts the Akçin fault zone and displaces it up to 3 km in sinistral direction (A-B in Figure 10). Later on, it continues again in the west direction along the Kurudere drainage system for a distance of 17 km. Lastly, it joins with the Skyros fault zone in the North Aegean Sea and then terminates (Figures 1b and 15) (Papazachos et al., 1984; Pavlides et al., 1990; Koukouvelas and Aydın, 2002; Kürçer et al., 2015; Sakellariou and Tsampouraki-Kraounaki, 2019). The whole of lithofacies of both the older graben fill and the younger neotectonic basin fill, their internal synsedimentary structures, and the top to bottom stratigraphical relationships are observed well in the Çan coal mining quarry excavated deeply inside the Çan superimposed basin (Figure 14) (Bilgin et al., 1976). In this basin. the underlying older fill begins with a polygenetic basal conglomerates on the erosional surface of the Upper Eocene-Oligocene volcanic rocks and then continues upward with the alternation of sand-stone, siltstone, tuff-tuffite, coal seams and a package of various deep lacustrine

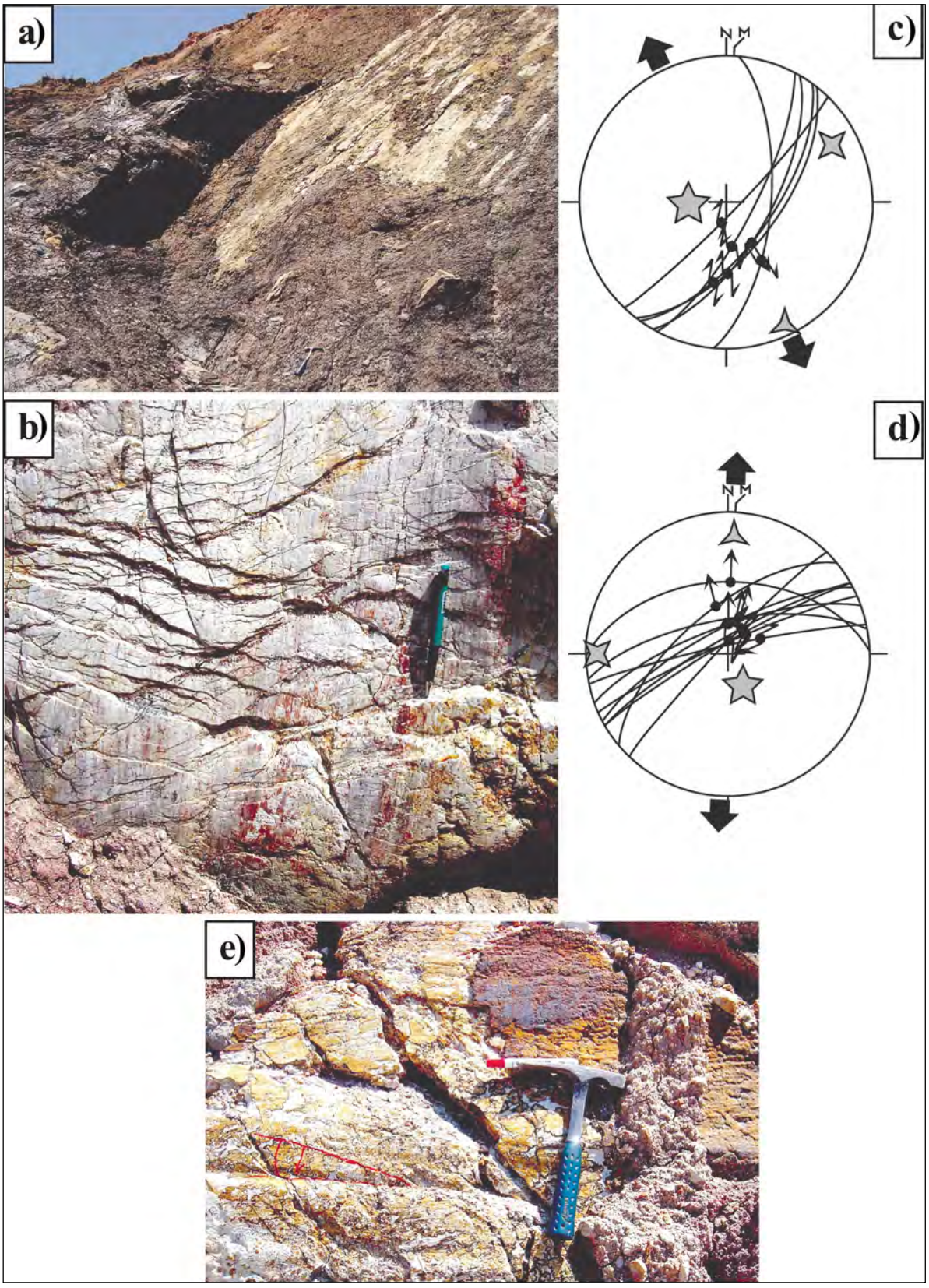

Figure 12- a and b) Close-up views of the Miocene oblique-slip normal fault slickensides, c and d) Stereographic plots of slip-plane data on Schmidt lower hemisphere stereonet respectively (diverging large arrows indicate extension directions); e) Close-up view of the active strike-slip fault slickenside with slip lines parallel to E-W direction.

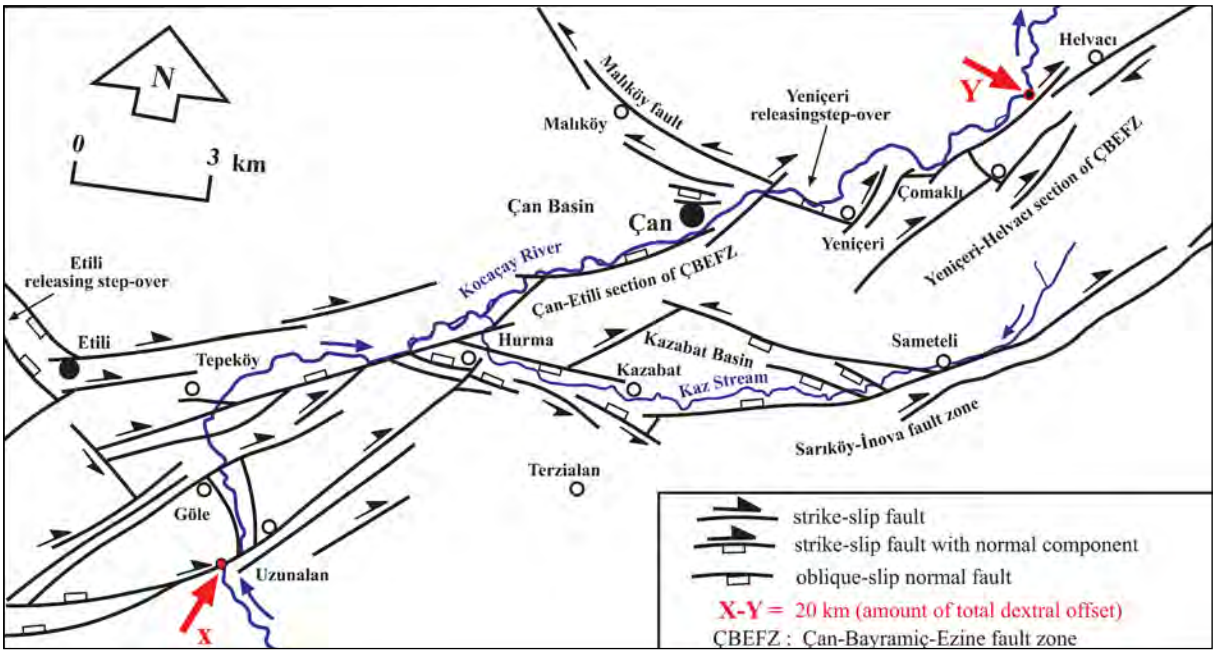

Figure 13- Simplified fault map and associated strike-slip basins. It illustrates the Kocaçay River displaced up to 20 km (X-Y = 20 km) in dextral direction by the Çan-Etili section of the ÇBEFZ.

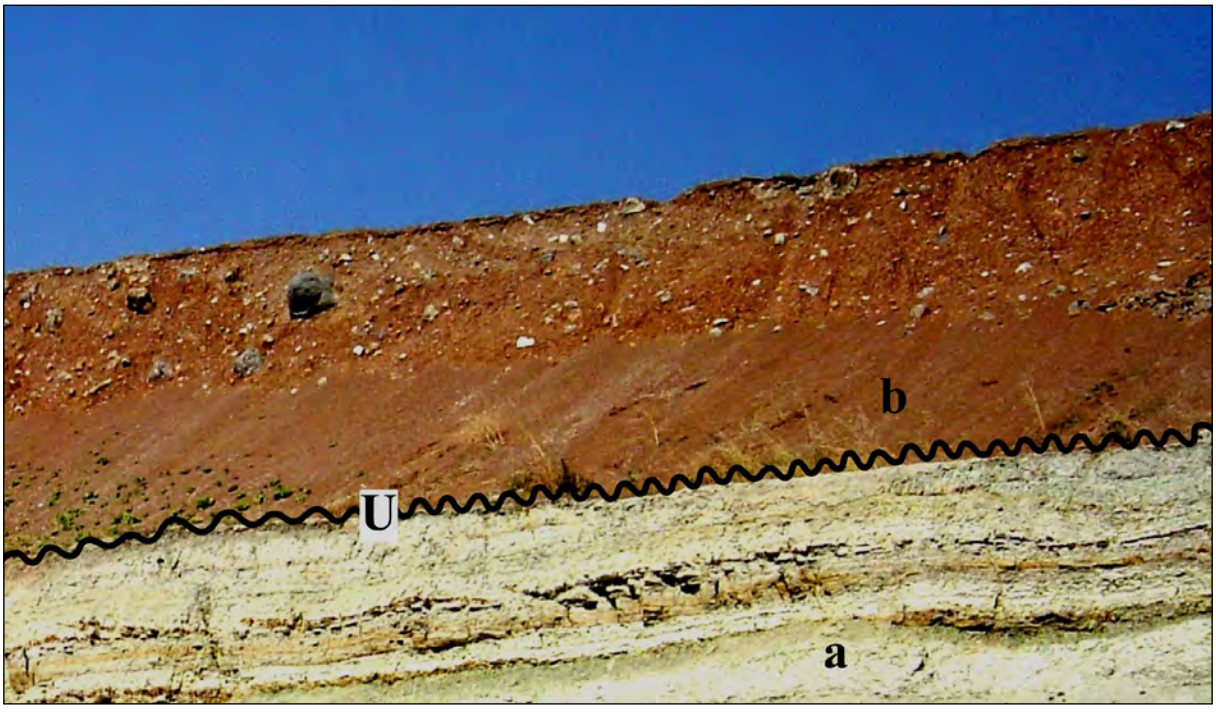

Figure 14- Field photograph illustrating the angular unconformity (U) separating older and deformed graben fill (a) from the flat-lying Quaternary neotectonic fill (b).

sedimentary lithofacies with coal seams intercalations. It is succeeded by a thick package of andesitic to basaltic volcanic breccia at the topmost (Figure 16).

This volcano-sedimentary sequence is overlain with an angular unconformity by the nearly flat-lying fluvial to gravity-induced sedimentary sequence of Quaternary age (Figures 13 and 16). The older sequence was deposited in a tectonically very active graben. This is indicated by some well-developed and preserved synsedimentary slump folds and growth faults (Figure 17).

This older graben fill was deformed and uplifted on a regional scale at the end of Miocene or most probably during Pliocene. This is revealed by the folds with the E-W-trending axes and thrust to reverse faults (Figures 17, 18 and 19).

The comparison of stratigraphical columns of both the superimposed and the pure pull-apart basins reveals that the site of the ÇBEFZ was a deep and very active lacustrine depositional setting accompanied by a volcanic eruption under the control of tensional tectonic regime and related normal faults, i.e., it was a graben during the Early-Middle Miocene; whereas, the site of the SIFZ was a high erosional area, such as a horst, during the same time slice. Starting from the Late Miocene onwards, an inversion occurred in

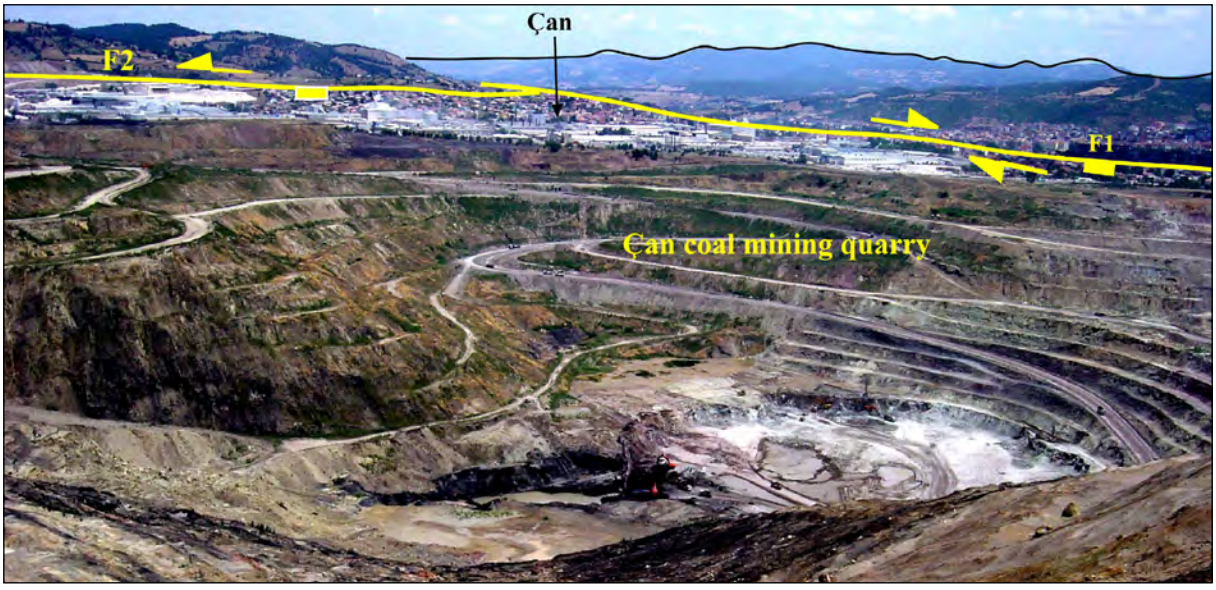

Figure 15- General view of the deeply excavated Çan coal mining quarry (view to SE). F1. ÇanEtili section of the Çan-Bayramiç-Ezine fault zone, and F2. Malıköy sinistral strike-slip fault.

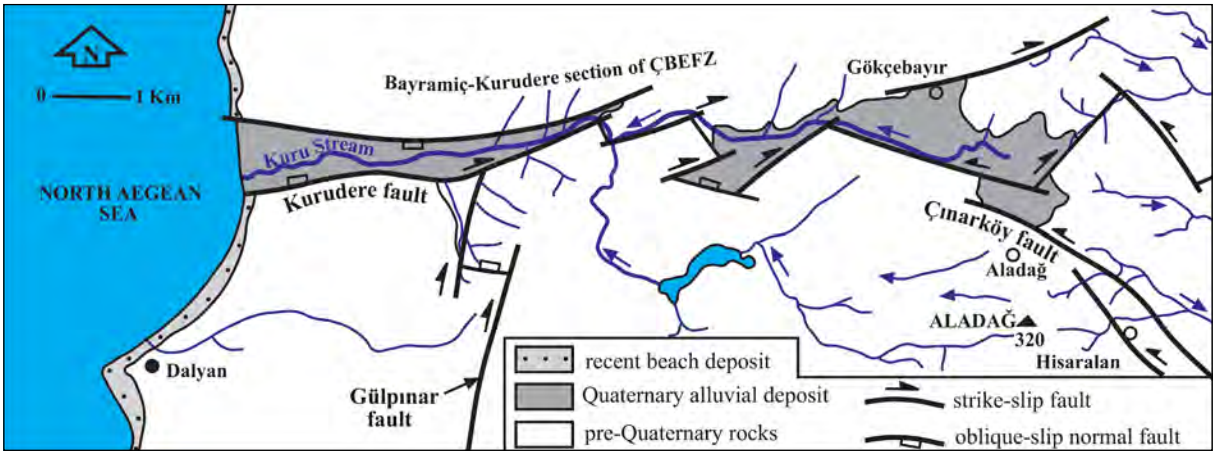

Figure 16- Neotectonic map of the Kurudere section of the Çan-Bayramiç-Ezine fault zone (ÇBEFZ).

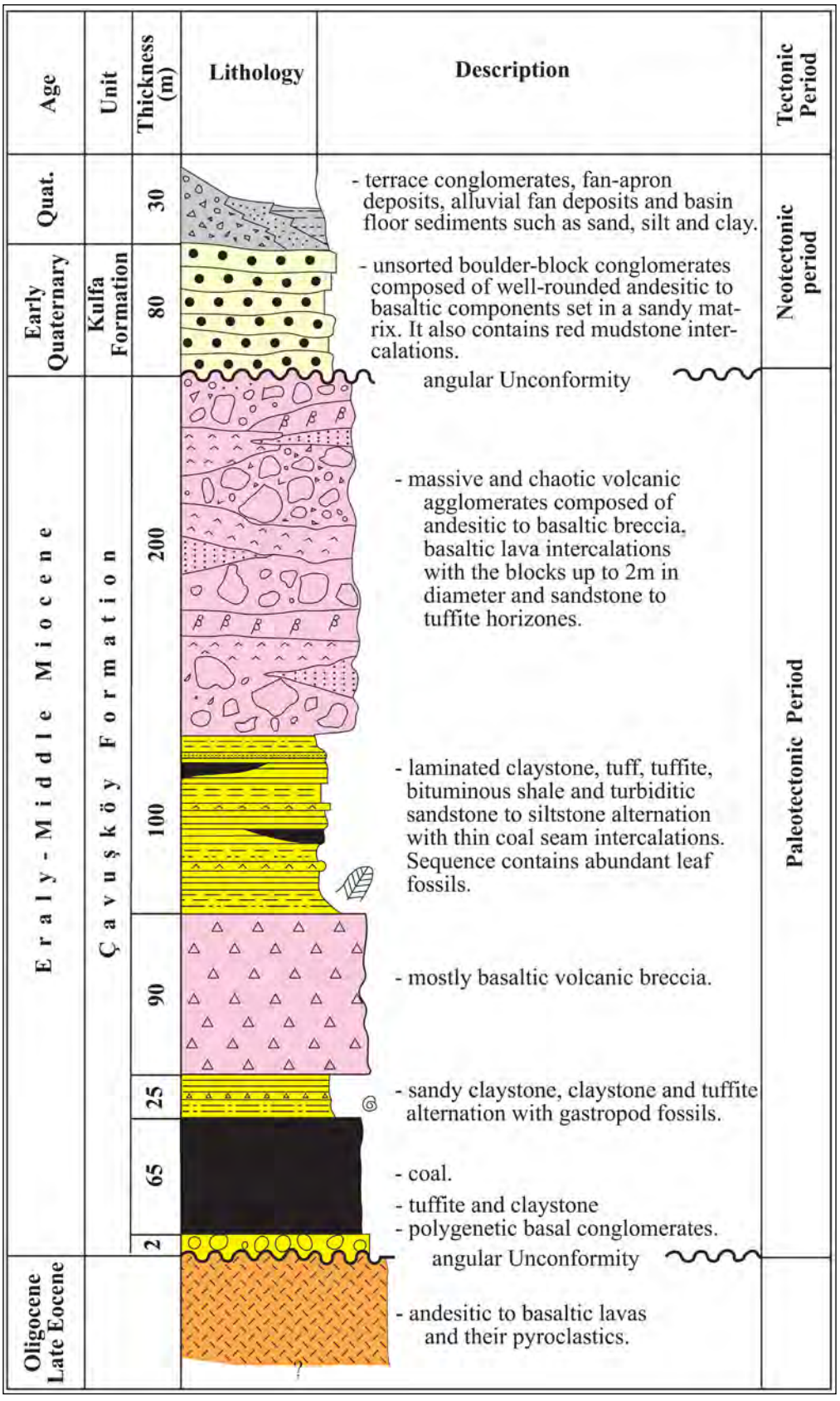

Figure 17- Generalized stratigraphical column of the Çan and Ezine-Bayramiç superimposed basins.

the tectonic regime, i.e., the tensional tectonic regime was replaced by the N-S-directed compressional tectonic regime. For this reason, the Miocene graben and its volcano-sedimentary sequence were deformed, uplifted and became an erosional area during the Late Miocene, or most probably in the Pliocene time. Starting from the Early Quaternary, both areas began to experience a strike-slip tectonic regime governed by a stress field state with the maximum principal compressive stress (σ_1) operating in approximately E-W direction. This new regime led to the reactivation of some older faults and formation of numerous new strike-slip faults. Thus, both the SIFZ and ÇBEFZ formed, and five pull-apart basins, which are drained by the Sarıköy Çay, Balıklı Çay, Kocaçay River and Karamenderes Çayı, developed within them.

3. Regional Geodynamics and Discussion

Both the Aegean Sea and western Anatolia, which comprise the west-southwesternmost frontal part of the Anatolian platelet (Figure 1a), have received much more attention in last three decades (Şengör and Yılmaz, 1981; Ercan et al., 1985; Seyitoğlu and Scott, 1991, 1996; Karacık and Yılmaz, 1998; Ring et al., 1999; Koçyiğit et al., 1999; Yılmaz et al., 2000; Bozkurt, 2001; Koukouvelas and Aydın, 2002; Kaya et al., 2004; Erkül et al., 2005; Bozkurt and Rojay, 2005; Emre and Sözbilir, 2005; Jolivet and Brun, 2010). Although the Aegean Sea and western Anatolia are relatively smaller area, they contain various and complex tectonic processes and related structures such as the subduction tectonics, exhumed HP-LT metamorphic rocks, metamorphic core complexes, intracontinental transform fault (North Anatolian

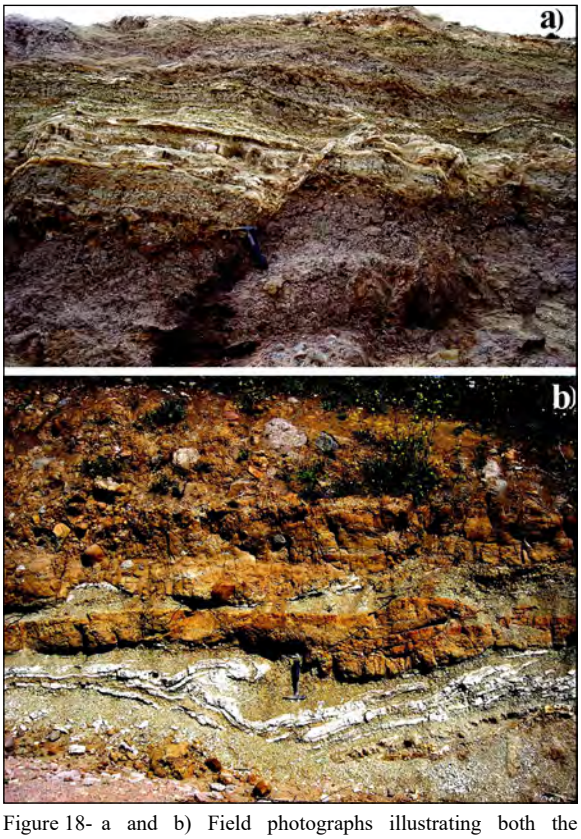

Figure 18- a and b) Field photographs illustrating both the synsedimentary growth fault (a) and slump fold (b) developed during the sedimentation in lower-middle Miocene Çan paleotectonic graben.

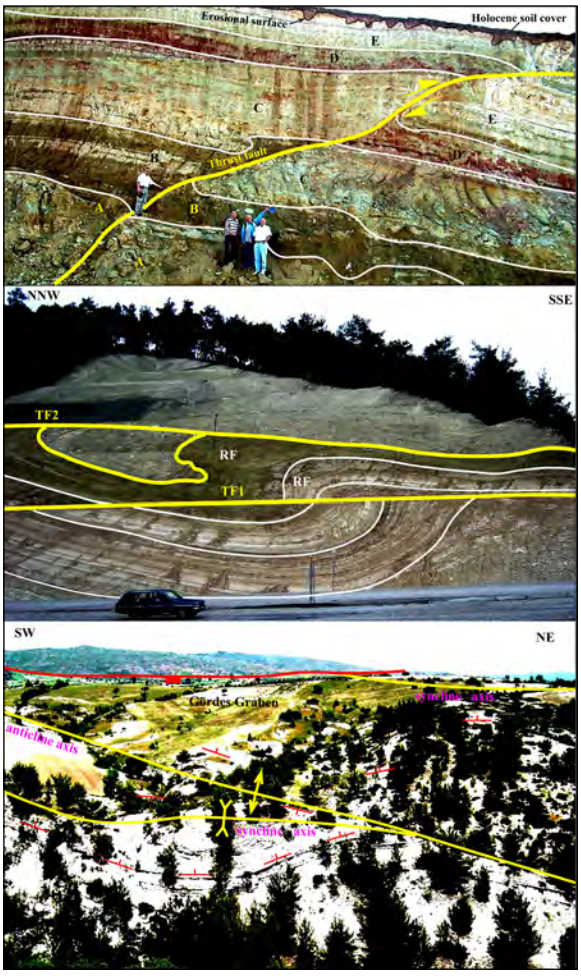

Figure 19- a) Field photograph of a Lower-Middle Miocene recumbent fold (RF) cut and offset by a thrust fault (TF1 and TF2), b) Field photograph illustrating a thrust-faulted to offset Lower-Middle Miocene fluvio-lacustrine sedimentary sequence of A, B, C, and D, and c) Field photograph illustrating the margin-boundary normal fault and folds with approximately E-W trending axes developed in the Miocene basin fill of the NE-trending Gördes graben.

Fault System), Tertiary-Quaternary magmatic rocks, trench, the Plio-Quaternary volcanic arc, back-arc rifting, orogenic collapse, widespread graben-horst system, strike-slip basins and their mutual interactions (Figure 1b).

Some of earlier studies (Şengör and Kidd, 1979, 1985; Dewey et al., 1986; Şaroğlu and Yılmaz, 1986) have reported that the continent-continent collision of Eurasian and African-Arabian plates and the entire demise of the intervening oceanic realm (southern branch of Neotethys ocean) imply to the end of paleotectonic period and onset age of the strike-slip faulting-dominated neotectonic period in eastern Türkiye. In contrast to the ideas of these authors, our detailed field studies (Koçyiğit et al., 2001; Aksoy et al., 2007; Çolak et al., 2012; Koçyiğit, 2013; Koçyiğit and Canoğlu, 2017) carried out directly in the field in a broad area covering both the eastern Anatolia and some parts of Lesser Caucasus indicated that: 1) There is an approximately 9 Ma long transitional period between the paleotectonic and neotectonic periods in eastern Türkiye, 2) the E-W trending folds, thrust-to reverse faults and ramp basins represent the Late Miocene-Middle Pliocene transitional period, and 3) the strike-slip neotectonic regime has commenced in the Late Pliocene. Because, for the wholesale establishment of a neotectonic regime in a region, it has to be preceded by a series of regional inversions such as magmatic activity, style of tectonic regime, deformation pattern, type of basin and sedimentation and the stress field state. Same kind of transitional tectonic periods have also been reported from various parts of Europe (e.g. Becker, 1993). The Late Miocene-Middle Pliocene transitional period separates the pre-Serravallian paleotectonic period from the Plio-Quaternary strike-slip neotectonic period. Starting from the Late Pliocene onwards, the southern part of the Eurasian plate was subdivided into a series of diverse-sized continental wedges bounded by the sinistral to dextral strike-slip faults. The largest of these continental wedges is the Anatolian platelet that has been escaping along its boundary faults, namely the dextral North Anatolian and the sinistral East Anatolian fault systems (NAFS and EAFS), in WSW direction onto the oceanic crust of the Mediterranean Sea since the Late Pliocene (Hempton, 1987; Koçyiğit and Beyhan, 1998).

The NAFS is an intracontinental transform fault structure. It accommodates the westward relative motion of the southerly located Anatolian Platelet (Figure 1a). However, the Anatolian platelet and its westward motion are being tried to be blocked and forced to move in south-southwestward direction by a barrier, namely the mainland Greece. This regional process resulted in a new stress field state, in which the greatest principal compressive stress (σ_1) is operating in approximately E-W direction (Şengör, 1980). Thus, the bifurcation of the NAFS into three major strands, numerous fault zones to single faults, their bending at ~30° towards south to the just west of the Lake Ulubat-Bandırma-Tekirdağ imaginary line (X-Y in Figure 1b) and blocking and forcing of the Anatolian platelet to move southwestwards by the mainland Greece altogether changed the architecture of the westernmost section of the NAFS, and led to the emergence of a new neotectonic province in central to northern Aegean Sea and their nearby onshore areas. It includes the southernmost part of the Rhodope Massif, Thrace basin, the western half of the Sea of Marmara region, Biga Peninsula, Gulf of Edremit, İzmir to Doğanbey Gulfs, and all of central to northern Aegean Sea. This domain is here termed as the central to northern Aegean neotectonic province. It is now under the control of a prominent strike-slip neotectonic regime and related structures (Koçyiğit and Gürboğa, 2021). This new neotectonic domain is outlined by the NNE-trending Balıkesir-İzmir fault zone (BIFZ) to east (Uzel and Sözbilir, 2008; Koçyiğit, 2015; Koçyiğit, 2020), and the E-W-trending Metsa fault zone, which also shapes the southern foot of the Rhodope Massif along the Greece-Bulgarian state border, to north-northwest (Protopopova and Botev, 2020). Along these two major structures, the central to northern Aegean strike-slip neotectonic regime and related structures interact with the extensional neotectonic regimes in both the southwest Anatolia-Türkiye and throughout Bulgaria (Pavlides et al., 1990; Kaya et al., 2004; Uzel and Sözbilir, 2008; Koçyiğit, 2015; Sakellariou and Tsampouraki-Kraounaki, 2019; Koçyiğit, 2020). Based on tensor solution diagrams of earthquakes and the kinematic analyses of slip-plane data obtained from faults, the prominent extension directions change slightly between NNW and NNE in both Southwestern Anatolia and Bulgaria (Koçyiğit, 1984; Nalbant et al., 1998; Koçyiğit et al., 1999; Yılmaz et al., 2000; Koçyiğit, 2005; Tan et al., 2008; Kalafat et al., 2011; Koçyiğit, 2015; Sözbilir et al., 2016; Protopopova and Botev, 2020). This extension direction fits well with the general indirect extension (σ_3) in the central to northern Aegean strike-slip

neotectonic domain owing to the contraction operating in approximately E-W direction (Gökaşan et al., 2012; Koçyiğit and Gürboğa, 2021).

In the further east of northwestern Anatolia (around Kargı-Ilgaz area district, outside the study area) (Ayhan and Koçyiğit, 2010), the NAFS bifurcates into three major strands. These are informally: 1) northern strand, 2) central strand and 3) southern strand (Figure 1b). Around Sea of Marmara, the northern strand is represented by the Hendek-Yığılca (HYFZ), northern Marmara (NMFZ), Işıklar (IFZ) to Ganos fault zones and the North Aegean trough (Koukouvelas and Aydın, 2002; McNeill et al., 2004; Görgün et al., 2010; Karimi et al., 2014); the central strand by the Kaynaşlı-Gölyaka-Akyazı (KGAFZ) and the Sapanca-Yalova fault zones (SYFZ) (Figure 1b). However, the southern strand consists of numerous fault zones, fault sets and single faults. The most common of them are the Dokurcun (DFZ), Geyve-İznik (GIFZ), Yenişehir (YFZ), Demirtaş-Taşlık (DTFZ), Edincik-Denizkent (EDFZ), Karabiga (KFZ), Lapseki (LPZ), Sarıca (SFZ), Sarıköy-İnova (SIFZ), Çan-Biga-Ezine (ÇBEFZ), Skyros-Biga (SB), Truva (TF), Gülpınar (GFZ), Yenice-Gönen (YGFZ), Danişment-Pazarköy (DPFZ), Ilıca-Darıca (IDFZ), Bursa (BFZ), Manyas (MFZ), Edremit-Havran (EHFZ), and the Tuzla (TFZ) fault zones to single faults (Figure 1b) (Barka, 1992; Armijo et al., 1996; Koçyiğit, 1988; Koçyiğit et al., 1999; Ring et al., 1999; Okay et al. 1990; Koçyiğit et al., 2000; Kaya and Foulger, 2000; Sözbilir et al., 2003; Koçyiğit, 2009; Sakellariou and Tsampouraki-Kraounaki, 2019). Additionally, in the area between City of Bursa and Lake Ulubat, the southern strand of the NAFS intersects with both the WNW-trending İnönü-Eskişehir Fault System (IEFS) and the NNE trending Balıkesir-İzmir fault zone (BIFZ) (Figure 1b). Both northwestern Anatolia and northern Aegean Sea are crossed and subdivided into numerous strike-slip basins, troughs and structural highlands (pressure ridges) by the faults comprising the NAFS. The most common strike-slip faulting-related structures are the Sakarya basin (SB), the Sapanca-İzmit trough, the Armutlu pressure ridge, the northern Marmara Sea trough, Ganos pressure ridge, Saros-Sporadhes troughs along both the northern and middle strands; the Geyve basin, the İznik trough, Yenişehir basin, the Gemlik basin, the Bandırma-Gemlik trough, the Edincik pressure ridge, the Sarıköy, İnova Kazabat, Çan, Bayramiç-Ezine, Gönen and Yenice basins along the southern strand of the NAFS (Figure 1b).

The BIFZ, MFZ, YGFZ, EHFZ, TFZ, GFZ, and the Truva fault (TF) were previously studied well (Tutkun et al., 2006; Kürçer et al., 2008, 2012, 2017, 2019; Yaltırak et al., 2013; Sözbilir et al., 2016; Sümer et al., 2018; Koçyiğit and Gürboğa, 2021) (readers are referred to these papers). In contrast to these studies, the SIFZ and the ÇBEFZ are still ill-defined and have not been studied in detail. Whereas these two basins, their fills and margin-boundary faults include significant structural and stratigraphic data for the solution of onset age of the neotectonic regime, total displacement and slip rate. For this reason, the SIFZ, the ÇBEFZ and related basins were studied in detail based on the field geological mapping carried out directly in the field in the frame of the present paper (Figure 1b). Five pull-apart basins were developed along the SIFZ and ÇBEFZ. These are, from NE to SW, the Sarıköy, İnova, Kazabat, Çan and Bayramiç-Ezine basins. First three basins are the fault-wedge type of pure pull-apart basins developed along the SIFZ during the Quaternary time. This is indicated by the angular unconformity between the overlying flat-lying Quaternary basin fill and the underlying severely deformed pre-Quaternary basement rocks (Figure 8). However, the rest two basins, namely the Çan and Bayramiç-Ezine basins, are superimposed depressions with two basin fills separated by the intervening angular unconformities (Figure 16). This observation reveals that these two basins have developed episodically. Consequently, the stratigraphy of these pull-apart basins reveals strongly that the formation age of the SIFZ is Quaternary (Koçyiğit and Gürboğa, 2021). This also reveals that the onset age of the strike-slip neotectonic regime in Biga Peninsula is the Early Quaternary (Koçyiğit and Gürboğa, 2021). Whereas it was reported as the Late Miocene-Pliocene in most of the previous works (Herece, 1985, 1990; Siyako et al., 1989; Karacık and Yılmaz, 1998; Yılmaz et al., 2000; Kürçer et al., 2008, 2019). Some new geographic and geological markers were obtained in terms of the detailed field geological mapping. These are the offset drainage systems and rock units. Some of them are: 1) the Balıklı Çayı was offset up to 12 km by the SIFZ in dextral direction (X-Y in Figure 3), 2) in the same way, the Permo-Triassic Karakaya Complex has been cut and displaced up to 12 km by the SIFZ in dextral direction (X-Y in Figure 4), 3) the Kocaçay River was offset up to 20 km by the ÇBEFZ in dextral direction (X-Y in Figure 12), and 4) the southern boundary of the Lower-Middle Miocene volcano-sedimentary

sequence in Bayramiç-Ezine basin was crossed and displaced up to 30 km in right lateral direction (Figure 7 in Yılmaz et al., 2000). In the case of the uniform slip rate, there is a close relationship among the age, total displacement and slip rate of an active fault or fault zone. This can be explained by a simple equation (Slip rate = total displacement/age). In this equation the total displacements are 12 km and 20 km, the age of the active faults is Early Quaternary, i.e., 2.588 My BP. Consequently, the slip rate on both the SIFZ and the ÇBEFZ are 4.6 mm /yr and 7.7 mm/yr respectively.

4. Results

Based on data presented in the foregoing chapters, the followings are concluded:

1. In the present, the study area is under the control of a strike-slip neotectonic regime commenced in the early Quaternary. This is proven by the regional angular unconformity separating the folded to thrust-faulted pre-Quaternary rocks and the non-deformed Quaternary strike-slip basin fill. It is also evidenced by the new stress field state with a principal compressive stress (σ_1) operating approximately in E-W direction, whereas it was more or less vertical to sub-vertical in position before the Quaternary period.

2. SIFZ and related basins developed on the uplifted erosional surface of the pre-Miocene rocks. For this reason, the Sarıköy, İnova and Kazabat depressions are pure strike-slip basins of the Quaternary age. In contrast to them, the ÇBEFZ and related basins formed on the uplifted and deformed erosional surface of the Lower-Middle Miocene graben and associated fill. Therefore, Çan and Ezine-Bayramiç depressions are superimposed basins, and the most faults comprising the ÇBEFZ are the reactivated older structures inherited from the Miocene extensional paleotectonic period.

3. Based on both the structural and the geographic markers, the total dextral strike-slip displacements accumulated on the SIFZ and the ÇBEFZ are 12 km and 20 km, respectively. These displacements correspond to an approximately 4.6 mm/year and 7.7 mm/year slip rates on the SIFZ and ÇBEFZ, respectively.

4. The longest fault segments are the 14 km long Tahtalı and the 15 km long Güllüce faults. Based on the maximum lengths of fault segments, the magnitude of peak earthquakes to be originated from these segments are Mw = 6.4 and 6.5 respectively.

5. Both the SIFZ and the ÇBEFZ are active. This is also indicated by the historical earthquakes. In the present, there might be a seismic gap. The return period of peak earthquakes to be resulted from these fault zones seem approximately as 500 years and 400 years, respectively.

References

Aksoy, E., İnceöz, M., Koçyiğit, A. 2007. Lake Hazar basin: a negative flower structure on the East Anatolian fault system (EAFS), SE Turkey. Turkish Journal of Earth Sciences 16, 319-338.

Ambraseys, N. N. 2002. The seismic activity of the Marmara Sea Region for the last 2000 years. Bulletin of the Seismological Society of America 92(1), 1-18.

Armijo, R., Meyer, B., King, G. C. P., Rigo, A., Papanastassiou, D. 1996. Quaternary evolution of the Corinth Rift and its implication for the late Cenozoic evolution of the Aegean, Geophysical Journal International 126, 11-53.

Armijo, R., Meyer, B., Navarro, S., King, G., Barka, A. 2002. Asymmetric slip partitioning in the Sea of Marmara pull-apart: a clue to propagation processes of the North Anatolian fault? Terra Nova 14(2), 80-86.

Ayhan, E., Koçyiğit, A. 2010. Displacement and Kinematics of February 1, 1944 Gerede Earthquake (North Anatolian Fault System, Turkey: Geodetic and Geological Constraints. Turkish Journal of Earth Sciences 19, 295-311.

Barka, A. A., Kadinsky-Cade, K. 1988. Strike-slip fault geometry in Turkey and its influence on earthquake activity. Tectonics 7, 66-684.

Barka, A. A., 1992. The North Anatolian Fault. Annales Tectonicae 6, 174-195.

Becker, A. 1993. An attempt to define a neotectonic period for central and northern Europe: Geologische Rundschau 82, 67-83.

Bilgin, Y., Özgen, S., Has, F., Özbakır, M., Sağıroğlu, A., 1976. Çanakkale-Çan Kömür Yatağı Fizibilite Araştırması. Rapor No: 5771, 24 (unpublished).

Bingöl, E., Akyürek, B., Korkmazer, B. 1973. Biga yarımadasının Jeolojisi ve Karakaya formasyonunun bazı özellikleri. Cumhuriyet'in 50. yılı Yerbilimleri Kongresi Tebliğleri 70-77.

Bozkurt, E. 2001. Neotectonics of Turkey-a synthesis. Geodinamica Acta 14, 3-30.

Bozkurt, E., Rojay, B. 2005. Episodic, two-stage Neogene extension and short-term intervening compression in Western Turkey: field evidence from the Kiraz Basin and Bozdağ Horst. Geodinamica Acta 18, 299-316.

Çolak, S., Aksoy, E., Koçyiğit, A., İnceöz, M. 2012. Palu-Uluova strike-slip basin on the East Anatolian Fault System, Turkey: transition from paleotectonic period to neotectonic period. Turkish Journal of Earth Sciences 21 (4), 547-570.

Dewey, J. F., Hempton, M. R., Kidd, W. S. F., Şaroğlu, F., Şengör, A. M. C. 1986. Shortening of continental lithosphere: the neotectonics of Eastern Anatolia-a young collision zone. Coward, M.P., Ries, A.C. (Ed.), Collisional Tectonics. Geological Society, London, Special Publications 19, 3-36.

Duru, M., Pehlivan, Ş., Dönmez, M., Ilgar, A., Akçay, A. E. 2007. 1/100.000 ölçekli Türkiye Jeoloji Haritaları Bandırma-H18 Paftası. Maden Tetkik ve Arama Genel Müdürlüğü 102, Ankara.

Emre, T., Sözbilir, H. 2005. Küçük Menderes Grabeni doğu ucundaki andezitlerin (Başova-Kiraz-İzmir) jeolojisi, petrografisi ve jeokimyası. Bulletin of the Mineral Research and Exploration 131, 1-19.

Emre, E., Erkal, T., Tchepalyga, A., Kazancı, N, Keçer, M., Ünay, E. 1998. Doğu Marmara Bölgesinin Neojen-Kuvaterner'deki evrimi. Bullettin of the Mineral Research and Exploration 120, 289-314.

Emre, Ö., Awata, Y. 2003. Neotectonic characteristics of the North Anatolian Fault System in the eastern Marmara region. In Emre, Ö., Awata, Y., Duman, T.Y. (Eds.), Surface Rupture Associated with the August 17, 1999 İzmit Earthquake. General Directorate of Mineral Research and Exploration of Turkey, Special Publication Series: 1, 31-39, Ankara.

Emre, Ö., Doğan, A., Özalp, S., Yıldırım, S. 2011. 1/250.000 ölçekli Türkiye Diri Fay Haritası, Bandırma. NK35-11b Paftası. Maden Tetkik ve Arama Genel Müdürlüğü, Türkiye Diri Fay Haritası Serisi-3, 55.

Emre, Ö., Doğan, A., Yıldırım, C. 2012. Biga yarımadasının diri fayları ve deprem potansiyeli. Yüzer, E., Tunay, G. (Ed.). Biga Yarımadası'nın Genel ve Ekonomik Jeolojisi. Maden Tetkik ve Arama Genel Müdürlüğü, Özel Yayın Serisi-28, 163-198.

Engin, T., Özkan, Y. Z., Sarı R., Şen, P., Gedikoğlu, A., Özpeker, I. 2012. Biga Yarımadası'nın Metalojenezi, 207-272. In Yüzer and Tunay (Ed.), Biga Yarımadasının Genel ve Ekonomik Jeolojisi 28.

Ercan, T., Satır, M., Kreuzer, H., Türkecan, A., Günay, E., Çevikbaş, A., Ateş, M., Can, B. 1985. Interpretation of new chemical, isotopic and radiometric age data for western Anatolian Cenozoic volcanics. Geological Society of Turkey Bulletin 28, 121-136.

Erkül, F., Helvacı, C., Sözbilir, H. 2005. Stratigraphy and geochronology of the Early Miocene volcanic units in the Bigadiç borate basin, western Turkey. Turkish Journal of Earth Sciences 14, 227-253.

Gökaşan, E., Görüm, T., Tur, H., Batuk, F. 2012. Morpho-tectonic evolution of the Çanakkale Basin (NW Anatolia): evidence for a recent tectonic inversion from transpression to transtension. Geo-Marine Letters 32(3), 227-239.

Görgün, E., Bohnhoff, M., Bulut, F., Dresen, G. 2010. Seismotectonic setting of the Karadere-Düzce branch of the North Anatolian Fault Zone between the 1999 İzmit and Düzce ruptures from analysis of İzmit aftershock focal mechanisms. Tectonophysics 482, 170-181.

Hempton, M. R. 1987. Constraints on Arabian plate motion and extensional history of Red Sea. Tectonics 6, 687-705.

Herece, E. 1985. The fault trace of the 1953 Yenice-Gönen earthquake and some examples of recent tectonic events in the Biga Peninsula of Northwest Turkey. MSc Thesis, Pennsylvania State University, 143 (unpublished).

Herece, E. 1990. 1953 Yenice-Gönen deprem kırığı ve Kuzey Anadolu Fay sisteminin Biga Yarımadasındaki uzantıları. Bulletin of the Mineral Research and Exploration, 111, 47-59.

Jolivet, J., Brun, J. P. 2010. Cenozoic geodynamic evolution of the Aegean. International Journal Earth Science (Geologische Rundschau) 99, 109-138.

Kalafat, D., Güneş, Y., Kekovalı, K., Kara, M., Deniz, P., Yılmazer, M. 2011. Türkiye için 1900 yılından bu yana revize edilmiş ve genişletilmiş deprem kataloğu (M≥4.0). Boğaziçi University Publications 1049, 640.

Karacık, Z., Yılmaz, Y. 1998. Geology of ignimbrites and the associated volcano-plutonic complex of the Ezine area, Northwestern Anatolia. Journal of Volcanology and Geothermal Research 85, 251-264.

Karimi, B., McQuarrie, N., Lin, J.S., Harbert, W. 2014. Determining the geometry of the North Anatolian Fault East of the Marmara Sea through integrated stress modeling and remote sensing techniques. Tectonophysics 623, 14-22.

Kaya, O., Foulger, G. R. 2000. KD-GB gidişli Ege yapısal çekirdeğinin evrimi ve güncel biçim değiştirmedeki yeri. Batı Anadolu'nun Depremselliği Sempozyumu, İzmir, Proceedings, 15-20.

Kaya, O., Ünay, E., Saraç, G., Eichhorn, S., Hassenruck, S., Knappe, A., Pekdeğer, A., Mayda, S. 2004. Halitpaşa transpressive zone: implications for an Early Pliocene compressional phase in central western Anatolia, Turkey. Turkish Journal of Earth Sciences 13, 1-13.

Koçyiğit, A. 1984. Güneybatı Türkiye ve yakın dolayında levha içi yeni tektonik gelişim. Geological Society of Turkey Bulletin 27, 1-16.

Koçyiğit, A. 1988. Tectonic setting of the Geyve basin: age and total displacement of the Geyve Fault Zone. Journal of Pure and Applied Science 21, 81-104.

Koçyiğit, A. 2005. Denizli Graben-Horst System and the eastern limit of the West Anatolian continental extension: basin fill, structure, deformational mode, throw amount and episodic evolutionary history, SW Turkey. Geodinamica Acta 18, 167-208.

Koçyiğit, A. 2006. Çan Kömür Havzasının jeolojik yapısı, yapısal analizi ve fayların kazılara etkisi. METU, Faculty of Engineering, Department of Geological Engineering, Active Tectonics and Earthquake Research Laboratory. Project No. 2006-03-05-2-00-13, 20 (unpublished).

Koçyiğit, A. 2009. Neotectonics of Biga Peninsula: Biga fault system, NW Turkey. 62nd Geological Congress of Turkey, Ankara, Abstracts, 42 [in Turkish and English].

Koçyiğit, A. 2011. Gönen (Balıkesir) ruhsat sahalarının Aktif tektonik yönden değerlendirilmesi. METU, Faculty of Engineering, Department of Geological Engineering, Active Tectonics and Earthquake Research Laboratory. Project No. 11-03-09-1-0018, 43 (unpublished).

Koçyiğit, A. 2013. New field and seismic data about the intraplate strike-slip deformation in Van region, East Anatolian plateau, E. Turkey. Journal of Asian Earth Sciences 62, 586-605.

Koçyiğit, A., 2015. An overview on the main stratigraphic and structural features of a geothermal area: the case of Nazilli-Buharkent section of the Büyük Menderes Graben, SW Turkey. Geodinamica Acta 27(2-3), 84-108.

Koçyiğit, A. 2020. İzmir ili Seferihisar ilçesi 2107 no.lu jeotermal işletme ruhsatı ile 1586 no.lu arama ruhsatlarının bulunduğu sahanın jeolojik çalışması ve toplanan verilerin değerlendirilmesiyle ilgili teknik rapor. Middle East Technical University, Department of Geological Engineering, Active Tectonics and Earthquake Research Laboratory, 81 (unpublished).

Koçyiğit, A., Altıner, D., Farinacci, A., Nicosia, Conti, M. A. 1991. Late Triassic Aptian evolution of the Sakarya divergent margin: implications for the opening history of the northern Neo-Tethys, in northwestern Turkey, Geological Romana 27, 81-99.

Koçyiğit, A., Beyhan, A. 1998. A new intracontinental transcurrent structure: the Central Anatolian Fault Zone, Turkey. Tectonophysics 284, 317-336.

Koçyiğit, A., Canoğlu, M. C. 2017. Neotectonics and seismicity of Erzurum pull-apart basin, East Turkey. Russian Geology and Geophysics 58, 99-122.

Koçyiğit, A., Gürboğa, Ş. 2021. Active tectonics of Gülpınar-Tuzla area (Biga Peninsula, NW Turkey): the source of 6 February-24 March 2017 earthquake cluster. Bulletin of the Mineral Research and Exploration 166, 85-112.

Koçyiğit, A., Yusufoğlu, H., Bozkurt, E. 1999. Evidence from the Gediz graben for episodic two-stage extension in Western Turkey. Journal of the Geological Society of London 156 (3), 605-616.

Koçyiğit, A., Ünay, E., and Saraç, G. 2000. Episodic graben formation and extensional neotectonic regime in west central Anatolia and the Isparta Angle: a case study in the Akşehir-Afyon graben, Turkey. Bozkurt, E., Winchester, J.A. and Piper, J. D. A. (Ed.). Tectonics and Magmatism in Turkey and the Surrounding Area. Geological Society, London, Special Publications 173, 405-421.

Koçyiğit, A., Yılmaz, A., Adamia, S., Kuloshvili, S. 2001. Neotectonic of East Anatolian Plateau (Turkey) and Lesser Caucasus: implication for transition from thrusting to strike-slip faulting. Geodinamica Acta 14, 177-195.

Koukouvelas, I. K., Aydın, A. 2002. Fault structure and related basins of the North Aegean Sea: Tectonics 21(5), 1016.

Kürçer, A., Chatzipetros, A., Tutkun, S. Z., Pavlides, S., Ateş, Ö., Valkaniotis, S. 2008. The Yenice-Gönen active fault (NW Turkey): active tectonics and palaeoseismology. Tectonophysics 453, 263-275.

Kürçer, A., Chatzipetros, A., Tutkun, S. Z., Pavlides, S., Özden, S., Syrides, G., Vouvalides, K., Ekinci,

Y. L. 2012. An assessment of the earthquakes of ancient Troy, NW Anatolia, Turkey, 171-200. In Sharkov (Ed.). Tectonics - Recent advances. Ankara.

Kürçer, A., Yalçın, H., Gülen, L., Kalafat, D. 2015. 8 January 2013 Mw = 5.7 North Aegean Sea earthquakes and its seismotectonic significance. Geodinamica Acta 27, 175-188.

Kürçer, A., Özaksoy, V. Özalp, S., Uygun Güldoğan, Ç., Özdemir, E., Duman, T. Y. 2017. The Manyas fault zone (southern Marmara region, NW Turkey): active tectonics and paleoseismology, Geodinamica Acta 29(1), 42-61.

Kürçer, A., Özalp, S., Özdemir, E., Uygun Güldoğan, Ç., Duman, T. Y., 2019. Active tectonic and paleoseismologic characteristics of the Yenice-Gönen Fault, NW Turkey, in light of the 18 March 1953 Yenice-Gönen Earthquake (Ms=7.2). Bulletin of the Mineral Research and Exploration 159, 29-62.

McNeill, L.C., Mille, A., Minshull, T. A., Bul, J. M., Kenyon, N. H. 2004. Extension of the North Anatolian Fault into the North Aegean Trough: Evidence for transtension, strain partitioning, and analogues for Sea of Marmara basin models. Tectonics 23, 1-12.

Meade, B. J., Hager, B. H., McClusky, S. C., Reilinger, R., Ergintav, S., Lenk, O., Barka, A., Özener, H. 2002. Estimates of seismic potential in the Marmara Sea region from block models of secular deformation constrained by global positioning system measurements. Bulletin of the Seismological Society of America 92, 208-215.

Nalbant, S. S., Hubert, A., King, G. C. P. 1998. Stress coupling between earthquakes in northwest Turkey and the north Aegean Sea. Journal of Geophysical Research 24, 469- 486

Okay, A., Siyako, M., Bürkan, K. A. 1990. Biga Yarımadası'nın jeolojisi ve tektonik evrimi. Geology and tectonic evolution of Biga Peninsula. TPAG Bulletin 2(1), 83-121.

Papazachos, B. C., Kiratzi, A., Hatzidimitriou, P., Rocca, A. 1984. Seismic faults in the Aegean area. Tectonophysics 106, 71-85.

Pavlides, S., Mountrakis, D., Kilias, A., Tranos, M. 1990. The role of strike-slip movements in the extensional area of Northern Aegean (Greece). A case of transtensional tectonics. Annales Tectonicae IV/2, 196-211.

Protopopova, V., Botev, E. 2020. Evaluation and comparative analysis of stress and deformations in seismic hazard zones in Bulgaria and adjacent lands. Annals of Geophysıcs 63, 2.

Ring, U., Laws, S., Bernet, M. 1999. Structural analysis of a complex nappe sequence and Late orogenic basins from the Aegean island of Samos, Greece. Journal of Structural Geology 21, 1575-1601.

Sakellariou, D., Tsampouraki-Kraounaki, K. 2019. Plio-Quaternary Extension and Strike-Slip Tectonics in the Aegean. In Duarte (Ed.). Transform Plate Boundaries and Fracture Zones, 339-374.

Seyitoğlu, G., Scott, B. C. 1991. Late Cenozoic crustal extension and basin formation in West Turkey. Geological Magazine 128, 155-166.

Seyitoğlu, G., Scott, B. C. 1996. The age of Alaşehir graben (west Turkey) and its tectonic implications. Geological Journal 31, 1-11

Sipahioğlu, S., Matsuda, T. 1986. Geology and Quaternary fault in the İznik-Mekece area. In: Işıkara, A. M., Honkura, Y., (Ed.). Electric and Magnetic Research on Active Faults in the North Anatolian Fault Zone. Tokyo Institute of Technology, Tokyo, 25-41.

Siyako, M., Bürkan, K. A., Okay, A. İ. 1989. Tertiary geology and hydrocarbon potential of the Biga and Gelibolu peninsulas. Bulletin of Turkish Petroleum Geologists 1, 183-199.

Sözbilir, H., İnci, U., Erkül, F., Sümer, Ö. 2003. An intermittently active transform zone accommodating N-S Extension in Western Anatolia and its relation to the North Anatolian Fault System. International Workshop on the North Anatolian, East Anatolian and Dead Sea Fault Systems: Recent Progress in Tectonics and Paleoseismology, and Field Training Course in Paleoseismology, Ankara, Poster Session, 2.

Sözbilir, H., Özkaymak, Ç., Uzel, B., Sümer, Ö., Eski, S., Tepe, Ç. 2016. Palaeoseismology of the Havran-Balıkesir Fault Zone: evidence for past earthquakes in the strike-slip-dominated contractional deformation along the southern branches of the North Anatolian fault in northwest Turkey. Geodinamica Acta 28, 254-272.

Sümer, Ö., Uzel, B., Özkaymak, Ç., Sözbilir, H. 2018. Kinematics of the Havran-Balıkesir Fault Zone and its implication on geodynamic evolution of the Southern Marmara Region, NW Anatolia. Geodinamica Acta 30(1), 306-323.

Şahin, S. Y., Örgün, Y., Güngör, Y., Göker, A. F., Gültekin, A. H., Karacık, Z. 2010. Mineral and whole-rock geochemistry of the Kestanbol Granitoid (Ezine-

Çanakkale) and its mafic mikrogranular enclaves in Northwestern Anatolia: evidence of felsic and mafic magma interaction. Turkish Journal of Earth Sciences 19, 101-122.

Şaroğlu, F., Yılmaz, Y. 1986. Doğu Anadolu'da neotektonik dönemdeki jeolojik evrim ve havza modelleri. Bulletin of the Mineral Research and Exploration 107, 73-94.

Şaroğlu, F., Emre, Ö., Boray, A. 1987. Türkiye'nin diri fayları ve depremsellikleri. Maden Tetkik ve Arama Genel Müdürlüğü, Report No: 8174, 394 (unpublished).

Şaroğlu, F., Emre, Ö., Kuşcu, İ. 1992. Türkiye Diri Fay Haritası. Maden Tetkik ve Arama Genel Müdürlüğü, Ankara.

Şengör, A. M. C. 1980. Türkiye'nin neotektoniğinin esasları. Türkiye Jeoloji Kurumu, Conference Series 2, Ankara, 40.

Şengör, A. M. C., Kidd, W. S. F. 1979. Post-collisional tectonics of the Turkish-Iranian plateau and a comparison with Tibet. Tectonophysics 55, 361-376.

Şengör, A. M. C., Yılmaz, Y. 1981. Tethyan evolution of Turkey: a plate tectonic approach. Tectonophysics 75, 181-241.

Şengör, A. M. C., Görür, N., Şaroğlu, F. 1985. Strike-slip faulting and related basin formation in zones of tectonic escape: Turkey as a case study. Biddle and Christie-Blick, (Ed.). Strike-Slip Faulting and Basin Formation. Society of Economic Paleontologists and Mineralogists, Special Publications 37, 227-264

Tan, O. M., Tapirdamaz, C., Yörük, A. 2008. The earthquake catalogues for Turkey. Turkish Journal of Earth Science 17, 405-418.

Tutkun, S. Z., Pavlides, S., Chatzipetros, A. 2006. Morphotectonics of Troy fault (NW Turkey), European Geosciences Union General Assembly, Vienna, Austria, 2-7 April 2006, Geophysical Research Abstracts, 8, 06536.

Uzel, B., Sözbilir, H. 2008. A first record of a strike-slip basin in Western Anatolia and its tectonic implication: the Cumaovası basin. Turkish Journal of Earth Sciences 17, 559-591.

Wells, D. L., Coppersmith, S. R. 1994. New empirical relationships among magnitude rupture length, rupture width, rupture area and surface displacement. Bulletin of Seismological Society of America 84, 974-1002.

Wilcox, R. E., Harding, T. P., Seely, D. R. 1973. Basic wrench tectonics. AAPG 57, 74-96.

Yaltırak, C., İşler, E. B., Aksu, A. E., Hiscott, R. H. 2013. Evolution of the Bababurnu Basin and shelf of the Biga Peninsula: Western extension of the middle strand of the North Anatolian Fault Zone, Northeast Aegean Sea, Turkey. Journal of Asian Earth Sciences 57, 103-119.

Yılmaz, Y., Genç, S. C., Gürer, O. F., Bozcu, M., Yılmaz, K., Karacık, Z., Altunkaynak, F., Elmas, A. 2000. When did the western Anatolian grabens begin to develop? In Bozkurt, Winchester and Piper, Tectonics and Magmatism in Turkey and the Surrounding Area. Geological Society, London, Special Publications 173, 353-384.

Bulletin of the Mineral Research and Exploration

http://bulletin.mta.gov.tr

First Mammuthus (Elephantidae) findings from Samsun district (Türkiye)

Ebru ALBAYRAK[a*]

[a]*General Directorate of Mineral Research and Exploration, Natural History Museum, Ankara, Türkiye*

Research Article

Keywords:
Elephantidae, Mammuthus Meridionalis, Mammuthus Trogontherii, Quaternary, Samsun.

Received Date: 03.07.2022
Accepted Date: 13.10.2022

ABSTRACT

Located between Africa, Asia and Europe, Anatolia is a crossroads for the migration of many mammals such as elephantids. For this reason, important fossils belonging to different species of elephantids were found from various localities. In this study, mammoth molars found in Samsun-Ladik were examined. As a result of the examination, *M. meridionalis* and *M. trogontherii* were identified for the first time from this region. Although the number of fossils examined is very small, the results obtained are very important as *Mammuthus* was identified for the first time from Samsun. When considered together with the *Mammuthus* species identified from Anatolia so far, the results obtained from Samsun will provide information about the distribution of the *Mammuthus* genus in Anatolia and the changes it has undergone.

1. Introduction

Anatolia, paleogeographically, has a very important position during the migration of the Elephantidae (elephants) between Africa, Asia and Europe. The genus *Mammuthus* of the Elephantidae family, which is one of the most important mammal families of the Quaternary period, draws a lot of attention due to the important changes it has shown in a short time against the climate and environmental changes that took place in the Quaternary period. From approximately 3 million years ago until the end of the Pleistocene, mammoths found in Eurasia underwent very significant changes including shortening and heightening of the cranium and mandible, increase in molar hypsodonty (HI), increase in plate number (P), and thinning of dental enamel. Based on these changes, European mammoths have conventionally been divided into three chronospecies: Early Pleistocene *M. meridionalis*, Middle Pleistocene *M. trogontherii*, and Late Pleistocene *M. primigenius* (Maglio, 1973; Lister, 1996; Lister et al., 2005). However, after some studies in recent years, there have been discussions about earlier primitive mammoth species (Lister and Van Essen, 2003; Markov, 2012; Albayrak, 2017; Rabinovich and Lister, 2017).

Various studies have been made on *Mammuthus* fossils found in Turkey to date (Falconer, 1857; Şenyürek, 1960, 1961; Becker-Platen and Sickenberg, 1968; Sickenberg et al., 1975; Adam, 1988; Dayan, 1989; Mayda, 2002; Albayrak and Lister, 2012; Boulbes et al., 2014). The first of these studies was done by Falconer (1857). He identified the molars found in Erzurum as a new species, *Elephas armeniacus*, and due to the morphological similarity of these molars to *M. trogontherii* found in Europe, Maglio (1973) considered them to be synonyms and renamed the material from Europe as *M. armeniacus*. However, the validity of *E.* (*Mammuthus*) *armeniacus* as a species is

Citation Info: Albayrak, E. 2023. First Mammuthus (Elephantidae) findings from Samsun district (Türkiye). Bulletin of the Mineral Research and Exploration 172, 141-148. https://doi.org/10.19111/bulletinofmre.1188761

**Corresponding author: Ebru ALBAYRAK, ebru.albayrak@mta.gov.tr*

controversial. Adam (1988) revealed that the samples were insufficient and that these molars were similar to the molars of the Asian elephant (*E. maximus*). For this reason, the fossils from Erzurum that are accepted as *Mammuthus* by some researchers and *Elephas* by others will not be discussed in this study.

The fossils examined in this study are those found in different old coal mines in Samsun-Ladik and delivered to museums mostly by local people. Although the localities where the fossils were found are not known exactly, the fact that the data of *Mammuthus* were obtained for the first time around Samsun provides very important data for the Quaternary fauna of Anatolia.

2. Locality

The fossils in this study were found in various places in the Ladik district of Samsun. Ladik is located in the south of Samsun city center, close to the provincial border of Amasya (Figure 1). Since the fossils in the study were found incidentally from the coal mines in that region, there is little information about the exact locality and stratigraphic level. Although there are various studies on the geology of the region (such as Öztürk, 1979; Aktimur et al., 1992; Gültekin et al., 2011), there is not enough study on the Quaternary.

3. Materials and Methods

The specimens studied in this study are the fossils found in Samsun-Ladik by citizens and delivered to museums. Specimens 55LAD01 and 55LAD02 were delivered to the MTA Natural History Museum and the others were delivered to the Samsun Museum.

Terminology follows Maglio (1973). Upper molars are indicated by upper-case letters, lowers by lower-case. The small lamella in the anterior and posterior of the tooth and does not extend to the root of the tooth, unlike the lamellae, and therefore merges with the lamella behind or in front of it, is called the talon in the upper tooth and the talonid in the lower tooth and is expressed with an x. The small posterior element of a last molar (M3/m3) when extending to the base of the crown and thus not technically a talon is termed

Figure 1- Geographic position of Samsun-Ladik (modified from Google Earth).

platelet and abbreviated p. All measurements were taken according to Aguirre (1969), Maglio (1973) and Lister (1996). The number of missing lamellae as a result of fracture or wear in the anterior part has been estimated according to the condition of the anterior roots (Sher and Garutt, 1987).

4. Systematic Paleontology

Ordo : Proboscidea Illiger, 1811.

Family : Elephantidae Gray, 1821.

Genus : *Mammuthus*, Brookes, 1828.

Type species : *Mammuthus meridionalis* (Nesti, 1825).

Age: Early Pleistocene.

Material: Right upper M3 (55LAD01) (Figure 2a, b).

Description: The tooth is broken anteriorly. Since the roots are not visible in this part, it is not clear how many lamellae are missing. There is a small deficiency in the posterior part, but the shape of the posterior part is similar to that of M3. The measurements are given in Table 1. The tooth has 7 lamellae and posterior talon. Cementum is quite thick (11 mm). The lamella frequency is low (LF: 4.67). The enamel has the characteristics of *M. meridionalis*; thick and very few wrinkles towards the edges of the lamellae, slightly more wrinkled in the middle, anterior and posterior expansions of the enamel in the middle of the enamel loop, and almost equal enamel rings. Although the height cannot be measured precisely because all the lamellae are worn, it is seen that the tooth has a low crown. When the measurements of the tooth and the enamel structure are examined in detail, it is identified as *M. meridionalis*.

Ordo : Proboscidea Illiger, 1811.

Family : Elephantidae Gray, 1821.

Genus : *Mammuthus*, Brookes, 1828.

Type species : *Mammuthus meridionalis* (Nesti, 1825).

Age: Early Pleistocene

Material: Left upper M2 (55LAD03) (Figure 2c, d)

Description: The tooth has 7 lamellae and posterior talonids. The measurements are given in Table 1. It is broken anteriorly, but according to the shape and root structure of the tooth, approximately 2 lamellae are missing from the anterior which makes the number of the plates 9. The lamella frequency is low (LF: 4.81). The height could not be measured precisely because all the lamellas were worn. However, it can be said that the tooth has a low crown. Enamel has typical *M. meridionalis* features; anterior and posterior expansions of the enamel in the middle part, less enamel wrinkles towards the edges, a few prominent and large enamel folds in the middle and enamel thickness. According to the measurements and enamel structure, this tooth is identified as *M. meridionalis*.

Ordo : Proboscidea Illiger, 1811.

Family : Elephantidae Gray, 1821.

Genus : *Mammuthus*, Brookes, 1828.

Type species : *Mammuthus trogontherii* Pohlig, 1885.

Age: Middle Pleistocene.

Material: Right upper M3 (55LAD02) (Figure 2e, f).

Description: The tooth is broken anteriorly. However, according to the first roots, it is clear that two lamellae are missing. In this case, the tooth has 20 lamellae and a platelet. The measurements are given in Table 1. Cement is thin (5 mm). The fact that the tooth has a high crown (HI: 1.74) and a high lamella count (P: 20) indicates that this tooth may be *M.*

Table 1- Measurements of the molars of *Mammuthus* specimens from Samsun-Ladik. Measurements in round brackets are considered not to present original values due to wear. Measurements in square brackets are estimates of original values. LAD is for Ladik.

Specimen	Number of plates	Width	Height	Hypsodonty index	Lamellar frequency	Enamel thickness
55LAD01 (M3)	-7p	113.4	(130.3)	(1.15)	4.67	3.68
55LAD02 (M3)	-18p [20p]	108.4	188.8	1.74	6.83	2.68
55LAD03 (M2)	-7x [10]	103.9	(122.0)	(1.18)	4.81	3.2

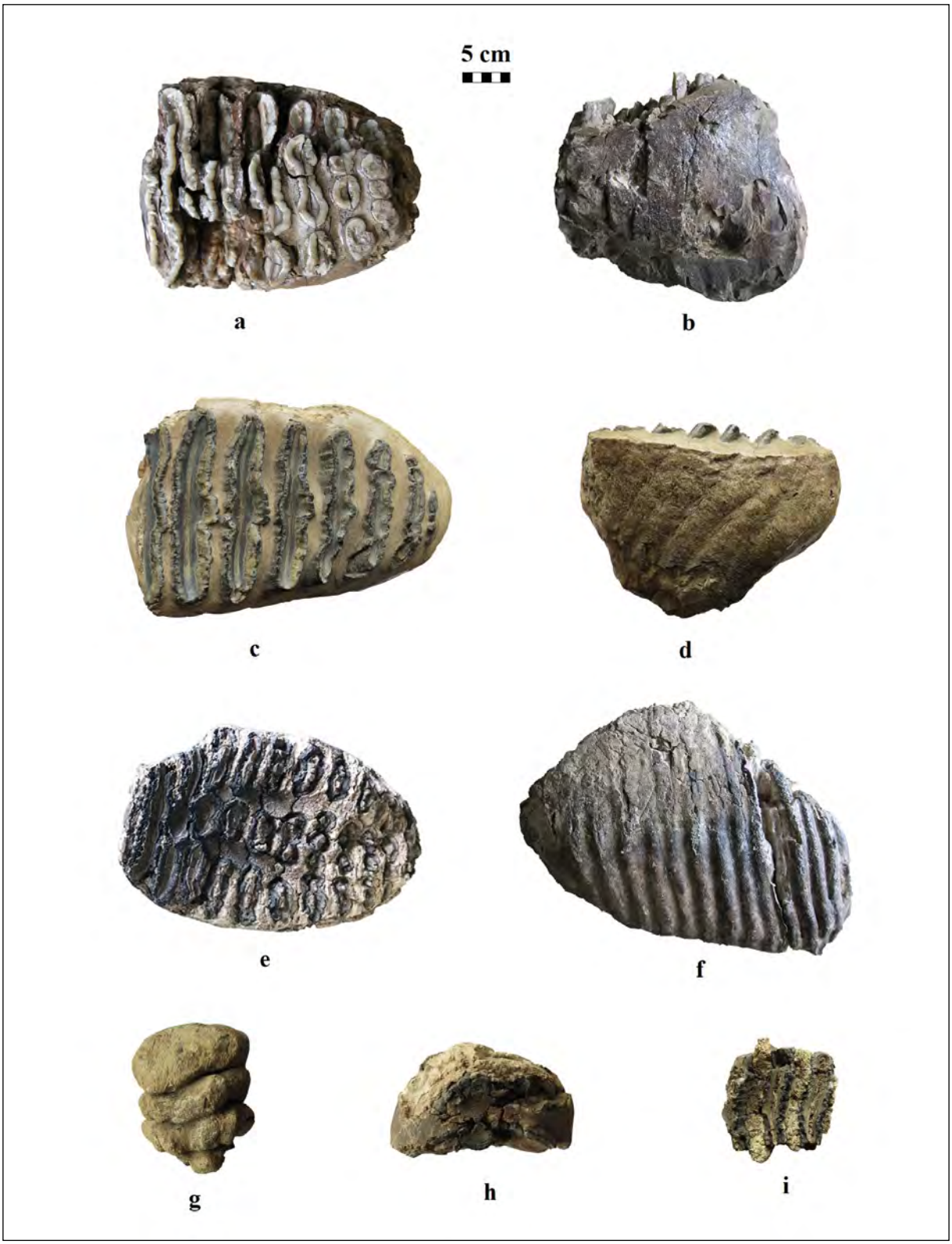

Figure 2- The molars examined in this study. 55LAD01, *Mammuthus meridionalis*, a) occlusal view, b) labial view (M3, right, MTA Natural History Museum); 55LAD03, *Mammuthus meridionalis*, c) occlusal view, d) labial view (M2, left, Samsun Museum); 55LAD02, *Mammuthus trogontherii*, e) occlusal view, f) lingual view, (M3, right, MTA Natural History Museum); 55LAD04, g) occlusal view (fragment of a molar, Samsun Museum); 55LAD05, h) occlusal view (fragment of a molar, Samsun Museum); 55LAD06, cf. *Mammuthus*, i) occlusal view (fragment of an upper molar, Samsun Museum).

trogontherii. The lamella frequency is high (LF: 6.83). The less worn lamellae have subequal enamel rings and anterior and posterior expansions in the middle part. The enamel is thinner and has more wrinkles in the middle of the lamellae, while there is less wrinkles towards the edges. Except for the wrinkles, there is no obvious fold in the middle. When the measurements and the structure of the enamel are examined, this tooth is identified as *M. trogontherii.*

Ordo : Proboscidea Illiger, 1811.

Family : Elephantidae Gray, 1821.

Material: Fragments of upper molars (55LAD04, 55LAD05).

Description: 55LAD04 (Figure 2g) has last 3 posterior lamellae and probably is the upper M1. No lamella has been worn, so the tooth is not sufficient for any diagnosis. 55LAD05 (Figure 2h), consisting of 2 posterior lamellae and posterior talon, probably belongs to the upper M1. Seen from the occlusal surface, the worn lamellae show several subequal enamel rings, generally seen in *Mammuthus*. However, it is not possible to make a diagnosis because there are very few lamellae of the tooth and their measurements could not be taken.

Ordo : Proboscidea Illiger, 1811.

Family : Elephantidae Gray, 1821.

Genus: cf. *Mammuthus*, Brookes, 1828.

Material: Fragment of upper molar (55LAD06) (Figure 2i).

Description: It consists of 3 lamellae from the middle part of probably the upper molar. The lingual and labial parts are worn. The way the enamel is wrinkled and worn resembles that of *Mammuthus*. While the enamel wrinkle is less at the lingual and labial sides, it increases towards the middle, and there is an anterior and posterior expansion in the middle of the enamel loop, and there are few enamel folds where this expansion occurs. Necessary measurements could not be taken because most of the tooth is missing. Therefore, a definitive diagnosis has not been made, but according to the enamel structure, it is thought to be *Mammuthus* sp.

5. Discussion

In this study, mammoth molars found in old coal mines were examined. Although there are few fossils, some of which consist of only tooth fragments, it is very important because it is the first data from the Quaternary period from Samsun.

M. meridionalis has been identified from several localities in Anatolia so far (Table 2). Among them, *M. meridionalis* identified from Eskişehir-Yukarisöğütönü has primitive features. Especially the lamella number (x11p) and lamella frequency (3.93) of m3 (no: 1853) is quite low for typical *M. meridionalis*. Therefore, these fossils were identified as primitive *M. meridionalis*, morphologically between *M. rumanus* and *M. meridionalis*, as an early mammoth (Albayrak and Lister, 2012; Albayrak, 2017). According to the revised biochronological zonation of the continental Neogene of Europe and Western Asia, the faunal composition at Yukarısöğütönü is Villanyian, MN17, approximately 2.2-1.8 Ma. (De Bruijn et al., 1992). M2 (2221B), identified from Konya-Zengen, has typical *M. meridionalis* features. However, the other two incomplete m3s have low lamella frequency and lamella number, similar to the Yukarısöğütönü fossils (Albayrak and Lister, 2012). Although the number of fossils found in Zengen is low, *M. meridionalis* specimens from Zengen can be considered at a close evolutionary level with those from Yukarısöğütönü.

Table 2- Comparative measurements for M3 of *M. meridionalis* from Turkey and Maglio (1973). a) Mayda, 2002, b) Albayrak and Lister, 2012, c) Boulbes et al., 2014. The measurements given by Maglio (1973) are the average of the measurements of M3s found from various localities belonging to *M. meridionalis*. Measurements in round brackets are considered not to present original values due to wear.

Specimen	Number of plates	Width	Height	Hypsodonty index	Lamellar frequency	Enamel thickness
55LAD01 (M3)	-7p	113.4	(130.3)	(1.15)	4.67	3.68
2306 (M3)[a]	x12p	119.5	134.1	1.2	3.93	3.67
MTA2[b]	-8.5x	96.5	(117.0)	(1.21)	5.0	3.3
PV-1469[c]	-9	(107.0)	-	-	4.5	3.8
Maglio (1973)	12.8	104.8	122.7	1.25	4.9	3.3

Mayda (2002) identified the molar tooth found from Aşağıçobanisa (west of Turkey) (Early-Middle Pleistocene, MNQ 19-20) as *M. meridionalis*. This specimen has a higher lamellar frequency and thinner enamel than the Yukarısöğütönü and Zengen specimens (Table 2, MTA2). Boulbes et al. (2014) suggested that the large mammal assemblage, including *Archidiskodon meridionalis meridionalis*, identified in the Denizli Basin (southwest of Turkey), is similar to the Southern and Western European Late Villafranchian and may be older than 1.2 Ma. *M. meridionalis* identified here has typical *meridionalis* features (Table 2, PV-1469).

The number of plates, hypsodonty index, lamella frequency and enamel thickness of 55LAD01 examined in this study were similar to those found in localities other than Yukarısöğütönü. It is also consistent with the measurements given by Maglio (1973) for the typical *meridionalis*.

55LAD03 has slightly more primitive features than *M. meridionalis* M2 (2221B) found from Konya-Zengen and typical *M. meridionalis* for which Maglio (1973) gives the average of its measurements (Table 3). Although the number of plates is not very low, the lamellar frequency is slightly lower and the enamel is a little thicker. With such a small number of specimens, Early Pleistocene can be considered for the age of *M. meridionalis* specimens found in Ladik.

M. trogontherii has been identified from three localities in Anatolia so far: Erzurum-Pasinler, Amasya-Suluova and Konya-Dursunlu. Since M3 is not among the specimens from Pasinler, it was not used for comparison in this study. M3 identified from Suluova, with its high crown (HI: 1.68), high lamella count (x19p) (Table 4) and enamel wear pattern on the occlusal face fall within the limits of *M. trogontherii*. The tooth from the Eski Çeltek Coal Mine in Suluova was found from the Pleistocene layer overlying the Eocene aged layer. According to the latest studies in this region, the age of *M. trogontherii* found in Suluova is dated to approximately 1 mya (Erturaç et al., 2019).

Dursunlu, another locality where *M. trogontherii* was identified, is an interesting locality with its *Mammuthus* specimens. According to palaeomagnetic analysis, the minimum age is 780.000 years. Studies on micromammals indicate, from the presence of *Allophaiomys nutiensis*, that the fauna of Dursunlu can be correlated with Lower Biharian faunas of Les Valerots (France) and Monte Peglia (Italy) which are considered to be about 900.000 years old (Güleç, 1996; Güleç et al., 1997). Transitional populations between *M. meridionals* and *M. trogontherii* are seen between 1.0-0.7 Ma in many localities in Europe (Lister et al., 2005; Lister and Stuart, 2010). M3 (42-DUR-1-41) (Table 4) and m3 (42-DUR-1-40) found in Dursunlu were identified as *M. trogontherii*. On the other hand, dp4 (42-DUR-1-29) is similar to *M. meridionalis* (Albayrak and Lister, 2012). For this reason, it can be thought that the Dursunlu mammoths show transitional group characteristics, similar to localities in the same age range in Europe.

When 55LAD02 is compared with Suluova and Dursunlu *M. trogontherii* specimens, similar to them it is seen to have a high hypsodonty index and lamella frequency and a thin enamel. Although the lamella frequency is higher than the other samples, it would not be appropriate to make a more detailed comparison with a single molar. Therefore, the age of *M. trogontherii* from Ladik, can be considered as approximately 1.0-0.5 years old.

Table 3- Comparative measurements for M2 of *M. meridionalis* from Turkey and Maglio (1973). a) Albayrak and Lister, 2012. The measurements given by Maglio (1973) are the average of the measurements of M2s found from various localities belonging to *M. meridionalis*. Measurements in round brackets are considered not to present original values due to wear. Measurements in square brackets are estimates of original values.

Specimen	Number of plates	Width	Height	Hypsodonty index	Lamellar frequency	Enamel thickness
55LAD03 (M2)	-7x [10]	103.9	(122.0)	(1.18)	4.81	3.2
2221B (M2)[a]	x8x	87.8	(107.1)	(1.22)	5.27	2.97
Maglio (1973)	9.7	86.8	113.9	1.31	5.1	2.9

Table 4- Comparative measurements for M3s of *M. trogontherii* from Turkey and Maglio (1973). a) Albayrak and Lister, 2012. The measurements given by Maglio (1973) are the average of the measurements of M3s found from various localities belonging to *M. trogontherii*. Measurements in round brackets are considered not to present original values due to wear. Measurements in square brackets are estimates of original values. DUR is for Dursunlu, SUL is for Suluova.

Specimen	Number of plates	Width	Height	Hypsodonty index	Lamellar frequency	Enamel thickness
55LAD02 (M3)	-18p [20p]	108.4	188.8	1.74	6.83	2.68
42-DUR-1-41 (M3)[a]	x18p	109.0	(165.4)	(1.52)	6.13	2.79
05SUL01 (M3)[a]	x19p	108.2	181.8	1.68	6.41	2.73
Maglio (1973)	18.6	85.2	162.5	1.99	6.5	2.2

6. Results

With this study, *Mammuthus* was identified for the first time in Samsun. Although the exact localities of the fossils are not known and the number of fossils is low, the results are very important since there is no record of Quaternary large mammals from Samsun until today. *M. rumanus*, the earliest representative of mammoths in Europe, one of the most important animal groups of the Quaternary period, probably appeared in Africa about 3.5 mya and then spread to Southern Europe via the Levant (Markov and Spassov, 2003; Markov, 2012). Due to its location, Anatolia has been a very important transition point during the dispersal of the *Mammuthus* genus from Africa to Europe and Asia. Mammoth fossils of different ages have been identified from different localities in Anatolia with the studies carried out to date. The presence of Early Pleistocene aged *M. meridionalis* and Middle Pleistocene aged *M. trogontherii* in Samsun shows that this region is very important for Elephantids and Quaternary fauna. Suluova, a locality where *M. trogontherii* was previously found, is located very close to Ladik (Figure 1). Although the fossils found in both localities are few in number, this region seems to have a potential for the Quaternary mammal fauna and distribution of the genus *Mammuthus*. For this reason, it is thought that much more detailed and important data will be obtained about the Anatolian Quaternary mammal fauna, which has not yet been revealed in detail, with detailed geological and paleontological studies to be carried out in this region in the future. And also, this study demonstrates that the coal-mines in this region must include Early and early Middle Pleistocene sediments.

Acknowledgements

I am deeply grateful to the people who found the fossils studied in this study and delivered them to museums and made this work possible. I would like to thank the Samsun Museum Directorate and the museum staff for giving me the opportunity to study the fossils in their museum and for their help during the study. Adrian LISTER, the editor of the journal and anonymous reviewer helped to improve the manuscript.

References

Adam, K. D. 1988. Über pleistozäne Elefanten-Funde im Umland von Erzurum in Ostanatolien, Ein Beitrag zur Namengebung von *Elephas armeniacus* und *Elephas trogontherii*, Stuttgarter Beiträge zur Naturkunde. Geologie und Paläontologie 146, 1-89.

Aguirre, E. E. 1969. Revisión sistemática de los Elephantidae por su morfología y morfometría dentaria, Estudios Geológicos 25, 123-177, 317-367.

Aktimur, H. T., Ateş, Ş., Yurdakul, M. E., Tekirli, M. E., Keçer, M. 1992. Niksar-Erbaa ve Destek dolayının jeolojisi. Bulletin of the Mineral Research and Exploration 114, 25-36.

Albayrak, E. 2017. A new primitive elephantid from Turkey. Quaternary International 445, 43-49.

Albayrak, E., Lister, A. M. 2012. Dental remains of fossil elephants from Turkey. Quaternary International 276-277, 198-211.

Becker-Platen, J. D., Sickenberg, O. 1968. Die unterpleistozanan Kiese von Eskişehir (Anatolien) und ihre Saugetierfauna. Mitteilungen aus dem Geologischen Institut der Technischen Universität Hannover 8, 7-20.

Boulbes, N., Mayda, S., Titov, V. V., Alçiçek, M. C. 2014. Les grand mammiferes du Villafranchien supérieur des travertins du Bassin de Denizli (Sud-Ouest Anatolie, Turquie). L'Antropologie 118, 44-73.

Dayan, E. 1989. Über pleistozäne Elefanten-Funde im Umland von Erzurum in Ostanatolien, Ein Beitrag zur Fundgeschichte des *Elephas trogontherii* im Becken von Pasinler, Stuttgarter Beiträge zur Naturkunde. Geologie und Paläontologie 147, 1-21.

De Bruijn, H., Daams, R., Daxner-Höck, G., Fahlbusch, V., Ginsburg, L., Mein, P., Morales, J., Heizman, E., Mayhew, D. F., Van Der Meulen, A. J., Schmidt-Kittler, N., Telles Antunes, M. 1992. Reports of the Regional Committee on Mediterranean Neogene Stratigraphy Working Group on Fossil Mammals, Reisenburg 1990. Newsletter on Stratigraphy 26(2/3), 65-118.

Erturaç, M. K., Erdal, O., Sunal, G., Tüysüz, O., Şen, Ş. 2019. Quaternary evolution of the Suluova Basin: implications on tectonics and palaeonvironments of the Central North Anatolian Shear Zone. Canadian Journal of Earth Sciences 56, 1239-1261.

Falconer, H. 1857. On the species of Mastodon and elephant occuring in the fossil state in Great Britain, Part I: Mastodon. Quaterly Journal of the Geological Society of London 13, 307-360.

Güleç, E. 1996. New findings on the first inhabitats of Anatolia from the Dursunlu site: a preliminary appraisal. Çağlar Boyunca Anadolu'da Yerleşim ve Konut Sempozyumu-Habitat II, 3-14 Haziran 1996, İstanbul, 211-216.

Güleç, E., Clark, D., Curtis, G., Gilbert, A., Gilbert, H., Howell, F. C., Karabıyıkoğlu, M, Saraç, G., Sevim, A.,Ünay, E. 1997. The Early Pleistocene lacustrine deposits of Dursunlu, preliminary results. INTER-INQUA Colloquium, 28 March-1 April 1997, Ankara-Turkey, 69-74.

Gültekin, F., Hatipoğlu, E., Fırat Ersoy, A. 2011. Hydrogeochemistry, environmental isotopes and teh origin of the Hamamayağı-Ladik thermal spring (Samsun, Turkey). Environmental Earth Sciences 62, 1351-1360.

Lister, A. M. 1996. Evolution and taxonomy of Eurasian mammoths. Shoshani, J, Tassy, P. (Ed.). The Proboscidea: Evolution and Palaeoecology of Elephants and Their Relatives. Oxford University Press, Oxford, 203-213.

Lister, A. M., Stuart, A. J. 2010. The West Runton mammoth (*Mammuthus trogontherii*) and its evolutionary significance. Quaternary International 28(1-2), 180-209.

Lister, A. M., Van Essen, H. 2003 *Mammuthus rumanus* (Ştefănescu), the earliest mammoth in Europe. Petculescu, A., Ştiucă, E. (Ed.). Advances in Vertebrate Paleontology Hen to Panta, Institute of Speleology, Bucharest, 46-52.

Lister, A. M., Sher, A. V., Van Essen, H., Wei, G. 2005. The pattern and process of mammoth evolution in Eurasia. Quaternary International 126-128, 49-64.

Maglio, V. J. 1973. Origin and Evolution of the Elephantidae. Transactions of the American Philosophical Society 63, Part 3, 1-149.

Markov, G. N. 2012. *Mammuthus rumanus*, early mammoths and migration out of Africa: some interrelated problems. Quaternary International 276-277, 23-26.

Markov, G. N., Spassov, N. 2003. Primitive mammoths from Northeast Bulgaria in the context of the earliest mammoth migrations in Europe. Petculescu, A., Ştiucă, E. (Ed.). Advances in Vertebrate Paleontology Hen to Panta, Instituite of Speleology, Bucharest, 53-58.

Mayda, S. 2002. Aşağıçobanisa (Manisa-Turgutlu) ve çevresi kum ocağı Neojen-Kuvaterner omurgalı faunalarının paleontolojik incelenmesi. Yüksek Lisans Tezi, Ege Üniversitesi, Fen Bilimleri Enstitüsü, 105.

Öztürk, A. 1979. Ladik-Destek yöresinin stratigrafisi. Türkiye Jeoloji Kurumu Bülteni 22, 27-34.

Rabinovich, R., Lister, A. M. 2017. The earliest elephants out of Africa: taxonomy and taphonomy of proboscidean remains from Bethlehem. Quaternary International 445, 23-42.

Sher, A. V., Garutt, V. E. 1987. New data on the morphology of elephant molars. Transactions of the USSR Academy of Sciences. Earth Science Sections 285, 195-199.

Sickenberg, O., Becker-Platen, J., Benda, L., Berg, D., Engesser, B., Gaziry, W., Heissig, K., Humermann, K. A., Sondaar, P. Y., Schmidt-Kittler, N., Staesche, U., Steffens, P., Tobien, H. 1975. Die Gliederung des höheren Jungtertiärs und Altquartärs in der Türkei nach Vertebraten und ihre Bedeutung für die internationale Neogen-Stratigraphie, Geologisches Jahrbuch 15, 1-167.

Şenyürek, M. 1960. Ankara Üniversitesi'nde muhafaza edilen fosil fil kalıntılarına dair bir not. Türk Tarih Kurumu Belleten 24(96), 693-695.

Şenyürek, M. 1961. The molar of an *Archidiskodon* from Akdoğan. Türk Tarih Kurumu Belleten 25(99), 339-353.

Bulletin of the Mineral Research and Exploration

http://bulletin.mta.gov.tr

Paleoecological investigation of the Miocene (23.03-5.33 mya) rodents (Mammalia: Rodentia) in Anatolia

Erratum

Erratum: In the article of Vural, H., Özkurt, Ş. Ö. 2023. Paleoecological investigation of the Miocene (23.03-5.33 mya) rodents (Mammalia: Rodentia) in Anatolia. Bulletin of the Mineral Research and Exploration 170, 15-30 (doi: https://doi.org/10.19111/bulletinofmre.1139009), there are several uncited or quoted passages. For this, the authors apologise to the readers. In this paper, additional explanations are reported and necessary corrections are made in defective parts of the article.

1. In the first paragraph of the page 15, there is an uncited/quoted passage which was corrected as in the following:

Order Rodentia is suggested to have first appeared in the Late Paleocene (Hartenberger, 1998) and the Early Paleocene (Wu et al., 2012). This group includes more than 40% of the entire mammals, with 30 families and over 2.000 species (Carleton and Musser, 2005). The addition of paleontological findings to these numbers may provide a better understanding regarding the diversity of rodents (Chaline and Mein, 1979). Their worldwide distribution except Antarctica and some oceanic islands reflects that they have adapted to almost all habitat types (Erdal, 2017).

2. In the second paragraph of the page 15, there is an uncited/quoted passage which was corrected as in the following:

The Anatolian mainland was formed by the collision of the Arabian Plate with Eurasia in the Middle Miocene. The elevation of Anatolia provided a land bridge, allowing for the trans-continental migration of species (Şengör, 1980). The formation of Paratethys Sea was completed in the Oligocene, and terrestrial areas around it increased during the Early Miocene (Rögl, 1999). Connections formed over the Indian Ocean during the Middle Miocene. Towards the end of this period, migration routes between Paratethys and the Mediterranean closed off as a result of the collision between Eurasia and the Arabian Plate (Rögl, 1999). Land masses expanded due to the gradual retraction of Paratethys during the Miocene, and therefore, the fossil records in Anatolia are mostly recognized in Neogene terrestrial deposits (Kaya, 2017).

3. In the second paragraph of the page 16, there is an uncited/quoted passage which was corrected as in the following:

The fossil pollen analyses indicate the existence of open habitats in Central and Western Anatolia during the Early Miocene, as well as moist and swampy habitats in the western parts (Akgün et al., 2007; Akkiraz et al., 2011; Kayseri Özer et al., 2014). Ecological environments with humid forests are also reported in Anatolia in the Early Miocene (Fortelius et al., 2014).

Page 16, Material and Methods

Citation for the NOW database is not Fortelius et al. 2014, it must be like this:

The NOW Community (2023). New and Old Worlds Database of Fossil Mammals (NOW). Licenced under CC BY 4.0. Retrieved (year of data download) from https://nowdatabase.org/now/database/.

4. In the first paragraph of the section 3.2 (Middle Miocene Rodentia from Anatolia and Their Localities)

in page 20, there is an uncited/quoted passage which was corrected as in the following:

Although the paleoecological structure of the Middle Miocene is similar to that of the Early Miocene, the tropical regions shifted towards the north during this period because of expanding glaciation. As tropical areas expanded over Eurasia, the mammalian diversity in these regions also increased (Kaya, 2017).

5. In the first paragraph of the Result section in page 25, there is an uncited/quoted passage which was corrected as in the following:

During the Early Miocene, Anatolia had a paleoenvironment with low seasonality and the mammal species adapted to humid environments (Fortelius et al, 2014).

6. In the last paragraph in page 25, there is an uncited/quoted passage which was corrected as in the following:

The Middle Miocene is generally characterised by humid habitats, but dry areas are also known to sporadically exist (Fortelius et al., 2002).

7. In the first paragraph in page 26, there is an uncited/quoted passage which was corrected as in the following:

During the Middle Miocene, the diversity of family Gliridae declined drastically which also coincides with the increase in biodiversity of murines and emergence of open habitats (Kaya and Kaymakçı, 2013). The Anatolian land is known to have experienced warmer temperatures and a humid paleoecology during the Middle Miocene (Akkiraz et al., 2011), however, hypsodonty measurements suggest the existence of more open, grassland ecosystems here (Fortelius et al., 2014). The discovery of Gliridae species in Anatolia points to the existence of deciduous forests during the Middle Miocene (Kaya and Kaymakçı, 2013).

8. In the third paragraph in page 26, there is an uncited/quoted passage which was corrected as in the following:

A glimpse at the paleoecology of the Late Miocene suggests widespread presence of open habitats and an increase in the number of open land adapted mammal species. The dominance of open areas during this period led to a change in the fauna, and the period is characterized by *Myomimus* species (Kaya and Kaymakçı, 2013). Furthermore, fossil pollen analyses yielded a dry ecology throughout the inner parts of Anatolia (Akgün et al., 2007).

9. In the first paragraph in page 27, there is an uncited/quoted passage which was corrected as in the following:

Members of the family Gliridae are reported in the Late Eocene and diversify in the Miocene (Freudenthal, 1997). In Anatolia, this family is represented by the genera *Gliridinus*, *Glis*, *Vasseuromys*, *Microdyromys*, *Paraglirulus*, *Miodyromys*, and *Bransatoglis* ((Kaya and Kaymakçı, 2013). In Europe and Eastern Mediterranean, environmental changes from the Middle to the Late Miocene led to a dramatic decline in the population of Gliridae species.

10. In the last part of first paragraph in page 27, there is an uncited/quoted passage which was corrected as in the following:

In the family extant Gliridae in Turkey, unlike the genus *Myomimus*, *Dryomys* has adapted for climbing trees. While *Myomimus* lives in wooded parts of the open areas in Anatolia, *Dryomys* prefers bushy and mountainous forests (Kurtonur and Özkan, 1991; Nowak, 1999; Holden, 2005).

ACKNOWLEDGEMENT

İsmail Ahmad ABİR (Malaysia)
Sami Oğuzhan AKBAŞ (Türkiye)
İsmail AKKAYA (Türkiye)
Mohammad Ayaz ALAM (Chile)
Tvalchrelidze ALEXANDER (Georgia)
Muzaffer Özgü ARISOY (Türkiye)
Gökhan ATICI (Türkiye)
David BANKS (UK)
Yavuz BEDI (Türkiye)
Özcan BEKTAŞ (Türkiye)
Aleksey BENDEREV (Bulgaria)
Foued BOUAİCHA (Algérie)
Gülcan BOZKAYA (Türkiye)
Aydın BÜYÜKSARAÇ (Türkiye)
Fatma CANASLAN ÇOMUT (Türkiye)
Boris CHAUVİRÉ (France)
Ziyadin ÇAKIR (Türkiye)
Emin ÇİFÇİ (Türkiye)
Ayşen DAVRAZ (Türkiye)
Somaye DERVİKAND (Iran)
Michael DİEDERİCH (Germany)
Ünal DİKMEN (Türkiye)
Feyza DİNÇER (Türkiye)
Yaşar ERGUN GÖKTEN (Türkiye)
Zeynal Abiddin ERGÜLER (Türkiye)
Orkun ERSOY (Türkiye)
Chemseddine FEHDİ (Algérie)
Novi GANEFİANTO (Indonesia)
Glenn Umali GOLLA (Philippinnes)
Muhittin GÖRMÜŞ (Türkiye)
İsmail Noyan GÜNER (Türkiye)
Aynur HAKYEMEZ (Türkiye)
William HAPPER (USA)
Klaus G. HİNZEN (Germany)
Hani Asadi HOVEİZİAN (Iran)
Ming-Liang HUANG (China)
Fayaz HUSSAİN (Pakistan)
Ghoulem IFRENE (USA)
Doina IROFTİ (USA)
Ali İMER (Türkiye)
Abdelhakim JİLALİ (Morocco)
Tümay KADAKCİ KOCA (Türkiye)
Reyhan KARA GÜLBAY (Türkiye)
Mehmet Kayra KARACAHAN (Türkiye)
Hüseyin KARAKUŞ (Türkiye)
Muhittin KARAMAN (Türkiye)
Ali İhsan KARAYİĞİT (Türkiye)
Amr Abdelnassar Ali KHALIL (Tükiye)
Hayati KOÇ (Türkiye)
Demet Banu KORALAY (Türkiye)
Ceren KÜÇÜKUYSAL (Türkiye)
Ayşegül Feray MEYDAN (Türkiye)
Ahmet ORHAN (Türkiye)
Ayşe ORHAN (Türkiye)
Nazire ÖZGEN ERDEM (Türkiye)
Emre ÖZGÜR (Türkiye)
Serkan ÖZTÜRK (Türkiye)
Sevim ÖZULUKALE DEMİRBİLEK (Türkiye)
Johannes PIGNATTI (Italy)
Vera PİRES (Portugal)
Adam POROWSKİ (Poland)
James PUCKETTE (Amerika Birleşik Devletleri)
Venkatesh RAGHAVAN (Japan)
Gülcan SARP (Türkiye)
Manuel SİNTUBİN (Belgium)
Hasan SÖZBİLİR (Türkiye)
Deniz ŞANLIYÜKSEL YÜCEL (Türkiye)
Senem TEKİN (Türkiye)
Krishna TİWARİ (India)
Asuman TÜRKMENOĞLU (Türkiye)
Emin ULUGERGERLİ (Türkiye)
İnan ULUSOY (Türkiye)
Ogün Ozan VAROL (Türkiye)
Alaaddin VURAL (Türkiye)
Ergül YAŞAR (Türkiye)
Koray YILMAZ (Saudi Arabia)
Erkan YILMAZER (Türkiye)
Önder YÖNLÜ (Türkiye)
Galip YÜCE (Türkiye)
Elena Yurievna ZAKREVSKAYA (Russia)

Publication Rules for the "Bulletin of the Mineral Research and Exploration"

1. Purposes

- To contribute to the establishment of scientific communication issues in earth sciences both in Türkiye and internationally.
- To contribute to economic (mining, oil and gas, geothermal etc.), environmental and social (geoheritage etc.) studies in Türkiye and in the World.
- To make the earth science scientific research and applications made by the MTA on publicly known,
- To use the bulletin as an effective tool in the international publication exchange by keeping it at a high level in terms of quality, scope and format,

2. Scope-Attribute

In order for manuscripts to be published in the Bulletin of the Mineral Research and Exploration, they must have at least one of the following qualifications:

2.1. Research Articles and Reviews

2.1.1. Original Scientific Researches

- Such articles cover original scientific research and its results that contribute to the fundamental issues of earth sciences, research and evaluation of underground resources, and examine the environmental problems in terms of earth sciences,
- It covers research that apply new approaches and methods in solving problems related to earth sciences.

2.1.2. Review Articles

- They cover studies that compile previous research on subjects of earth sciences with a critical approach and put forward a new opinion on that subject.

2.2. Criticism and Response Articles

- Articles that criticize all or part of an article of the bulletin in the latest issue are published in the following first issue, if submitted within six months at the latest from the date of publication digitally.
- Before the publication, review articles are sent to the responsible author of the criticized article to make a response.
- If the criticism is not responded within foreseen time, the criticism letter is published alone, subsequent replies are not published. Replies are not allowed to be re-criticized.
- In criticizing and replying, scientific discussion and ethical rules should be followed. Criticism and response manuscripts should not exceed four pages, including figures, if available.

2.3. Brief Notes

- In "Brief Notes" section of the Bulletin of the Mineral Research and Exploration, the brief, objective and concise articles reflecting the data obtained from scientific researches and applications carried out in the area of earth sciences or new findings related to previously unknown geosciences in Türkiye are given place.
- The articles arranged in the "Brief Notes" section are published without waiting in the first or in the second issue the latest, after the date they are sent to the Chair of the Editorial Board in order to ensure rapid communication.
- Articles requested to be published in the "Brief Notes" section should not exceed four pages, including all figures and tables.

3. Submission and Acceptance for Manuscripts

- The manuscripts submitted to be published in the Bulletin of the Mineral Research and Exploration should be prepared in ENGLISH in accordance with the Publishing Rules of the Bulletin of the Mineral Research and Exploration, and submitted via electronic application at http://dergi.mta.gov.tr/index.php.
- The manuscript must not have been previously published partially or completely elsewhere (except in abstract form).
- Manuscripts submitted with the request for publication in the Bulletin of the Mineral Research and Exploration should not exceed 30 pages, including all illustrations. The articles exceeding 30 pages can be published if deemed appropriate by referees and editors.
- In the submitted manuscript, the number of figures and tables should be given in proportion to the main text in a ratio of 1/3.
- Corresponding author is asked to suggest at least three referees for the evaluation of the manuscript. (The proposed referees and the authors should not have any joint work within the last two years).

- Manuscripts that do not comply with the Publishing Rules for the Bulletin of the Mineral Research and Exploration in terms of quality and form are directly returned without being examined in terms of content.
- Manuscripts deemed appropriate in terms of format are sent to at least two expert referees for review by the Editorial Board of the Bulletin of the Mineral Research and Exploration.
- Authors should make the referee corrections and suggestions sent to them within 20 days and upload to the system.
- Comments from referees are evaluated by the Editors and associated editors. Manuscripts deemed necessary to be corrected are sent back to the authors with a request for correction. Whether the suggested corrections have been made or not is checked by the Editorial Board.
- In the revision proposals given by the editors and referees, if there are suggestions that are not accepted by the author and have not been corrected, a report explaining the reason for rejecting these suggestions by the author should be sent to the Editorial Board together with the corrected copies.
- After the last control at the printing stage, the pre-print of the manuscript is sent to the authors in pdf format and the printing control is requested.
- Articles, not accepted for publication are not returned to the authors, for the unpublished articles, a letter is written to the responsible author indicating the reason for rejection.

4. Language and Period of Publication

- The Bulletin of the Mineral Research and Exploration is published three times a year, each issue as being in English (printed and online) and in Turkish (online) languages.
- The spelling rules of the Turkish Language Association are valid for the spelling rules for the Turkish issue. However, in spelling of the words related to earth sciences, the spelling forms of technical terms are used in accordance with the decision of the Editorial Board (For example; underground, ground, earth's crust, etc.).

5. Spelling Draft

- The text of the manuscripts to be sent for the first review with the request to be published in the Bulletin of the Mineral Research and Exploration should be written in A4 (29.7 x 21 cm) size, word format, Times New Roman 10 pt., normal with 2.0 line spacing.
- At the bottom, top, left and right of the page 2.5 cm indent must be left. Formulas that require the use of special letters and symbols should be presented in computer media.
- In all subtitles, the initials of all words must be capital. First degree headings to be used in the article should be written in Times New Roman, 10 pt., bold and left aligned by giving numbers. Secondary headings should be written in Times New Roman, 10 pt., normal font and left aligned by giving numbers. Third-degree headings should be written in Times New Roman, 10 pt., italic font and left-aligned by giving numbers. Fourth-order headings should be written in Times New Roman, 10 pt., italic, aligned to the left, without giving numbers, and the text should continue after the title without a colon and a paragraph (see example article: www.dergi.mta.gov.tr).
- One blank line should be left after paragraphs in the text.
- Paragraph headings should be written 0.5 mm indentation.
- One article should respectively contain;

  -Title

  -Author's Name and Surname and * sign

  - Abstract

  - Keywords

  - Introduction

  - Main Text

  - Discussion

  - Results

  - Acknowledgements

  - Reference sections.
- Line and page numbers must be added to the article text.

5.1. Title of the Article

- The title should reflect the subject of the article as briefly, clearly and adequately as possible. Subjects that are not sufficiently covered in the article should not be included in the title. The first letter of the title

should be capitalized and the other words should be in lowercase letters (except for proper names) in Times New Roman, 10 pt. and bolded.

5.2. Author Name, Address and E-Mail Address

- The first name of the authors should be in lowercase (except the first letter), and the surname should be in capital letter and without any title.
- Only the name of the organization should be specified in the occupational address after the name and surname of the authors (position should not be specified).
- ORCID number should be taken from www.orcid.org and placed under the address.
- In articles written by more than one author, numbers should be placed on surnames of the authors, the address information should be included in the bottom line with a single line spacing. In this section, the corresponding author of the article should be indicated by using an asterisk (*) and the corresponding author's e-mail, telephone and other contact information must be provided.
- Abbreviations should not be used in writing the author's name and address. Addresses should be given in Turkish in Turkish publication (online) and in English in English publication (printed).

5.3. Abstract

- Abstract should be written at a level that can be understood without referring to the other parts of the article.
- The abstract should be organized as a brief presentation of the sections in the article, reflect the purpose of the article, be informative, and should be written in a way to emphasize new data and results on the subject.
- Short and simple sentences should be used in writing the abstract.
- In the abstract, there should not be any reference to other parts and illustrations of the article or to other articles.
- Information not mentioned in the main text should not be included in the abstract.
- The abstract should not exceed approximately 200 words and should be written as a single paragraph.
- Abstract should be written in Times New Roman, 10 pt., normal text with single line spacing.
- "ABSTRACT" should not be placed for the articles to be included in "Brief Notes" section.
- The English abstract should be given under the heading "ABSTRACT".

5.4. Keywords

In order to facilitate searches, five keywords that will indicate the general content of the article should be selected and specified in this section. Words used in the title should not be repeated.

5.5. Introduction

- In this section, the necessary information for preparatory and facilitative to understand the article such as the purpose of the study, its location, methods of study and previous reviews on the subject should be given.
- If an unusual way is followed in naming, classification and abbreviations within the text of the manuscript, its reason should be stated in this section.
- Each of the topics to be included in this section can create a separate paragraph or a subtitle can be given for each of them when necessary (e.g. method, material, terminology and etc.).
- This section can again be used when reminder information is needed to facilitate the understanding of the article (e.g. statistical information, formulas, experimental or application methods and etc.).

5.6. Main Body of Article

- Constitutes the main body of the article.
- In this section, the data, findings and opinions that are intended to be transferred to the reader on the subject are mentioned.
- The data used in other parts of the article such as "Abstract", "Discussions", "Results" originate from this part.
- Care should be taken not to deviate from the purpose stressed in the "Introduction" section of the article when dealing the topics. Information that does not contribute to the achievement of the purpose of the article or that is not used to reach the conclusion should not be included.
- All data used in this section and all opinions put forward should be proven by the findings obtained from the studies or based on a source by reference.

• The way and method to be followed in handling the topics vary according to the characteristics of the topics covered.

• Subject headings in necessary numbers with different stages should be used in this section.

5.7. Discussions

• The data and findings objectively conveyed in the "Main Text" section of the article should be discussed by the author in this section. Discussions should be separate from the "Results" section.

5.8. Results

• New data and findings obtained from the review that constitutes the subject of the article should be stated concisely and concretely in this section.

• Subjects that are not adequately addressed and / or covered in the main text should not be included in this section.

• The results can be given as items in order to emphasize the research results and make the expression understandable.

5.9. Acknowledgements

• In this section, important contributions in the realization of the study, which is the subject of the article, are indicated. An attitude that will distract this section from its main purpose should not be taken in the Acknowledgements.

Contribution should be stated as short and concise as possible to the persons and/or organizations that provided assistance (reading, writing, language assistance, etc.) during the research, and should not take an attitude that would distract this section from its main purpose.

5.10. References

• In this section, only the documents mentioned in the article should be included in complete.

• Abbreviations should be avoided in naming the publications and journals.

• The mentioned documents should be written in Times New Roman and 9 pt.

• The first line of the references should be written as justified to the left margin of the page, and the other lines should be written by giving a hanging indent value of 1.25.

• The references should be listed in alphabetical order, taking into account the surnames of the authors.

• If one author has more than one work in the same year, lowercase alphabet letters should be used right after the year of publication and the letters should be italic (e.g. Saklar, 2011*a, b*).

• If more than one document of the same author is cited, first his / her single-name publications in chronological order, then double-names according to the chronological order, and then multi-names according to chronological order should be given.

For example:

Corradini, C. 2007. The conodont genus Pseudooneotodus Drygant from the Silurian and Lower Devonian of Sardinia and the Carnic Alps (Italy). Bollettino-Societa Paleontologica Italiana 46 (2/3), 139-148.

Corradini, C., Serpagli E. 1999. A Silurian conodont biozonation from late Llandovery to end Pridoli in Sardinia (Italy), In Serpagli (Ed.), Studies on conodonts: Proceedings of the 7th European Conodont Symposium. Bollettino della Società Paleontologica Italiana 37 (2-3) (1998), 255-273.

Corradini, C., Corriga, M. G. 2010. Silurian and lowermost Devonian conodonts from the Passo Volaia area (Carnic Alps, Italy). Bollettino della Società Paleontologica Italiana 49 (3), 237-253.

Corradini, C., Corriga, M. G. A. 2012. Pridoli – Lochkovian conodont zonation in Sardinia and the Carnic Alps: implications for a global zonation scheme. Bulletin of Geosciences 87 (4), 635-650.

Corradini, C., Leone, F., Loi, A., Serpagli, E. 2001.Conodont Stratigraphy of A Highly Tectonised Silurian-Devonian Section in The San Basilio Area (Se Sardinia, Italy). Bollettino Della Societa Paleontologica Italiana 40 (3), 315-323, 1 Pl.

Corradini, C., Pondrelli, M., Serventi, P., Simonetto, L. 2003. The Silurian cephalopod limestone in the Monte Cocco area (Carnic Alps, Italy): conodont biostratigraphy. Revista Española de Micropaleontologia 35 (3), 285-294.

Corradini, C., Corriga, M. G., Männik, P., Schönlaub, H. P. 2015. Revised conodont stratigraphy of the Cellon section (Silurian, Carnic Alps). Lethaia 48 (1), 56-71.

- If documents of different authors with the same surname are mentioned, they should be written in alphabetical order, considering their first names.
- If documents of different author(s) with the same surname are mentioned in the same year, they should be cited as given below. Same publication rule should be applied for the single author.

For example:

"Usta, M., Yetiş, C., Nazik, A. 2018. Anamur (Mersin) dolayının stratigrafisi ve Kambriyen yaşlı kuvarsitler ile dolomitlerin endüstriyel hammadde potansiyeli. Çukurova Üniversitesi Fen ve Mühendislik Bilimleri Dergisi 35, 6, 11-22, Adana"

should be cited as (Usta, M. et. al., 2018)

"Usta, D., Ateş, Ş., Çoban, M., Deveci, Ö, Sağlam, F.M. 2014. Adıyaman-Sincik-Hilvan arasındaki bölgenin stratigrafisi ve kaya türü özellikleri. 67. Türkiye Jeoloji Kurultayı Bildiri Özleri, Ankara, 98-99"

should be cited as (Usta, D. et. al., 2018)

"Usta, M. 2018. Anamur (Mersin) dolayının stratigrafisi ve Kambriyen yaşlı kuvarsitler ile dolomitlerin endüstriyel hammadde potansiyeli. Çukurova Üniversitesi Fen ve Mühendislik Bilimleri Dergisi 35, 6, 11-22, Adana"

should be cited as (Usta, M., 2018)

"Usta, D. 2014. Adıyaman-Sincik-Hilvan arasındaki bölgenin stratigrafisi ve kaya türü özellikleri. 67. Türkiye Jeoloji Kurultayı Bildiri Özleri, Ankara, 98-99"

should be cited as (Usta, D., 2018)

- If the document is in a periodical publication (if it is an article), information about the document is given in the following order: Authors ' surname, first letters of the authors' first names. Year of publication. The name of the article. The name of the publication in which the article was published, volume number and / or issue number with the first letters in capital, the numbers of the first and last page of the document. Punctuation marks like comma and etc. after journal names should not be used.
- In the examples below, the information about the mentioned documents is organized according to different document types, taking into account the punctuation marks.

For example:

Gürsoy, M. 2017. Munzur Dağları Alt Miyosen çökelleri mollusk topluluğu ve paleoekolojisi (Doğu Anadolu, Türkiye). Maden Tetkik ve Arama Dergisi 155, 75-99.

Pamir, H. N. 1953. Türkiye'de kurulacak bir Hidrojeoloji Enstitüsü hakkında rapor. Türkiye Jeoloji Bülteni 4 (1), 63-68.

Robertson, A. H. F. 2002. Overview of the genesis and emplacement of Mesozoic ophiolites in the Eastern Mediterranean Tethyan region. Lithos 65, 1-67.

- If the document is a book: authors' surnames, authors' first names. Year of publication. Title of the book with capital letters. The name of the publishing organization or the name of the publication in which the document was published, the volume and / or issue number, and the total number of pages of the book should be specified, respectively.

For example:

Einsele, G. 1992. Sedimentary Basins. Springer Verlag, 628.

Ketin, İ., Canıtez, N. 1956. Yapısal Jeoloji. İTÜ, 308.

Meriç, E. 1983. Foraminiferler. Maden Tetkik ve Arama Genel Müdürlüğü Eğitim Serisi, 26, 280.

- If the document is published in a book containing the articles of various authors, the usual order for the document included in a periodical publication is followed until the end of the document title. Then the editors' surnames and initials and the abbreviation of the editor word "Ed." is written in parentheses. Then, the title of the book in which the document is located is written with the first letters in capital letters. Name of publishing organization. The place of publication, the volume number of the publication in which the document was published, and the numbers of the first and last pages of the document should be written.

For example:

Anderson, L. 1967. Latest information from seismic observations. Gaskell, T. F. (Ed.). The Earth's Mantle. Academic Press. London, 335-420.

Göncüoğlu, M. C., Turhan, N., Şentürk, K., Özcan, A., Uysal, S., Yalınız, K. 2000. A geotraverse across northwestern Türkiye. Bozkurt, E., Winchester, J. A., Piper, J. D. A. (Ed.). Tectonics and Magmatism in Türkiye and the Surrounding Area. Geological Society of London. Special Publication, 173, 139-162.

• If it is desired to specify the name of a book in which the writings of various authors are collected as a document; following the surnames and names of the book's editors, in parentheses the "Ed." statement is written. Year of publication. Title of the book with capital letters. The name of the publishing organization or the name of the publication in which the document was published, the volume and / or issue number and the total number of pages of the book should be specified.

For example:

Gaskel, T. F. (Ed.). 1967. The Earth's Mantle. Academic Press, 520.

• If the document is "published abstract", information about the document is given in the following order: Authors' surnames, authors' first names. Year of publication. Name of the document (paper). The name, date and place of the meeting where the paper is published, and the first and last page numbers in the book containing the abstract should be written.

For example:

Öztunalı, Ö., Yeniyol, M. 1980. Yunak (Konya) yöresi kayaçlarının petrojenezi. Türkiye Jeoloji Kurumu 34. Bilim Teknik Kurultayı, Ankara, 36.

Yılmaz, Y. 2001. Some striking features of the Anatolian geology. 4. International Turkish Geology Symposium, 24-28 Eylül 2001, Adana, 13-14.

• If the mentioned document has not been published like report, lecture notes and etc., the word "unpublished" should be written at the end of the information about the document in parentheses after the information about the document is given in the usual order for the document in a periodical publication.

For example:

Akyol, E. 1978. Palinoloji ders notları. EÜ Fen Fakültesi Yerbilimleri Bölümü, 45, İzmir (unpublished).

Özdemir, C., Biçen, C. 1971. Erzincan ili, İliç ilçesi ve civarı demir etütleri raporu. Maden Tetkik Arama Genel Müdürlüğü, Rapor No: 4461, 21, Ankara (unpublished).

• For unpublished courses, seminars and similar notes, the course organizer after document name. The place of the meeting. Title of the book and relevant page numbers should be given.

For example:

Walker, G.R., Mutti, E. 1973. Turbidity facies and facies associations. Society for Sedimentary Geology Pacific Section Short Course. Annaheim. Turbitides and Deep Water Sedimentation, 119-157.

• If the document is a thesis; author's surname, initial of the author's first name. Year of publication. Name of the thesis. The type of the thesis, the university where it was given, the total number of pages, its province and the word "unpublished" are written in parentheses.

For example:

Akıllı, H. 2019. Polatlı-Haymana (Ankara) civarı sıcak sularının izotop jeokimyası (δ18O, δD, 3H, δ13C, δ34S, 87Sr/86Sr) ve ana iz element bileşimleri ile incelenmesi. PhD Thesis, Ankara University, 255, Ankara (unpublished).

Argun Aktan, Ö. 2019. Marmara Denizi Batı Kıta Sahanlığı Yüzeysel Çökellerinde Jeojenik ve Antropojenik Ağır Metal Zenginleşmesine Yönelik Araştırmalar (Şarköy Kanyonu, KB Türkiye). MSc Thesis, Ankara University, 179, Ankara.

• Anonymous works should be arranged according to the publishing institution.

For example:

MTA. 1964. 1/500.000 ölçekli Türkiye Jeoloji Haritası, İstanbul Paftası. Maden Tetkik ve Arama Genel Müdürlüğü, Ankara.

• For the documents that are in print, no date is put after the name of the author, the name of the article and the source to be published should be specified and the word “in print” and / or “in review” should be written at the end (in parentheses).

For example:

Ishihara, S. The granitoid and mineralization. Economic Geology 75th Anniversary (in press).

• Information downloaded from the Internet should be given in the form of the name of the institution, its web address, and the date on which the web address was accessed. Turkish references should be given directly in Turkish and should be written in Turkish characters.

For example:

ERD (Earthquake Research Department of Türkiye). http://www.afad.gov.tr. 3 March 2013.

• While citing the source, the original language should be adhered to, and the title of the article should not be translated.

6. Illustrations

• All of the drawings, photographs, plates and tables used in the article are referred to as “illustrating”.

• Illustrations should be used when their use is unavoidable or when they make the subject easier to understand.

• In the selection and arrangement of the format and size of the illustrations, an attitude should be made to prevent loss of space as much as possible considering the page length and layout of the bulletin.

• The number of illustrations used should be proportional to the size of the text.

• All illustrations should be submitted in separate files regardless of the text.

• Abbreviations should not be used in illustration explanations in the text and should be numbered in the order of mention within the text.

• Photographs and plates must be submitted as a computer file in which all details can be seen for the examination of the article, with EPS, TIFF or JPEG extension and at least 300 dpi resolution.

6.1. Figures

• Drawings and photographs other than the plate to be included in the article are evaluated together as “Figure” and numbered in the order of mention in the text.

• The figures should be prepared in computer considering the dimensions of a single column width as 7.4 cm or double column width as 15.8 cm. The figure area with its caption should not exceed 15.8x21 cm.

• While preparing the figures, unnecessary details should not be included and care should be taken not to use more space than necessary for the transfer of information.

• In figure descriptions, a space should be left after the word “Figure” is written, and the number is given in the usual sequence number, followed by a hyphen (-) and a space again, and a description of the relevant figure should be written. If the figure legend exceeds the bottom lines, the following lines should to be written after the “Figure 1-” statement alignment. Figure descriptions should be created as follows, without exceeding the edges of the figure and justified on both sides.

For example:

Figure 1- The district of Sandıklı (Afyon); a) geological map of the southwest, b) the general vertical section of the study area (Seymen, 1981), c) Türkiye’s most important neotectonic structures (modified from Koçyiğit, 1994).

• Drawings should be drawn in computer properly, clean and with care.

• The use of thin lines that may disappear when minimized in figures should be avoided.

• Symbols or letters used in all drawings should not be less than 2 mm (7 pt.) in Times New Roman.

• All standardized symbols used in the drawings should preferably be explained in the drawing, if they are too long then they should be explained in the figure below.

• Bar scale should be used in all drawings and the north direction should be indicated on all maps.

• The name of the author, description of the figure, figure number should not be included in the drawing.

• Photographs should reflect the aims of the subject and should be in adequate numbers.

• Figures should be framed.

6.2. Plates

• Plates should be used in cases where multiple photographs are required to be printed together on a special paper.

• Plate dimensions must be equal to the size of the bulletin's usable area of the page.

• Figure numbers should be written under each of the figures on the plate and bar scale should be used.

• Original plates must be attached to the final copy to be submitted in the case of acceptance of the manuscript.

• Figures and plates should be numbered among themselves and independently. Figures should be numbered with Latin numerals and plates with Roman numerals (eg Figure 1, Plate I).

• There should be no explanation text on the figures inside the plate.

6.3. Tables

• All tables should be arranged in word format and should be prepared in Times New Roman.

• Tables should not exceed the size of 15x8 cm together with the table caption.

• Table explanations should be created without exceeding the edges of the figure and justified as in the example below.

For example:

Table 1- Hydrogeochemical analysis results of geothermal waters in the study area.

7. Nomenclature and Abbreviation

• Abbreviations must be in the accepted international or national form. Unusual nomenclature and abbreviations that are not standardized in the article should be avoided. In cases where it is deemed necessary to use such nomenclature and abbreviations, the way and method followed should be explained.

• There should not be a dot between the words initials used in standard abbreviations (such as MTA, DSİ).

• Abbreviations of geography aspects should be made in English (N, S, E, W, NE and etc.).

The word group to be abbreviated should be written clearly where it is mentioned first time and the abbreviation should be given in parentheses, then only the abbreviated form should be written throughout the article.

• Systems with international validity (m, inch, etc.) should be used as the unit of measure. Decimals should be separated with commas in Turkish articles and with a period in English articles.

• The names of figures, plates and tables in the article should not be abbreviated. For example, "As seen in the generalized stratigraphic section of the region (Figure 1) …….".

7.1. Chronostatigraphic and Geochronologic Nomenclature

• "International Chronostratigraphic Chart" (https://stratigraphy.org/chart), which is updated annually by the International Stratigraphic Committee, should be taken into consideration in chronostratigraphic and geochronological nomenclature.

• Position within a chronostratigraphic unit can be expressed in adjectives indicating the position, for example: lower, middle, upper and etc. When using these adjectives, it should be decided whether the lower, middle and upper distinction is formal / informal in the International Chronostratigraphic Chart.

For example:

lower Miocene, Upper Holocene and etc.

• When stating the time where a geochronological unit is, temporal adjectives such as; early, middle, late and etc. are used. When using these adjectives, the International Chronostratigraphic Chart should be taken into consideration to decide whether the adjectives begin with capital or lowercase letters.

For example:

early Miocene, Late Holocene etc.

7.2. Paleontological Nomenclature and Spelling of Fossil Names

• Original names of fossils should be used.

For example:

Nummulites with limestone

• Fossil genus and species names are written in italics, cf., aff. and gr. etc. expressions are written as normal (perpendicular). When writing fossil names for the first time, the surnames of the people who identify them and the year in which they were first defined should be written. In later uses, the surnames and the year in which they are defined may not be written. The surnames and dates of identifiers coming at the end of the fossil names are not references, they should not be included in the mentioned documents.

For example:

Alveolina aragonensis Hottinger, 1960 not a reference.

Alveolina cf. *aragonensis* Hottinger, 1960 not a reference.

Alveolina aff. *aragonensis* Hottinger, 1960 not a reference.

Alveolina gr. *aragonensis* Hottinger, 1960 not a reference.

• After the first use of the same genus in the text is written clearly, it can be abbreviated as in the example so that it will not be confused with another genus in later use.

For example:

Alveolina aragonensis, A. polathensis, A. ellipsoidalis etc.

• If the date is in parentheses after the person describing it after the name of the fossil in the text, this is a reference and should be included in the mentioned documents.

For example:

Alveolina aragonensis Hottinger (1960) is a reference.

• The following rules should be taken into account when writing the systematic paleontologic section.

a. First of all, genus, species and subspecies to be identified should be written in hierarchical order like the order, upper family, family type species and so on. Later, the species to be described should be written together with the surnames and date of the people who defined the subspecies name. If there is a photograph of the described fossil, the plate or figure with the photograph should be added under the fossil name. The names of the authors listed here are not references, so they are not included in the reference.

For example:

Order: Foraminiferida Eichwald, 1830

Superfamily: Alveolinacea Ehrenberg, 1839

Family: Alveolinidae Ehrenberg, 1839

Type Genus: *Borelis* de Montfort, 1808

Type Species: *Borelis melenoides* de Montfort, 1808
= *Nautilus melo* Fichtel and Moll, 1798

Borelis vonderschmitti (Schweighauser, 1951)

(Plate II, Figure 3-5 or Figure 3A-H).

b. Similar or synonyms (synonym) list should be left-aligned in chronological order. The page and figure number of the synonymous fossil in the relevant study should be included in the synonymous list. Authors in the synonymous list are references and must be included in the references.

For example:

1951 *Neoalveolina vonderschmitti* **Schweighauser**, page 468, Figures 1-4.

1974 *Borelis vonderschmitti* (Schweighauser), **Hottinger**, page 67, plate 98, Figures 1-7.

c. After the synonymous list is given, the definition, explanations (similarities and differences), dimensions, material, stratigraphic distribution (according to the characteristics of the fossil) should be written.

d. If the fossil is defined for the first time (new species) in the systematic paleontology section, the origin of the name, holotype, type locality, material, description, explanation (similarity and differences), age and geographical distribution, dimensions (according to the features that define the fossil) should be written. Photographs of the fossil identified for the first time by the authors must necessarily be placed in plates or figures.

e. Bar scale indicating the size of fossils must be used definitely in plates / figures.

8. References

• In the references to be made in the Main Text, only the surnames of the authors and the publication year of the mentioned article should be specified. Referencing should be arranged according to one of the following examples:

• Referring to a publication with a single author (in chronological order):

-Altınlı (1972, 1976) defined the Bilecik sandstone in detail.

It is known that the fold axes of the Devonian and Carboniferous units around İstanbul are N-S trending (Ketin, 1953, 1956; Altınlı, 1999).

• Referring to a publication with two authors:

- The upper parts of the unit include Ilerdian fossils (Sirel and Gündüz, 1976; Keskin and Turhan, 1987, 1989).

• Referring to a publication with more than two authors:

- According to Caner et al. (1975), the Alıcı formation reflects the conditions of fluvial environment.

- Unit disappears by wedging towards E (Tokay et al., 1984).

• Referring to a reference in another publication:

It is known that Lebling mentioned about the existence of Liassic around Çakraz (Lebling, 1932; Charles, 1933).

• When referring to the works of the authors with the same surname in the same year, referring the authors' first names by writing their initials:

- Many studies have been done in the field of structural geology in the study area (Gutnic et al., 1979; Yılmaz A., 1983; Yılmaz, İ., 1983; Poisson et al., 1984 etc.).

9. Prints Sent to Authors

Two copies of the relevant issue published in the Bulletin of the Mineral Research and Exploration are sent to the authors.

10. Terms of Publication and Copyrights

• Some or all of the articles to be published in the Bulletin of the Mineral Research and Exploration should not have been published before.

• Authors who submit a publication to the Bulletin of the Mineral Research and Exploration are deemed to have accepted the bulletin's publication rules in advance.

• The copyright of the manuscripts accepted for publication and converted into publications belongs to the General Directorate of Mineral Research and Exploration (MTA).

The authors of the study sign the relevant forms within the scope of the provisions specified in the Regulation of the Editorial Board regarding the transfer of copyright and submit them to the Editorial Board. After the publication of the article, MTA may pay royalty fees to the authors of the article for their declarations within the scope of the "Regulation on the Editorial and Processing Fees to be paid by the Public Organizations and Institutions".

NOTE: Information and forms about Bulletin of the Mineral Research and Exploration can be accessed from the website: http://dergi.mta.gov.tr/index.php.

172

BULLETIN OF THE MINERAL RESEARCH AND EXPLORATION

2023

Phone : +90 (312) 201 10 00
Fax : +90 (312) 287 91 88
Adress : MTA 06530 - Ankara - TÜRKİYE
www.mta.gov.tr

BULLETIN OF THE MINERAL RESEARCH AND EXPLORATION

2023 172 ISSN : 0026-4563 E-ISSN : 2651-3048

CONTENTS

Research Articles